ENHANCED PREDICTIVE CAPABILITY OF STORM SURGE MODELS IN THE BAY OF BENGAL

Von der Fakultät für Bauingenieurwesen der Rheinisch-Westfälischen Technischen Hochschule Aachen zur Erlangung des akademischen Grades eines Doktors der Ingenieurwissenschaften genehmigte Dissertation

vorgelegt von

Vagamare Ganapati Shashank

Berichter: Chair Prof. Dr. S. A. Sannasiraj
Univ.-Prof. Dr.-Ing. Holger Schüttrumpf
Prof. Dr. V. Sriram
Prof. Dr.-Ing. Jürgen Jensen
Prof. Dr. Manu Rao
Tag der mündlichen Prüfung: 14.03.2025

DEPARTMENT OF OCEAN ENGINEERING
INDIAN INSTITUTE OF TECHNOLOGY MADRAS, CHENNAI – 600036, INDIA

INSTITUTE OF HYDRAULIC ENGINEERING AND WATER RESOURCES MANAGEMENT
RWTH AACHEN UNIVERSITY, AACHEN–52074, GERMANY

ENHANCED PREDICTIVE CAPABILITY OF STORM SURGE MODELS IN THE BAY OF BENGAL

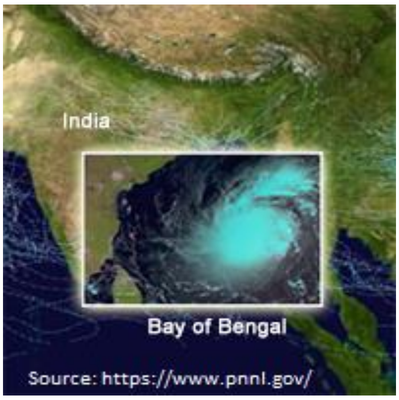

A THESIS

Submitted by

V G SHASHANK

for the award of the degree

of

DOCTOR OF PHILOSOPHY

March 2025

I dedicate this dissertation to my Parents

LIST OF PUBLICATIONS BASED ON THIS THESIS

The publications arising from the work mentioned in this thesis are as follows.

REFEREED JOURNALS BASED ON THE THESIS

1. **Shashank V G**, Sriram V, Sannasiraj SA. Improvements in wind field hindcast for storm surge predictions in the Bay of Bengal: A case study for the tropical cyclone Varadah. *Applied Ocean Research*. 2022 Oct 1;127:103324. DOI: https://doi.org/10.1016/j.apor.2022.103324.
2. **Shashank V G**, Sriram V, Schüttrumpf H, Sannasiraj SA. A new surge index incorporates cyclone track approach angle information for the Bay of Bengal. *Coastal Engineering*. 2024 Mar 1;188:104429. DOI: https://doi.org/10.1016/j.coastaleng.2023.104429.
3. **Shashank V G**, Sriram V, Schüttrumpf H., Sannasiraj SA., Investigation of morphodynamic response to the storm-induced currents and waves in the Bay of Bengal, *Applied Ocean Research*, Volume 153, 2024, 104285, ISSN 0141-1187, https://doi.org/10.1016/j.apor.2024.104285.

PUBLICATIONS IN CONFERENCE PROCEEDINGS

1. **Shashank V G**, Sriram V, Holger Schüttrumpf, Sannasiraj S A "Effect of Bottom Friction and Wind Drag Coefficient on Tropical Cyclone Storm Surge Hindcast in the Bay of Bengal" International Association for Hydraulic Environmental Engineering and Research-Asia Pacific Division, physical conference. Singapore: Springer Nature Singapore, 2022. DOI: https://doi.org/10.1007/978-981-97-6009-1_51
2. **Shashank V G**, Sriram V, Sannasiraj S A.Statistical Model for the prediction of tropical cyclone potential surge height for the Bay of Bengal coast. *ICOE Conference.* 2023-April, Germany.
3. **Shashank V G**, Sriram V, Holger Schüttrumpf, Sannasiraj S A "Investigation of cyclone's influence on coastal morphological changes along the nearshore areas using numerical modeling" *Imaginaries of Climate Futures: Cross Regional Insights to get from Knowledge to Action Conference,* 10–12 of September 2024, Berlin, Germany

ACKNOWLEDGMENTS

I am profoundly grateful to my doctoral supervisor, Prof. S. A. Sannasiraj, for accepting me as his PhD student and for his guidance and support in providing me with an opportunity to work as a Joint Doctoral researcher between IIT Madras and RWTH Aachen University. His remarkable expertise, multitasking abilities, and understanding of challenges faced by student researchers have been a constant source of inspiration. I feel incredibly fortunate to have him as my mentor.

I am profoundly grateful to my co-supervisor, Prof. V. Sriram, whom I always regarded as my main supervisor throughout my PhD journey. His achievements, friendly nature, and extensive research connections have been a constant inspiration. Despite his busy schedule, he always responded quickly to my queries and provided invaluable support in navigating challenges. His enthusiasm for exploring new ideas has greatly influenced my work on storm surge modeling, making my thesis comprehensive and innovative.

I am deeply grateful to my doctoral supervisor at RWTH Aachen University, Prof. Holger Schüttrumpf, for his guidance, support, and the opportunity to conduct my research at the IWW. His mentorship, trust, and encouragement to explore freely have been invaluable to my growth as a researcher. I admire his straightforwardness, multitasking skills, and teachings on discipline in academic research. It has been a privilege to work under his mentorship.

I am sincerely grateful to Prof. V. Sundar for his motivations and insightful discussions in Aachen, which guided me in my research and taught me the importance of discipline. His wisdom on balancing life and career has left a lasting impact on me.

I am sincerely grateful to Assoc. Prof. Sourav Sil at IIT Bhubaneswar for his mentorship, which enabled me to publish my first journal article and laid the foundation for my PhD journey. His guidance greatly shaped my research skills.

I am thankful to IIT Madras for providing the HTRA fellowship. I am also grateful to the IIT Madras-RWTH Aachen Indo-German Program (IGP) and the ABCD Future

Environmental Leaders Scholarship 2024 for financially supporting my research stay in Germany. A special thanks to Mrs. Rupa Pandit for her assistance with the visa process and scholarship transfer.

I sincerely thank the Doctoral Committee members, Assoc. Prof. Soumendra Nath Kuiry, Prof. Suresh Kumar G, Dr. Narendran K, and Prof. Nilanjan Saha for the valuable feedback. I am grateful to the Faculty of Civil Engineering, RWTH Aachen University, for accepting me as a joint doctoral student

My sincere thanks to my colleagues at IWW, Dr.-Ing Jan Oetjen, Dr.-Ing. Julian Hofmann, Ms. Anne Morzer, Ms. Prabha Nageswaran, Ms. Ina, Mr. Philipp Henkes, Prof. Anatara Dasgupta, and others—for their warmth and support. Special thanks to Mr. Philipp Mieser for the enriching countless conversations. I am also grateful to my Aachen friends from IIT for their companionship throughout my PhD journey.

I sincerely thank all my well-wishers at IIT Madras for their support throughout my journey. Special thanks to Dr.-Ing. Harish Selvam for his invaluable guidance during my research stay in Aachen, and Dr. Shagun Aggarwal for his technical assistance and inspiration. I appreciate Dr. Satish Samayam for his constant motivation and Dr. Shashwat, Dr. Sithik, Dr. Vineesh, Dr. Gracy Margret, and others for their support. I am also grateful to Mr. Narendhiran, Dr. Muthuselva Kumar, Mr. Krishnavelu, Mr. Vijay Prakash, Mr. Abdul Rehman, Mr. Rajkumar, Mr. Aditya Chopra, and Mr. Prasad Owk for their timely assistance whenever I needed it.

I extend my heartfelt gratitude and love to my parents, Mr. G. B. Wagamare and Mrs. Sucheta Wagamare, for their constant support and sacrifices. I am also thankful to my brother, Mr. Shubham Wagamare, for his encouragement. I appreciate the continuous support of my friend, Ms. Saubhagyalaxmi Swain, during my PhD journey. A special thanks to Chandrashekhar Sir and the late CNMD Sir for their guidance and inspiration during my schooling. Finally, I am grateful for the everlasting grace of my saviour, God, Lord Krishna, for leading me through this journey.

-V. G. Shashank

ABSTRACT

An enhanced understanding of Tropical Cyclones (TCs) in the Bay of Bengal (BoB) and their impact on coastal processes due to storm surge, wind waves, and coastal inundation is crucial for protecting densely populated areas. These events cause significant damage. An enhanced understanding of TCs and their nearshore impacts is vital for improving forecast accuracy, disaster preparedness, developing resilient coastal defences, and effective planning. This understanding also supports mitigating socio-economic and environmental impacts by fostering sustainable management strategies and promoting ecosystem conservation.

The present study examines the storm surge through numerical and statistical modeling approaches. Storm-driven waves, coastal inundation, and changes in nearshore bed morphology are analyzed using a coupled hydrodynamic-wave-morphodynamic modeling framework. The main motivation of the study is to enhance predictive capabilities using both statistical and numerical modeling approaches with a simplified methodology by thoroughly understanding cyclones and their impact on coastal dynamics.

For the numerical modeling approach, the study employs hydrodynamic models (ADCIRC and TELEMAC-2D), wave models (SWAN and TOMAWAC), and the morphodynamic model (GAIA) to investigate the nearshore impacts on water levels, wind waves, inundation, and morphodynamic bed evolution caused by the storms in the BoB. Since the cyclonic wind is the primary force for predicting surges and inundations, a better representation of TC wind fields is vital. Therefore, it focuses on improving the cyclonic wind field hindcast for the BoB. It proposes an enhanced blended wind field approach in which the five parametric wind models [Jelesnianski, Rankine vortex, Willoughby, Holland, and Generalized Asymmetric Holland (GAHM)] are assessed. Two global wind datasets from the European Centre for Medium-Range Weather Forecasts (ECMWF) Reanalysis and Weather Research Forecast (WRF) model are considered as background wind fields to drive the coupled ADCIRC+SWAN model. A blending approach smoothly superimposes the parametric and background wind fields. Further, the sensitivity analysis is performed on the predicted storm surges, wind waves,

and coastal inundation due to different cyclone wind models. A blended wind model based on GAHM and WRF is found to better simulate the background wind field with the internal structure of the cyclone in the BoB region.

Further, it is noted that studying nearshore morphological bed evolution due to cyclones is important as it impacts coastal stability, sediment transport, and erosion. The understanding aids in effective coastal management and disaster mitigation. Therefore, the present study adopts a coupled hydrodynamic (TELEMAC-2D) -wave (TOMAWAC) -morphodynamic (GAIA) model to investigate morphodynamic changes during storm surges. Here, the TELEMAC model is considered over the ADCIRC model because it includes a built-in morphodynamic module within the TELEMAC system. It introduces a modified parametric wind model to enhance wind field representation near and far from the cyclone center. This model is simpler and computationally efficient compared to the previously used blended wind field (GAHM+WRF). The simulated storm surges and wind waves are validated with in-situ observations during TC Hudhud (2014) and TC Varadah (2016), and the simulated morphodynamic bed evolution is validated with field measurements made after the landfall of TC Nivar (2020). Further, the performance of different bed load transport formulations is evaluated to predict morphodynamic bed evolution during TC Nivar (2020) under storm-induced currents and waves. It is found that the Engelund-Hansen model is most effective for only current-induced bed evolution, while the Bijker model excels for combined current and waves along the open coast of BoB. Incorporating the effect of waves along with current has enhanced the predictive capability of the coupled model framework.

The statistical modeling approach introduces a novel Tropical Cyclone Surge Potential Index (TCSPI) to estimate potential peak surge levels from tropical cyclones near landfall points along the entire BoB coastline. Statistical models are generally considered for predicting storm surges as they offer more computationally efficient estimates than numerical models. The proposed TCSPI incorporates atmospheric parameters that are often readily available in real-time for BoB along with bathymetry information. The inclusion of approach angle information leads to improvements in the TCSPI over other existing surge indices. Further, it utilizes renowned regression-based supervised machine learning (ML) models on small data samples to rapidly predict peak surge height across an extensive coastal region of BoB using the same atmospheric characteristics and bathymetry information that are considered in the TCSPI at the landfall time frame. Peak surge values for historical TC events in the BoB, derived from TCSPI, ADCIRC, and ML models, are compared with observations. The errors associated with TCSPI are comparatively lower when the dataset sample size is smaller. The consideration of approach angle information in the TCSPI improves the accuracy of the overall prediction of peak surge height associated with historical TCs by up to 17% and 19% for observed and ADCIRC-simulated peak surges, respectively.

Further, using the TCSPI model, a surge hazard map is being created for the eastern coast of India for effective long-term planning along the coastal districts that necessitate accurate estimates of peak surge heights associated with cyclones. Traditional methods for developing surge hazard maps rely on complex, fully physics-based numerical models requiring synthetic cyclone tracks, making the process intricate and time-consuming. Using historical data from the IMD (1982–2022), return periods are being determined based on cyclone wind speeds at landfall for each Indian coastal state. Additionally, climate change projections from the IPCC are being considered. A simple and computationally efficient methodology is being developed to estimate peak surge heights and then used to create surge hazard maps. Peak surge heights for various return periods are being estimated along the coastal districts of the Indian east coast. For a 100-year return period, it is observed that about a 10 m maximum surge occurs along the northern BoB, and 19 out of 30 coastal districts show high vulnerability to storm surges, with peak surges increasing by 10% to 18% due to climate change.

Keywords: Storm Surge, ADCIRC, Wind wave, Inundation, Parametric wind model, Global wind model, Blended wind field. TELEMAC-2D, Wind Waves, Morphodynamic Bed Evolution, Tropical Cyclone Surge Potential Index, Machine Learning, Surge Hazard Map.

CONTENTS

LIST OF TABLES

LIST OF FIGURES

NOTATIONS

h_*: Characteristics of shelf depth

A_{34}: Area of surface wind speed greater than 34-knot

A_{340}: Reference value for the average of A_{34} value of selected storms.

B_g: Shape parameter of GAHM

H_{FS}: Storm forwarding speed

H_{LF}: Landfall similarity

H_{Rmax}: Storm similarity

H_{TRK}: Storm track similarity

H_{CP}: Central pressure deficit similarity

L_*: Characteristics of shelf width

P_c: Minimum central atmospheric pressure

P_n: Ambient pressure,

R_0: Rossby Number at $r = R_{max}$ (GAHM)

R_1: Radial extent from the center of the cyclone till the parametric wind field is effective

R_2: Radial extent beyond the smoothed transitional zone (between R_1 and R_2), where the background wind field is effective.

R_{50}: Measure of radius to 50-knot (26 m/s) winds,

R_{max}: radius of maximum wind

V_{max}: 1 or 3-minute maximum sustained wind speed

V_{mov}: Wind vector induced by the moving component

V_t: Cyclone's translation speed

W_{PBL}: Wind reduction factor

W_{bac}: Background wind field

W_{par}: Parametric model wind field

Z_{B0}: Initial bed level.

Z_{BC}: Computed bed evolution by the model

Z_{BM}: Field measured bed evolution

Z_b: Bed elevation above datum

t_*: storm duration,

t_∞: Time scale for equilibrium surge,

Ψ_t: linear dimensionless empirical functions to describe the relative influence of storm duration

Ψ_x: linear dimensionless empirical functions to describe the relative influence of storm size

Ψ_θ: linear dimensionless empirical functions to describe the relative influence of storm approach angle

ΔZ_{BM}: Bed level measured error

$\nabla\cdot$: Divergence operator

a: Characteristic coastal geometry for forward speed

B: Shape parameter of Holland model.

D and E are deposition and erosion rates, respectively.

f: Coriolis force,

IKE_{TS}: Integrated kinetic energy of hurricane

L_{30}: Distance between shoreline and 30 m bathymetry contour

n: Porosity of the bed material at the bed surface

q_r: Power law by Murty et al., (2016)

r: Radial distance

R: Storm size

S: Storm forward speed

S_{DP}: Mapping surge damage potential

X: Shape parameter that adjusts the velocity distribution in the radial direction.

β: Wind inflow angle approximation

γ: Damp factor

θ: Storm approach angle

ρ: Density of air

φ: Scaling parameter introduced in GAHM

$P(r)$: Pressure at radius r from the cyclone's centre

$V(r)$: Gradient cyclone wind formula

dV: Elements volume

V_{maxo}: Reference constant for V_{max}

S_o: Reference constant for S

R_o: Reference constant for R

L_{300}: Reference constant for L_{30}

L_{400}: Reference constant for L_{40}

ΔP: Storm pressure deficit

C_f: Bottom friction coefficient

C_D : Wind drag coefficient

g : Acceleration due to gravity

H: Water depth

K_s : Roughness coefficient of Nikuradse

k : von Karman constant

z_0 : Bottom roughness parameter

τ_b : Bottom stress

ABBREVIATIONS

ADCIRC: Advanced Circulation

ANN: Artificial Neural Networks

AS: Arabian Sea

BJ: Bijker's formula

BL: Bailard's formula

BMD: Bangladesh Meteorology Department

BoB: Bay of Bengal

CC: Correlation Coefficient

CCS: Climate Change Scenario

CS: Cyclonic Storm

DB: Dibajnia and Watanabe formula

EB: Einstein-Brown formula

ECMWF: European Center for Medium-RangeWeather Forecasts

EH: Engelund-Hansen formula

EnTR: Ensembles of Trees

ESCS: Extremely Severe Cyclonic Storm

GA: Genetic Algorithm

GAHM: Generalized Asymmetric Holland Model

GBM: Ganges-Brahmaputra-Meghna

GEBCO: General Bathymetric Chart of the Oceans

GP: Genetic Programming

GPR: Gaussian Process Regression

GWCE: Generalized Wave Continuity Equation

H*Wind: National Oceanic and Atmospheric Administration (NOAA)/Hurricane Research Division's (HRD's) Real-time Hurricane Wind Analysis System

HL80: Holland 1980

HSI: Hurricane Surge Index

IMD: Indian Meteorological Department

INCOIS: Indian National Centre for Oceanic Information Services

JMA: Japan Meteorological Agency

JTWC: Joint Typhoon Warning Centre

LR: Linear Regression

MDMH: Myanmar Department of Meteorology and Hydrology

ML: Machine Learning (ML)

MPM: Meyer-Peter-Muller formula

NCEP: National Center for Environmental Prediction

NHC: National Hurricane Center

NIO: North Indian Ocean

PMSS: Probable Maximum Storm Surge

QGIS: Quantum Geographic Information System

RMSE: Root Mean Squared Error

RSMC: Regional Specialized Meteorological Centre

RV: Rankine Vortex model

SCS: Severe Cyclonic Storm

SDP: Surge Damage Potential

SESSP: Semi Empirical Storm Surge Prediction

SLOSH: Sea, Lake, and Overland Surges from Hurricanes Model

SS: Surge Scale

SSFT: Storm Surge Forecasting Tool

SSHS: Saffir–Simpson hurricane scale

SSI: Storm Surge Index

SuCS: Super Cyclonic Storm

SVJ: Soulsby-van Rijn

SVM: Support Vector Machine

SWAN: Simulating WAves Nearshore

TC: Tropical Cyclone

TCHPS: Tropical Cyclone Hazard Prone Scales

TCSI: Tropical Cyclone Surge Index

TCSPI: Tropical Cyclone Surge Potential Index

TOMAWAC: TELEMAC-based Operational Model Addressing Wave Action Computation

TR: Regression Tree

VR: van Rijn’s formula

VSCS: Very Severe Cyclonic Storm, Cyclonic Storm

W-C: White-Colebrook

WL06: Willoughby model

WMO: World Meteorological Organisation

WRF: Weather Research Forecast

WSSI: Weighted Storm Similarity Index

CHAPTER 1

INTRODUCTION

1.1 STORM SURGES IN THE BAY OF BENGAL

The term "storm surge" denotes an unusual increase in water level triggered by tropical cyclones (TCs) and is highly energetic, causing devastating damage along coastal locations such as coastal flooding, salinization, damage of coastal infrastructure and loss of lives. Therefore, predicting storm surges is essential to avoiding the massive destruction of coastal habitats, ecosystems and economic losses. The Bay of Bengal (BoB) is one of the most cyclone-prone regions in the world, with TCs often leading to devastating storm surges that pose significant hazards to coastal communities. It is noted that BoB experiences TCs five times more than the Arabian Sea in the North Indian Ocean (NIO) (Sahoo and Bhaskaran, 2016).

BoB is semi-enclosed in nature, and its funnel-shaped conjunction will steer the direction of the storm approaching the land. India boasts a coastline measuring approximately 11,098 km, with 9,845 km bordering the mainland and, specifically, 5,490 km constituting the extent along the coastal regions of the eastern Indian seaboard (MHA, 2024). The maximum depth in the deep waters of the BoB reaches approximately 4,694 meters (15,400 feet). This depth is found in the Sunda Trench, which lies to the southeast of the BoB, extending towards the Andaman and Nicobar Islands and continuing to the west of Indonesia (as shown in Fig. 1.1). The different coastal states of the eastern Indian coastline experience cyclones of different return periods. Major river systems, such as the Mahanadi River in Odisha, the Krishna and Godavari in Andhra Pradesh, and the Hooghly in West Bengal, increase the susceptibility of the coastal areas in concern to sea level rise and the resulting inundation caused by the storm surges. According to the 2011 census, there are 250 million people living in all of the coastal districts along the Indian coast, constituting approximately 20% of the Indian population (Dhiman et al., 2016). For the coastal authorities judicial planning, preparedness, and relief procedures, understanding the quantitative risk analysis in terms of the depth and horizontal extent of the floods caused by the surges is essential. The historical data signifies that the TCs move mostly in the northwest direction in the BoB (Priya et al., 2022; Bell et al., 2020), Along Indian east coast, the continental shelf width varies sigficantly, which affects the storm surges propagation. Ocean heat content, sea surface temperature, Coriolis force, eddy dispersion in the open ocean, troposphere vorticity, relative humidity, vertical wind shear, and upper ocean stratification are some of the variables that affect the formation of cyclones in the tropical regions (Girishkumar and Ravichandran, 2012; Tory et al., 2013; Mandal et al., 2018; Priya et al., 2022). According to reports, the deadliest cyclones in history, with the greatest destruction and fatalities, happened along the BoB coast (Dube et al., 1997). The 1737 cyclone, the 1970 Bhola Cyclone, and the 1999 Odisha Cyclone were the deadliest TCs over the NIO region, affecting nearly 300,000 casualties (Dube et al., 2008). More people died as a result of these storms than from the 2004 Indian Ocean tsunami, which affected nearly 2,28,000 casualties (United States Geological Survey, 2008). The extent of casualties affected by TCs has drastically lowered due to improved emergency management practices (Needham et al., 2015). However, the massive loss of property due to TCs is still a challenge that needs to be addressed. For example, the recent Extremely Severe Cyclone (ESCS) Hudhud (2014) and Super-Cyclone (SuCS) Amphan (2020) were the most expensive TC over the BoB region, causing a loss of more than USD 20 billion (State of the World Climate 2020).

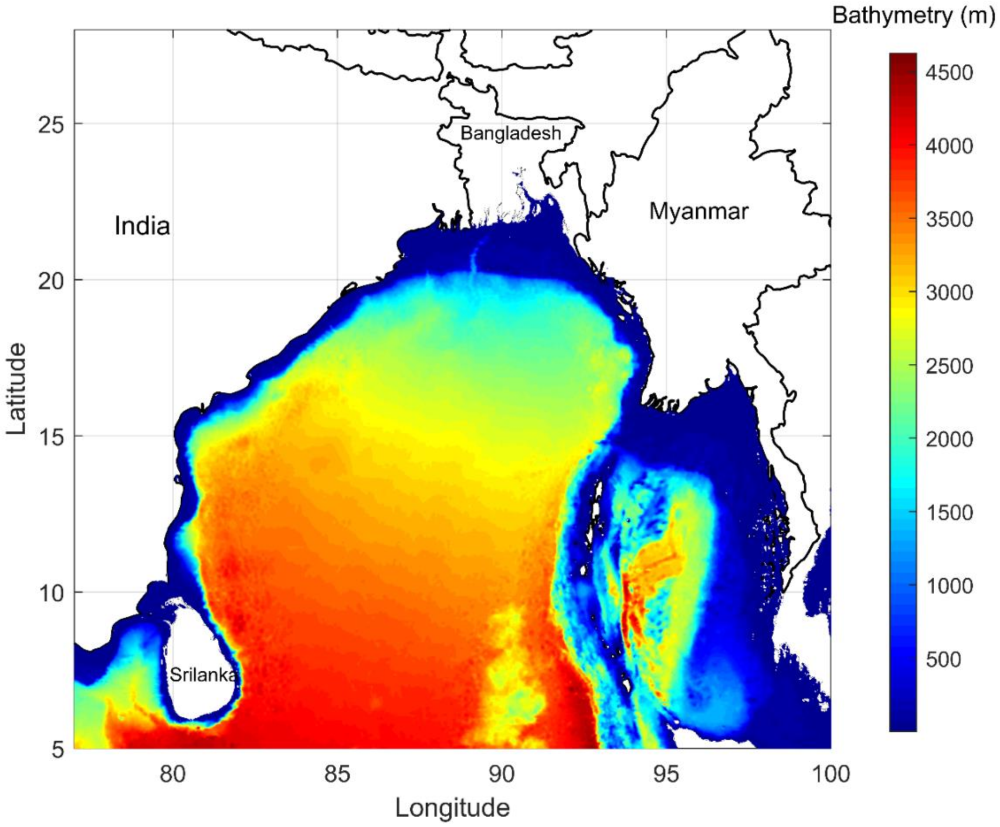

Fig 1. 1. The entire BoB domain's bathymetry depth (in meters) is indicated by the colour bar, obtained from the General Bathymetric Chart of the Oceans (GEBCO).

Implementing innovative early warning systems for public awareness reduced fatalities to less than 200 (Zhao et al., 2019; Mishra et al., 2020; Khan et al., 2021). Around 40% of the world's population lives in low-lying cities within a range of hundred kilometers from the coastline (Martinez et al., 2011), making coastal stretches more vulnerable to extreme weather events. Due to mankind's actions, the earth's temperature is rising, the accurate and timely forecasts and warnings accompanying storm surges and associated coastal parameters are paramount to mitigating the threats to assets and lives caused by these storms along the coasts.

Along the coastal areas, storm winds, storm surges, and coastal flooding are mostly responsible for property damage and fatalities. Therefore, it is necessary to comprehend the risk elements responsible for extreme storm winds and associated storm surges. Accurate prediction and mapping of these surges are important for efficient mitigation and management of disasters. Modeling storm surges is crucial because it enables better forecasting, risk assessment, and decision-making for coastal communities, helping to mitigate the devastating impacts of these natural disasters. Storm surge modeling typically involves two main approaches: numerical modeling and statistical modeling. Statistical modeling uses historical data and statistical techniques to identify patterns and predict future surges based on past events. Its advantages include simplicity, faster computation, and the ability to provide quick estimates with limited data. However, it is less accurate for predicting extreme events outside the range of observed data and struggles to capture complex, dynamic interactions in storm systems. On the other hand, numerical modeling relies on mathematical equations to simulate the physical processes governing storm surges, such as wind, pressure, and ocean dynamics. This approach offers higher accuracy and can predict a wide range of scenarios, including unprecedented conditions. However, it requires significant computational resources, complex data inputs, and expertise to set up and interpret, making it more costly and time-consuming. Machine learning is an emerging approach that combines aspects of both statistical and numerical methods, offering potential improvements in predictive accuracy and efficiency. The present study addresses various key aspects of storm surge modeling and hazard assessment in the BoB, providing a comprehensive approach to improving our understanding and prediction capabilities.

1.2 MODELING OF CYCLONIC WIND FIELD

The crucial factor influencing the storm surge, wind wave, inundation, and morphological bed evolution prediction is the cyclonic wind (Wu et al., 2018, Han et al., 2022). Therefore, a better representation of cyclonic wind fields is vital. The cyclonic wind field dictates the distribution and intensity of winds around a TC, which in turn influences the surface stress exerted on the ocean. This stress generates waves and pushes seawater towards the coast, leading to a surge. An accurate wind field model captures the complex structure of the cyclone, including variations in wind speed, direction, and asymmetry, ensuring that the surge model can realistically simulate the resulting surge height and coastal inundation. Without precise modeling of the cyclonic wind field, the storm surge predictions could be significantly off, leading to either overestimation or underestimation of the hazard, which could impact emergency planning and response. Typically, numerical modeling for predicting storm surges employs three broadly categorized types of models: parametric wind models, global or background wind models, and blended wind fields.

1.2.1 Parametric wind models

Numerous parametric cyclonic wind models have been presented in the past, like Jelesnianski (1966), Holland (1980), and Rankine Vortex (Depperman, 1947). A limited number of atmospheric input parameters like, pressure drop, maximum sustained wind speed, storm size, and the geographic coordinates of the storm center, are utilized by these cyclonic parametric wind models to recreate the storm structure (Fleming et al., 2007). Parametric models are effective, simple, and inexpensive to compute. As a result, they are widely used and serve as an excellent substitute when precise determination of the driving parameters is required. Despite their superior ability to regenerate the storm strucure, these parametric wind models have the drawback of being unable to adequately depict distribution of wind distribution farther distance from the cyclone center (Murty et al., 2016, 2020; Liu et al., 2018; Chen et al., 2019; Hsiao et al., 2020).

1.2.2 Background wind models

Background wind models such as MERRA-2 (Modern-Era Retrospective Analysis for Research and Applications, Version 2) from NASA (National Aeronautics and Space Administration) and ERA5 (ECMWF Reanalysis 5th Generation) from ECMWF (European Centre for Medium-Range Weather Forecasts) are widely used reanalysis datasets. These reanalysis data depict the cyclonic wind fields with better accuracy away from the cyclone center. But they are too rough to depict a high-vorticity extreme TC wind (Hemer et al., 2010; Jeong et al., 2012), leading to an underestimation of maximum wind near the cyclone's center than the actual values (Hodges et al., 2017). Incorporating the wind field from the operational WRF model effectively resolves the underestimation of wind distribution at larger radial distances from the cyclone eye by the parametric models. The consideration wind field derived from WRF model improves the precision of wind field forecasts in the outer areas of cyclonic systems and provides a more accurate assessment of surge and inundation along extensive coastal areas (Kowaleski et al., 2020). However, WRF models cannot be used as a routine operational forecast of cyclonic winds because they are computationally expensive to account for mesoscale and synoptic-scale convection processes (Pandey and Rao. 2018).

1.2.3 Blended wind model

The blended wind field approach is an advanced and accurate presentation of cyclonic wind fields (Pan et al., 2016). In this approach, the wind data obtained from the parametric model for the region close to the cyclone centre is superimposed with the background field derived from the global wind model. The reason for this is that parametric models typically give better depiction of wind fields near to the centre of the cyclone. In regions far away from the cyclone eye, the wind fields from global models are more accurate than those from parametric models. The basic idea behind the blended wind field approach is to make use of on each model's advantages (i.e., parametric and global wind models) while mitigating their respective limitations.

1.2.4 Advancements in cyclonic wind field hindcasting

The Jelesnianski wind formulation was previously used in a several studies to represent the storm structure from the available track parameters (Rao et al., 2010, 2013) in the NIO basin. However, at a distance away from the storm center, it is underestimated. Murty et al., (2016) incorporated a 3/5-power law to the actual Jelesnianski model, providing a fairly accurate values of wind values at distances away from the storm center. Pandey and Rao. (2018) incorporated the 3/5-power law to the actual Jelesnianski wind formulation only away from the radius of the maximum wind region (R_{max}) keeping the same original Jelesnianski model within the radius of the maximum wind region. The incorporation of modifications has shown better accuracy than the original formulation in representing cyclone wind profiles for the BoB. The symmetric Holland model (H80, Holland 1980) has emerged as the most popular cyclostrophic model in a numerous studies pertaining to the cyclones (Wang et al., 2020; Muis et al., 2016; Bhaskaran et al., 2013, 2014; Mattocks and Forbes, 2008). Jakobsen and Madsen. (2004); Das. (2018); Gao et al., (2018) demonstrated the wind speed behaviour of storm for different Holland shape parameter B values at the R_{max} and away from the eye. Willoughby and Rahn. (2004) observed cyclone center region was poorly approximated using H80. Further, it is noticed that the cyclostrophic approximation caused poor approximation of storm wind away from the R_{max} region. In order to overcome this, the Generalized Asymmetric Holland model (GAHM) was introduced (Gao et al., 2018). This model considers inclusion of the translation component of a cyclone, eleminating the cyclostrophic approximation, the composite wind method, and frictional inflow corrections to the existing H80 model.

Previously, Phadke et al., (2003); Das (2018) compared radial wind profiles of Rankine Vortex, Jelesnianski, and Holland wind schemes and found that contrast to the Jelesnianski and H80, the rankine vortex model results in a shorter peak and a more progressive declination of the wind speed moving away from the center. An experiment was conducted by Salcines et al., (2019) to test six widely recognized parametric wind models, evaluating the resulting wind and wave fields in the Gulf of Mexico. The analysis suggested that while a specific wind model might be the most suitable for representing a certain event. However, a particular wind model or a combination of parametric wind models cannot assure the same accuracy when considering the large number of cyclonic events across any basin. A system was developed by Qi et al., (2009) and Torres et al., (2019) using the Northeast Coastal Ocean Forecasting System (NECFOS), based on the WRF model. This system combines both forecast and hindcast capabilities with synthetic vortices, along the northeastern U.S. coast. When compared to conventional parametric wind models, their results demonstrated that the NECFOS-WRF wind model is more accurate and better at handling uncertainty in replicating the internal structure of cyclones as well as the background ambient wind distribution. Murty et al., (2020) included the blended wind technique for the BoB region using the formulations presented by Pan et al., (2016) and Shao et al., (2018), to provide a seamless transition between the background wind field and the parametric model. In this study, the ECMWF global wind data considered as the background wind field, while the wind fields near the cyclone eye are estimated using the H80 parametric model. Chen et al., (2019); Hsiao et al., (2019, 2020, 2021); and Chang et al., (2021) experimented with the blended wind field approach to the Pacific Ocean basin, using Rankine Vortex and H80 as a parametric model to estimate wind fields near the cyclone eye and superimposing with different global reanalysis wind data as background wind field.

1.3 MORPHODYNAMIC RESPONSES TO THE STORM SURGES

1.3.1 Significance of studying morphodynamic response during cyclones

Studying the morphodynamic response of nearshore coastal regions during cyclonic events is essential for several critical reasons. Firstly, cyclones generate powerful waves and storm surges that can cause significant erosion, reshaping coastlines and altering natural habitats. Understanding these changes helps in predicting the impacts on coastal infrastructure and ecosystems. Secondly, morphodynamic studies provide insights into sediment transport, influencing beach nourishment and coastal stability. This knowledge is vital for designing effective coastal defense mechanisms. These studies also support the development of accurate models for predicting future changes due to climate change. Overall, understanding morphodynamic responses enhances our ability to protect coastal communities, infrastructure, and natural resources from the devastating effects of cyclonic events.

1.3.2 Modeling of morphodynamic response during storm surges

The coupling of hydrodynamic, wave, and morphological models is crucial in understanding the complex interactions between hydrodynamics, wind waves, and morphodynamics in coastal environments (van Wiechen et al., 2023). This integration allows for a more realistic representation of feedback mechanisms, such as the influence of waves on currents, as well as the interaction of current and waves on sediment movement and vice versa. This integrated modeling approach provides insightful information about the evolution of the seabed, aiding in the prediction of morphodynamics and evaluation of potential vulnerabilities during storm surges. Such simulations are vital for coastal management and disaster preparedness, providing a proactive means of mitigating the impacts of storm surges on coastal communities (Ribas et al., 2015). Generally, two-dimensional (2D) and three dimensional (3D) are commonly used in coastal engineering to simulate both short-term and long-term morphodynamic processes. The 3D models are effective in large-scale problems as they capture vertical variations in flow, sediment transport, and stratification, providing a more detailed representation of physical processes like sediment resuspension, and enhancing accuracy in regions with complex bathymetry (Warner et al., 2008). However, they are computationally expensive and less practical for large-scale predictions. In contrast, 2D models simplify computations by averaging over depth, reducing computational costs while maintaining reasonable accuracy for large domains (Sanchez et al., 2016). Therefore, this study focused on exploring morphodynamic responses during storms considering a 2D model approach.

Previously, a few studies have been conducted to investigate morphodynamic response using coupled modelling framework. Kury et al., (2014) used a 2D finite volume model simulating supercritical coastal flows. This flow model is coupled with the wave-action (CMS-Flow) and morphodynamic (Lund-CIRP) model to simulate morphological changes caused by storm surges for an idealized coast. Results show that the coupled model accurately simulates extreme conditions and morphological changes, validated through experimental dam-break tests and severe storm scenarios. Considering the impact of vegetation during breaching events, Nienhuis et al., (2021) utilized the Delft3D hydrodynamic and morphodynamic model (Deltares, 2014) to calibrate the morphology at the barrier. Khazaei et al., (2021) utilized a coupled FVCOM based hydrodynamic-wave-morphodynamic model for the Green Bay and demonstrated that that how morphodynamics in this region is affected by riverine inflow and atmospheric forcing. In order to evaluate the impact of bed friction on sediment transport pattern during the storm Ivan (2004) and Katrina (2005), Passeri et al., (2018) utilized the Xbeach model. Their findings demonstrated that bed friction caused during storm Katrina (2014) affected the coastal morphology more than storm Ivan (2004). This is due to significant to rise in water levels caused by the storm Katrina. Ma et al., (2024) presented a finite volume-based coupled flow-wave-sediment-transport model to estimate the sediment movement along the Santa Rosa Island caused during the storm Ivan. Their findings demonstrate the accuracy of the model in predicting the sediment transport patterns resulting from the storm surge. Han et al., (2022) implemented a coupled Delft3D and Xbeach to investigate the storm surge hydrodynamical process and the morphological response of the beach to the TC Ampil (2018) along the Shanghai coast region of eastern China. Results show that the wind-induced surge was the main contributor to the total storm surge, with beach foreshore sand transported offshore by the storm and returned onshore by mild waves during recovery.

To the author's best of knowledge, three studies have been conducted to predict coastal morphodynamics in the NIO region. Nandhakumar et al., (2022) evaluated the performance of five different total sediment transport formulae [i.e., Engelund and Hansen, (1967), Ackers and White, (1973), van Rijn (1984a, b), Wu et al., (2000), and Yang and Lim (2003)] using hydro-morphodynamic model along the macro tidal estuary and a micro-tidal estuary. The result shows that Ackers and White (1973) performed better, followed by van Rijn, (1984a, b) and Engelund and Hansen, (1967) formulations. The impact of mangrove ecosystems on hydro-morphodynamics in the BoB is examined by Fanous et al., (2023). Experimental comparisons with and without mangroves based on tidal forcing simulations carried out. Results indicated that mangrove ecosystems can successfully lower water levels and flow velocities by ≥97% and prevent erosion of sediments when compared to non-mangrove enviornment. Both Nandhakumar et al., (2022) and Fanous et al., (2023) analyzed morphological bed evolution accounting for long-term tidal influences and did not incorporate the impact of wind-induced waves. Rohini et al., (2023) employed an internally coupled hydrodynamic-wave-morphodynamic model (Telemac2D+Tomawac+Sisyphe) to study the TC event Nivar (2020) and validated their results with field measurements. However, this study did not use empirical formulations such as Bijker's (1968), Soulsby-van Rijn (Soulsby, 1997), Bailard's (1981), and Dibajnia and Watanabe's (1992), which consider the effects of both waves and currents in predicting morphodynamic bed evolution. Instead, Rohini et al., (2023) used the Engelund and Hansen, (1967) formulation to predict changes in the morphodynamic bed due to storm-induced currents and the currents influenced by storm-induced waves. It should be noted that Engelund and Hansen, (1967) formulation does not consider the effects of waves in predicting morphodynamic bed evolution.

1.4 STATISTICAL MODELING OF STORM SURGE

1.4.1 Why statistical modeling of storm surge is necessary?

In the present study, the shift to statistical modeling of storm surge from numerical modeling is attributed to following key reasons:

- Data Efficiency: Statistical models can utilize historical data more effectively, enabling quicker assessments without the extensive computational resources required for numerical models.
- Simplified Analysis: Statistical approaches often provide a more straightforward framework for analyzing storm surge trends and relationships, making it easier to interpret results for decision-making.
- Parameter Uncertainty: Numerical models may involve complex parameterizations and assumptions, which can introduce uncertainty; statistical models can offer more robust estimates by directly relating observed data to surge events.
- Rapid Prototyping: Statistical models can be developed and updated more quickly in response to new data, facilitating timely forecasts and risk assessments.
- Broad Applicability: Statistical methods can be applied across different regions and scenarios without the need for extensive recalibration, providing a versatile tool for various contexts.
- Focus on Extremes: Statistical modeling is particularly proven to be effective for estimating the storm surge, aiding in risk management and planning.
- Integration with Other Data: Statistical approaches can easily incorporate various datasets (e.g., sea level rise, climate variables), enabling a more thorough comprehension of surge dynamics.

Statistical modeling of storm surges involves use of statistical techniques to predict the magnitude and impact of storm surges. This modeling relies on historical data, physical parameters, and regression methods to estimate the likelihood and severity of storm surges at different locations. Statistical modeling of storm surges are majorly associated with classification of storm surges by analyzing patterns in historical surge data, helping to categorize surges based on intensity and frequency. This classification improves predictive accuracy for future events, linking specific surge levels with potential cyclone categories. By doing so, it enhances preparedness efforts, guiding emergency responses according to expected surge severity.

Classifying cyclone storm surges is essential for assessing potential impacts on coastal regions, enabling more accurate risk management and disaster preparedness. Different surge classes help predict flooding extents, infrastructure damage, and necessary evacuation measures. This classification aids in designing coastal defenses and informing the public based on surge severity. For instances, India Meteorological Department (IMD) has classified the low-pressure systems in the NIO. This has been used for nearly forty years by the Regional Specialized Meteorological Centre (RSMC) in India to categorize TC strength. Similarly, the Saffir–Simpson hurricane scale (SSHS) has been used for about fifty years by the National Hurricane Center (NHC, NOAA) to classify the TC strengths in the United States of America (Islam et al., 2021). However, NHC recently updated that the SSHS doesn't take other potentially deadly hazards like tornadoes, storm surges, or rainfall into account (NHC, NOAA). Countries prone to TC, including Japan, Bangladesh, and Australia, also use the classification scale provided by the World Meteorological Organisation (WMO) to warn their coastal communities, where the WMO category has a linear relationship with evacuation intent (JMA, 2022; BMD, 2022; Bureau of Meteorology, 2022). However, these TC hazard-prone scales (TCHPS) are widely criticized for a poor measure of the destructive potential of TCs because they depend only on wind-induced structural damage (Needham and Keim, 2011). The destruction potential can be quantified by considering deadly hazards such as storm surges, rainfall, and flooding (Rezapour and Baldock, 2014). These deadly potential hazards do not necessarily scale with the intensity of TCs alone (Powell and Reinhold, 2007; Irish et al., 2008; Islam et al., 2021). Present study is mainly focused on storm surge hazard potential in the BoB, India. A peculiar aspect of the TCHPS is that, unlike the Richter scale (Boore, 1989), the resulting magnitudes are quantified. The TCHPS has a range of properties assigned to it (Kantha, 2008). For example, Super Cyclone (SuCS) can have maximum sustained wind speeds greater than 120 knots. This means that a change of just one knot in maximum speed can make shift in the category. Thus, a SuCS is downgraded to Extreamly Severe Cyclonic Storm (ESCS) once its maximum sustained wind speed decreases from 120 to 119 knots, even when the wind speed has not changed much.

Further, Islam et al., (2021) argue that even during landfall time frames, TCs often weaken, though storm surge potential is still increasing or vice versa in the BoB. Thus, a lower category TCHPS can affect higher storm surge. For example, Very Severe Cyclonic Storm (VSCS), such as Bulbul (2019), highlighted the risk posed by a weakening tropical storm. Bulbul approached the northeastern Indian state of West

Bengal coast as a Severe Cyclone Storm (SCS) with a maximum sustained wind speed of 60 knots before further weakening and making landfall. It generated a maximum peak surge height of ~ 2.5 m above astronomical tide, as reported by IMD. Another recent example from the same year, Fani (2019), highlighted as the risk posed by a strengthening tropical storm that approached the eastern Indian state of Odisha coast as an ESCS category storm, with a maximum wind speed of 100 knots. This resulted in a ~ 1.5 m peak surge above astronomical tide near the landfall location, as reported by IMD. In light of the potentially lethal nature of storm surge, there is a clear need for methods to characterize the TC surge potential more effectively for the Indian coasts.

1.4.2 Factors Affecting Storm Surges

Numerous studies have shown that the extent of surges is influenced significantly by several parameters based on numerical surge modeling. Poulose et al., (2018) conducted numerical simulations to investigate the effect of varying width of continental shelf on storm surges. The results showed that along the idealised west coast of India, storm surge increased by roughly 12 cm for every 10 km increase in shelf width. Storm surge responses and their sensitivity to various storm parameters such as cyclone intensity, bathymetry, translational speed, and approach angle with respect to the coast were investigated by Weisberg and Zheng (2006) in the Tampa Bay of Florida. The results concluded that storm surge is sensitive to the all the parameters considered in the investigation. Irish et al., (2008) evaluated the effect of storm size on peak surge heights for various bottom slopes for the Gulf of Mexico using numerical model simulations. The research indicates that in shallow coastal areas, storm surges become more pronounced and intensify as the size of hurricanes increases. A similar analysis along the eastern North Carolina coast was previously reported by Peng et al., (2004). In order to understand the effect of hurricane forward speeds on storm surges, Rego and Li (2009) carried out a numerical modelling experiment of storm surges along the Louisiana coast. The results show that increasing the translational speed of the storm increases peak surge heights and decreases the flood volume. A similar conclusion was also previously reported by Jelesnianski, (1966) concerning the effect of translational speed on storm surges. The study by Sebastian and Behera, (2022) examines how both gradual and rapid cyclone intensification influence peak water levels and current, with a focus on identifying vulnerable areas along the east coast of India using numerical model. Research finding indicates that for rapidly intensifying cyclones over the continental shelf, the intensification period led to an approximate 10–18% rise in peak water levels, while gradually intensifying cyclones had a negligible effect. The previously mentioned simulation studies based on numerical models highlighted the limitation of relying solely on wind speed as the key factor affecting the storm surges.

Several studies also found that other factors including coastal geometry and TC approach angle are affecting storm surges (Jelesnianski, 1966; Flierl and Robinson, 1972; Mercer et al., 2002; Weisberg and Zheng, 2006; Irish et al., 2008; Zhang, 2012; Sahoo and Bhaskaran. 2017; Zhang and Li. 2019). Pandey and Rao. (2019) carried out a numerical experiment to investigate the effect of the storm track approach angle on the storm surges considering actual and idealized bathymetry with a straight coastline and uniform shelf width. The simulations for idealized bathymetry show that the maximum storm surge increases by about 15% for tracks land falling 60^{o}–90^{o} than the tracks land falling 10^{o}–60^{o}, while it decreases by about 13% from 90^{o}–170^{o}. The simulation for actual bathymetry along the east coast of India shows maximum surge occurs at 90^{o}, while the least occurs at 20^{o} and 160^{o}, respectively. Sebastian et al., (2019) conducted a numerical experiment to understand how variations in the approach angle influence the interaction between tide and surge along Chennai's narrow continental shelf and concave coastal shape during TC Thane. The findings indicate that at the landfall location, the highest surge height occurs with an approach angle of 75°, followed by 105°, and is lowest at an angle of 45°. However, these studies examine the effect of approach angle on storm surges at specific landfall locations along the west coast of BoB.

1.4.3 Evolution Of Surge Indices

In the early 20th century, storm surges were estimated with the help of a simple empirical method developed based on field observations (Proudman, 1954; Reid, 1956; Conner et al., 1957; Harris, 1959). SSHS (Table 1.1) was developed in 1969. NHC uses this scale to indicate the expected range of storm surges caused by the intensity of the storm until 2019 (NHC, NOAA). However, this scale has led misunderstanding among coastal communities regarding potential storm surges. Thus, several studies (Kantha, 2006; Powell and Reinhold, 2007; Kantha, 2008; Irish et al., 2008; Hebert et al., 2008;

Rezapour and Baldock, 2014; Islam et al., 2021) have criticized SSHS as an inappropriate measure of storm surge along the coasts.

Table 1.1. Saffir-Simpson Hurricane Scale

Saffir–Simpson category	Max 1-min sustained wind speed			Storm surge (m)
	Knots	kmph	ms^{-1}	
Category 1	64–82	119–153	33–42	1.2–1.5
Category 2	83–95	154–177	43–49	1.8–2.4
Category 3	96–112	178–208	50–58	2.7–3.7
Category 4	113–136	209–251	59–70	4.0–5.5
Category 5	≥137	≥252	≥71	>5.5

Kantha (2006) was one of the first who criticized the SSHS and asserted that SSHS does not take into account storm size, which is an essential determinant of cyclone hazards, and proposed the Hurricane Surge Index (HSI) based on best track parameters which include TC intensity (V_{max}) and radius of hurricane-force wind (R) within which the wind speed exceeds 34 knots (17.5 ms^{-1}) at landfall time from the Joint Typhoon Warning Center (JTWC).

$$HSI = \left(\frac{V_{max}}{V_{max0}}\right)^2 \left(\frac{R}{R_0}\right) \tag{1.1}$$

where the subscript 0 refers to climatological reference constants. In this study V_{max0} is 33 ms^{-1}, and, R_0 is 96.6 km. The wind effect is inversely proportional to the water depth. As a consequence, in shallow waters, wind stress is often dominant over the inverse barometer effect (Bertin, 2014). HSI has a quadratic dependence on V_{max} the input of wind stress at the water's surface is directly related to ${V_{max}}^2$. The linear dependence of HSI on the storm radius is due to the strong size dependence on mild slopes where the wind stress-driven surge is dominant along the roughly linear strip of the coastline (Irish et al., 2008; Nielsen et al., 2009; Islam et al., 2021).

Based on numerical simulation results, Irish et al., (2008) presented an empirical relation between peak surge, storm intensity, storm size and bottom slope. However, Irish et al., (2008) clearly recommended to not use their empirical relation as a surge model. The proposed empirical relation was just meant to show the dependence of surges on different atmospheric variables.

Powell and Reinhold. (2007) proposed a scale based on the integrated kinetic energy (IKE_{TS}) of storm wind greater than the tropical storm force (18 ms^{-1}, Category 1, SSHS) for mapping surge damage potential (S_{DP}) along the US coast as:

$$S_{DP} = 0.676 + 0.43\sqrt{IKE_{TS}} - 0.0176\left(\sqrt{IKE_{TS}} - 6.5\right)^2$$
$$IKE_{TS} = \int_v \frac{1}{2}\rho {V_{max}}^2 dV \tag{1.2}$$

where $\rho = 1.25$ kg/m^3 density of air, (dV) is storm domain volume.

Das et al., (2009) developed a regression and data-based Storm Surge Forecasting Tool (SSFT) to predict storm surge height in Coastal Mississippi based on the weighted storm similarity index (WSSI). This index is defined by TC track position, pressure drop, storm size along with storm forward speed from and compared it with an existing synthetic TC database.

$$WSSI = \left(aH_{LF} + bH_{cp} + cH_{Rmax} + dH_{FS}\right)H_{TRK} \tag{1.3}$$

where H_{LF} is landfall similarity, H_{cp} is central pressure deficit similarity, H_{Rmax} is storm similarity, H_{FS} is storm forwarding speed, and similarity, H_{TRK} is storm track similarity. Here *a*, *b*, *c*, and *d* are weighting factors whose summation is one.

Irish and Resio, (2010) constructed an improved dimensionless and continuous surge scale (SS) index based on the systematic study of the storm surge phenomenon using numerical models along the US coasts.

$$SS = \Delta P \frac{L_*}{h_*} \Psi_x\left(\frac{R}{L_*}\right) \Psi_t\left(\frac{t_*}{t_\infty}\right) \Psi_\theta(\theta) \tag{1.4}$$

where L_*, and $h_*$are the characteristics of shelf width and depth, respectively, and ΔP, R, θ, t_* and t_∞ are storm pressure deficit (Mb), storm size, approach angle, storm duration, and time scale for equilibrium surge, respectively. Ψ_x, Ψ_t, and Ψ_θ are the linear dimensionless empirical functions to describe the relative influence of storm size, duration, and approach angle respectively. However, Irish and Resio, (2010) simplified the equation by ignoring the dependence of the approach angle and time dependence in Eqn. (1.4), assuming their impact is insignificant on storm surges (Rezapour and Baldock, 2014). Thus, the final form of the equation is given as:

$$SS = a\Delta P L_{30} \Psi_x \left(\frac{R}{L_{30}}\right) \tag{1.5}$$

where, a = 0.000243. The study found the horizontal distance (km) between the shoreline and the 30 m depth contour (L_{30}) for the width characteristics (L_*) is quite reasonable. Also, the studies (Irish and Resio. 2010; Chavas et al., 2013) suggested characteristic width scale (L_{30}) considered to be an optimal scale for the generation of storm surges. Although SS demostrates enhancement over the earlier indices (SSHS, HSI, and S_{DP}) for estimating surge potential, Kantha, (2010) argued that the use of ΔP does not characterize landfalling storms. Furthermore, it is suggested to take into account of the forward speed (S) of the TCs in Eqn. (1.5), as the temporal response of TCs is influenced by the ratio between the storm's residence time scale and the shelf's response time scale. Hence, Kantha, (2010), (2013) proposed Storm Surge Index (SSI) by incorporating modifications to Eqn. (1.4) in which ΔP term was replaced by V_{max} and introduced TC forward speed information. Further, dimensionless functions Ψ_x, and Ψ_t in the exponential form, replacing the previously used linear form was introduced.

$$SSI = \left(\frac{V_{max}}{V_{max0}}\right)^2 \left(\frac{L_{30}}{L_*}\right) \Psi_x \left(\frac{R}{L_{30}}\right) \Psi_t \left(\frac{RV_{max}}{L_{30}S}\right) \tag{1.6}$$

here the term S is the forward speed (in ms^{-1}) of the cyclone, $\Psi_x(x)$ = $1\text{-}e^{-3x}$ and $\Psi_t(t)$ = $1\text{-}e^{-0.04t}$. The linear dependence of TC forward speed on surge index is due to increase in the forward speed of TC causes an increase in storm surge along the open coast since TC forward speed tends to coincide with the long-wave propagation speed of the water (Thomas et al., 2019). Further, Rezapour and Baldock. (2014) estimated the rank of hurricane severity based on damage and death toll after hurricane landfall along the US coast based on the meteorological aspects of hurricanes. Thus, the proposed Tropical Cyclone Surge Index (TCSI) is given as follows:

$$TCSI = \left(\frac{V_{max}}{V_{max0}}\right)^2 \left(\frac{A_{34}}{A_{340}}\right) \tag{1.7}$$

where A_{34} is the area of surface wind speed greater than 34-knot, and the reference value A_{340} is the average of A_{34} value of selected storms from the NOAA Real-time Hurricane Wind Analysis System (H*Wind; Powell et al., 1998) database. Further, Islam et al., (2021) proposed a storm surge hazard potential index (SSHPI) and estimated peak surge hazard potential for the Japan coast using Japan Meteorological Agency (JMA) TC track data by incorporating modifications to the earlier existing Eqns. (1.1), (1.5), and (1.6), given as:

$$SSHPI = \left(\frac{V_{max}}{V_{max0}}\right)^2 \left(\frac{R_{50}}{R_{500}}\right) \left(\frac{S}{S_0}\right)^a \left(\frac{L_{30}}{L_*}\right) \tag{1.8}$$

where R_{50} is a measure of radius to 50-knot (26 m/s) winds, a is the characteristic coastal geometry: for open coast, a = 1, and for semi-enclosed bay, $a = -1$, and the reference constants V_{max0}, R_{500}, S_0, and L_* are defined as 25.72 ms^{-1}, 175 km, 9.72 ms^{-1}, and 40 km respectively.

Ormondt et al., (2021) presented a new semi-empirical storm surge prediction (SESSP) method which estimates storm surge along open coasts as a function of space and time based on the results of hydrodynamic model simulations. The proposed SESSP is an improvement to the follow-up study by Irish et al., (2008). The simulations were considered over an idealized bathymetry and coast using thousands of synthetic tracks. These synthetically generated tracks are based on varying bathymetry and track parameters, including approach angle. The SESSP method can predict the storm surges at landfall with an associated margin of error ranging from 30 to 35 cm with the model simulation results. However, the present study chooses to build upon the work by Islam et al., (2021) rather than Ormondt et al., (2021) because the scope of our study is focused on predicting peak surge height nearest to the landfall frame (location and time) since a peak storm surge height at landfall location leads to more extensive coastal flooding and increased damage to coastal structures. This aligns with the scope of previous studies by Kantha, (2008), (2010), (2013); and Irish and Resio, (2010). Further, the results show that SSHPI, considering actual bathymetry and coastline relying on limited historical parameters, demonstrates better accuracy than SESSP in predicting peak surge height. In spite, SESSP relies on numerous synthetic track simulations from idealized hydrodynamic model setups resulting in associated comparatively higher errors than SSHPI. Moreover, developing an index that is based on the results of hydrodynamic simulations does not promise its reliability in predicting peak surge height during real-time cyclone events. Because a hydrodynamic model inherently proved to have some error with the observation, especially when considering a large number of cyclone events (Salcines et al., 2019). This can possibly compound SESSP's observation-based errors even more

1.4.4. Machine Learning Models

In addition to numerical modeling, data-driven Machine Learning (ML) modeling with synthetic storm simulation databases has gained increased attention in the last decade since it has the advantage of drastically reducing computational time and improving accuracy as compared to high-fidelity numerical models based on physics (Irish et al., 2009; Taflanidis et al., 2013a, b; Cialone et al., 2015; Hashmi et al., 2016; Jia et al., 2016; Kyprioti et al., 2021; Lee et al., 2021; Ayyad et al., 2022; Chao et al., 2022). ML models are, without complex theory, often used to build surrogate models for various applications. Along the BoB region, specifically for the Odisha coast, Sahoo and Bhaskaran, (2019a, b) incorporated Artificial Neural Networks (ANN), Genetic Algorithm (GA), and Genetic Programming (GP) to predict storm surge and inundation for the different landfall location considering about 200 synthetic track datasets consists of track intensity, location, direction, and translation speed as an input variable for training the models. A statistical-based index model is grounded in traditional statistical methods with explicit, often simpler relationships between variables, while a machine learning model leverages data-driven learning to identify complex patterns and make predictions with greater flexibility and complexity. Data-driven ML modeling with synthetic storm simulation databases has gained increased attention in the last decade since it has the advantage of drastically reducing computational time and improving accuracy as compared to high-fidelity numerical models based on physics (Irish et al., 2009; Taflanidis et al., 2013a, b; Cialone et al., 2015; Hashmi et al., 2016; Jia et al., 2016; Kyprioti et al., 2021; Lee et al., 2021; Ayyad et al., 2022; Chao et al., 2022).

1.5. STORM SURGE HAZARD MAP

1.5.1. What is storm surge hazard map?

Storm surge hazard maps are visual tools that depict areas at risk of flooding due to storm surges. These maps are created using data from past/future storm events based on hydrodynamic simulations. They highlight zones with varying levels of risk, often indicating potential flood depths and the extent of land that could be affected. The primary purpose of storm surge hazard maps is to inform emergency planning, guide development away from high-risk areas, and help communities prepare for potential evacuations. These maps are essential for reducing loss of life, minimizing property damage, and enhancing the overall resilience of coastal areas against storm surges.

1.5.2. Why storm surge maps are required?

According to reports, as sea surface temperatures have risen in recent decades, and hence the strength of TCs (Niyas et al., 2009; Singh et al., 2000; IPCC, 2007; 2013a, 2013b; Parth Sarthi et al., 2015, Vyshnavi et al., 2023), It will only make future coastal floods worse. Analysing the historical data of TCs in the BoB is the most effective method for tackling this issue. It offers an opportunity to comprehend how their paths, intensities, and landfall locations behave, as well as a probable method of assessing the cyclone hazard (Nadimpalli et al., 2021). A reliable warning system requires accurate data on storm surges. Therefore, for emergency response plans and improved coastal infrastructure development, a realistic assessment of storm surges along the coast is essential. Understanding the return period of wind intensity scenarios is crucial for assessing the potential impact and frequency of storm surges along vulnerable coastal areas. A storm surge hazard map based on return periods provides valuable information about the likelihood of extreme wind events, aiding in effective disaster preparedness and response planning (Lechtenbörger, 2006). Thus, planning and readiness components of coastal management depend on the TC hazard proneness levels. Such a map enables authorities to prioritize resource allocation for infrastructure development, evacuation plans, and resilient coastal management strategies (Šakić Trogrlić et al., 2022). Creating a storm surge hazard map aligns with the need for proactive measures to mitigate the impact of TCs, ultimately safeguarding lives and minimizing economic losses along the Indian east coastline.

1.5.3. Advancements in storm surge hazard mapping

In the literature, to develop the surge hazard map, several studies have adopted fully physics-based numerical models to compute the peak surge heights. The use of such numerical models requires an effort to generate synthetic tracks. This makes the process of creating hazard maps complicated and time-consuming. IMD has published (Kalsi et al., 2007), hazard-prone coastal districts along the entire coast of India based on PMSS considering the historical frequency and maximum wind strength of TCs data collected from 1891 to 2008, based on the simulation results obtained from the storm surge model developed by IIT Delhi (Dube et al., 2009). Several studies have used synthetically generated tracks to feed the hydrodynamic model to develop storm surge hazard maps (Nayak and Bhaskaran, 2014; Sahoo and Bhaskaran, 2016; Rao et al., 2019, 2020; Sridharan et al., 2022). Synthetic tracks for the BoB region are typically generated by shifting historical tracks to the target area (Jain et al., 2010; Rao et al., 2013) or developed using the inverse distance method (Nayak and Bhaskaran, 2014; Sahoo and Bhaskaran, 2016; Sahoo and Bhaskaran, 2018; Rao et al., 2010, 2013; Jain et al, 2010). The techniques used are essentially derived from the empirical track model presented by Vickery et al, (2000). The corresponding surge values for different return periods along the coastal states of the Indian east coast are then estimated using a hydrodynamic model. The probable maximum surge levels are determined using fixed track characteristics such as ΔP and V_{max} obtained through the statistical distribution of historical cyclone data for different return periods. However, As the cyclone nears its landfall point, V_{max} steadily rises to its peak value before declining. These variations in V_{max}, along with other storm features related to the cyclone track, were not considered in the aforementioned research. Moreover, the studies reviewed have utilized the highest recorded V_{max} values along cyclone tracks from historical data to assess the most extreme surge scenarios. When such constant maximum storm features are considered in a hydrodynamic simulation, more water will be pushed toward the coast, leading to overestimated peak surge values. To overcome this issue, Sridharan et al., (2022) proposed a method for calculating the wind intensity for different return periods and other storm parameters that varies across the track. The intensity of various return periods is calculated at each eye position using a statistical approach. The findings imply enhanced surge values can be obtained by changing track parameters using the suggested methods. However, the suggested approach to feed the hydrodynamic model to generate a surge hazard map is complex and highly time-consuming. Moreover, the storm surge hazard map was produced by Sridharan et al., (2022) only for the small stretch along the northern portion of Tamil Nadu's coastline. Bushra et al., (2019) developed a computationally efficient statistical 2D copula model to estimate the annual probability between storm surge observations and wind speeds 12 hours before landfall, specifically for predicting return period surge values along the BoB coast. Their findings suggest that in a worst-case scenario, the BoB region could experience wind speeds of 62 m/s and surge heights of at least 8.0 meters, on average, once every 311.8 years. However, Sridharan et al., (2022) found that the surge values for the Tamil Nadu coast, based on return periods, were excessively high and significantly overestimated. Exaggerating storm surge predictions can lead to significant impacts on the costs of coastal protection and emergency planning. Conversely, underestimating them can result in devastating consequences due to inadequate mitigation strategies. It is essential to enhance the accuracy of predicting maximum surge values for coastal areas, considering varying return periods of wind speeds and other related track parameters

1.6. RESEARCH GAPS

- While several studies have applied the blended wind field approach to different ocean basins. However, no assessment has been conducted to select the appropriate parametric and background wind models to superimpose within the blended wind field. Choosing a parametric wind model that better depicts the wind field close to the cyclone eye region is crucial in the blended wind field approach. Also, it is necessary to choose a background wind field that better depicts the wind field in the area far away from the cyclone center. However, the blended wind field approach entails complexity, as it involves a separate procedure to possess the wind field data from the global wind field model sources to superimpose with a parametric model. This is due to the spatial and temporal resolution of the input data may not consistently align the cyclonic wind field features from different model sources (parametric and global) throughout the storm duration. Consequently, relying on wind fields from global models such as WRF or the Unified Model (UM) can incur high computational costs (Silva et al., 2014) within the blended wind field approach. Therefore, there is also a need to improve the parametric wind models by incorporating modifications. This is because parametric models are simple and computationally efficient.

- Several semi-empirical equations are available in the existing literature for estimating the total bedload transport rate in cases involving currents alone (without considering wave effects) as well as those considering both currents and waves. However, there is no study available in the open literature that has investigated the performance of various semi-empirical formulas for total bedload transport during storm surges along open coastlines of BoB. Specifically, it is crucial to understand which semi-empirical formulas for the total bed transport are better suited for the prediction of morphological bed evolution in the open coasts of the BoB during storm surges.

- The shift from numerical to statistical index modeling is driven by the need for greater computational efficiency in predicting storm surges. From the literature, It is noted that the importance of consideration of approach angle is not yet clear within the statistical-based surge index models, However, several numerical investigations have shown the importance of consideration of approach angle in storm surge generation Further, previous studies considered mostly the synthetic track parameters within the Machine Learning models, which are based on hypothetical assumptions. Also, the literature reveals that all existing studies have focused solely on meteorological parameters, with none incorporating bathymetric data as an input for Machine Learning (ML) models to estimate storm surges. The literature also highlights the need to compare statistical index-based models with statistical ML models to predict peak surge height when considering low number dataset samples.

- It is noted that all the aforementioned studies have generated synthetic tracks to feed the hydrodynamic model to derive the storm surge values for the respective periods to generate the surge hazard maps. It should be noted that generating synthetic tracks and running hydrodynamic simulations are complex and computationally time-consuming processes to develop storm surge hazard maps. Enhancing the forecast accuracy of probable maximum surge values for the coast with different return periods of V_{max} and other associated track parameters is necessary. Also, we need a system that is simple, accurate, and computationally highly efficient for creating the surge hazard map.

1.7. OBJECTIVES

The primary objective of the study is to enhance the predictive capabilities of the both numerical and statistical storm surge models for the BoB. The primary objective is supported by the following sub-objectives:

Sub-objective 1: To bring improvements in wind field hindcast for the accurate prediction of storm surges and associated wind wave, coastal inundation and nearshore morphodynamic bed evolution using numerical model in the BoB.

Sub-objective 2: Develop a novel statistical based surge potential index model for the BoB for effective and accurate prediction of storm surges and apply the model to create surge hazard maps.

1.8. SCOPE OF PRESENT STUDY

- Enhance the accuracy of wind field representations in the BoB region by evaluating the performance of parametric and global wind models, focusing on their effectiveness near and away from cyclone centers.
- Enhance the accuracy of storm surge predictions along the coastal stretches of the BoB by implementing an enhanced blended wind field approach based on the evaluation of different wind models.
- Enhance the accuracy of cyclonic structure representation by developing a modified parametric wind model that accounts for a better depiction of wind fields, both near and distant cyclone effects, based on performance evaluation of different parametric wind models.
- Perform numerical simulations to understand the sensitivity of atmospheric forcing from different wind models on storm surges, wind waves, and coastal inundation.

- To investigate and analyze morphodynamic changes in nearshore coastal areas caused by storm-induced currents and waves in the BoB by implementing a tightly coupled hydrodynamic, wave, and morphodynamic model framework.
- To assess and identify the most suitable empirical formulations for total bed transport that effectively account for the impact of storm-induced currents and waves, in order to enhance the prediction of morphodynamic bed evolution along the open coast of the BoB.
- To develop a novel statistical-based Tropical Cyclone Surge Potential Index (TCSPI) model that provides accurate and efficient predictions of peak surge heights along the BoB coast.
- For the rapid prediction of peak surge height implement regression-based supervised machine learning models across the extensive coastal regions of the BoB.
- To determine how different modeling approaches influence the accuracy of peak surge height predictions in the BoB, the performance of various predictive models, including the TCSPI, ADCIRC, and machine learning techniques, will be assessed and compared
- Develop an effective, simple, and efficient methodology to create a surge hazard map using return periods and projected climate change scenarios along Indian eastern coastline.

1.9. LAYOUT OF THE THESIS

The thesis of the present study comprises seven chapters and is organized as follows.

Chapter – 1: This chapter introduces storm surges and the physical characteristics of the BoB basin. This chapter discusses numerical modeling and its importance. This includes recent advancements in enhancing cyclonic wind field modeling. This chapter briefly introduces numerical modeling of storm surges, wind waves, and morphodynamics. This chapter introduces statistical modeling of storm surges, highlighting its significance, recent advancements, and its application in developing surge hazard maps.

Chapter – 2: This chapter outlines the overall methodology of the thesis. Governing equations of the numerical models. The methodology used to predict water levels, wind waves, and morphodynamics using improved cyclonic wind fields within the numerical model is presented. It discusses the development of surge index model and ML models. Model validation and comparison methodologies are presented, including the application surge index model in developing surge hazard maps.

Chapter – 3: This chapter outlines the evaluation of different parametric and global wind models for the BoB. An effective methodology was presented to enhance the blending technique. The model validation and application are presented. A sensitivity analysis of storm surge, wind waves, and coastal inundation based on different atmospheric wind models is presented. The chapter ends with a summary.

Chapter – 4: This chapter outlines the setting up of a coupled hydrodynamic, wave, and morphodynamic model for the BoB to investigate nearshore morphodynamics during cyclones. A new modified parametric wind model for the BoB was introduced within the coupled framework for atmospheric forcing. Evaluating different bed load transport formulations under storm conditions is presented. The chapter ends with a summary.

Chapter – 5: This chapter outlines the development of a statistical-based Tropical Cyclone Surge Potential Index (TCSPI) model and the development of ML models for predicting peak surge height in the BoB. Various datasets are considered in the development of TCSPI and ML models. A methodology to validate TCSPI and ML models. Comparison and analysis of the performance of TCSPI, ML, and numerical models.

Chapter – 6: This chapter outlines enhancements made to the TCSPI model. Validation of improvised TCSPI model for the historical cyclone cases. The Surge Calculator website is presented. An Efficient methodology for generating a surge hazard map using the TCSPI model is presented. A surge hazard map based on different return periods and climate change scenarios is presented for the Indian east coast. The chapter ends with a summary.

Chapter – 7: The entire research work is summarized, and specific conclusions drawn from the study are presented in this chapter. The future scope of the present study is also suggested in the end.

The flowchart presented in Fig. 1.4 outlines the structure of this thesis, which focuses on storm surge modeling and its applications. The thesis employs both statistical and numerical modeling approaches. In the statistical modeling section, the development and application of TCSPI are discussed. The numerical modeling section covers the applications of hydrodynamic modeling, coupled hydrodynamic and wave modeling, and coupled hydrodynamic, wave, and morphodynamic modeling, as presented below.

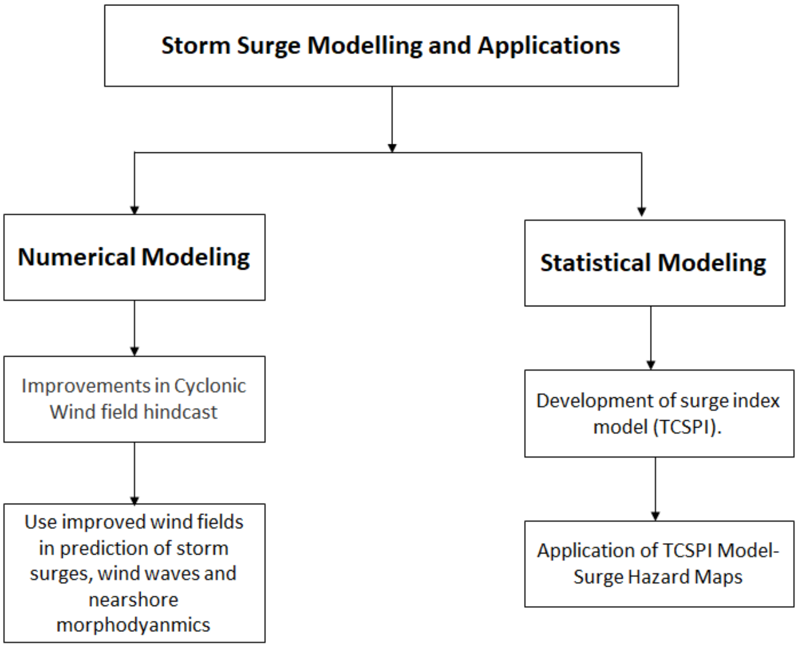

Fig 1. 2. Structure of the thesis

CHAPTER 2

METHODOLOGY

2.1. GENERAL

Different cyclonic wind models considered in the study are discussed briefly. An effective methodology to enhance the blended wind field approach is discussed. Further, the description of coupled hydrodynamic, wave, and morphodynamic frameworks is briefly discussed. The methodology of evaluating the performance of different bed load transport formulations in predicting the morphodynamic bed evolution during storm-induced currents and waves is presented. The chapter outlines the geographical characteristics of the domain of interest and the diverse data utilized in developing statistical-based TCSPI and ML models. It also delves into the specific methodology employed in the development, execution, validation, and comparison of statistical and numerical models for predicting peak surge height in the BoB. Further, this chapter discusses the application of TCSPI model in developing the surge hazard map, considering return period estimates and climate change scenarios.

2.2. NUMERICAL MODELING

The present study employs TELEMAC-2D and ADCIRC models for hydrodynamic simulations, SWAN and TOMAWAC for wave modeling, and the GAIA model for morphodynamic simulations. Brief description of these models is as follows

2.2.1. ADCIRC Model

Numerical simulations were performed using the ADvanced CIRCulation 2-dimensional depth-integrated (ADCIRC-2DDI) hydrodynamical model. The model uses Galerkin finite element method to solve the Generalized Wave Continuity Equation (GWCE) and vertically integrated momentum equation on the unstructured triangular grid. In the ADCIRC, the weeting and drying technique is incorporated along the land boundary of the domain while the ocean boundary conditions are determined at the open boundary of the domain (Kolar et al., 1994a, b; Luettich and Westerrink, 2002)

2.2.2. TELEMAC-2D Model

The hydrodynamic simulations are performed using the TELEMAC-2D model. This model uses the finite-element method with triangular elements in its computational mesh to solve the Saint-Venant equations (shallow water equation) (Hervouet et al., 1995, Bates et al., 1995). Long-period wave propagation, the influence of Coriolis force, the impact of wind and atmospheric pressure, turbulence, constant or fluctuating bed friction, flooding or drying effect, and other meteorological phenomena can all be simulated using TELEMAC-2D. Hervouet (1999) provided more details on the solution techniques used in TELEMAC-2D.

2.2.3. Governing equations of hydrodynamic models

The GWCE is a reformulation of the shallow water equations used in hydrodynamic modeling to improve numerical stability (Lynch and Gray, 1979). It combines continuity and momentum equations to better handle wave propagation and reduce numerical errors in computational simulations. The primitive continuity equation for an incompressible flow is given by:

$$L = \frac{\partial H}{\partial t} - \frac{\partial (UH)}{\partial x} + \frac{\partial (VH)}{\partial y} = 0 \tag{2.1}$$

The GWCE is derived using Eqn. (2.1) as:

$$\frac{\partial L}{\partial t} + \tau L = 0 \tag{2.2}$$

Where τ is the tunining parameter. τ is function of bathymetry depth (h) and is related by following condition.

$$\tau = \begin{cases} 5 \times 10^{-3} \;\; if\; h > 200m \\ 0.11 \;\; if\; h < 1m \\ \frac{1}{10h} \;\; if\; 1m < h < 200m \end{cases} \tag{2.3}$$

Expanding Eqn. (2.2), the finite element formulation for the GWCE continuity equation is given by:

$$\frac{\partial^2 \zeta}{\partial t^2} + \tau_0 \frac{\partial \zeta}{\partial t} + \frac{\partial J_x}{\partial x} + \frac{\partial J_y}{\partial y} - UH \frac{\partial \tau_0}{\partial x} - VH \frac{\partial \tau_0}{\partial y} = 0 \tag{2.4}$$

Where

$$J_x = Q_x \frac{\partial U}{\partial x} - Q_y \frac{\partial U}{\partial y} + fQ_y - \frac{g}{2}\frac{\partial \zeta^2}{\partial x} - gH \frac{\partial \left[\frac{p_s}{g\rho_0} - \alpha\eta\right]}{\partial x}$$
$$- \frac{\tau_{(sx,wind)} + \tau_{(sx,wave)}}{\rho_0} - \frac{\tau_{bx}}{\rho_0} + M_x - D_x \tag{2.5}$$

$$J_y = Q_x \frac{\partial V}{\partial x} - Q_y \frac{\partial V}{\partial y} + fQ_y - \frac{g}{2}\frac{\partial \zeta^2}{\partial y} - gH \frac{\partial \left[\frac{p_s}{g\rho_0} - \alpha\eta\right]}{\partial y}$$
$$- \frac{\tau_{(sy,wind)} + \tau_{(sy,wave)}}{\rho_0} - \frac{\tau_{by}}{\rho_0} + M_y - D_y \tag{2.6}$$

The vertically integrated momentum equation for currents are:

$$\frac{\partial U}{\partial t} - U\frac{\partial U}{\partial x} + V\frac{\partial V}{\partial y} - fV = -g\frac{\partial}{\partial x}\left[\zeta + \frac{p_s}{g\rho_0} - \alpha\eta\right]$$
$$- \frac{\tau_{(sx,wind)} + \tau_{(sx,wave)}}{\rho_0 H} - \frac{\tau_{bx}}{\rho_0 H} + \frac{M_x - D_x}{H} \tag{2.7}$$

$$\frac{\partial V}{\partial t} - U\frac{\partial V}{\partial x} + V\frac{\partial V}{\partial y} - fU = -g\frac{\partial}{\partial y}\left[\zeta + \frac{p_s}{g\rho_0} - \alpha\eta\right]$$
$$- \frac{\tau_{(sy,wind)} + \tau_{(sy,wave)}}{\rho_0 H} - \frac{\tau_{by}}{\rho_0 H} + \frac{M_y - D_y}{H} \tag{2.8}$$

where, U and V are “depth-averaged velocities” in the x and y directions, respectively, while ζ denotes “elevation of the free surface from its mean position”. The total water column thickness H, is the sum of ζ and h. The fluxes in the x and y directions per unit width, Qx and Qy, are given by UH and VH. The parameter τ_0 is used to optimize phase propagation characteristics. “Coriolis parameter” is denoted by f, and g is “acceleration due to gravity”. P_s is “atmospheric pressure at the free surface”, while ρ_o is “reference water density”. α stands for “effective elasticity factor of the Earth”, and η is “Equilibrium tidal potential in a Newtonian framework”, $\tau_{(s,wind)}$ and $\tau_{(s,wave)}$ are “surface stresses by wind and waves”, respectively, $\tau_{(b)}$ is “bottom stress”, M is “vertically integrated lateral stress gradients” and D is “momentum dispersion”.

ADCIRC employs Equations (2.4), (2.7), and (2.8) as its governing equations, while TELEMAC-2D utilizes Equations (2.1), (2.7), and (2.8). The GWCE used in ADCIRC provides stability advantages over traditional shallow water equations used in TELEMAC-2D, especially for large, unstructured grids in coastal simulations. This reduces numerical spurious oscillations and enhances stability in low-gradient areas, making ADCIRC more efficient and reliable for large-scale storm surge forecasting than TELEMAC-2D (Lynch and Gray, 1979). However, the present study also used TELEMAC-2D due to its versatility in simulating 2D shallow water flows and its tight coupling options for waves, sediment, in detailed river and estuary simulations.

2.2.4. SWAN Model

The unstructured version of the third generation Simulating WAves Nearshore (SWAN) numerical model was developed at Delft University of Technology specifically to simulate waves in coastal and near-shore environments. (Holthuijsen et al., 1993; Booij et al., 1999). The SWAN model solves the spectral action balance equations in the unstructured triangular grid.

2.2.5. TOMAWAC Model

Present study uses the TELEMAC-based Operational Model Addressing Wave Action Computation (TOMAWAC) model. This is a third-generation spectral wave-propagation model that accounts for critical processes such as the effect of wave generation by wind, white-capping, nonlinear wave-wave interaction, refraction, shoaling, and dissipation (Benoit et al., 1996). The model uses the finite elements formulation for discretizing the sea domain; it is based on the computational subroutines of the TELEMAC system.

SWAN and TOMAWAC both utilize spectral wave equation to solve the action density balance, as given in Eqn. (2.9), yet each is tailored for different strengths in wave modeling. SWAN is optimized for computational efficiency in coastal zones, focusing on diffraction, wave breaking, and handling complex bathymetry, making it ideal for nearshore applications. In contrast, TOMAWAC is designed for seamless integration with other TELEMAC modules, allowing dynamic wave-current interactions suited for detailed hydrodynamic studies in environments like coastal, estuaries and river outflows. Together, they offer complementary capabilities for comprehensive wave and hydrodynamic simulations.

$$\frac{dN}{dt} = \nabla \cdot (Cg\ N) = \frac{S_{in} - S_{out}}{\sigma} \tag{2.9}$$

where $N\ (t,x,\sigma,\theta)$ is the wave action density, which is related to the energy density E by N=E/σ, with σ being the relative angular frequency of the waves. C_g is the group velocity of the waves. $\nabla \cdot (C_g\ N)$ is the divergence of the wave action flux in physical and spectral space. S_{in} represents the energy source terms, which may include wind input and wave growth. S_{out} represents the energy sink terms, including wave breaking, white capping, and bottom friction.

2.2.6. GAIA model

GAIA is the latest open-source module for sediment transport and bed evolution within the TELEMAC-MASCARET modeling system (Tassi et al., 2023). GAIA is based on the historical SISYPHE morphodynamic model, which has undergone numerous modifications, adjustments, and optimizations. In order to reduce roundoff errors, GIAIA uses dry mass to determine the amount of each sediment class in the bed rather than volume, as used in SISYPHE (Audouin et al., 2019). To the author, no study in the open literature has incorporated the GAIA model in the (BoB). The sediment transport module calculated the movement of non-cohesive sediments and seabed level changes caused by waves and currents, and the bed evolution scheme predicted the subsequent bed level changes. In GAIA, the bedload fluxes are estimated in terms of (dry) mass transport rate per unit width (kg/m s) without pores:

$$Q_{mb} = \rho_s Q_b \tag{2.10}$$

Q_b represents the vector of volumetric transport rate per unit width (m²/s), comprising the components (Q_{bx} and Q_{by}) in the x and y directions, respectively, ρ_s the sediment density (kg/m^3). The non-dimensional sediment transport rate Φ_b is given by Wu, (2007).

$$\Phi_b = \frac{Q_b}{\sqrt{g(s-1)d^3}} \tag{2.11}$$

where $s = \rho_s/\rho$ represents the relative density, ρ is the water density (kg/m³), d denotes the sand grain diameter (m), and g is the acceleration due to gravity (m/s²). Various empirical formulas for calculating Φ_b can be chosen by the user. The different sediment transport rate formulas incorporated in the GAIA model are listed in Table. 2.1. Most of these formulas are based on experimental studies, with sediment properties adhering to the constraints of the chosen formulation. Brief description of each of these models is given in Appendix B section. The minimum grain size (median particle diameter, d_{50}) limit applicable to each sediment formulation (Bayram et al., 2001; Tassi and Villaret, 2014) is also indicated in Table 2.1.

Table 2.1. Gaia uses bedload transport formulae. 'No' is used to indicate formulas that do not specifically account for the effect of waves. 'Yes' indicates formulas that take the effect of waves into account.

SL. No.	Bedload transport formula	Effect of waves	Minimum grain size limit (mm)	Source
1	Meyer-Peter-Muller (MPM) formula	No	0.4	Meyer-Peter and Müller, (1948)

2	Einstein-Brown (EB) formula	No	0.25	Rouse (1949) and Einstein (1950)
3	Engelund-Hansen (EH) formula	No	0.15	Engelund and Hansen (1967)
4	van Rijn's (VR) formula	No	0.20	van Rijn (1984)
5	Bijker's (BJ) formula	Yes	0.10	Bijker, (1968)
6	Soulsby-van Rijn (SVJ) formula	Yes	0.10	Soulsby (1997)
7	Bailard's (BL) formula	Yes	0.10	Bailard (1981)
8	Dibajnia and Watanabe (DB) formula	Yes	0.10	Dibajnia and Watanabe (1992)

Bedload, suspended load, or both sediment transport modes can be taken into consideration at the simultaneously when calculating the bed evolution by solving the mass conservation equation for sediment or the Exner equation (Garcia, 2008), which is expressed as.

$$(1-n)\frac{dZ_b}{dt} + \nabla . Q_{mb} = D - E \quad (2.12)$$

where n is the porosity of the bed material at the bed surface, Z_b is the bed elevation above datum (m), and $\nabla\cdot$ is the divergence operator and D and E are deposition and erosion rates, respectively. More detailed information about the GAIA model is presented in Tassi et al., (2023). In this study 250 the porosity and density of non-cohesive sediment are considered to be 0.4 (Van Rijn, 1989) and 2650 kg/m³ (Tassi and Villaret, 2014), respectively, for estimating morphodynamic bed evolution using different sediment transport rate formulations.

2.2.7. Coupled ADCIRC+SWAN

The coupled ADCIRC+SWAN is employed to account for the effect of wind wave-induced impact on surges for the case study TC Varadah in the present study. Water surface elevations, currents, and wind fields are first simulated using the ADCIRC model. These variables are then provided as input to the SWAN model to produce radiation stresses and associated gradients, which are then sent to the ADCIRC as a forcing function.

2.2.8. Coupled TELEMAC-2D+TOMAWAC+GAIA

The hydrodynamic model (TELEMAC-2D), wave model (TOMAWAC), and morphodynamic model (GAIA) are coupled with each other and resolved on the same computational mesh. At each time step, the hydrodynamics variables (velocity field, water levels, and bed shear stress), as well as wave variables (significant wave height, wave peak period and mean wave direction), are transferred into the morphodynamic model, which sends back the updated bed evolution to the hydrodynamic and wave model.

2.3. METHODOLOGY FOR NUMERICAL MODELING

Five well-known parametric wind models—the Jelesnianski (SLOSH), Rankine Vortex (RV), Willoughby (WL06), Holland (HL80), and Generalised Asymmetric Holland Model (GAHM)—as well as two global wind models—the Weather Research Forecast (WRF) and the European Centre for Medium-Range Weather Forecasts (ECMWF)—were evaluated in the present study with measurements that were available in BoB. The equations of each parametric wind model are detailed in Chapter─3. The performance of each wind model is assessed based on observation wind data sourced from in-situ buoy measurements (INCOIS). After examining the most effective wind model for this area. The assessment results introduce two enhanced cyclonic wind fields: one based on a blended wind field approach following Pan et al., (2016) and the other using a modified parametric wind model. Using the coupled ADCIRC+SWAN model, the current work sheds light on the variations in the simulated surge, wind wave, and inundation caused by the various atmospheric driving wind models.

Further, among the two enhanced cyclonic wind fields developed, the wind field approach that offers the more reliable, computational efficiency, and simplicity, with accuracy remaining within acceptable limits, will be used in a coupled hydrodynamic-wave-morphodynamic model for atmospheric forcing to predict the water levels, wind waves and morphodynamic changes resulting from overwash during TCs in the BoB. In the present study, the coupled hydrodynamic (TELEMAC-2D) -Wave (TOMAWAC) –Morphodynamic (GAIA) models were used for the simulations.

Further, evaluation the performances of four semi-empirical sediment transport models (Meyer-Peter-Muller (MPM), Einstein-Brown (EB), Engelund-Hansen (EH), and van Rijn (VR)) for scenarios with only currents, and four models (Bijker (BJ), Soulsby-van Rijn (SVJ), Bailard (BL), and Dibajnia and Watanabe (DB)) within the GAIA model of coupled framework for scenarios with both currents and waves for predicting morphodynamic bed evolution during TC Nivar (2020).

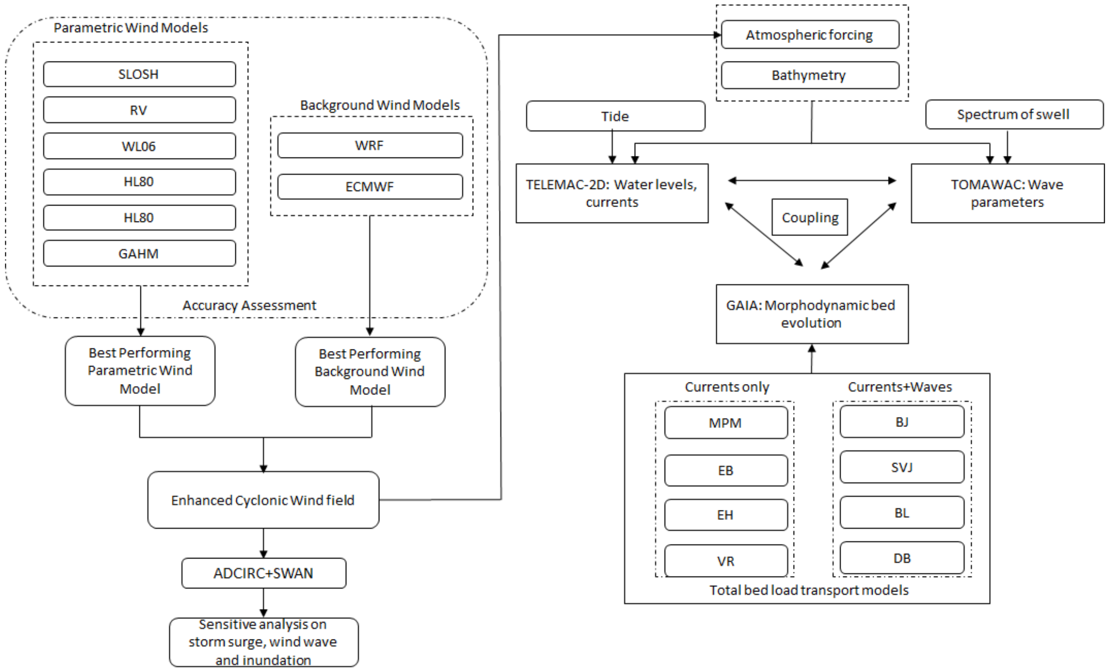

Fig 2.1. Brief overview of methodology for numerical modeling

2.4. METHODOLOGY FOR STATISTICAL MODELING

The shift from numerical to statistical storm surge modeling is driven by enhanced data efficiency and simplified analysis. This method efficiently predicts storm surges while incorporating various readily accessible parameters to understand surge dynamics better. A novel Tropical Cyclone Surge Potential Index (TCSPI) equation is introduced that is well suited for the BoB region. This equation is based on readily available cyclone track atmospheric and bathymetry parameters. The estimated TCSPI values are regressed with the observed peak surge height values at the landfall. The least squares-fit between surge height and TCSPI provides an empirical relationship. These empirical equations are used to estimate potential peak surge height. Further, the estimated potential peak surge height and observed peak surge height are validated. Chapter─5 provides a thorough discussion of the TCSPI model.

Further, slight modifications incorporated to the TCSPI for the enhanced accuracy and this model is made accessible for public use through IITM Surge calculator website (https://iitmaisurge.in/). This enhanced model is further used as an application for developing the surge hazard map for the Indian east coast. The Indian east coast is home to four coastal states: West Bengal, Odisha, Andhra Pradesh, and Tamil Nadu. Using historical track data from IMD (1982–2022), return periods are estimated using Weibull distribution for the track parameters i.e., wind speed, forward speed at the landfall time frame for each maritime state along the Indian east coasts. This proposed methodology ensures simple, accurate, and computationally efficient without the need to generate synthetic tracks and estimation of the return period of cyclone central pressure drop information. The estimation of peak surge heights is made for different return periods in combination with climate change scenarios (CCS) by increasing the present storm wind speed as per the International Panel for Climate Change (IPCC) projections. A concise summary of the methodology is illustrated in the flow chart depicted in Fig. 2.2. Chapter─6 provides a thorough discussion on the surge hazard map.

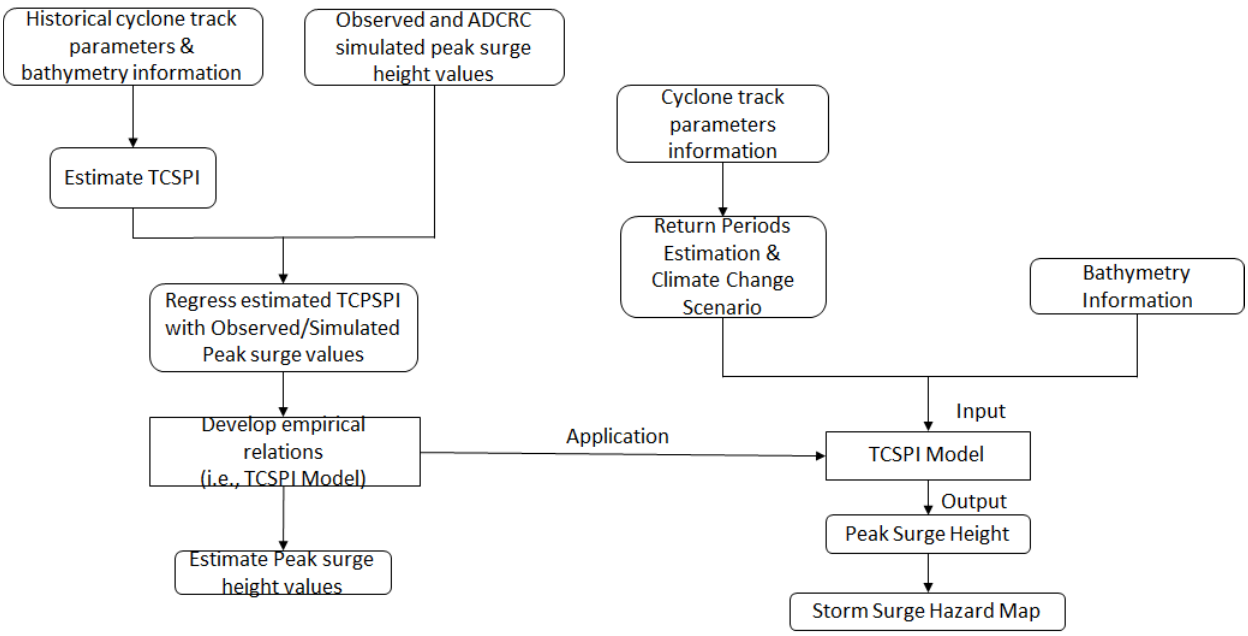

Fig 2.2. Brief overview of the methodology for statistical modeling

2.5. SUMMARY

The chapter provides a comprehensive evaluation of various models and methodologies used in predicting and analysing storm surges. It begins with an overview of enhanced cyclonic wind field, based on evaluation of various wind parametric and background wind models to improve the accuracy of storm surge, wind wave and morphodynamic bed predictions. Further, this enhanced wind field is used within the coupled hydrodynamic –wave –morphodynamic model frame work evaluating different bed load transport formulations during cyclones, providing a nuanced understanding of how sediment movement can influence storm surge dynamics. The development of statistical-based index models for the BoB and it’s application in storm surge prediction are discussed. A key focus is on the effective and efficient development of surge hazard maps, which are crucial for disaster preparedness and mitigation are also presented.

CHAPTER 3

MODELING OF CYCLONIC WIND FIELD[1]

3.1. GENERAL

Modeling the cyclonic wind field is vital for predicting storm surges, as wind intensity and structure directly impact surge height and inundation extent. Accurate wind field representation ensures that models capture the dynamics of wind-driven water movement along the long stretch of coast, improving surge forecasts. The literature indicates that the blended wind field approach is an advanced method that superimposes a parametric wind model with a background wind model. This approach superimposes the strengths of parametric and background wind models to more precisely predict wind conditions near the cyclone center and at greater distances, effectively overcoming the limitations of each model. There is no consensus on the selection appropriate parametric and background wind models in the blending technique. This study introduces a methodology to enhance the blended wind field by evaluating various parametric and background models.

3.1.MODEL DESCRIPTION AND METHODOLOGY

The present study uses ADCIRC and coupled ADCIRC+SWAN model. Details about the model description are given in Chapter─2.

3.1.1. Atmospheric Forcing Models

The wind field is one of the primary inputs for estimating the surges using ADCIRC Standalone and ADCIRC+SWAN. The study discusses some commonly used hindcasting of wind fields based on parametric and global wind models. The five commonly adopted wind models are Rankine Vortex, (1947), Jelesnianski, (1966), Holland, (1980), Willoughby et al., (2006), and Generalized Asymmetric Holland

[1] This work is published in: "Shashank, V. G., Sriram, V., & Sannasiraj, S. A. (2022). Improvements in wind field hindcast for storm surge predictions in the Bay of Bengal: A case study for the tropical cyclone Varadah. Applied Ocean Research, 127, 103324. https://doi.org/10.1016/j.apor.2019.102048 40"

Model (2013), respectively. The global wind field obtained from the assimilation model (i.e., ECMWF reanalysis) and operational weather model (i.e., WRF) are used in the present study.

3.1.1.1.Rankine Vortex Model (RV)

The Rankine vortex serves as a basic parametric model for describing the wind profile of a TC. The model was first proposed by Depperman, (1947), drawing from the classical Rankine vortex approximation (Rankine, 1882). It presumes that within the radius of maximum wind, the velocity increases in a linear fashion, while beyond this radius, the velocity decreases inversely with the radial distance (r).The gradient wind speed distribution $V(r)$ is given by Eqn. (3.1).

$$V(r) = \begin{cases} V_{max}\left(\frac{r}{R_{max}}\right), & 0 \leq r \leq R_{max} \\ V_{max}\left(\frac{R_{max}}{r}\right)^{X}, & r > R_{max} \end{cases} \tag{3.1}$$

where, V_{max} is the 1-minute maximum sustained wind speed, r is radial distance, R_{max} is the radius of maximum wind, and X is the shape parameter that adjusts the velocity distribution in the radial direction. Hughes, (1952) empirically estimated the value of X to be in the range of 0.4–0.6 from observed TCs. X = 0.5 was usually adopted (Riehl, 1954; Phadke et al., 2003; Salcines et al., 2019; Das, 2018), and the same was adopted in the present study.

3.1.1.2.Jelesnianski Model (SLOSH)

The parametric wind model, also famously known as the Sea, Lake, and Overland Surges from Hurricanes (SLOSH) model, is one of the widely used parametric wind models for the NIO region (Jelesnianski. 1966). Houston et al., (1999) validated this model with observation-based surface wind fields. The gradient wind speed distribution is expressed as

$$V(r) = V_{max}\left(\frac{2rR_{max}}{R_{max}^2 + r^2}\right) \tag{3.2}$$

3.1.1.3.Willoughby et al. (2006) Model (WL06)

Willoughby et al., (2006) developed a wind profile based upon a sample of 493 cyclonic system profiles from aircraft observations. In the WL06 model, the wind intensity grows proportionally to a power of the radius within the eye and diminishes exponentially beyond the eye, following a seamless polynomial transition across the eyewall. This approach accounted for the average exponent in the power-law (n = 0.79) and the mean decay length of X = 243 km. The gradient wind profile for the WL06 is expressed as

$$V(r) = \begin{cases} V_{max}\left(\dfrac{r}{R_{max}}\right)^{n}, & 0 \leq r \leq R_{max} \\ V_{max}e^{\left(-\frac{r-R_{max}}{X}\right)}, & r > R_{max} \end{cases} \tag{3.3}$$

3.1.1.4.Holland Model (HL80)

Holland (1980) introduced an analytical framework to describe the radial patterns of pressure gradients and wind speed distributions of the storm. The equations of the HL80 model are expressed as

$$P(r) = P_c + (P_n - P_c)e^{-(\frac{R_{max}}{r})^{B}} \tag{3.4}$$

$$V(r) = \sqrt{V_{max}^{2}e^{1-\left(\frac{R_{max}}{r}\right)^{B}}\left(\frac{R_{max}}{r}\right)^{B} + \left(\frac{rf}{2}\right)^{2}} - \left(\frac{rf}{2}\right) \tag{3.5}$$

$$B = \frac{V_{max}^{2}\rho e}{(P_n - P_c)} \tag{3.6}$$

where f is Coriolis force, P_c is the minimum central atmospheric pressure, Pn is the ambient pressure, Pr is the pressure at radius r from the cyclone's center; B is the shape parameter derived from Eqn. (3.6) considering cyclostrophic assumption. B controls the eye diameter and steepness of the tangential velocity gradient using Eqn. (3.6). Mattocks and Forbes (2008) further improved the shape parameter and proposed a more detailed equation to calculate the parameter B as given in Eqn. (3.6), in which V_{max} is computed as $[(V_m - V_t)/W_{PBL}]$. Here, is the 1-minute maximum sustained wind speed of the cyclone, Vt is the cyclone's translation speed, $WPBL$ is a wind reduction factor determined at the gradient wind flow level positioned above the impact zone of the planetary boundary layer. It is set to 0.80 to adjust the wind speeds down to the surface (Powell and Black, 1990), and ρ is the density of air (assumed to be constant at 1.15 kg/m^3 in the Holland parameter model).

3.1.1.5.Generalized Asymmetric Holland Model (GAHM)

GAHM was developed by (Gao et al., 2013, 2018), which differs from the existing HL80 model with adjustments that remove the presumption of cyclostrophic balance at R_{max}. Further, employing a linear combination of parameter sets derived from the isotachs available in each quadrant. The radial pressure and gradient wind profile for the GAHM are expressed as:

$$P(r) = P_c + (P_n - P_c)e^{-\varphi(\frac{R_{max}}{r})^{B_g}} \quad (3.7)$$

$$V(r) = \sqrt{V_{\max}^2\left(1+\frac{1}{R_0}\right)e^{1-\left(\frac{R_{max}}{r}\right)^{B_g}}\left(\frac{R_{max}}{r}\right)^{B_g} + \left(\frac{rf}{2}\right)^2} - \left(\frac{rf}{2}\right) \quad (3.8)$$

where R_0 is the Rossby Number at $r = R_{max}$, given as $R_0 = V_{max}/R_{max}f$. $V_{max} = [(V_m - \gamma V_t)/W_{PBL}]$, in which γ is damp factor $= V(r)/V_{max}$ and B_g is shape parameter (same as HL80, without assuming cyclostrophic balance), given as, $B_g = B(1 + 1/R_0)e^{\varphi-1}/\varphi$. φ is the scaling parameter used in GAHM, given by $\varphi = 1 + (1/R_0)/B_g(1 + 1/R_0)$.

Except for GAHM, in the rest of the above parametric models, the surface pressure-wind field follows a modified rectangular hyperbola as a function of radius (Schloemer, 1954). The pressure field is obtained from Eqn. (3.4). GAHM follows a pressure-wind profile obtained from Eqn. (3.7).

Traditionally SLOSH, WL06, RV, and HL80 parametric wind models were used for an azimuthally constant R_{max} either from the empirical formulations (Zhao et al., 2021) or the "best track" datasets and do not account for the translational speed of the storm to generate its vortex winds. The numerical study by Xie et al., (2011) showed significant sensitivity to the water level and coastal flooding to the asymmetry of a cyclonic wind field. Qiao et al., (2019) showed that the wind field obtained from the symmetric wind model predicts higher error with respect to the observed wind data near the cyclone center region than the wind field obtained from the asymmetric wind model. Murty et al., (2020) reported a few exceptions while implementing the blended wind field with the measured data in the BoB. The parametric wind formulation based on the symmetric Holland model preserves the inner core region of the cyclone, causing certain limitations associated with the blended wind fields. Hence, the study suggested that further improvement in the blending formulation can be made by considering the asymmetric nature of the cyclonic wind field in the blending technique. Hence, in the present study, modifications are employed to obtain the asymmetry nature of the cyclone's wind field to compute the gradient wind profile for SLOSH, RV, WL06, and HL80 parametric models. The azimuthally constant R_{max} is replaced with directionally varying $R_{\max}(\theta)$, where θ is the azimuthal angle around the center of the storm computed using the brute-force marching method (Xie et al., 2006). It can ensure the different radii of several characteristic wind speeds (e.g., the radii of 34-, 50- and 64-knot wind speeds obtained from JTWC forecast advisories. Further, the asymmetric parametric wind models for each quadrant rely solely on the largest specified wind velocity and radius available. Due to the intricate nature of actual cyclonic structures, utilizing all forecasted wind data is essential to enhance the accuracy of the parametric wind model. Hence in the GAHM, a new composition method was implemented to generate a weighted composite wind field in which a linear weighting of the parameter set is computed from all available isotachs in each quadrant. A detailed explanation for the multiple isotachs approach can be referred to in Gao et al., (2013, 2018).

In addition, considering the asymmetry nature of the wind profile, the moving velocity of the cyclone center was superimposed with storm vortex winds for all the parametric wind models based on the approach proposed by Jelesnianski, (1966) approach. The total wind vector V can be expressed as

$$V = V(r) + V_{mov} \tag{3.9}$$

$$V_{mov} = V_t \left(\frac{rR_{max}}{R_{max}^2 + r^2} \right) \tag{3.10}$$

where V_{mov} is the wind vector induced by the moving component, and $V(r)$ is the gradient wind vector induced by the rotating component of the different parametric wind models.

Further, following the empirical formulations (Bretschneider, 1972), the wind inflow angle (β) approximation was applied to account for frictional convergence to the wind field. The inflow angle was increased linearly from 10° at the storm center to 20° at R_{max} and then to 25° at $1.2R_{max}$, and to remain at 25° beyond $1.2R_{max}$ as given in Eqn. (3.11). This was also used by Lin and Chavas, (2012). Therefore, all the parametric wind models considered in the present study are asymmetric with respect to the cyclone center, which is in marked contrast to the past studies in BoB.

$$\beta = \begin{cases} 10° \left(1 + \frac{r}{R_{max}}\right) & r < R_{max} \\ 20° + 25\left(\frac{r}{R_{max}} - 1\right), & R_{max} \le r \le 1.2R_{\max} \\ 25°\,, & r \ge 1.2R_{max} \end{cases} \tag{3.11}$$

The TC events are obtained from the JTWC that consists information of surface wind parameters and relevant atmospheric track parameters, the 1-minute maximum sustained wind (V_{max}), the coordinates of the hurricane center and the radial pressure gradient ($P_n - P_c$). The shape parameter (B and B_g), translational speed (V_t) and $R_{max}(\theta)$ are pre-computed in the four storm quadrants for the available radii isotaches of the 34-, 50-, and 64-knot winds in four (northeast, southeast, southwest, and northwest) quadrants R34 (θ), R50 (θ), R64 (θ) with θ = (45,135,225, 315) in the Asymmetric Wind Input Preprocessor (ASWIP), integrated within ADCIRC, and append to input prior to initiating ADCIRC simulations.

3.1.1.6.ECMWF Wind

The ECMWF wind dataset features a spatial resolution of 0.25° and is available at 3-hour temporal intervals. Used as an atmospheric forcing within the hydrodynamic model. The ECMWF reanalysis assimilation model integrates dynamic, physical, and coupled ocean wave components. This model operates based on six fundamental governing equations that are defined within geographic space and time coordinate systems (Persson and Grazzini, 2007).

3.1.1.7.WRF Wind

For background wind field information, the operational research WRF model was considered in the study. The schemes for determining the physical parameters considered in the study are discussed by Sandeep et al., (2018). The WRF simulation was extracted during the cyclonic activity period. The extracted wind data with a spatial resolution of 3 km and temporal resolution of 3 hours as the forcing fields to the model were employed in the present study.

3.1.1.8.Blending Model

As mentioned previously, neither the parametric nor the global wind models were performing better individually. Thus, blending methods were used ("Pan et al., 2016; Shao et al., 2018; Qiao et al., 2019; Asher et al., 2019; Chen et al., 2019; Hsiao et al., 2019, 2020; Murty et al., 2020; Chang et al., 2021; Selvaraj et al., 2022"). When superimposing the parametric and background fields, the blending technique should offer a smooth transition between the two wind fields. The blending technique proposed by Pan et al., (2016) is used in this study since it performs better in our numerical study cases. The specific expression for blended wind field W_{Blend} is expressed as follows:

$$If\ r \leq R_1\ then\ W_{Blend} = W_{par}$$

$$If\ R_1 \leq r \leq R_2\ then\ W_{Blend} = (1-\alpha) \times W_{par} + \alpha \times W_{bac}$$

$$If\ r \geq R_2\ \ then\ W_{Blend} = W_{bac}$$

Where, α is the blending factor given as $\alpha = \frac{r-R_1}{R_2-R_1}$

W_{par} refers to the parametric model wind field, W_{bac} is the background wind field, R_1 is the radial extent from the center of the cyclone till the parametric wind field is effective, R_2 is radial extent beyond the smoothed transitional zone, where the background wind field is effective. Previous studies have shown that the blending factor, a transitional function in the blended wind field, is a critical parameter (Qiao et al., 2019). The detailed procedure for blending methodology can be found in Pan et al., (2016).

3.1.2. Evaluation of parametric wind models for the BoB

In this section, the wind field obtained from the parametric wind models is investigated for the past cyclonic events in the BoB. Complex models may provide different conclusions for a small number of events (Salcines et al., 2019). Hence, we have considered the past ten cyclonic events that occurred in the last ten years, as shown in Fig. 3.1. The model-simulated winds are compared to the winds from deep-water moored buoys (BD09, BD10, and BD11). The Indian National Centre for Ocean Information Services (INCOIS) provided the observed data. Table 3.1 lists the locations of the buoys used in the evaluation. Venkatesan et al., (2013) provide information on the sensors employed in the buoy. Table. 3.2 shows the list of cyclones and their classification as per the Indian Mereology Department (IMD) and the observation buoy station. For validation, 72 hours of observed data in the nearest location is considered for each cyclone case.

The validation results are estimated in terms of Root-Mean-Square Error (RMSE) and Correlation Coefficient (CC) for all the five parametric wind models, as shown in Fig. 3.2. GAHM performs better with an RMSE of 3.15 m/s and CC of 0.74. Besides GAHM, RV also performed better with an RMSE of 3.53 m/s and CC of 0.62. However, SLOSH, WL06, and HL80 are underestimating the observed values (RMSE and CC) for most of the cyclonic events considered in the study.

It is evident that the winds generated by GAHM using the multiple-isotach approach and elimination of cyclostrophic assumption compared better with the observed wind data in BoB. While, despite considering asymmetric modifications in SLOSH, RV, WL06, and HL80, GAHM performed better in the BoB region. This analysis is the overall comparison of the wind field using the parametric wind model. However, to understand better the performance of each of these models, a typical TC Varadah is considered further.

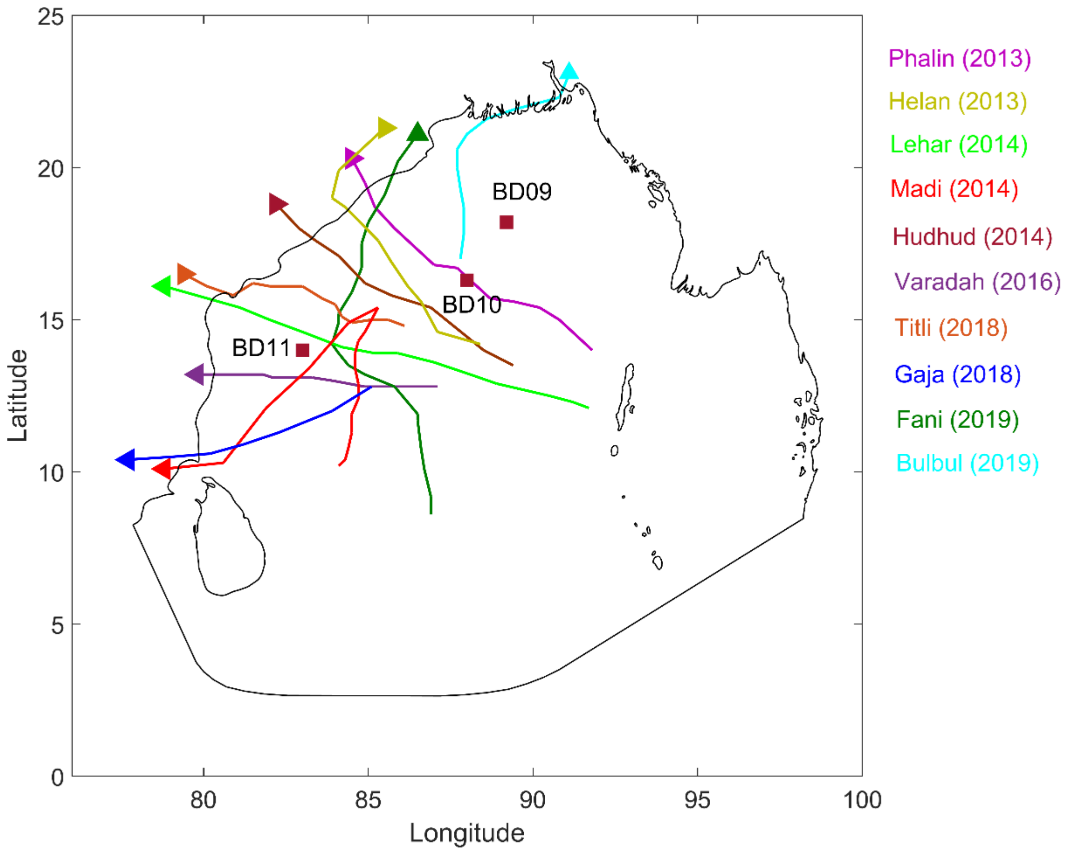

Fig 3.1. Tracks of the different cyclonic cases that occurred in the past decade (2010-2020) in the BoB

Table 3.1. Details of the buoy locations

Buoy	Latitude	Longitude
BD09	18°N	89°E
BD10	16.3°N	88°E
BD11	14°N	83°E

Table 3.2. List of cyclones and the corresponding classification made by IMD and nearest available observed buoy considered to that particular each of the cyclonic track for 72 hours (3 days).

Cyclone Case	**IMD Classification**	**Cyclone start time**	**Cyclone end time**	**Observed Buoy Station**
Phalin	ESCS	10-10-2013:00	13-10-2013:00	BD09

Helan	SCS	19-11-2013:00	22-11-2013:00	BD11
Lehar	VSCS	25-11-2013:00	28-11-2013:00	BD11
Madi	VSCS	07-12-2013:00	10-12-2013:00	BD11
Hudhud	ESCS	09-10-2014:00	12-10-2014:00	BD10
Varadah	VSCS	09-12-2016:12	12-12-2016:12	BD11
Titli	VSCS	09-10-2018:00	12-10-2018:00	BD10
Gaja	VSCS	14-11-2018:00	17-11-2018:00	BD11
Fani	ESCS	30-04-2019:00	03-05-2019:00	BD10
Bulbul	VSCS	08-11-2019:00	11-11-2019:00	BD10

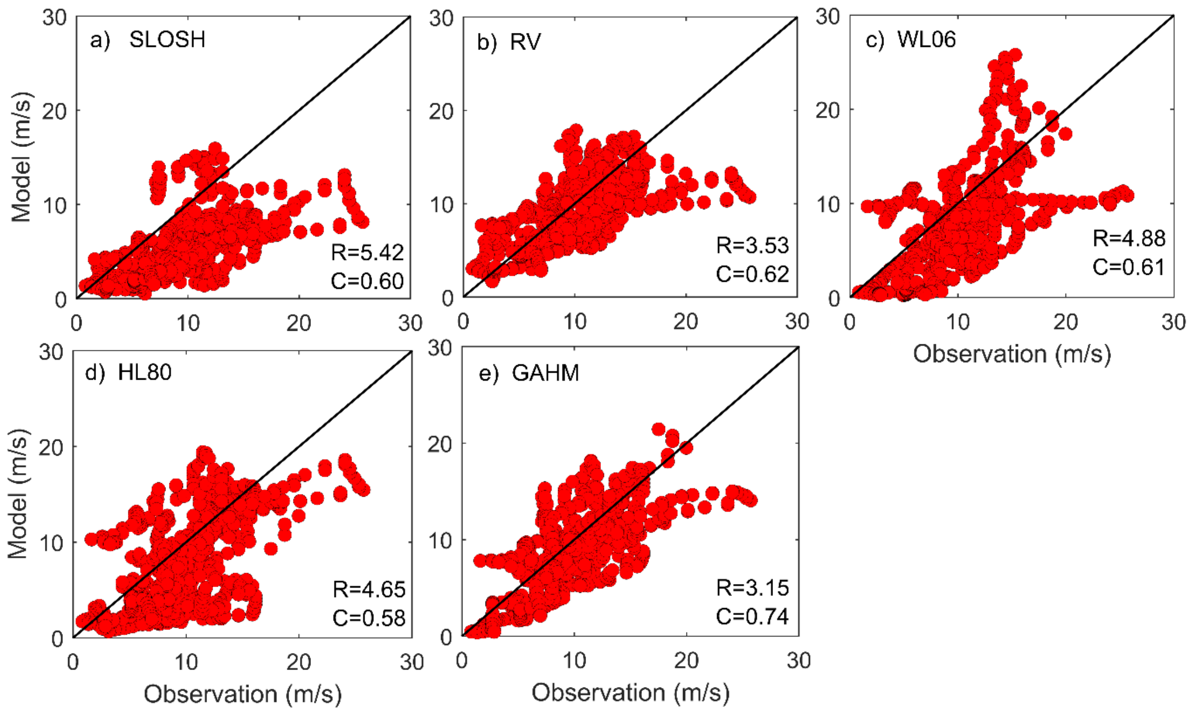

Fig 3.2. In the x-axis, observed wind speed from buoy locations and the y-axis corresponds to simulated wind speed from a) SLOSH, b) RV, c) WL06, d) HL80, and e) GAHM models. ‘R’ and ‘C’ denote RMSE and correlation coefficients, respectively.

3.1.3. Varadah Cyclone and Model Setup

TC Vardah is one of the most intense cyclones formed in the BoB in 2016 and is classified as a VSCS by IMD. The cyclone system reached its lowest pressure at 975 hPa, with a maximum 1-minute sustained wind speed of 41.15 m/s. This low-pressure system initially developed as a depression on December 6, close to the Malay Peninsula. It gradually intensified into a cyclonic storm on 8 December, maintaining to move generally on a westward track. The cyclonic system consolidated into a SCS on 10 December. Due to favorable conditions for further development, the cyclonic system Vardah intensified to a VSCS on 11 December with a 1-minute sustained wind speed of 41.15 m/s and a minimum central pressure of 975 hPa. TC Vardah weakened into a SCS on 12 December and made landfall (09:30-11:30 UTC) on the north coast of Tamil Nadu near the Chennai location, with a wind speed of 30.5 m/s. Afterward, it rapidly weakened into a depression due to land interaction. The best track estimate from JTWC, along with the bathymetry of the region, is shown in Fig. 3.3a. The temporal variation of the wind speed and surface pressure are shown in Fig. 3.3b.

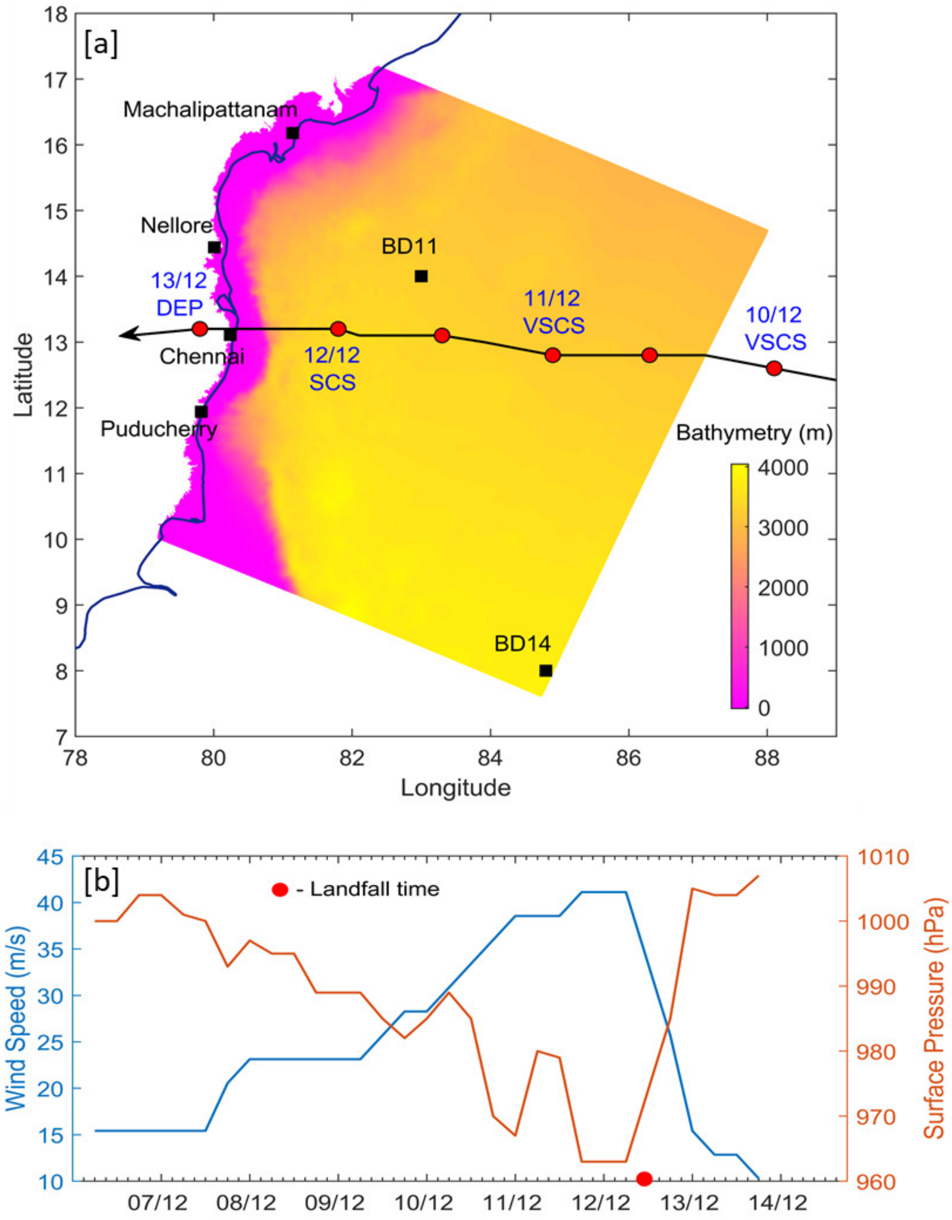

Fig. 3.3. (a) The Best track data for the TC Varadah (source: JTWC) is shown by the black line, with center points marked at 1200 UTC for each day from December 10 to December 13, 2016.The bathymetry depth of the entire domain from GEBCO is indicated by the colour bar. Black square dots indicate buoys BD11, which are located nearer to the cyclonic track, and BD14, which is away from the cyclonic track. (b) The JTWC track data from December 7–15, 2016, showing the temporal variation of surface pressure (in hPa) and wind speed (in m/s). The red dot represents the time of landfall.

In the present study, both the ADCIRC Standalone (uncoupled) and coupled ADCIRC+SWAN model simulations for TC Varadah are investigated. A hybrid bottom friction formulation with a drag coefficient of 0.0028 is used in the simulation. In GWCE, the weighting factor (τ_0) and horizontal eddy viscosity coefficient are taken to be 0.01 and 4 m^2/s, respectively. The model's time step was chosen to be 3 s. The model time step for SWAN and the coupling time interval were set to 600 s. This was sufficient to capture the nonlinear interaction effects due to changing water levels and currents on the resultant wave field (Bhaskaran et al., 2013). A wetting and drying algorithm is also activated with a minimum depth threshold of 0.5 m to delineate the wet and dry elements. The domain's tidal forcing is calculated using Le Provost's tidal database (Le Provost et al., 1998). The triangular unstructured grid consists of 157,390 elements and 308,909 nodes (see Fig. 3.4). Node spacing ranges from 80 meters near the coast to a maximum of 12 km in the open ocean. The GEBCO database provides the inland topography and ocean bathymetry at a 15-second resolution (Weatherall et al., 2015). Furthermore, the boundary of the coastal grid (Fig. 3.4b) is represented by the 10-m contour line along the land (Bhaskaran et al., 2014).

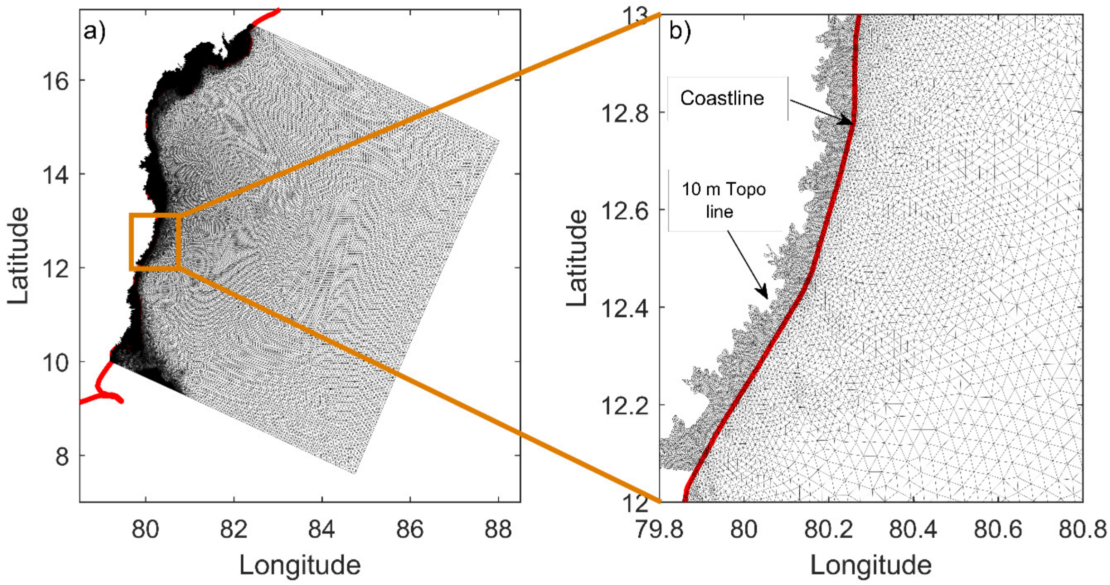

Fig 3.4. (a) The unstructured triangular grid covering the entire study area and (b) a zoomed-in view of the grid near the Chennai coastline. The red line depicts the zero-contour coastline, while the land boundary is considered up to a 10 m topography contour line.

3.2. RESULTS AND DISCUSSIONS

3.2.1. Comparison of the different atmospheric wind fields for the TC Varadah

The spatial profiles of wind fields computed from asymmetric parametric wind models and background wind models during the stronger duration of TC Varadah are shown in Fig.3.5. It can be observed that RV is predicting better away from the cyclone center region due to its nature of gradient wind profile equation. However, wind intensity tends to diminishes too quickly away from the storm center for SLOSH. The WL06 winds did show few similarities to that of SLOSH winds. The HL80 and GAHM winds shared a lot of similarities. The differences were mostly observed in the outer region of the asymmetric nature of the cyclone due to the usage of the multiple-isotach approach in the GAHM. The maximum rotating component of wind speed produced by GAHM was 38.9 m/s, whereas, for SLOSH, RV, WL06, and HL80 models, the maximum rotating component of wind speed predicted was 36 m/s along the track of TC Varadah. The background wind fields obtained from WRF and ECMWF winds were much more complex than those of the simple parametric wind models. The wind field obtained from the operational research WRF model produces very strong wind gusts at the radius of maximum wind with maximum rotating component wind speed indicating 44 m/s. In contrast, ECMWF reanalysis wind produces a significantly weaker rotating wind field with a maximum wind speed of 14 m/s along the track of TC Varadah.

It was observed from the spatial distribution of wind field in WRF and ECMWF, R_{max} is higher than the observation made by JTWC. Whereas the R_{max} predicted by parametric wind fields are relatively less than the global wind models. Further, it was observed that the center of the cyclone depicted by the ECMWF deviated by a few degrees away from JTWC best track data, which was also reported previously by Walsh, (1997) and Landman et al., (2005).

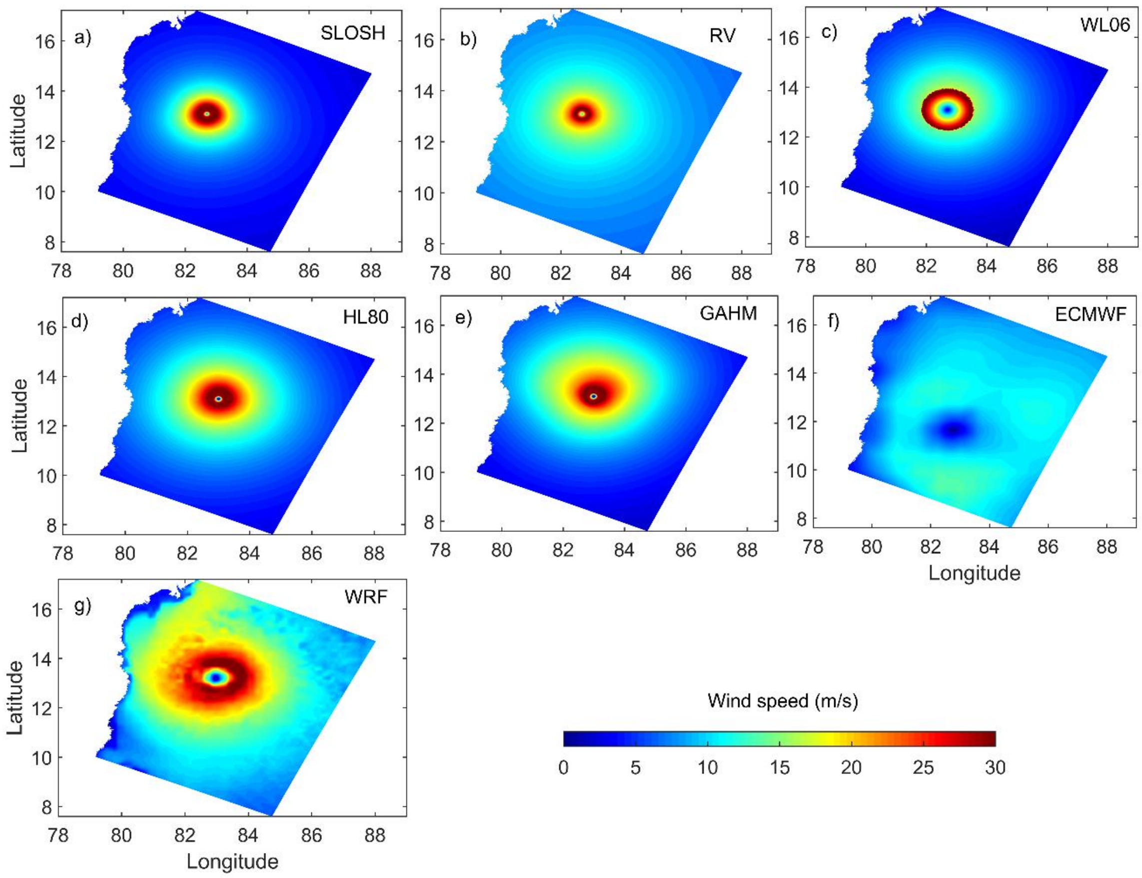

Fig 3.5. Spatial distribution of the magnitude of cyclonic wind fields from a) SLOSH, b) RV, c) WL06, d) HL80, e) GAHM, f) ECMWF, and g) WRF wind models on 11 December 2016 at 12:00 UTC.

Fig. 3.6 shows the comparisons of radial profile among the SLOSH, RV, WL06, HL80 and GAHM at the snapshot time. Generally, from the radial profile observation, it can be seen that GAHM has predicted higher wind speed at R_{max} compared to the rest of the parametric wind models. In contrast, RV and WL06 models had predicted lower wind speeds. Further, it can be observed that moving far away from the cyclone center, RV has predicted high intensity while the rest of the other model winds are gradually reducing. The contour lines for 17.5 m/s (34-kt), 25.5 m/s (50-kt), and 33 m/s (64-kt) are shown for each wind snapshot at the matured stage of TC Varadah. Fig. 3.6a shows the South-West (SW) to North-East (NE) cross-section winds and Fig. 3.6b shows the North-West (NW) to South-East (SE) cross-section winds. The observed isotaches at radii from the JTWC "best track" are also plotted as vertical line segments for reference. For a perfect match between the modelled and the observed isotaches, the radial profiles should meet close to the tip of the line segments at the same height.

The statistical estimation from all the parametric wind models and observed isotaches at radii are shown in Table. 3.3. The GAHM had an almost perfect comparison with a mean wind speed, having a standard deviation ranging from 1.57 to 2.77 m/s. The SLOSH and HL80 have a good agreement with observation for the 33 m/s (64-kt) observed isotach but failed at the lower isotaches. The RV and WL06 winds behaved poorly, and the results also had an extensive spread compared to other parametric models.

The parametric wind model wind fields over the cyclone durations are compared with the field observations at BD11 and BD14 (as shown in Fig. 3.3a). It can be seen that the location of BD11 is closer to the track of TC Varadah compared to BD14, which is located at the outer region of TC Varadah. The comparison between the different parametric wind models and the global wind model to understand the influence is shown in Fig. 3.7. It can be seen that GAHM performs better than the other parametric wind models at BD11, whereas RV predicts well at BD14 for this cyclone (Fig. 3.7a, and b). In the global or background wind models, WRF overestimates, and ECMWF underestimates the observed wind field at BD11. However, WRF performs well at BD14.

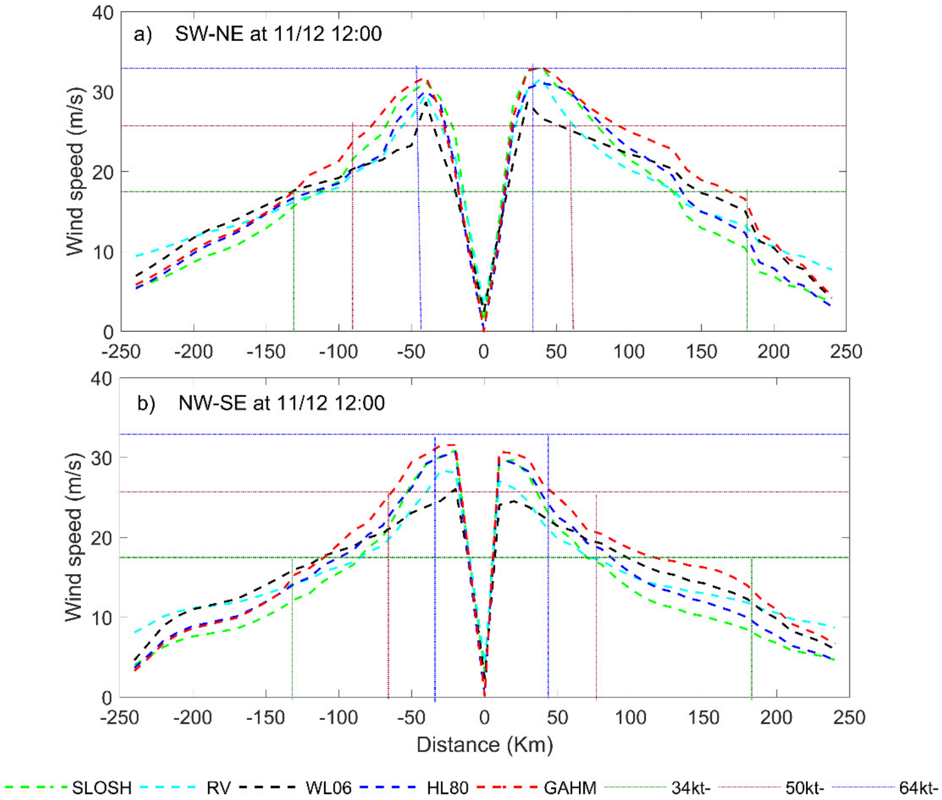

Fig 3.6. Comparison of radial wind profiles captured at matured stage (11 December 2016, at 1200 UTC) of the TC Varadah among the SLOSH, RV, WL06, HL80, and GAHM winds obtained from JTWC best track input. For a) South West-North East quadrant and b) North West-South East quadrant.

Table 3.3. Statistical analysis of modeled winds at radii to specified isotaches considering all the quadrants

	Mean (m/s)			Standard Deviation (m/s)		
Observed	Iso-17.5 (34kt-)	Iso-25.5 (50kt-)	Iso-33 (64kt-)	Iso-17.5 (34kt-)	Iso-25.5 (50kt-)	Iso-33 (64kt-)
SLOSH	11.74	22.60	29.37	3.13	2.37	3.85
RV	13.73	21.10	27.045	2.19	3.62	3.68
WL06	15.22	21.37	25.89	2.34	2.59	2.79
HL80	13.33	22.51	28.50	2.90	4.98	2.40
GAHM	15.95	24.5	30.05	1.57	2.77	2.71

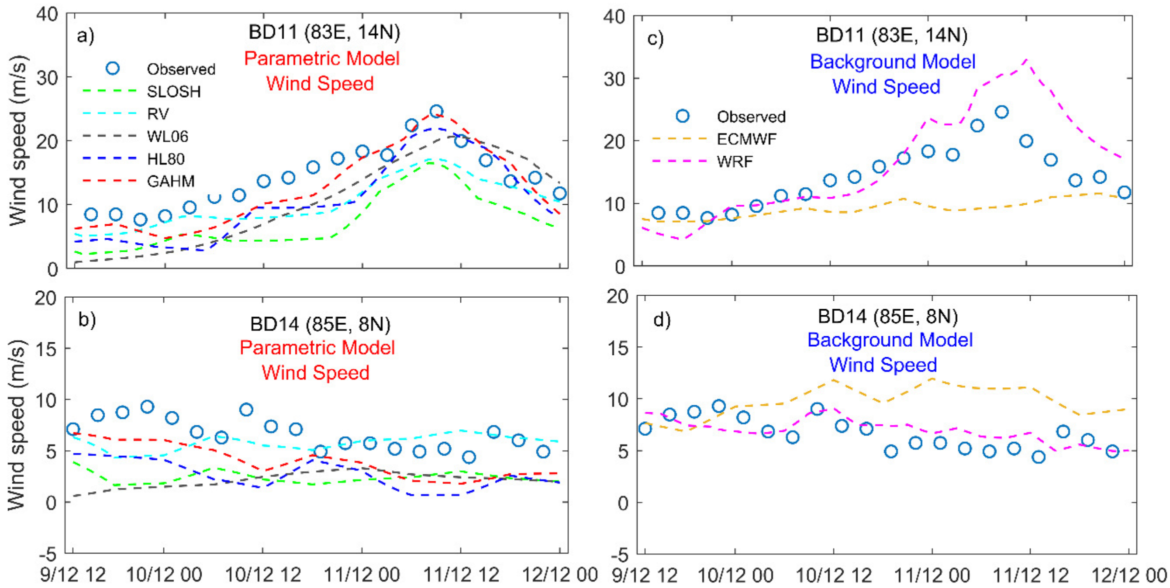

Fig 3.7. Comparison of simulated wind field from parametric TC Varadah wind models (i.e., SLOSH, RV, WL06, HL80, and GAHM) with the observed wind at a) BD11 and b) BD14. Comparison of simulated wind field from the background wind models (i.e., ECMWF and WRF) with the observed wind at c) BD11 and d) BD14.

3.2.2. Blended wind field

From the above analysis with different sources, it can be safely concluded that disadvantages of GAHM and WRF can be overcome by blending wind field together to represent the TC Varadah. Qiao et al., (2019) also attempted a similar blending technique with different parametric models. The spatial representation of the blended wind field (GAHM+WRF) is shown below in Fig. 3.8a. Comparing with Fig. 3.5, one could see a good representation in the inner and outer regions of the cyclone eye.

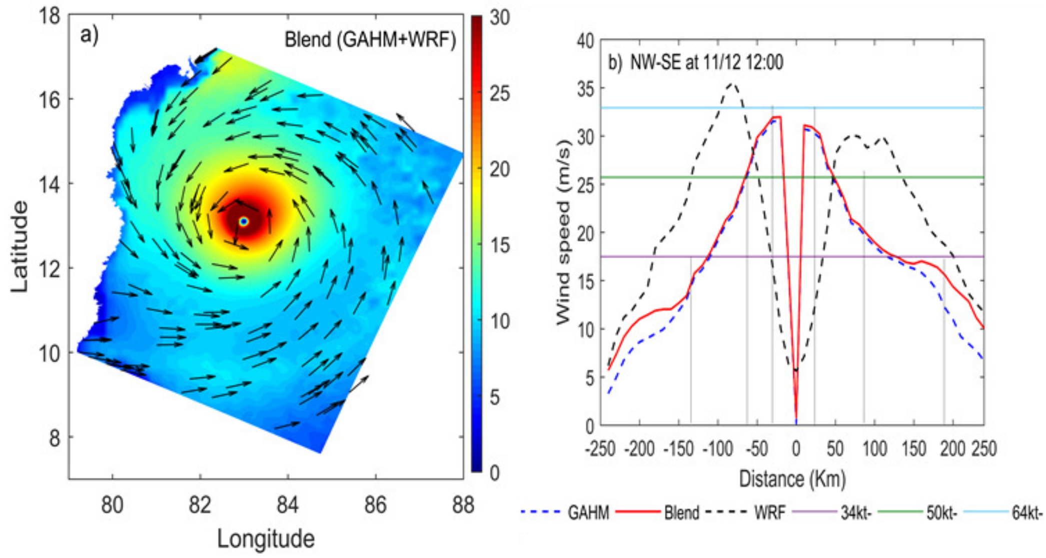

Fig 3.8. a) Depiction of the spatial distribution of blended wind field and b) radial profile of GAHM, WRF and blended wind fields for the TC Varadah cyclone captured on 11 December 2016, at 1200 UTC.

Fig. 3.8b depicts the radial profile of the parametric wind field of GAHM, the background wind field obtained from WRF, and the blended wind field (GAHM+WRF) captured on 11 December 2016, at 1200 UTC during the TC Varadah event. The radial profile from GAHM+WRF compares well with the JTWC advisory (R_{max} of about 45 km) and performs better than the WRF radius (about 100 km). The wind speed of 15 m/s at the outer region of GAHM+WRF agrees with observed data at BD14, which is situated at the outer core region of the TC Varadah, compared to GAHM. From the spatial analysis, it is evident that the blended wind field aligns with the parametric wind near the eyewall (inner core) while seamlessly transitioning to the WRF wind in the outer core region.

In order to evaluate the performance of parametric, background, and blended winds with the in-situ buoy measurements for TC Varadah in the BoB, a validation exercise has been conducted. Fig 3.9a illustrates that the WRF derived wind speeds are overestimated than those recorded by the buoy at BD11 (situated near cyclone track), while the wind speeds from GAHM and the blended model show good agreement with the observed data.

Similarly, Fig. 3.9b shows that the GAHM wind field underestimates with observed buoy wind at BD14 (far away from the cyclone track of Varadah). In contrast, the magnitude of WRF and blended winds are in good agreement with the observation. This indicates that the blended wind field closely follows the WRF wind pattern in the outer region of the cyclone, away from the storm center.

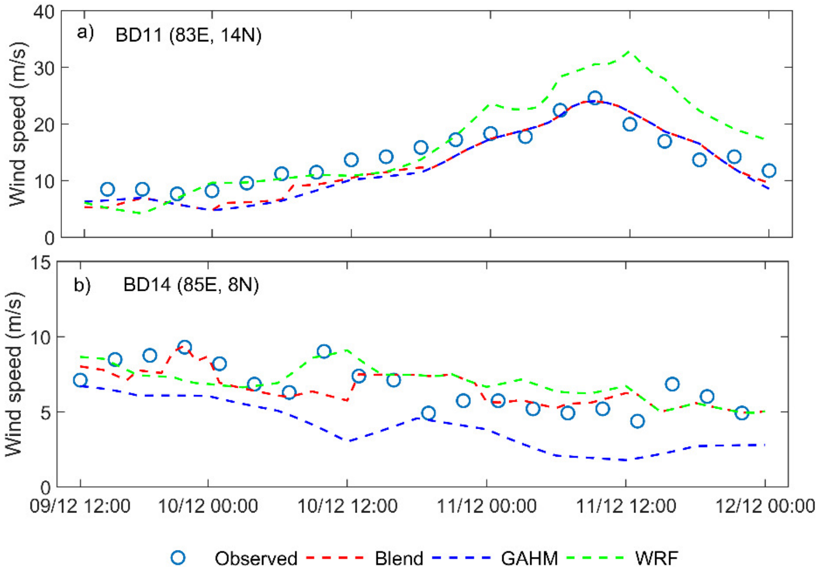

Fig 3.9. Comparison of GAHM, WRF, and Blended wind speed with observed buoy wind speed at a) BD11 (situated nearer along the cyclonic track) and b) BD14 (situated away from the cyclonic track) locations.

The validation results are estimated in terms of RMSE and Mean Bias Error (MBE) for both the buoys, as shown in Fig. 3.10. The errors corresponding to wind speed at BD11 are considerably less for GAHM, followed by HL80. In contrast, WRF wind shows an overestimation of wind with respect to the observed wind (negative value of MBE). Similarly, the errors corresponding to wind speed at BD14 are considerably less for WRF, followed by RV, while ECMWF indicates an overestimation of wind intensity with respect to the observed wind.

The errors associated with wind speed at the BD11 and BD14 buoy locations are notably lower for the blended wind field compared to the other wind models. This suggests that the blended wind field is more effective for operational applications, as indicated by the overall analysis.

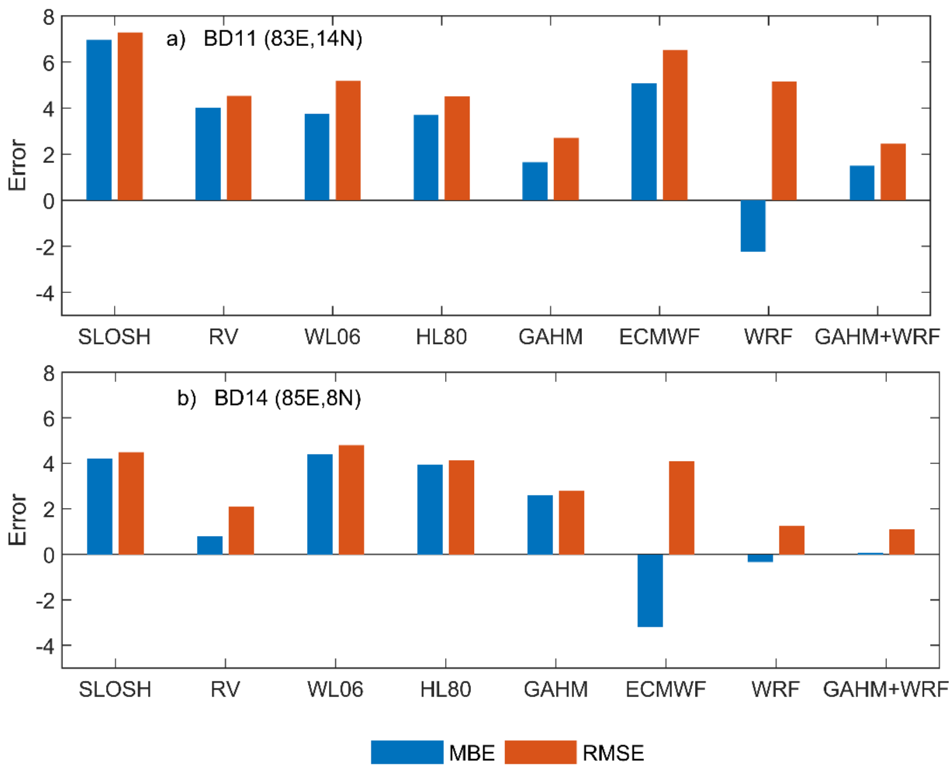

Fig 3.10. a) MBE and RMSE at BD11 buoy and b) BD14 buoy locations.

3.2.3. Impact on the surge, wind wave and inundation by different wind models

The importance of the parametric, global, and blended model for a TC Varadah has been discussed in the previous section, and the best parametric model for all the past decade cyclones in BoB has been brought out. Now, the variations or influence of this wind field on the surge, significant wave height, and inundation extent are discussed. As discussed previously, the simulations were carried out using ADCIRC standalone and coupled ADCIRC+SWAN model for the different atmospheric wind field forcing. The residual water levels, also known as surge residuals or storm-induced surges (Murty et al., 2014; Pandey and Rao, 2018), are computed by subtracting tides from total water levels. The cyclone intensity started reducing as the cyclone reached the land surface. The landfall for the TC Varadah occurred at 80.32°E, 13.2°N near Chennai coast, at the low tide (-0.27 m), on 12 December 2016, at 0900 UTC. Predominant signatures of the storm-induced surge are significantly observed for the different atmospheric wind fields considered in the study. Thus, the storm-induced surge predicted by different atmospheric wind fields is in good agreement with the forecast issued by the IMD report, except for ECMWF. IMD reported that "storm surge in low-lying parts of Chennai and Tiruvallur districts of Tamil Nadu and Nellore district of Andhra Pradesh ranged in height from 1 m to 1.5 m above the astronomical tide at the time of landfall".

The variation of the maximum water level on the right and left side of the landfall locations can be represented using the Hovmöller diagram (Fig. 3.11b). The ECMWF wind field is more surging towards the left side of the coast from the actual landfall location, as indicated by the JTWC advisory. The strong wind gust produced from the WRF wind field is causing increased maximum water levels along the right side of the coast from the landfall location. As a result, it provides a reliable approximation of the wind field at a distance from the cyclone's center. It offers more precise predictions of surge and flooding extent along extensive coastal areas compared to other wind models. Overall, the figure clearly shows that the blended wind model shows a better representation on either side of the cyclone landfall than the rest of the models. It should be noted that the blending of GAHM+WRF is only attempted, and the blending of WRF with other parametric models is not carried out since the performance of GAHM is better than the rest of the parametric models.

The ADCIRC standalone and coupled ADCIRC+SWAN models were used to calculate maximum storm-induced surge simulations. In both these simulations, the computed peak surge is observed near the landfall location near the Chennai coast (80.32°E, 13.2°N) on 12 December 2016, at 0900 UTC. The uncoupled simulation produced a maximum storm surge of approximately 0.95 m, while the coupled model simulation recorded around 1.10 m when using the blended wind field (GAHM+WRF) for the atmospheric forcing. The values of peak storm-induced surge for the SLOSH, RV, WL06, HL80, GAHM, ECMWF, and WRF atmospheric wind forcing are presented in Table. 3.4. The findings indicated that wave-induced radiation stresses led to a rise in surge heights ranging from approximately 13.68% to 24% for the varying atmospheric wind forces during the TC Varadah event. This is in good agreement with previous studies (Dietrich et al., 2011; Sheng et al., 2010).

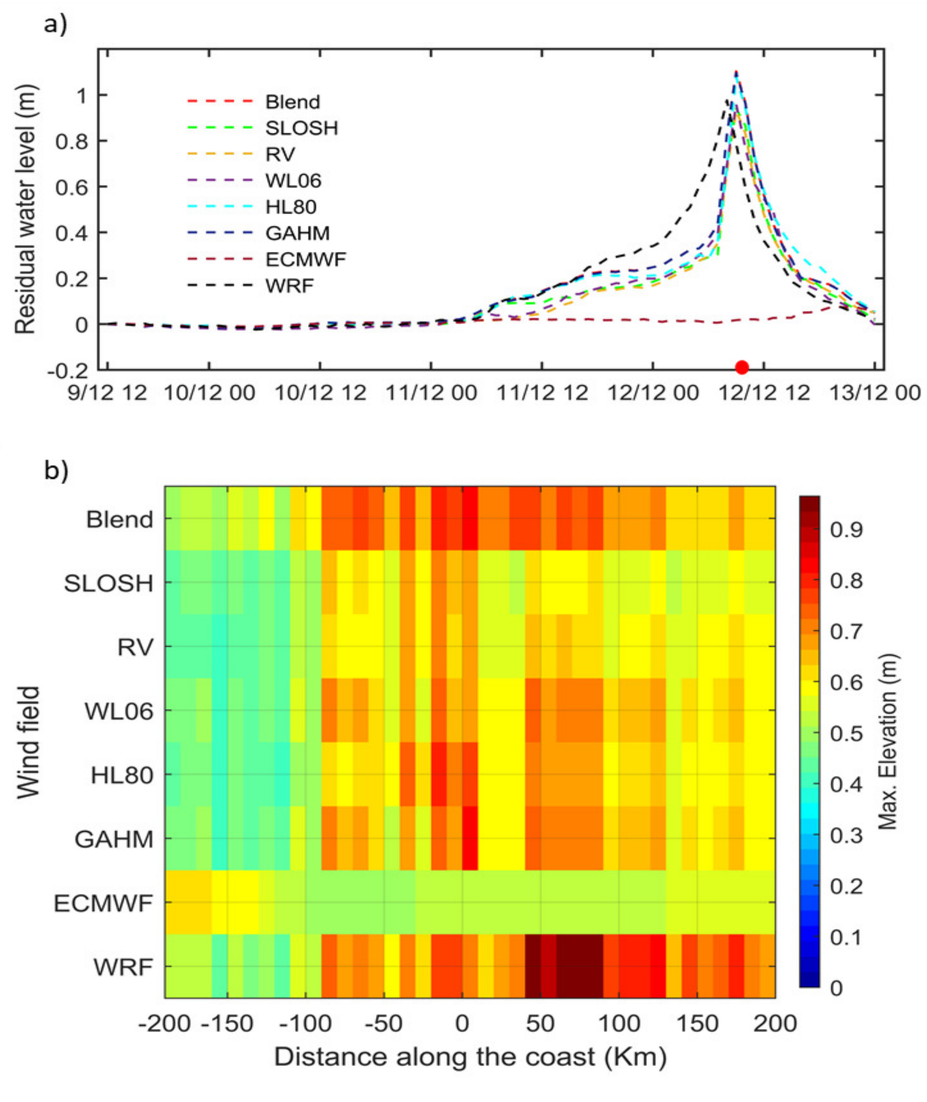

Fig 3.11.a) Using ADCIRC+SWAN, the storm-induced surge (m) caused by various atmospheric wind field forcing. The landfall time is shown by the red dot on the temporal plot (12 December 2016 0900 UTC) at the location 80.32°E, 13.2°N b). Hovmöller diagram indicating maximum water level (m) using coupled ADCIRC+SWAN for different atmospheric forcing that has been considered (along the y-axis). The distance measured along the coastline is referenced with the landfall point (80.32°E, 13.2°N) set as zero. Distances to the left of the landfall point are assigned negative values, while those to the right are given positive values.

Table 3.4. Computed maximum storm-induced surge due to uncoupled ADCIRC Standalone and coupled ADCIRC+SWAN models near the landfall location (80.32°E, 13.2°N) at landfall time (12 December 2016 0900 UTC)

Wind field	Storm Induced Surge (m)		
	ADCIRC Standalone	ADCIRC+SWAN	Percentage Change
Blend	0.95	1.10	16.36%
SLOSH	0.81	0.94	13.82%
RV	0.80	0.93	13.97%
WL06	0.82	0.95	13.68%
HL80	0.89	1.04	14.42%
GAHM	0.93	1.09	14.67%
ECMWF	0.018	0.025	24%
WRF	0.72	0.87	17.24%

The wave height evolves rapidly to the changes in a cyclone's wind field (Chen et al., 2019). Therefore, for the TC Varadah, the performance of the coupled hydrodynamic ADCIRC and SWAN model has been evaluated by comparing significant wave height from the different atmospheric wind field forcing with the observation (located about 150 km away from the landfall location at Krishnapattanam (80.14°E, 14.28°N)) as shown in Fig. 3.12a. Due to the poor wind field from ECMWF, the significant wave height ($H_{s)}$ is poorly estimated compared to the rest of the wind fields. In contrast, from WRF, H_s has been overestimated. The RMSE and MBE for all the atmospheric wind forcing models are shown in Fig. 3.12b. The errors corresponding to significant wave height (m) are considerably less for blended wind fields, followed by GAHM, HL80, RV, WL06, and SLOSH wind models. The negative value of MBE indicates an overestimation of significant wave height with respect to the observation due to the strong wind gust produced by the WRF model.

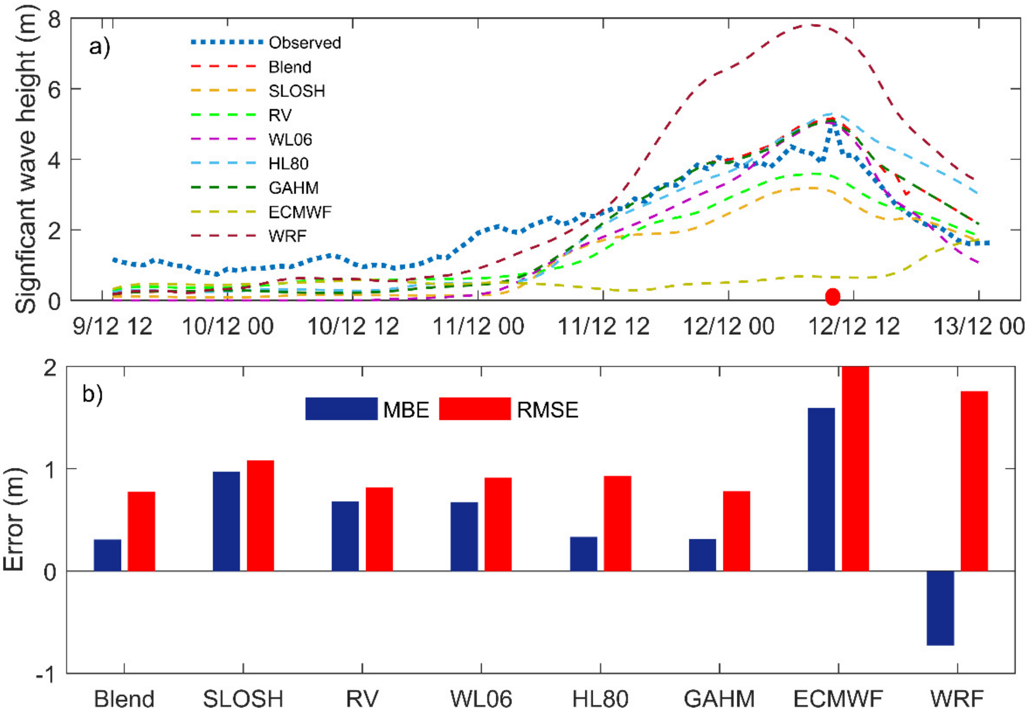

Fig 3.12. a) Comparison of simulated significant wave height from different atmospheric forcing with observed in-situ buoy measurement situated at Krishnapattanam location (80.14°E, 14.28°N). b) MBE and RMSE calculated in terms of significant wave height (m).

The peak wind speed from the different models needs to be analyzed to understand the variations of the significant wave height. The observed percentage of variations between peak wind speed from buoy data (BD11 & BD14) and the different models are shown in Table. 3.5. The parametric wind models (i.e., SLOSH, RV, WL06, HL80, and GAHM) underestimat peak wind speed from 2% to 29% compared with the observed wind speed at buoy BD11. Among all the parametric wind models, GAHM predicted peak wind speed is within 3%. The WRF wind simulation overestimated peak wind speed up to 24% compared with observed wind speed at BD11, while the differences are as high as 61% for the ECMWF winds.

Similarly, the resulting parametric wind models underestimate peak wind speed from 24% to 83% compared with the observed wind speed at BD14, situated far away from the cyclonic track. Among all the parametric wind models, RV predicted peak wind speed within 24% in the outer core region of the storm, followed by GAHM, SLOSH, HL80 and WL06, as indicated in Table. 3.5. The ECMWF wind overestimated peak wind speed up to 1.3% compared with observed wind speeds at BD14, and WRF wind is underestimated by 0.4%. Overall, the blended wind (GAHM+WRF) is underestimating with the least percentage of error at both BD11 (2%) and BD14 (18%) buoy locations. Table. 3.5 clearly shows that the larger deviation near the cyclone track wind field results in larger variations in the significant wave height. For example, a deviation of -29.1% in wind field leads to a deviation of -40% in significant wave height prediction. A similar observation was also pointed out by Torres et al., (2019). Overall, irrespective of the wind models (parametric, global, or blended), lesser deviations in the wind field are required to obtain a reasonable prediction of the significant wave height. Thus, GAHM and blended wind field are promising for the TC Varadah cyclone. Further, in the previous discussion over the past ten cyclone's wind fields, GAHM predicts better for the BoB region.

Table 3.5. Comparison of peak observed, simulated wind speed (m/s), and significant wave height (m) for different atmospheric wind forcing; error percentage in parentheses (negative values signify underestimation; positive values signify overestimation)

		Observed	WRF	ECMWF	Blended Wind	Parametric Wind Models				
						SLOSH	RV	WL06	HL80	GAHM
Wind Speed (m/s)	BD11	24.61	30.59 (+24.2%)	9.48 (-61.4%)	24.05 (-2.2%)	17.45 (-29.1%)	18.14 (-26.3%)	21.04 (-14.5%)	21.92 (-10.9%)	24.05 (-2.2%)
	BD14	9.30	9.26 (-0.4%)	9.43 (+1.3%)	7.58 (18.4%)	4.26 (-54.1%)	7.05 (-24.1%)	1.61 (-82.6%)	1.78 (-80.8%)	6.08 (-34.6%)
Significant Wave Height (m)		5.17	7.66 (+48.1%)	0.65 (-87.4%)	5.14 (-0.5%)	3.07 (-40.61)	3.41 (-34.1%)	5.02 (-2.9%)	5.28 (+2.1%)	5.11 (-1.1%)

The destruction that occurs due to inundation due to storm surges in the BoB is an crucial issue for the lively hood of the coastal community, which is highly populated along India's east coast. Both ADCIRC standalone and coupled ADCIRC+SWAN simulation shows that the coastline in the north of Tamil Nadu and south of Andhra Pradesh is affected by storm surges with varying magnitudes. The INCOIS predicted inundation for three selected coastal locations (Nellore, Chennai, and Kancheepuram) near the landfall is 300 m, 110 m, and 50 m, respectively. The computed onshore inundation extent at three selected coastal locations is shown in Fig. 3.13. The inundation distance varied from 30 m to 389 m for the different atmospheric forcing models considered in the study at the Nellore region. The highest inundation extent value of 389 m was predicted by the WRF wind model, followed by blended, GAHM, HL80, WL06, SLOSH, and RV wind forcing. The ECMWF wind has predicted the lowest inundation extent of 30 m along the low-lying areas of the coast of the Nellore district. Similarly, the computed coastal inundation extent ranges from 0 m to 140 m for the different atmospheric forcing considered in the study for both the Chennai and Kancheepuram regions. This is noticed from the inundation extent values presented in the table. 3.6, the ECMWF wind forcing predicts nil inland inundation along the coast of Chennai and Kancheepuram for the TC Varadah. The modeled surge penetration is higher at the Nellore coast compared to the Chennai and Kancheepuram coasts due to the low-lying area around the inland water body of Pullicat Lake. Overall the performance of the model computed inland inundation extent is in good agreement with the previous study (Bhaskaran et al., 2013) along the southern part of the east Indian coast.

It is observed that there is a significant difference in the inundation extent for the parametric and global atmospheric wind forcing models. But, there is no significant difference in the inundation extent observed among the parametric wind forcing models. Also, it is observed that there is no notable variation in the extent of inundation.with (ADCIRC+SWAN) and without wave radiation stress (ADCIRC Standalone) for the TC Varadah simulation. Thus, the horizontal extent of inundation is significantly influenced by the characteristics of the local nearshore topography, even though variations in surge heights caused by differing atmospheric conditions is relatively less.

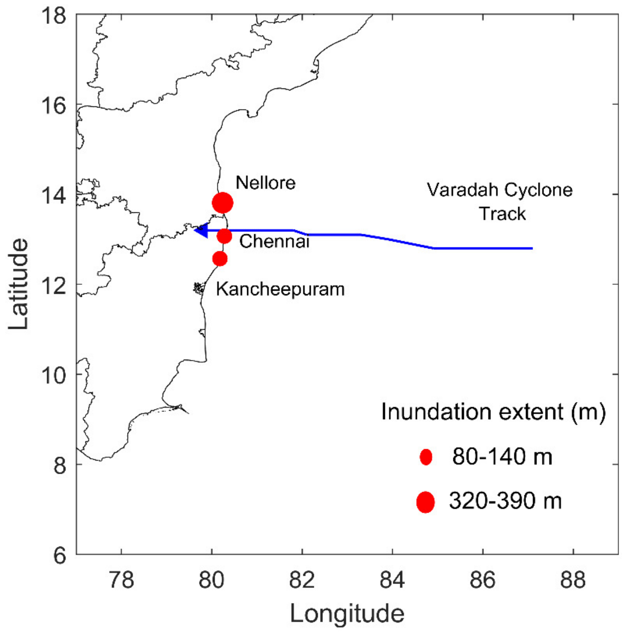

Fig 3.13. The model computed the inundation extent (in m) for the regions nearer to the landfall location along the coastline north of Tamil Nadu and south of Andhra Pradesh, which was affected by the storm Varadah.

Table 3.6. Model computed inland inundation extent (m) along the coastline of three district places nearer to the landfall region using ADCIRC Standalone and coupled ADCIRC+SWAN model.

Wind field	Inland Inundation extent (m)					
	Nellore (80.24E, 13.81N)		Chennai (80.27E, 13.04N)		Kancheepuram (80.21E, 12.66N)	
	ADCIRC Standalone	ADCIRC + SWAN	ADCIRC Standalone	ADCIRC + SWAN	ADCIRC Standalone	ADCIRC + SWAN
Blend	326	332	87	91	85	90
SLOSH	326	328	78	80	80	85
RV	326	326	80	82	78	80
WL06	330	330	85	85	80	80
HL80	326	331	88	88	88	90
GAHM	330	330	85	90	86	90
ECMWF	30	30	Nil	Nil	Nil	Nil
WRF	381	389	134	140	136	140

3.3.SUMMARY

The expressions of various types of parametric models and background models and their descriptions have been presented. A coupled ADCIRC+SWAN model setup for the BoB domain is presented. Evaluation of SLOSH, RV, WL06, HL80, and GAHM parametric models has been performed in the BoB considering 10 historical cyclonic events. Evaluation of wind field derived from ECMWF Reanalysis and WRF background wind models is performed. Based on the accuracy assessments the best-performing parametric and background wind model is used within the blending approach. Sensitivity to storm surge, wind wave, and inundation by the various wind models have been analyzed and comprehensively discussed.

CHAPTER 4

MORPHODYNAMIC RESPONSE TO THE CYCLONE EVENTS[2]

4.1. GENERAL

Modeling morphodynamic bed evolution during storm surges is vital for the BoB coast due to its susceptibility to cyclones and rising sea levels. It helps predicting seabed changes, guiding coastal management and disaster preparedness to protect communities, ecosystems, and infrastructure from erosion and sediment shifts. Most research has focused on the hydrodynamic effects of cyclones, with limited studies on their impact on morphodynamics along BoB coasts. Therefore, present study implements a coupled hydrodynamic wave and morphodynamic model framework. The prediction accuracy of storm surge, wind waves, and morphodynamic bed evolution depends on the accuracy of the wind field. Thus the present study introduce a modified parametric model for the BoB within the coupled model framework for the atmospheric forcing. Additionally, the study assesses various total bed load transport formulations for currents and waves to predict bed evolution during cyclones, evaluating their suitability for the open coast of the BoB region.

4.1. MODEL, DATA AND METHODOLOGY

Present study uses a coupled hydrodynamic (TELEMAC-2D) –wave (TOMAWAC) – morphodynamic (GAIA) model framework to simulate storm surges, wind waves, and sediment dynamics during TCs in the BoB. Section 2.2 of Chapter─2 provides detailed descriptions of the TELEMAC-2D, TOMAWAC, and GAIA models. The study examines the performance of eight different sediment transport formulations—both for currents alone and for currents along with waves—as listed in Table 2.1, using the

[2] This work is published in: "Shashank V G, Sriram V, Schüttrumpf H., Sannasiraj S. A., Investigation of morphodynamic response to the storm-induced currents and waves in the Bay of Bengal, Applied Ocean Research, Volume 153, 2024, 104285, ISSN 0141-1187, https://doi.org/10.1016/j.apor.2024.104285".

GAIA model to analyse morphodynamics during storm surges. Appendix B includes a brief description of each sediment transport formulation.

4.1.1. Atmospheric forcing

Present study introduced a new modified version of a parametric wind model for the BoB. Additionally, the study also evaluated the performance of two existing modified parametric wind models proposed for the BoB and compared them with the newly introduced model.

4.1.1.1.Murty et al., (2016)

Murty et al., (2016) incorporated a power law (q_r) fitted to the original Jelesnianski wind formulation (Jelesnianski, 1966). Murty et al., (2016) incorporated a value of q_r=3/5 based on numerical simulations. The selection of optimum (q_r) is important for depicting the wind field in the away from the cyclone center region. This slight modification to the existing Jelesnianski wind formulation offers a fairly accurate approximation of the surface wind patterns at a distance away from the cyclone's core. The gradient wind speed distribution $V(r)$ is given as:

$$V(r) = V_{max}\left(\frac{2rR_{max}}{R_{max}^2 + r^2}\right)^{q_r} \tag{4.1}$$

4.1.1.2.Pandey and Rao, (2018)

The study by Pandey and Rao. (2018) further added modifications to the wind field proposed by Murty et al., (2016). Pandey and Rao (2018) integrated the original Jelesnianski wind formulation (Jelesnianski, 1966) within the radius of maximum wind from the cyclone center ($r \leq R_{max}$) and used the modified Jelesnianski wind formulation proposed by Murty et al., (2016) beyond the R_{max} ($r > R_{max}$). Along with this, Pandey and Rao, (2018) also adjusted inflow angle uniformly 25°. Compared to the original Jelesnianski wind formulation, this adjustment led to a 30% reduction in the rate of exponential decay and an expansion in the radial reach of the wind within the cyclone's outer core area. The gradient wind speed distribution $V(r)$ is given as:

$$V(r) = V_{max}\left(\frac{2rR_{max}}{R_{max}^2 + r^2}\right) for \quad r \le R_{max}$$

$$V(r) = V_{max}\left(\frac{2rR_{max}}{R_{max}^2 + r^2}\right)^{q_r} for \ r > R_{max} \tag{4.2}$$

4.1.1.3. Generalized Asymmetric Holland Model + Rankine Vortex Model (GAHM+RV)

In present study, a new modified parametric model for atmospheric forcing is introduced which is based on an evaluation of various parametric wind models presented in Chapter‒3 where the performance of five renowned parametric wind models—SLOSH, RV, WL06, HL80, and GAHM—were analyzed for ten cyclonic events in the BoB. The wind profiles of different parametric wind models for the Varadah cyclone case study are also presented. The findings indicate that among the parametric models considered, GAHM (Gao et al., 2013, 2018) depicts the wind field near the cyclone center with better accuracy, while the RV model (Depperman, 1947) depicts the wind field with better accuracy for the areas away from the center. This finding motived to incorporate the wind field in the manner presented by Pandey and Rao, (2018), i.e., by integrating GAHM within the R_{max} ($r \le R_{max}$) and adopting the RV formulation beyond it ($r > R_{max}$). The gradient wind speed distribution for GAHM+RV model $V(r)$ is given as:

$$V(r) = \begin{cases} \sqrt{V_{\max}^2\left(1+\frac{1}{R_0}\right)e^{1-\left(\frac{R_{max}}{r}\right)^{B_g}}\left(\frac{R_{max}}{r}\right)^{B_g} + \left(\frac{rf}{2}\right)^2} - \left(\frac{rf}{2}\right) for \quad r \le R_{max} \\ V_{max}\left(\frac{R_{max}}{r}\right)^{0.5}, \quad r > R_{max} \quad for \ r > R_{max} \end{cases} \tag{4.3}$$

The terminologies used in the equations were explained in Chapter‒3. To the best of the author's knowledge, no study has incorporated the aforementioned parametric wind models within a coupled TELEMAC-2D+TOMAWAC+GAIA model framework for atmospheric forcing. The performance evaluation of the modified wind formulation for the BoB is discussed in Section 4.3.1. The best-performing wind model will subsequently be used in the computation of storm surges, wind waves, and morphological bed evolution using the coupled model framework.

4.1.2. Data

In order to cover both nearshore and deepwater regions effectively, the present modeling work uses a blended dataset from the GEBCO and the Shuttle Radar Topography Mission (SRTM) (Fig. 4.1a). The SRTM data provides a 30 m resolution. The GEBCO gridded bathymetry that is derived based on combination of satellite-derived gravity data with quality-controlled depth soundings to give a global 450 m resolution grid. For the nearshore coastal areas, a high-resolution data product is necessary for a realistic modelling of morphological bed evolution (Zhang et al., 2010). The researchers consider the hybrid-blended method employed in the study to be highly effective, providing an accurate prediction of potential surge formation and changes in nearshore bed morphology.

The present study examines three cyclones: TC Hudhud (2014), Varadah (2016), and Nivar (2020). The track information of the TCs has been sourced from the best track details provided by the JTWC. A concise overview of TC Varadah is provided in Chapter–3. Details about TC Hudhud (2014) and TC Nivar (2020) are described below.

ESCS Hudhud was a powerful TC that caused significant damage and fatalities along the eastern coast of India in October 2014. From a low-pressure system in the Andaman Sea on October 6, Hudhud intensified rapidly, becoming a VSCS by the IMD on October 10. On October 11, Hudhud rapidly intensified and formed an eye at its center on October 11. It reached peak strength with wind speeds of 59 m/s and a central pressure of 937 mbar before making landfall near Visakhapatnam on October 12.

VSCS Nivar significantly affected Tamil Nadu and Andhra Pradesh in late November 2020. A low-pressure system developed in the BoB near Tamil Nadu on November 22, strengthening into a depression by early November 23 and further intensifying into CS Nivar on November 24. The IMD issued cyclone warnings to Tamil Nadu, Pondicherry, and Sri Lanka. Nivar peaked as a VSCS on November 25, with wind speeds of 34 m/s and a central pressure of 975 hPa, making landfall near Marakkanam at midnight. By November 26, it had weakened to a deep depression.

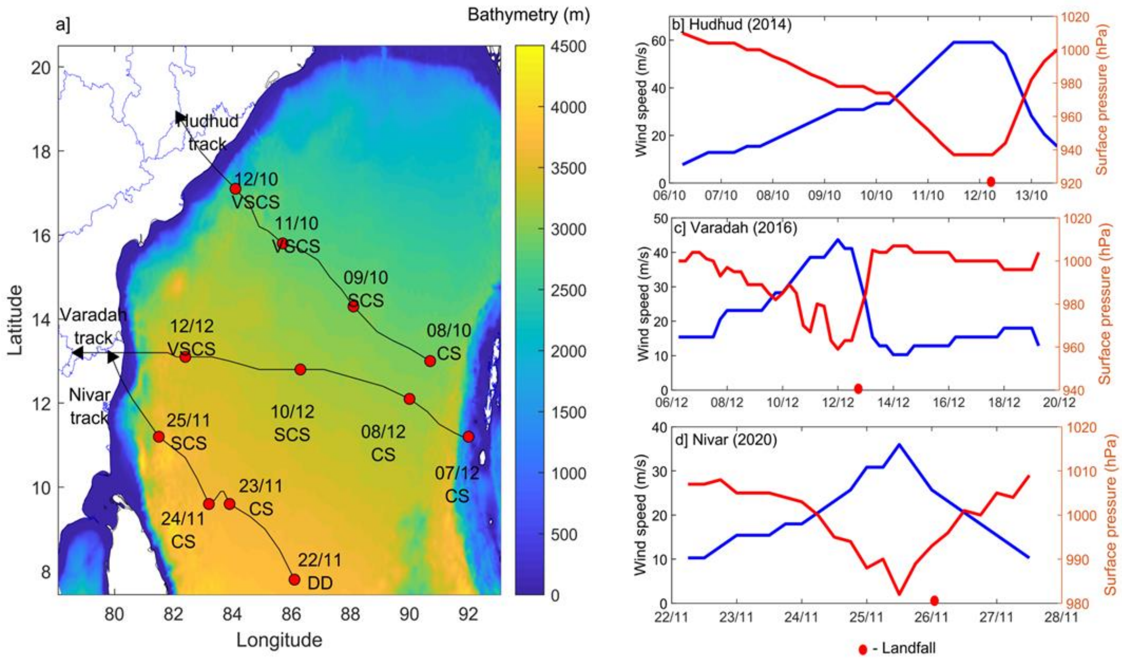

Fig 4. 1. (a) Best estimated track (source: JTWC) of the TC Hudhud (2014), Varadah (2016), and Nivar (2020). The color bar denotes the bathymetry depth of the whole domain from the blended dataset from SRTM and GEBCO. (b) The temporal variation of wind speed (m/s) and surface pressure (in hPa) from the JTWC track data for TC Hudhud, (c) Varadah, (d) Nivar, and the red dot on the time series plots indicate landfall time.

4.1.3. Model Setup

This present focuses on the open coastline along the eastern coast of India. A finite-element unstructured mesh for this region was generated using the Blue Kenue software package, incorporating blended SRTM+GEBCO bathymetry data. The details of the tuned parameters considered for the coupled numerical setup are provided in Table. 4.1.

Table 4. 1 Salient features of coupled numerical model setup

	TELEMAC-2D	TOMAWAC	GAIA
Bathymetry	SRTM+GEBCO + Field measured data	-	-
Method of discretization	Finite element	-	-
Mesh size	Nearshore coast: 35 m	-	-

	Open ocean: 4 km		
Number of elements	2,58,845	-	-
Number of nodes	1,31,502	-	-
Simulation period	8 days for TC Nivar (2020) 3 days for TC Hudhud (2014) and TC Varadah (2016)	-	-
Time step	20 s	1800 s	20 s
Tidal boundary condition	TPXO database Egbert and Erofeeva, (2002)		
Wind model	GAHM+RV		
Bottom stress formulation	Nonlinear spatially varying quadratic friction law		-
Law of bottom friction	Manning's law		-
Manning's coefficient	0.020		-
Wind drag law	Institute of Oceanographic Sciences, United Kingdom (Tassi and Villaret, 2014)		
Total sediment transport formula			Table. 2.1

4.1.4. Methodology

In the study, the evaluation of the newly proposed GAHM+RV model is performed and compared with the performance of modified wind field formulations proposed by Murty et al., (2016) and Pandey and Rao (2018) for the BoB. While various studies have compared the performance of different parametric wind models for the BoB (Das, 2018; Shashank et al., 2022; Sebastian et al., 2023), present study specifically focuses on evaluating and comparing only the modified approaches. This focus is due to the fact that modified cyclone wind field formulations have demonstrated greater accuracy than the original formulations for the BoB in recent literature.

Storm surge models can yield different conclusions for a small number of events (Salcines et al., 2019). Therefore, we have considered ten historical cyclonic events from the past decade (2010–2020), as depicted in Fig. 4.2. The model-simulated winds are compared with wind data collected from deep-water moored buoys (BD09, BD10, and BD11). INCOIS provides the observed wind data on its website. Table. 4.2 lists the buoy locations used in the present study, and Venkatesan et al., (2013) provided the sensor specifications. The cyclones, their classifications according to the IMD, and their corresponding observation buoy locations are provided in Table. 4.3. For validation of wind models, present study considered 72 hours of observed data from the nearest available buoy location for each cyclone case.

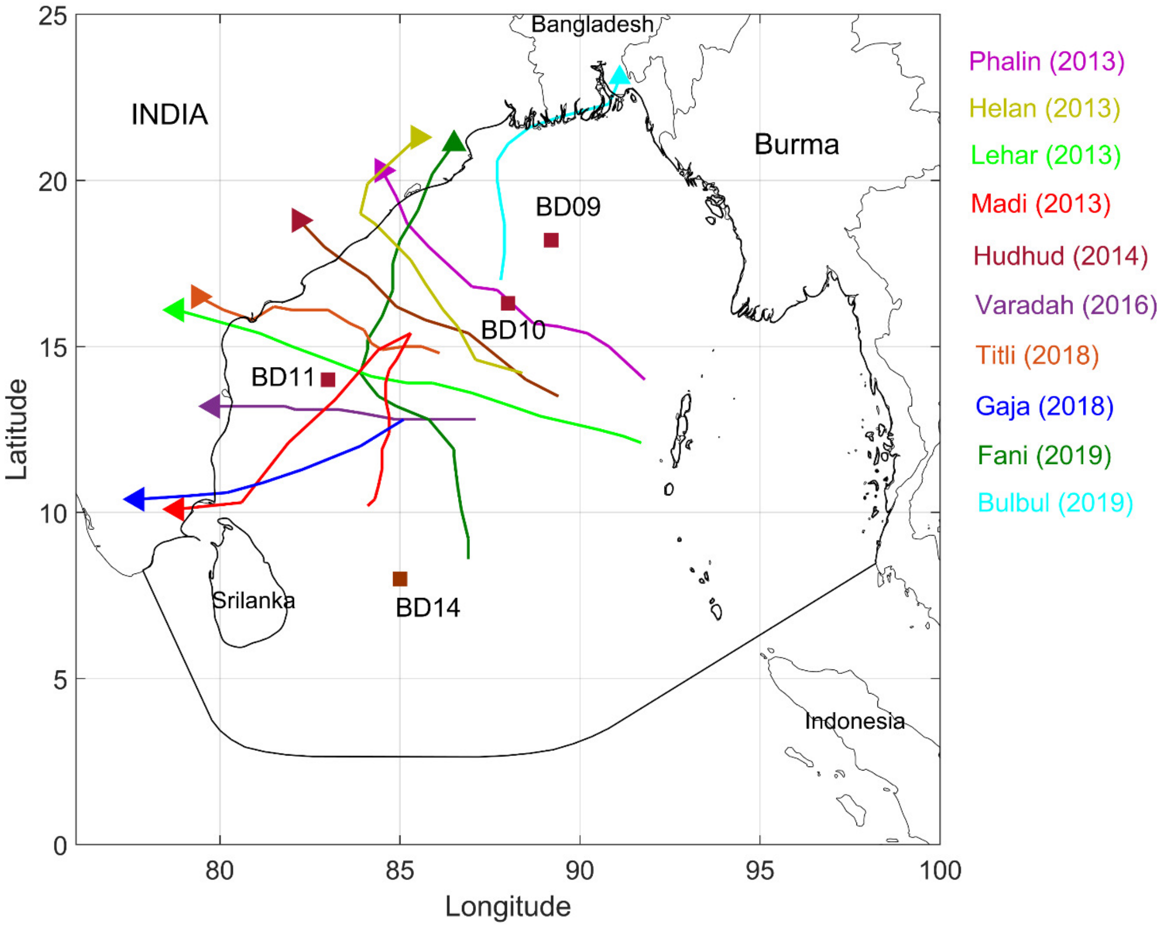

Fig 4. 2. Tracks of various cyclonic events that occurred in the Bay of Bengal over the past decade (2010–2020).

Table 4.2. Details of the buoy locations

Buoy	Latitude	Longitude
BD09	18°N	89°E
BD10	16.3°N	88°E
BD11	14°N	83°E
BD14	8°N	85°E

Table 4.3. A list of cyclones along with their classifications by the IMD and the nearest available observed buoy data used for each cyclonic track over a period of 72 hours (3 days).

Cyclone Case	**IMD Classification**	**Cyclone start time**	**Cyclone end time**	**Observed Buoy Station**
Phalin	ESCS	10-10-2013:00	13-10-2013:00	BD09
Helan	SCS	19-11-2013:00	22-11-2013:00	BD11
Lehar	VSCS	25-11-2013:00	28-11-2013:00	BD11
Madi	VSCS	07-12-2013:00	10-12-2013:00	BD11
Hudhud	ESCS	09-10-2014:00	12-10-2014:00	BD10
Varadah	VSCS	09-12-2016:12	12-12-2016:12	BD11
Titli	VSCS	09-10-2018:00	12-10-2018:00	BD10
Gaja	VSCS	14-11-2018:00	17-11-2018:00	BD11
Fani	ESCS	30-04-2019:00	03-05-2019:00	BD10
Bulbul	VSCS	08-11-2019:00	11-11-2019:00	BD10

The simulated morphodynamic bed evolution from the coupled model is validated against field measurements. In order to measure bed evolution, the morphodynamic response along the Tamilnadu coast is considered for the cyclonic event Nivar (2020), as shown in Fig 4.3a. Bathymetry measurements were conducted before and after Cyclone Nivar for a small area of approximately 1 square km near Pondicherry (Fig. 4.3b). Pre-storm bathymetry data (Fig. 4.3c) was collected on November 20, 2020, and post-cyclone field data (Fig. 4.3d) was gathered on November 28, 2020. Measurements were taken up to a water depth of 6 m. The difference in bathymetry between pre- and post-cyclone conditions is considered as the field-measured bed evolution (Fig. 4.3e). This measured bed evolution is within the range of ± 0.6 m. The pre-storm bathymetry data collected was utilized as the initial depth at the measured location (Fig. 4.3c) and combined with the blended SRTM+GEBCO data to generate the unstructured mesh for the model setup. Thus, the coupled numerical model simulations are carried out to evaluate the performance of different sediment transport formulations (Table. 2.1) considered in the morphodynamic model to predict the morphodynamic bed evolution during the combined action of storm-induced currents and waves. Thus, the simulated bed evolution for TC Nivar (2020) for each sediment transport formula using a coupled model is validated against field-measured bed evolution (Fig. 4.3e).

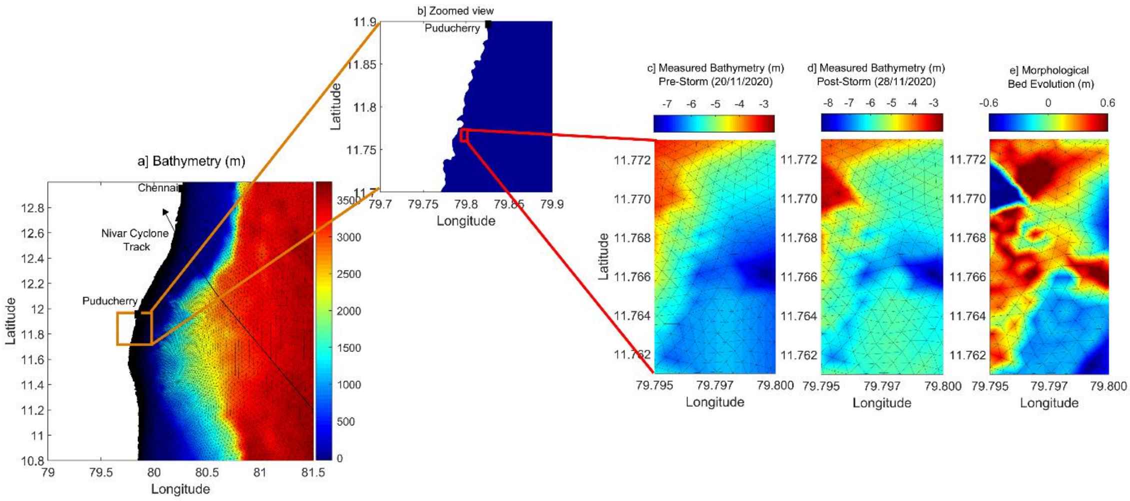

Fig 4. 3. a) Displays an unstructured mesh showing measured bathymetry (m) near the Puducherry area (highlighted by the orange box) along the Tamil Nadu coast. The black arrow line shows the track of Cyclone Nivar (2020). B) Enlarged view of measured bathymetry. c) Enlarged view of pre-storm measured bathymetry data. c) Enlarged view of post-storm measured bathymetry data. d) Measured morphodynamic bed evolution.

To assess the quality of the simulations and the impact of different sediment transport formulas, the present study employs the Brier Skill Score (BSS) as per VanRijn et al., (2003). The BSS, in general, is applicable for evaluating spatially varying quantities. The BSS formula proposed by Van Rijn et al., (2003) used is depicted as follows:

$$Brier\ Skill\ Score\ (BSS) = 1 - \left[\frac{\langle(|Z_{BC} - Z_{BM}| - \Delta Z_{BM})^2\rangle}{\langle(Z_{B0} - Z_{BM})^2\rangle}\right] \tag{4.4}$$

Where Z_{BC} computed bed evolution by the model is, Z_{BM} is field measured bed evolution, ΔZ_{BM} is bed level measured error. $\Delta Z_{BM} = 0.1$ m for bed level in field conditions (VanRijn et al., 2003). Z_{B0} is the initial bed level. The evaluation of BSS categorizes the quality of the simulated model results into five classifications, as shown in Table. 4.4.

Table 4.4 Classification of Brier Skill score by Van Rijn et al., (2003)

Score	Classification
<0	Bad
0–0.3	Poor
0.3–0.6	Reasonable
0.6–0.8	Good
0.8–1	Excellent

Furthermore, the best-performing sediment transport formulas from the validation results for both currents, and currents combined with waves, will be used to simulate the morphological bed evolution caused by the other two storms (i.e., Hudhud (2014), and Varadah (2016)) along the nearshore area of the open coast of the BoB to understand their suitability.

4.2. RESULTS AND DISCUSSIONS

4.2.1. Comparison of modified cyclone wind models for the BoB

Based on observed data from the nearest available buoy location for each of the historical cyclone events in the BoB (Fig. 4.2 and Table. 4.3), the performance of each of the three modified parametric wind models considered are shown in Fig. 4.4. The validation results are estimated in terms of RMSE and CC. The results indicate that the GAHM+RV model performs better with an RMSE of 3.07 m/s and CC of 0.77 as compared to modified wind models proposed by Pandey and Rao, (2018), and Murty et al., (2016). The modification to the original Jelesnianski, (1966) wind formulation proposed by Pandey and Rao, (2018) demonstrates better accuracy, with RMSE of 3.23 m/s and CC of 0.75, as compared to the modifications proposed by Murty et al., (2016), which has an RMSE of 3.39 m/s and CC of 0.74. The study by Shashank et al., (2022) showed that, for the same wind conditions, GAHM performed with RMSE of 3.15 m/s and CC of 0.74. While RV performed with an RMSE of 3.53 m/s and CC of 0.62. The combined strengths of the GAHM and RV models, which represent the wind field near the cyclone center ($r \leq R_{max}$) and away from the cyclone center ($r > R_{max}$) respectively shows better accuracy compared to the individual GAHM and RV as well. Fig. 4.4 also indicates that GAHM+RV performs better at lower wind speeds, as the data points are closer to the best-fit line. This demonstrates that GAHM+RV is more effective along the area farther from the cyclone center as compared to the modified wind formulations proposed by Pandey and Rao, (2018), and Murty et al., (2016). This analysis provides an overall comparison of the wind fields using the modified parametric wind models examined in the present study. To gain a more detailed understanding of each model's performance, a typical TC Varadah will be considered from this list.

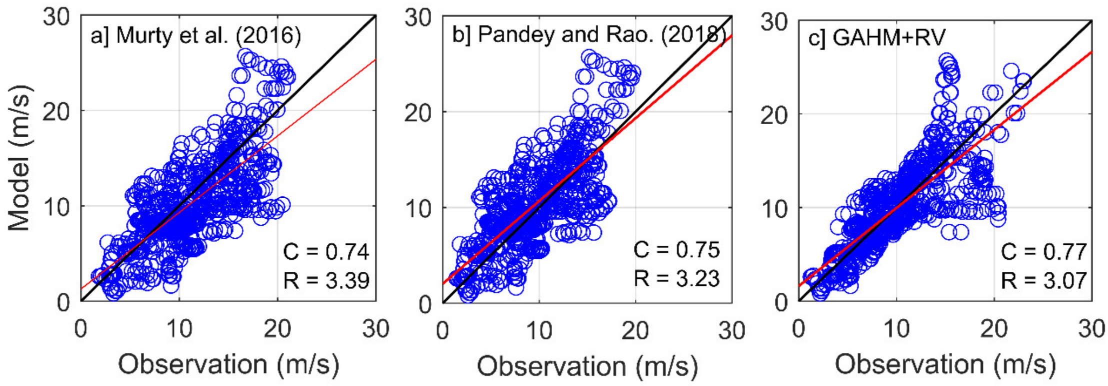

Fig 4. 4. In the x-axis, observed wind speed from buoy locations and the y-axis corresponds to simulated wind speed from a) Murty et al., (2016) b) Pandey and Rao, (2018) c) GAHM+RV models. 'R' and 'C' denote RMSE and correlation coefficients, respectively.

The spatial profiles of modeled wind fields from modified parametric wind formulations during the stronger phase of TC Varadah (2016) are shown in Fig. 4.5a, 4.5b, and 4.5c for Murty et al., (2016), Pandey and Rao, (2018) and GAHM+RV models, respectively. Additionally, variations in the spatial distribution of maximum wind speeds (m/s) from these models for the entire duration of TC Varadah are shown in Fig. 4.5d, 4.5e, and 4.5f for Murty et al., (2016), Pandey and Rao, (2018), and GAHM+RV models, respectively. It can be observed from the spatial distribution of modeled wind fields that the GAHM+RV model is predicting better away from the cyclone center region compared to the models by Pandey and Rao, (2018) and Murty et al., (2016). This improved performance is attributed to the robust gradient wind profile (Eqn. 4.3) proposed in the study. The GAHM+RV model generated a peak rotational wind speed of 37.5 m/s. In comparison, the models by Murty et al., (2016) and Pandey and Rao (2018) models produced maximum rotational wind speeds of 36.6 m/s and 35.7 m/s, respectively, along the track of TC Varadah. The modeled wind profiles and maximum wind speeds from the modified formulations proposed by Murty et al., (2016) and Pandey and Rao, (2018) exhibit similarity in the spatial distribution of wind patterns. However, the wind formulation by Pandey and Rao, (2018) demonstrates a slightly broader spatial distribution of winds, depicting the wind field more effectively away from the cyclone center compared to the formulation by Murty et al., (2016). This may be due to combined effect of incorporation of frictional inflow angle as specified in Pandey and Rao, (2018) and imposing the Murty et al., (2016) wind model away from the cyclone center region ($r > R_{max}$) while retaining the original Jelesnianski, (1966) wind field near the cyclone center ($r \leq R_{max}$) in the formulation as indicated in Eqn. (8.5).

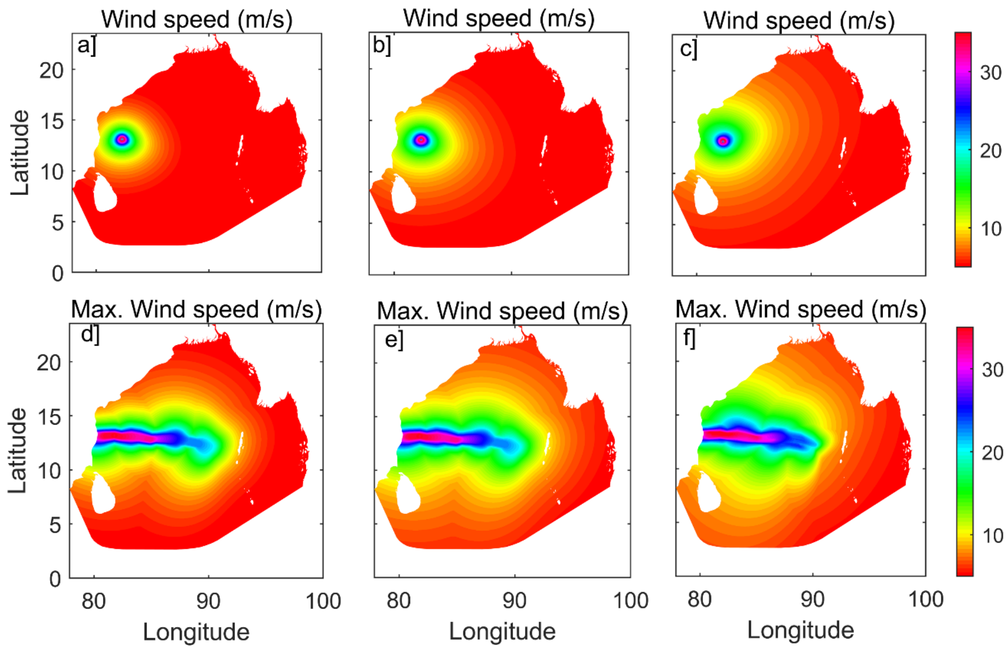

Fig 4. 5. Spatial distribution of the magnitude (m/s) of cyclonic wind fields from a) Murty et al., (2016) b) Pandey and Rao, (2018) c) GAHM+RV wind models captured on 11 December 2016 at 12:00 UTC. Maximum wind speed (m/s) patterns from d) Murty et al., (2016) e) Pandey and Rao, (2018) f) GAHM+RV wind models for the entire duration of TC Varadah (2016).

The time series of parametric wind model wind fields over the cyclone durations are compared with the field observations at BD11 and BD14 (as shown in Fig. 4.2). It can be seen that the location of BD11 is closer to the track of TC Varadah compared to BD14, which is located at the outer region of TC Varadah. It can be seen that GAHM+RV shows a better match at both BD11 (Fig. 4.6a) and BD14 (Fig. 4.6b) as compared to Murty et al., (2016), and Pandey and Rao, (2018) wind models. Murty et al., (2016), and Pandey and Rao, (2018) models show similarity in predicting time series as well. However, Pandey and Rao, (2018) wind model predicts the wind speed with better accuracy at both BD11 and BD14 than Murty et al., (2016) wind model, as shown in Fig. 4.6c. Additionally, it is observed that modifications made to the original Jelesnianski (1966) wind formulations by Murty et al., (2016) and Pandey and Rao (2018) show improved accuracy over the original Jelesnianski, (1966) formulations at both BD11 and BD14 compared to the original Jelesnianski (1966) wind formulation for the TC Varadah in the BoB (Shashank et al., 2022). Shashank et al., (2022) showed the blended wind field GAHM+WRF based on Pan et al., (2016) approach performing with RMSE of 2.45 m/s and 1.09 m/s at BD11 and BD14, respectively. While the proposed GAHM+RV is performing with RMSE of 2.51 m/s and 1.26 m/s at BD11 and BD14 respectively, as shown in Fig. 4.6c. This comparison shows that GAHM+RV closely matches the performance of the blended GAHM+WRF model with less computational cost. Therefore, for all the simulations, the present study employs a wind field derived from the GAHM+RV model within a coupled hydrodynamic, wave, and morphodynamic framework to simulate storm surge, wind-generated waves, and morphodynamic bed evolution.

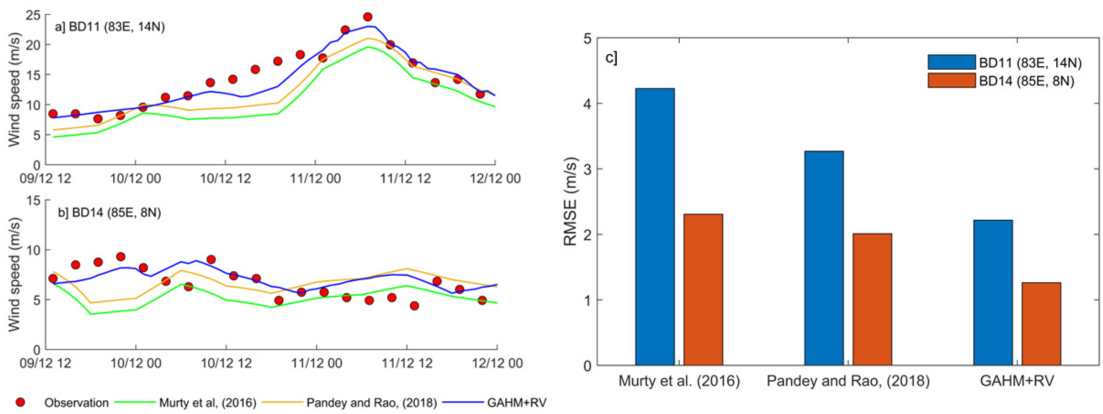

Fig 4. 6. Comparison of simulated winds from Murty et al., (2016), Pandey and Rao, (2018), and GAHM+RV models with the observed buoy wind speed at a) BD11 (situated nearer along the cyclonic track) and b) BD14 (situated away from the cyclonic track) locations. A) RMSE at BD11 and BD14 buoy locations for Murty et al., (2016), Pandey and Rao, (2018), and GAHM+RV wind models.

4.2.2. Validation of Hydrodynamic and Wind Wave models

The validation of simulated storm surges and wind waves was performed using the internally coupled TELEMAC-2D+TOMAWAC+GAIA models for TC Hudhud (2014) and TC Varadah (2016). The internally coupled model offers a more realistic depiction of storm surges by incorporating the wave-induced radiation stress effect and the effect of morphodynamic bed level changes on water levels within the model coupling approach. The in-situ observations from tide gauges and wave rider buoys are sourced from INCOIS.

4.2.2.1.Model validation for TC Hudhud (2014)

The TC Hudhud (2014) made landfall on 12 October 2014 at 0700 UTC. The spatial depiction of total water levels at the landfall is shown in Fig. 4.7a. The Predominant signatures of the storm-induced surge are significantly observed at the landfall. The simulated peak surge height is 1.22 m. This value is in good agreement with the forecast issued by the IMD report. The time series of simulated surge residuals from the coupled model is validated with observed residuals obtained from the nearest available tide gauge station located at Visakhapatnam (83.28°E, 17.68°N). The comparison shown in Fig. 4.7b demonstrates a good match between model computation and observation data with CC = 0.88 and RMSE = 0.26 m. This result agrees with the previous study by Murthy et al., (2020) and Pandey and Rao, (2018).

Similarly, the spatial plot depicting the significant wave height for TC Hudhud (2014) at landfall is shown in Fig. 4.7c. The simulated peak significant wave height reached up to 10 m on the right side of the landfall location. This finding aligns well with the SWAN simulation results reported by Samiksha et al., (2017). The validation of the time series of simulated significant wave height with the observed in-situ significant wave height observations (obtained from the Visakhapatnam wave rider buoy) during Hudhud (2014) is shown in Fig. 4.7. The modeled wave heights align closely with the observed wave heights, demonstrating good agreement. This is further supported by statistical evidence, with a high CC of 0.95 and RMSE of 0.90 m.

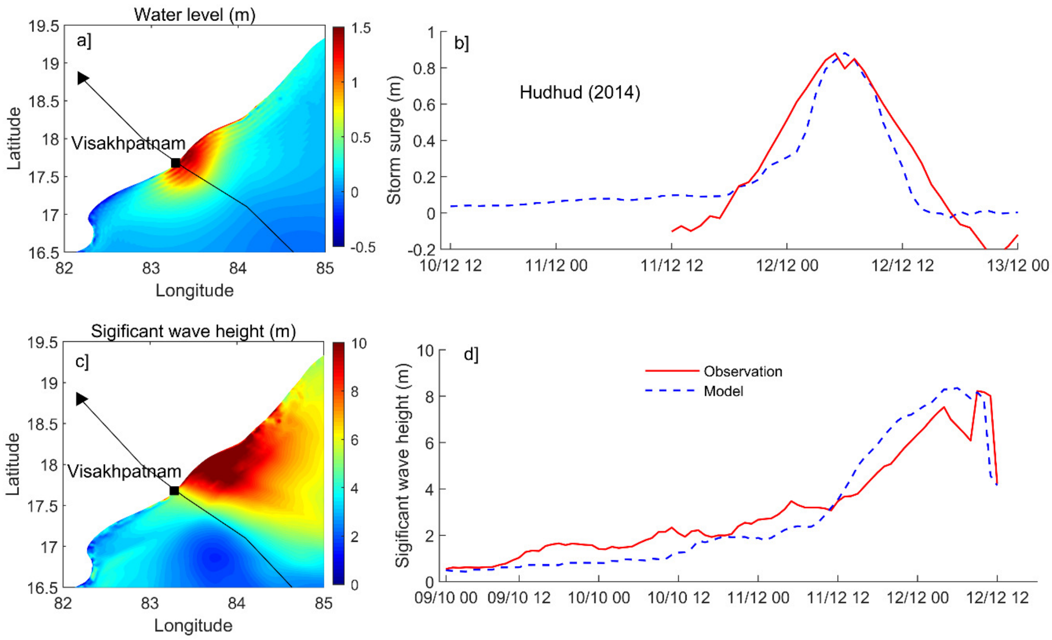

Fig 4. 7. a) Spatial depiction of total water levels (m), and significant wave height (m) at the landfall for TC Hudhud (2014). B) Validation of time series of simulated residual water levels, and (d) significant wave height with observation near Visakhapatnam. The black square dot represents the tide gauge station located near Visakhapatnam.

4.2.2.2.Model validation for TC Varadah (2016)

A similar validation practice was also performed for the TC Varadah (2016). The landfall of the TC Varadah occurred at 80.32°E, 13.2°N near the Chennai coast on 12 December 2016, at 0900 UTC. The special depiction of total water levels at the landfall is shown in Fig. 4.8a, and Fig. 4.8b shows a comparison between the time series of residual water levels derived from model simulations and those observed at the tide gauge location (80.33° E, and 13.25° N). The simulated peak surge height near the landfall is 0.98 m, which is in good agreement with the forecast provided in the IMD report. The comparison reveals a strong alignment between the model's calculations and the observed data with CC = 0.98 and RMSE = 0.09 m. This result agrees with the previous study by Rohini et al., (2022).

Similarly, the spatial plot depicting the significant wave height for TC Varadah (2016) at landfall is shown in Fig. 4.8c. The simulated peak significant wave height reached up to 8 m on the right side of the landfall location. This finding aligns well with the SWAN simulation results reported by Shankar and Behera, (2019). The validation of the time series of simulated significant wave height with the observed in-situ significant wave height observations (located about 150 km away from the landfall location at Krishnapattanam (80.14°E, 14.28°N) is shown in Fig. 4.8d. The modeled wave heights align closely with the observed wave heights, demonstrating good agreement. This is further supported by statistical evidence, with a high CC of 0.95 and a RMSE of 0.76 m.

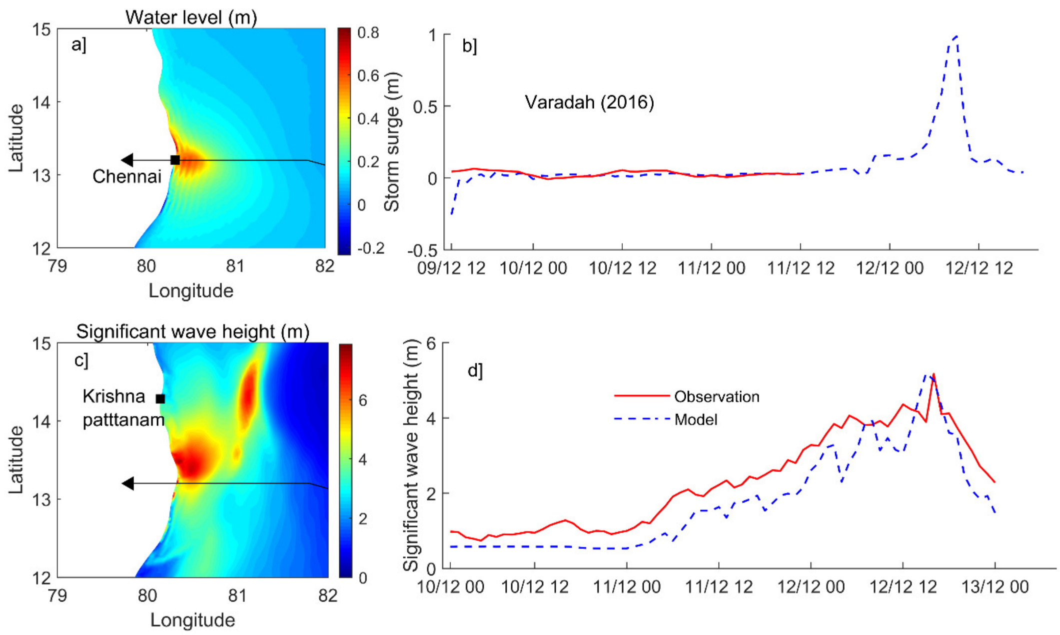

Fig 4. 8. a) Spatial depiction of total water levels (m) and © significant wave height (m) at the landfall for TC Varadah (2016). B) Validation of time series of simulated residual water levels, and (d) significant wave height with observation near Chennai. The black square dot represents the observation station located near Chennai.

4.2.3. Evaluation of different bed load transport formulations for TC Nivar (2020)

Eight simulations were conducted using different sediment transport formulations (Table. 2.1) within the coupled framework to investigate the impact of storm-induced currents and the current-wave interaction on bottom evolution. The first four formulas considered only currents, while the remaining four accounted for currents and waves. The performance of all sediment transport formulations is evaluated by comparing the simulated bed evolution from each formulation with the field-measured bed evolution (Fig. 8.4c) for TC Nivar (2020).

4.2.3.1.Effect of storm-induced currents on morphological bed evolution

Firstly, the effect of currents induced by storm Nivar (2020) on the morphodynamic bed evolution is assessed for the four different sediment transport formulations. When considering the effect of currents alone, the MPM, EB, EH, and VR formulations are valid for predicting morphological bed evolution. Fig. 4.9 presents the spatial predictions of morphological bed evolution by the MPM, EB, EH, and VR formulations. Table. 4.5 provides the estimated BSS values for these formulations. The spatial plots (Fig. 4.9) reveal that the morphological bed evolution predicted by the EH formulation (Fig. 4.9d) closely matches the field-measured morphological bed evolution (Fig. 4.9a) compared to the MPM, EB, and VR formulations. The BSS analysis indicates that the EH formulation's morphological bed evolution predictions are classified as good, with a skill score of 0.61. Nevertheless, the VR formulation's predictions are classified as reasonable, with a skill score of 0.33. The MPM and EB formulations are categorized as poor, with skill scores of 0.15 and 0.11, respectively. The BoB's coastal regions are characterized by fine to medium sediment sizes (Sarwar & Borthwick, 2023). Specifically, the sediments near the Puducherry coast are moderately well-sorted and display positive symmetrical skewness characteristics (Angusamy and Rajamanickam, 2007). The EH formula is more effective for predicting bed evolution in environments with finer sediments, whereas the MPM and EB formulas are better suited for coarser sediments. While the VR formula is comprehensive for a wide range of sediment sizes. However, it may not perform well under flow characteristics that have not met the threshold conditions (Saichenthur et al., 2022).

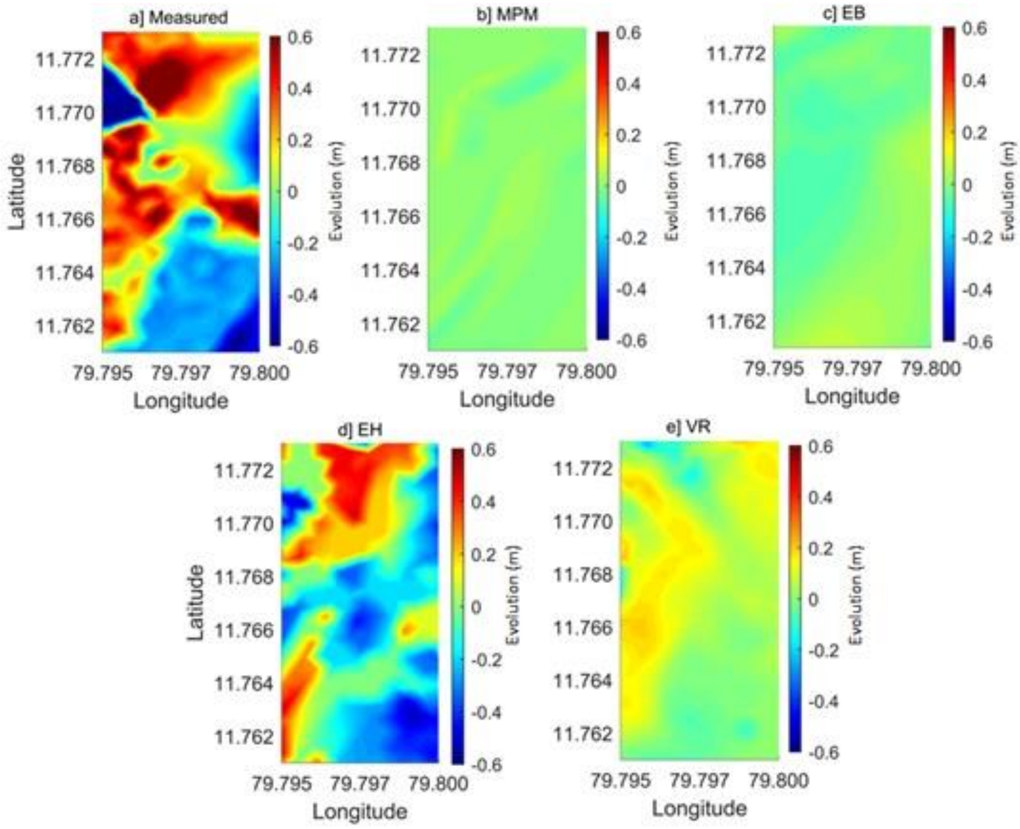

Fig 4. 9. a) Spatial representation of field-measured morphological bed evolution (m) near the Puducherry coast and the corresponding spatial predictions of morphological bed evolution (m) made by b) Meyer-Peter-Muller (MPM), c) Einstein-Brown (EB), d) Engelund-Hansen (EH), and e) van Rijn's (VR) formulations.

4.2.3.2.Effect of storm-induced Currents and waves on Morphological Bed Evolution

Further, the effect of currents and waves induced by storm Nivar (2020) on the morphodynamic bed evolution is assessed for the different sediment transport formulations. Fig. 4.10 presents the spatial predictions of morphological bed evolution by the BJ, SVR, BL, and DW formulations. Table. 4.5 provides the estimated BSS values for these formulations. The spatial plots (Fig. 4.10) reveal that the morphological bed evolution predicted by the BJ (Fig. 4.10b) and SVR formulation (Fig. 4.10c) shows a good comparison with the field-measured morphological bed evolution (Fig. 4.10a) than the BL and DW formulations. The BSS analysis indicates that the BJ formulation's morphological bed evolution predictions are classified as good, with a skill score of 0.70. However, the SVR formulation's predictions are classified as reasonable, with a skill score 0.51. The BL and DW formulations are categorized as poor, with skill scores of 0.21 and 0.09, respectively.

The spatial depiction in Fig. 4.10 shows that BJ and SVR predict morphological bed evolution within a measured range of ±0.6 m. However, the BJ pattern aligns more closely with the field-measured observations than SVR. BJ and SVR formulas are more effective for predicting bed evolution in environments with a sediment size of 0.1 mm under the combined action of currents and waves induced by storms. BJ is sensitive to bed roughness for the given sediment size (Bijker, 1992; Camenen and Larroudé, 2003), while SVR offers a comprehensive approach by considering both bed load and suspended load transport under wave and current conditions (Soulsby, 1997; Camenen and Larroudé, 2003; van Rijn, 2007). However, the BL and DW formulas indicate morphological bed evolution that does not approach zero but instead tends towards minimal values. This could be because the threshold values of the shear stresses in BL and DW formulations are not attained (Camenen and Larroudé, 2003). Also, both BL and DW formulations are specifically developed for wave-dominated environments and may not adequately account for the significant current interactions during storms in the BoB. Further, BL and DW formulations are based on data sets that do not entirely represent the open coast such as BoB's, which has unique hydrodynamic and sedimentation conditions, especially during storms. Thus, limiting their accuracies. In contrast, BJ and SVR formulations have been widely validated in various coastal settings, providing confidence in their applicability to the open coast of the BoB during storm conditions (Camenen and Larroudé, 2003).

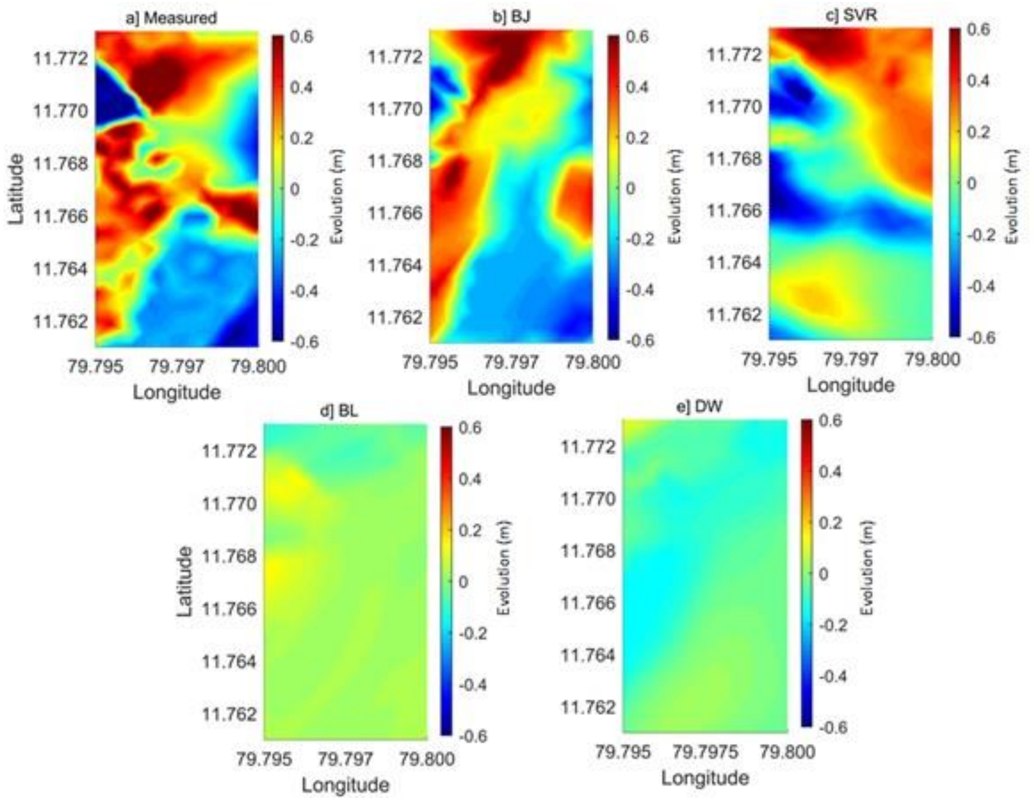

Fig 4. 10. a) Spatial representation of field-measured morphological bed evolution (m) near the Puducherry coast and the corresponding spatial predictions of morphological bed evolution (m) made by b) Meyer-Peter-Muller (MPM), c) Einstein-Brown (EB), d) Engelund-Hansen (EH), and e) van Rijn's (VR) formulations.

Table 4.5 Evaluation of various bed load transport models using the BSS metric and their corresponding categorization

Model	**Sediment Transport Equation**	**Brier Skill Score**	**Classification**
Currents (Telemac2D + GAIA)	Meyer-Peter-Muller formula	0.15	Poor
	Einstein-Brown formula	0.11	Poor
	Engelund-Hansen formula	0.61	Good
	van Rijn's formula	0.33	Reasonable
Wave + Currents (Telemac2D + TOMAWAC + GAIA)	Bijker's formula	0.70	Good
	Soulsby-van Rijn	0.51	Reasonable
	Bailard's formula	0.21	Poor
	Dibajnia and Watanabe	0.09	Poor

4.2.3.3. Cross shore variations of simulated morphological bed evolution

Present study also compares the cross-section of field-measured bed evolution with model-simulated bed evolution using the EH formulation for currents and the BJ formulation for currents combined with waves. This is because the BSS skill score indicates that EH and BJ formulations provide more accurate morphological bed evolution predictions than the other formulations considered (Table. 4.5) for currents and currents with waves, respectively. Therefore, in this section, the morphological bed evolution predicted by EH and BJ has been taken into consideration for analysis. Fig. 4.11a shows that six cross-sections were considered. Three are taken vertically from the South-North direction [i.e., cross-section 1-1' (Fig. 4.11b), cross-section 2-2' (Fig. 4.11c), and cross-section 3-3' (Fig. 4.11d)], and the three are taken horizontally from the west-east direction [i.e., cross-section 4-4' (Fig. 4.11e), cross-section 5-5' (Fig. 4.11f), and cross-section 6-6' (Fig. 4.11g)]. From the cross-section depictions, the morphodynamic bed evolution predicted by BJ formulation is in close match with the field measured bed evolution having RMSE=0.10 m and CC=0.95 compared to morphodynamic bed evolution predicted by EH formulation having RMSE=0.18 m and CC=0.93.

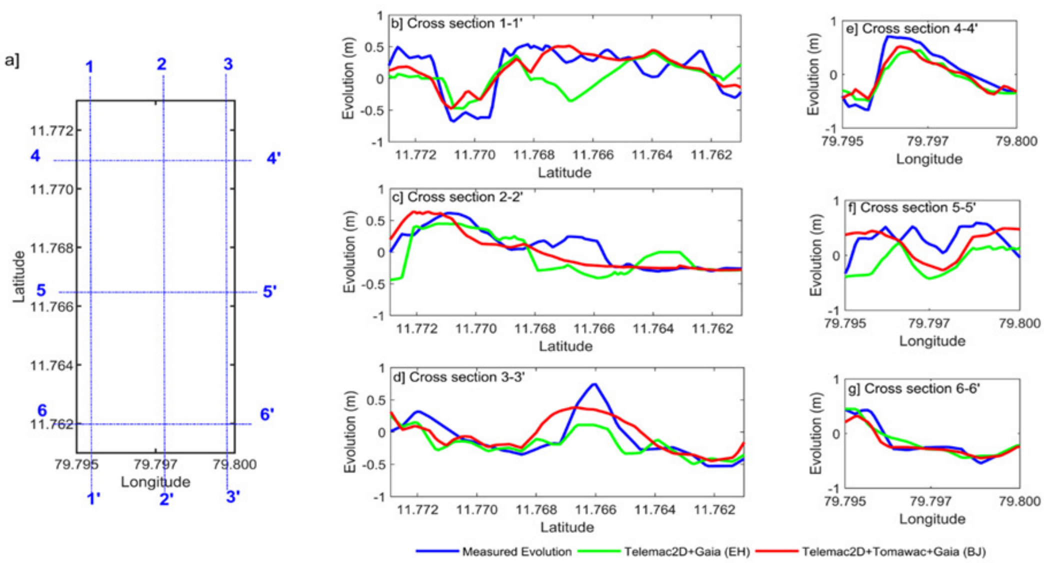

Fig 4. 11. Cross-sectional views over the field-measured bed evolution area, oriented south-north for a) section 1-1', b) section 2-2', and c) section 3-3'; and oriented west-east for d) section 4-4', e) section 5-5', and f) section 6-6'. The blue, green, and red

lines represent the measured bed evolution, the simulated bed evolution using the EH formulation, and the simulated bed evolution using the BJ formulation, respectively.

4.2.4. Simulation results for the TC Nivar (2020)

The spatial plot (Fig. 4.12) illustrates the coupled model simulation results of the impact during Nivar storm (2022) on nearshore coastal parameters, including currents, storm tide, significant wave height (m), and morphodynamic bed evolution. The modelled (GAHM+RV) wind speed of 32 m/s at landfall for TC Nivar (2020) (Fig. 4.12a) induces a current speed of up to 0.6 m/s (Fig. 4.12b). The wind stress at the landfall causes a maximum rise in water level up to 0.5 m (Fig. 4.12c). The wind-induced significant wave height reaches up to 3 m (Fig. 4.12d). Fig. 8.13e shows the simulated morphological bed evolution due to currents using the EH formulation, while Fig. 4.12f depicts the evolution from the combined effect of currents and waves using the BJ formulation. It is evident from Fig. 4.12f that incorporating waves with currents increases the magnitude and the extent of morphological bed evolution along the nearshore of the coastal region at landfall. Further, the comparison between Fig. 4.12e and Fig. 4.12f indicates that the effect of storm-induced currents is dominating morphological bed evolution. Thus, including the wave effect and currents enhances morphological bed evolution prediction capability by the coupled model framework. The analysis of the comparison of results from sections 4.3.3.1 and 4.3.3.2 and the discussion from section 4.3.3.3 lead to a similar conclusion.

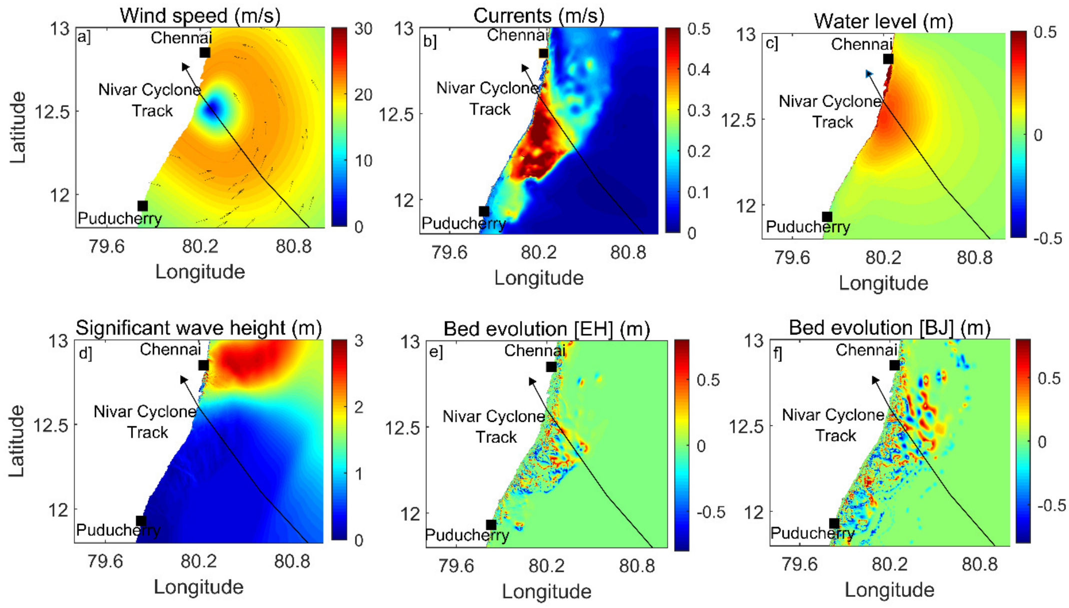

Fig 4. 12. depicts the following for TC Nivar (2020): a) Model-simulated wind speed (m/s) (GAHM+RV), b) Currents (m/s), c) Total water levels (m), d) Significant wave height (m), e) Predicted morphodynamic bed evolution using the EH formulation (currents only), and f) Predicted morphodynamic bed evolution using the BJ formulation (currents and waves).

4.2.4.1.Cross-shore analysis of simulated morphodynamic bed evolution

To understand the effect of cyclone-induced currents and waves on seabed morphological evolution in the nearshore coastal regions of the cyclone's landfall, the present study analyzed simulated cross-shore bed evolution profiles using the BJ formulation (currents with waves). This is because BJ predicted morphological bed evolution with a higher BSS metric is compared to other sediment transport formulations. The cross-shore profiles of simulated morphodynamic bed evolution and depth, extending up to 200 m in the shelf region, are shown in Fig. 4.13b, Fig. 4.13c, and Fig. 4.13d for the Chennai, near landfall, and Puducherry locations along the nearshore regions of Tamilnadu coast, respectively. These profiles are considered for 6 hours before, during, and 6 hours after the Nivar (2020) cyclone’s landfall. Each transect is approximately 50 km apart.

The storm-induced currents and waves affected the morphodynamic bed evolution up to 15 km extent from the Chennai coastline, as shown in Fig. 4.13b. Before six hours of landfall, the cross-section A–A' is predicted to evolve by up to ± 0.3 m. The bed eroded to a maximum of 0.30 m and accreted to a maximum of 0.55 m during the landfall. The bed evolution is described with accretion of 0.38 m from the initial bathymetry and erosion of magnitude 0.35 m after six hours from TC landfall. The effect of storm-induced currents and waves on morphodynamic bed evolution is more pronounced at cross-section B-B’ compared to cross-section A-A’. It can be observed that the simulated bed evolution affected up to 35 km extent from the coastline for the cross-section B-B’ near landfall, as shown in Fig. 4.13c. Before six hours of landfall, the cross-section B–B' is predicted to evolve by up to ± 0.25 m. The bed eroded to a maximum of 1.2 m and accreted to a maximum of 1 m during the landfall. The bed evolution is described with accretion of 1.10 m from the initial bathymetry and erosion of magnitude 0.95 m after six hours from TC landfall. However, the effect of storm-induced currents and waves on morphodynamic bed evolution is not so significant at cross-section C-C’ compared to cross-section B-B’. It can be observed that the simulated bed evolution affected up to 25 km extent from the coastline for the cross-section B-B’ at landfall, as shown in Fig. 4.13c. Before six hours of landfall, the cross-section C–C' is predicted to evolve by up to ± 0.25 m. The bed eroded to a maximum of 0.65 m and accreted to a maximum of 0.6 m during the landfall. The bed's evolution is described as accretion of 0.4 m from the initial bathymetry and erosion of 0.60 m after six hours from TC landfall.

It is observed that the bed undergoes more significant changes at the time of landfall across all transects. Specifically, the bed experiences notable accretion or erosion near the landfall area, with the rate of change decreasing further from the TC landfall. A higher magnitude bed evolution is predicted within a water depth of 25 meters and up to 15 km from the coastline. The bed evolution is more pronounced on the southern side (cross section C-C’) of the cyclone's landfall because of stronger storm-induced currents, whereas it is less significant on the right side, where storm-induced waves predominantly influence the area. Significant bed evolution occurs in shallow regions with gentle slopes, whereas areas with steeper slopes and deeper contours experience less bed evolution. The extent of bed evolution is significantly greater during landfall than before the storm. Post-storm bed evolution is somewhat reduced compared to the landfall period. This is due to peak winds, waves, and storm surges, causing substantial sediment transport, erosion, and deposition. Further, during post-storm the reduced energy levels of winds, waves, and currents lead to less sediment movement and a lower rate of bed evolution. While some sediment transport continues, changes are less dramatic than during landfall.

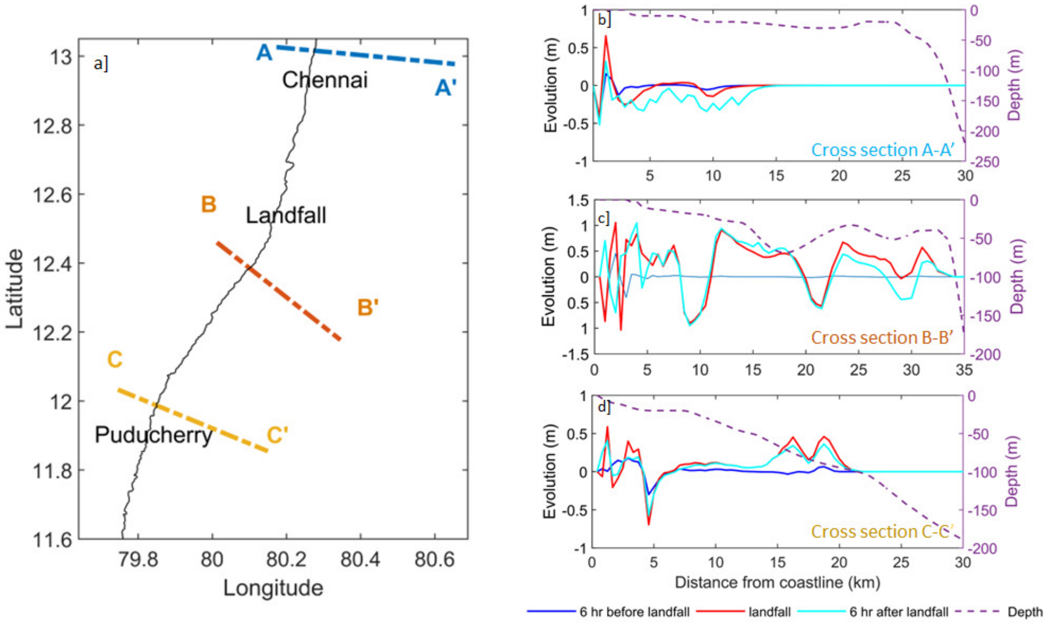

Fig 4. 13. a) Three transects were chosen for studying the morphodynamic bed evolution along the Tamil Nadu coast. b) Line plots illustrating the cross-shore profiles of morphodynamic bed evolution at transects b) A-A', c) B-B,' and d) C-C.' during TC Nivar (2020).

4.2.5. Morphodynamic bed evolution during TC Hudhud (2014) and Varadah (2016)

Section 4.3.3 demonstrates that the EH and BJ formulations are the most effective in predicting the bed evolution for the effects of currents and the combined effects of currents and waves, respectively. To understand the suitability of these formulations for other storm events along the open coast of the BoB, the present study used the same coupled model setup to simulate morphodynamic bed evolution due to current-wave interactions during TC Hudhud (2014) and TC Vardah (2016).

The modelled (GAHM+RV) wind speed of 57 m/s at landfall for TC Hudhud (2014) (Fig. 4.14a) induces a current speed of up to 1.2 m/s (Fig. 4.14b). The rise in total water level and significant wave height caused by TC Hudhud (2014) is discussed in section 4.3.2.1 Fig. 4.14c shows the simulated morphological bed evolution due to currents using the EH formulation, while Fig. 4.14d depicts the bed evolution due to the combined effect of currents and waves using the BJ formulation. Similarly, TC Varadah (2016) possesses a wind speed of 37.5 m/s at landfall (Fig. 4.14e), which induces a current speed of up to 0.75 m/s (Fig. 4.14f). The rise in total water level and significant wave height caused by TC Varadah (2016) is discussed in section 4.3.2.2. Fig. 4.14f shows the simulated morphological bed evolution due to currents using the EH formulation, while Fig. 4.14f depicts the bed evolution due to the combined effect of currents and waves using the BJ formulation.

The results indicate that the combined effect of currents and waves induced by TC Hudhud (2014) predicted bed evolution up to ±1.5 m, whereas TC Vardah (2016) predicted bed evolution up to ±1 m near landfall locations. It is evident from Fig. 4.14 that including waves along with currents amplifies the magnitude and extent of morphological bed evolution in the nearshore coastal region at landfall for both TC Hudhud (2014) and TC Vardah (2016). These findings are consistent with the results discussed in section 4.3.4 for TC Nivar (2020). These results demonstrate that the EH and BJ formulations can be applied to other cyclonic events along the open coast BoB to predict the morphodynamic bed evolution. However, the present does not guarantee that the same coupled model framework setup would predict morphodynamic bed evolution with the same accuracy for other storm events along the open coast of the BoB due to the limited availability of field-measured data for model validation assessment.

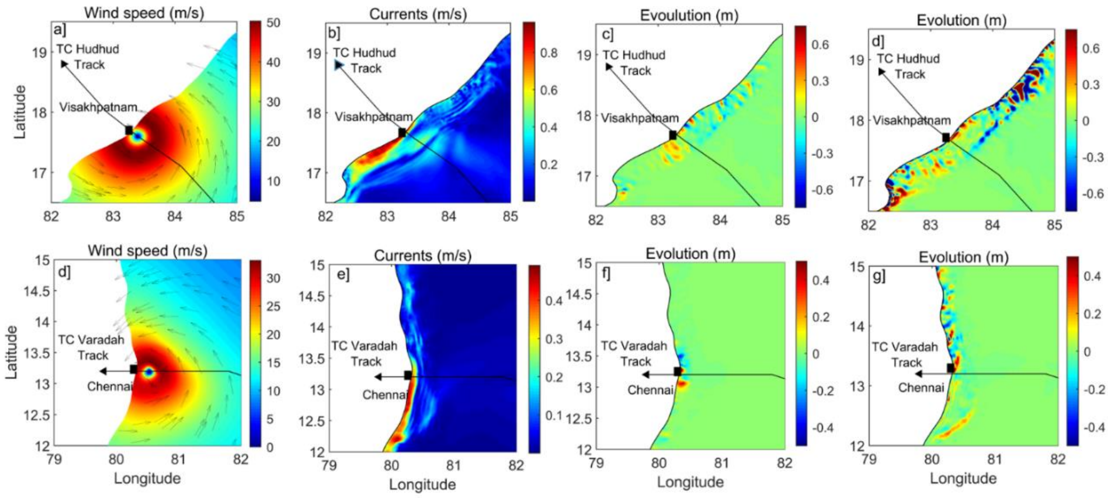

Fig 4. 14. shows the following for TC Hudhud (2014): a) Model-simulated wind speed (m/s) (GAHM+RV), b) Currents (m/s), c) Predicted morphodynamic bed evolution using the EH formulation (currents only), and d) Predicted morphodynamic bed evolution using the BJ formulation (currents and waves). For TC Vardah (2016): e) Model-simulated wind speed (m/s) (GAHM+RV), f) Currents (m/s), g) Predicted morphodynamic bed evolution using the EH formulation (currents only), and h) Predicted morphodynamic bed evolution using the BJ formulation (currents and waves).

4.3.SUMMARY

The description of the atmospheric and bathymetry data used in the study is detailed. The description of the individual hydrodynamic, wave, and morphodynamic models is detailed. The coupling framework is described. A modified wind field approach is presented. Validation and comparison with other modified wind models for the BoB are comprehensively analyzed and discussed. Model validation for the storm surges, wind waves, and morphodynamic bed evolution are comprehensively discussed. Evaluation of different total bed load transport formulations in predicting morphodynamic bed evolution caused due to storm-induced currents and waves is performed using the Brier skill score. Cross-shore and along-shore morphodynamic bed evolution profiles are analyzed during the cyclone events.

CHAPTER 5

STATISTICAL MODELING OF STORM SURGE[3]

5.1. GENERAL

A statistical-based storm surge model is crucial for effectively quantifying and communicating the risks associated with cyclonic disturbances, particularly for vulnerable coastal communities. Disaster managers and policymakers require a reliable, classification-based approach to assess potential damages and convey these risks to the public in a clear and actionable manner. This chapter delves into the development of such a statistical model tailored for the BoB, detailing its equation, the datasets used, and the creation of regression-based machine learning models specific to the region. It further explores the methodology for comparing the surge index model with machine learning approaches, alongside an evaluation and validation of the statistical model's performance. The chapter also offers a comparative analysis between the statistical models and the best-performing regression-based machine learning models, underscoring the importance of a robust, statistical approach in disaster risk management.

5.1. FORMULATION OF NEW SURGE INDEX

In the present study, we have proposed a non-dimensional and continuous tropical cyclone surge potential index. The mathematical formula of TCSPI adapts and developed over previously established Eqn. (1.1), (1.5), (1.6), and (1.8). Intensity (V_{max}), size (R), and bathymetry (L_{30}) information of the equations are adopted from Eqns (1.1), (1.5), and (1.6). Whereas the forward speed (S) and associated coastal geometry (a) information are adopted from Eqn. (1.8). Further, in the new formulations,

---

[3] This work is published in: "Shashank, V. G., Sriram, V., Schüttrumpf, H., & Sannasiraj, S. A. (2024). A new surge index with the incorporation of cyclone track approach angle information for the Bay of Bengal. Coastal Engineering, 188, 104429. https://doi.org/10.1016/j.coastaleng.2023.104429"

the angle of approach (θ) and associated coast geometry (b) information are incorporated.

$$TCSPI = \left(\frac{V_{max}}{V_{max0}}\right)^2 \left(\frac{R}{R_0}\right)\left(\frac{L_{30}}{L_*}\right)\left(\frac{S}{S_0}\right)^a \left(\frac{\theta}{\theta_0}\right)^b \tag{5.1}$$

$$\left(\frac{R}{R_0}\right) = \begin{cases} 1.5 \quad if \left(\frac{R}{R_0}\right) \geq 1.5 \\ \left(\frac{R}{R_0}\right) \quad if \ 0.5 < \left(\frac{R}{R_0}\right) < 1.5 \\ 0.5 \quad if \left(\frac{R}{R_0}\right) \leq 0.5 \end{cases} ; \quad \left(\frac{S}{S_0}\right)^a = \begin{cases} 1.5 \quad if \left(\frac{S}{S_0}\right)^a \geq 1.5 \\ \left(\frac{S}{S_0}\right)^a \quad if \ 0.5 < \left(\frac{S}{S_0}\right)^a < 1.5 \\ 0.5 \quad if \left(\frac{S}{S_0}\right)^a \leq 0.5 \end{cases}$$

$$\left(\frac{\theta}{\theta_0}\right)^b = \begin{cases} \left(\frac{\theta}{\theta_{01}}\right)^b \quad if\, \theta \leq 90° \\ \left(\frac{\theta}{\theta_{02}}\right)^{-b} \quad if\, \theta > 90° \end{cases} \qquad and \qquad \left(\frac{\theta}{\theta_0}\right)^b = 0.5 \ if \left(\frac{\theta}{\theta_0}\right)^b \leq 0.5$$

Storms that approach the coast perpendicular to the shoreline are more likely to produce the most significant storm surges (NHC, NOAA). This is because the strong winds associated with the storm are directed directly toward the shore, pushing seawater inland. In other words, wind stress is maximally aligned with the nearshore of the coast. This alignment results in the most significant storm surge potential because the wind forces push a large volume of water onto the shore. The water piles up and can result in extremely high surge levels. When a storm approaches the coast at an angle (oblique), here the wind stress is not as effectively aligned with the nearshore of the coastline. In this case, the surge potential may be somewhat reduced compared to a storm approaching perpendicular to the coast. In the present study, the angle θ of the cyclone refers to the measurement between the cyclone's track and the coastline located to the right of its landfall point (Sebastian et al., 2019). θ_0 is the reference approach angle which has a lower bound $\theta_{01} = 60°$, and an upper bound $\theta_{02} = 110°$. Earlier studies

(Pandey and Rao, 2019) have shown that the maximum peak surge is observed when the landfalling track is perpendicular (θ = 90°) to the coast, and the influence of approach angle on surge decreases as θ increases or decreases from the value θ = 90°. Several other studies ("Jelesnianski. 1966; Mercer et al., 2002; Weisberg and Zheng, 2006; Irish et al., 2008; Zhang, 2012; Zhang and Li, 2018; Islam and Takagi, 2020") have reported similar conclusions for the different ocean basin across the world. Based on the study by (Pandey and Rao. 2019), we assumed that the approach angle is influential on surge when θ is within the lower bound ($\theta_{01} = 60°$) and upper bound ($\theta_{02} = 110°$) and surge will be maximum when θ = 90°. For a better representation of the TC-induced surge hazard potential index, Islam et al., (2021) found that the upper and lower limits on TC size and forward speed are essential for unusual and infrequent TCs. Similarly, $(\theta/\theta_0)^b$ has been set up between the upper and lower bound (*0.5*≤ $(\theta/\theta_0)^b$≤*1.5*). $(\theta/\theta_0)^b$ is greater than or equal to 1 when θ lies between $\theta_{01}$and θ_{02}. When θ = 90° then $(\theta/\theta_0)^b$ will attain a maximum (i.e., 1.5), whereas θ is less or more than $90^{0,}$ then $(\theta/\theta_0)^b$ will be less than 1.5. The characteristic coastal geometry b associated with θ/θ_0 is similar to the characteristic coastal geometry a for (S/S_0). Based on the investigation, the appropriate values of a and b for the open and semi-enclosed coasts of BoB are obtained. The recommended coastal geometry values are a = b = 1 for the open coast (east and west coast of BoB) and a = 1, b = 0 for the semi-enclosed coast (i.e., Ganges-Brahmaputra-Meghna (GBM) delta in northern BoB) (as discussed in section 5.4.4).

V_{max0}, R_0, and S_0 are the climatologically averaged reference constant values for the BoB region and are defined as 33 ms^{-1}, 78 km, and 3.7 ms^{-1}, respectively. These historically averaged values are in good agreement with Priya et al., (2022). L_* is chosen to be 50 km. However, the values of V_{max0}, and L_* can be chosen in a way that makes TCSPI roughly equal in magnitude to the peak storm surge height. Since the mathematical form of $(V_{max}/V_{max0})^2$, and $(L_{30}\ /L_*)$ do not have bounds in Eqn. (5.1). In order to avoid extreme values biasing the index values, reference values are used for normalization. The effect of ΔP by replacing with V_{max} in TCSPI is also investigated. However, the influence of TC-induced wind waves, riverine inflow, rain stress, rain mass, and astronomical tide information is not included in the study to keep TCSPI simple. Therefore, TCSPI may underestimate or overestimate peak surge height for some TC events. TCSPI computes peak surge hazard potential near the landfall location point for each of the TC events that occurred along the entire coasts of the BoB that includes both open and bay coast region. However, the coastal inundation along the TCs landfall location remains beyond the scope of the study.

The historically available observed surge data are very limited for the BoB region. Therefore, the validation of the TCSPI model is also performed with the physics-based hydrodynamic model. The state of the art finite element-based ADCIRC model is used for simulations to compute the peak surge levels of historical TC events in the BoB.

Five supervised ML models, including the linear regression (LR), regression tree (TR), support vector machine (SVM), ensembles of trees (EnTR), and Gaussian process regression (GPR), are applied that can rapidly predict peak storm surge across an extensive coastal region of BoB from the same input parameter information that has considered in the TCSPI (i.e., V_{max}, R, S, L_{30}, and θ) at the landfall time frame. Lastly, the observed peak surge values for TC events that occurred in BoB were compared with those estimated by TCSPI, ADCIRC, and ML models.

5.2. DATA, MODEL, AND METHODOLOGY

5.2.1. Bay of Bengal domain

The study area includes the vast portion of the BoB that covers the coastlines of Sri Lanka, Eastern India, Bangladesh, and Myanmar. This covers up about 6,000 km (Mathiventhan and Jayasingam, 2018; Mishra 2016; Ahsan. 2013; Ramaswamy and Rao. 2014) with geographical uniqueness and various types of characteristic coastal geometry (Fig. 5.1), where the TCs historically have affected these regions.

In the study, the entire BoB coast is considered to be in terms of 3 distinct regions (as shown in Fig. 5.1). Region 1 is on the western side of BoB, including the coastline of east Sri Lanka and the east coast of India, which are prone to TCs. In this stretch, the seabed dips quickly up to 2,000 m or more after a narrow coastal strip (Prakash and Pant, 2020). Region 2, the northern part of BoB, known as the GBM delta, includes the coastline of India and Bangladesh. The GBM delta has a shallow area formed with sediments extending about 200 km south from the shoreline (Kuehl., 2005) (Fig. 5.2b). Region 3 is on the eastern side of BoB. This region covers only the northern part of the Myanmar coast (as shown in Fig. 5.1, and Fig. 5.2c). This is because it has been observed that no TC has made landfall in the shallow water region of the Andaman Sea along the southern part of the Myanmar coast (Fig. 5.3) based on the historical TC data from 1990─2021. Thus, this was not considered. The boxes (in Fig. 5.1) are meant to represent only the coasts of respective regions where cyclones have made landfall historically to distinguish the characteristic coastal geometry. The bathymetry data for the BoB region was obtained from the GEBCO database with a 15-second global bathymetric grid resolution. Quantum Geographic Information System (QGIS) was used to measure the closest horizontal distance between each landfall location of TC and the 30 m depth contour (L_{30}).

Further, Region 1 and Region 3 coasts are considered open coasts, and small islands are located nearer (<10 km range) to these regions of the open coasts. It is confusing to consider a landfall point to measure L_{30} and θ information when TCs pass over these small islands and reach the open coast. For example, Cyclonic Storm (CS) Maarutha (2017) passed over Sagu-kyun island (as shown in Fig. 5.2c) and reached the open coast of Myanmar (Region 3). In this case, we have assumed that Sagu-kyun island does not exist and therefore considered TC directly made landfall location over the open coast of Myanmar to measure the L_{30} and θ information. Moreover, IMD reported peak surge height is also observed along the open coast of Myanmar and not along the island. Considering such cases in the future for evaluating TCSPI, it is reasonable to assume that small islands do not exist and that the storm is directly landfalling along the open coasts of Region 1 and Region 2 in the BoB. However, this assumption does not apply to the coasts of Region 2, as there are numerous islands present in this region, and the coasts are cut by canyons formed by rivers (GBM delta) across which, historically, several TCs have made landfall.

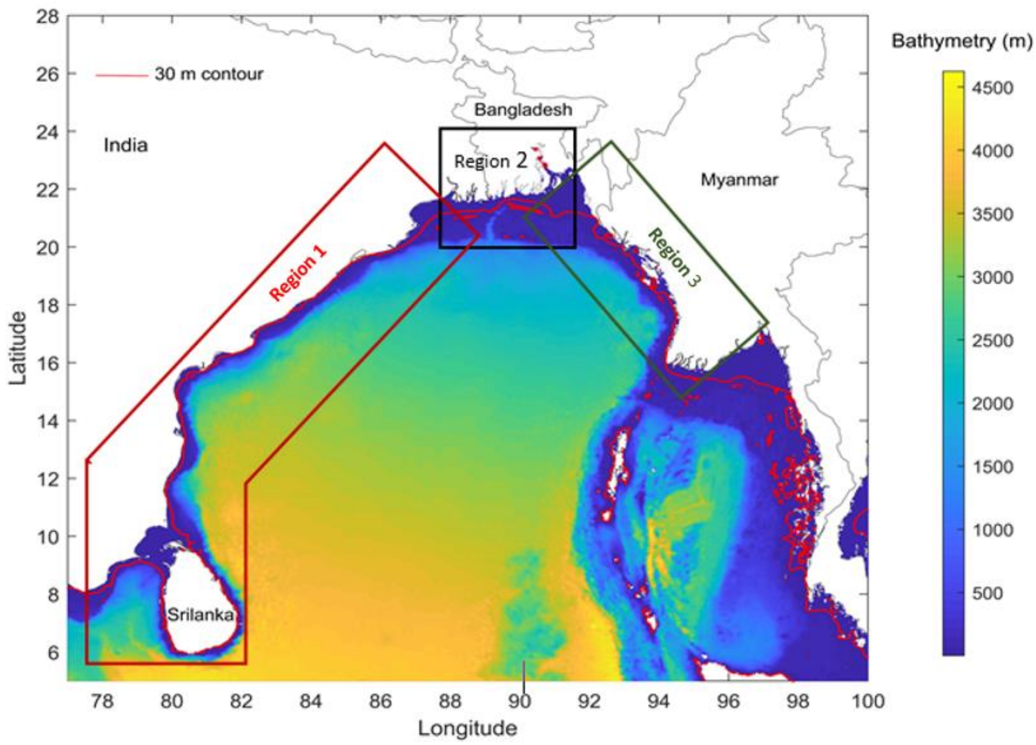

Fig 5. 1. The color bar denotes the bathymetry depth of the entire BoB basin constructed using GEBCO data. The red-bordered box indicates the western coast of BoB (Region 1), the black-bordered box indicates the northern coast of BoB (Region 2), and the green box indicates the eastern coast of BoB (Region 3). The red line indicates 30 m contour bathymetry

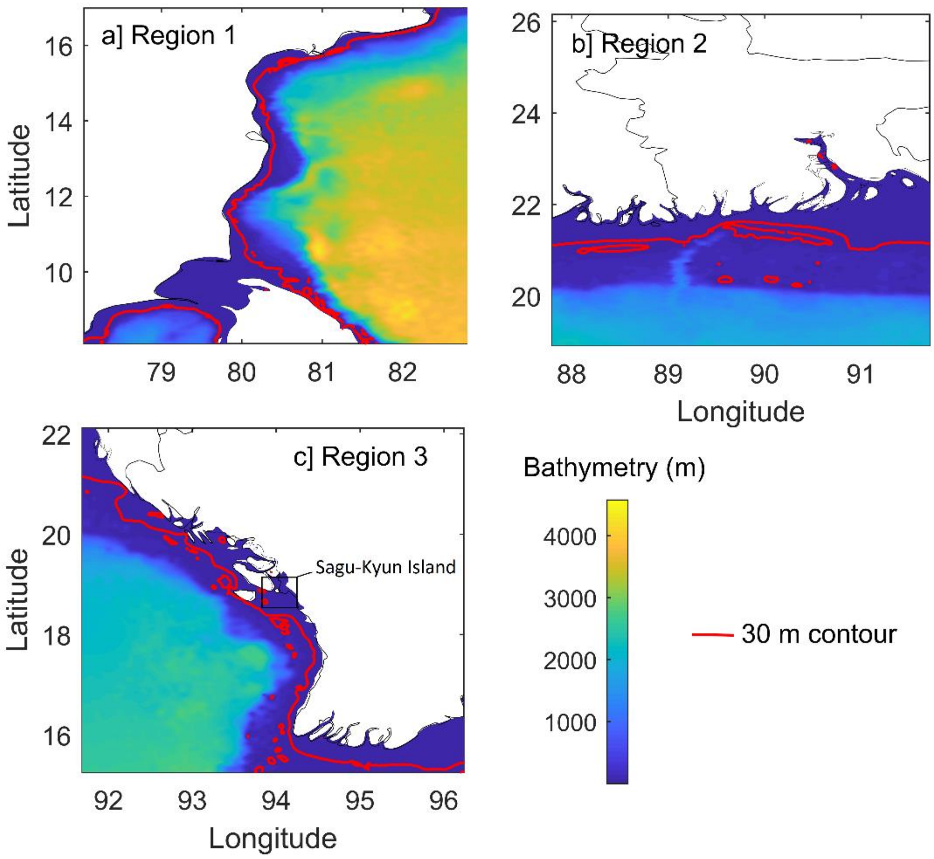

Fig 5. 2. The enlarged view of the coast of (a) Region 1, (b) Region 2, and (c) Region 3 of the BoB. The box represents Sagu-Kyun island along the coast of Region 3.

5.2.2. Track Data

In the present study, the best track archives from 1990─2021 were utilized since most of the historical observed surge data associated with TCs is available only for this period. The track parameters, such as track position, V_{max}, ΔP, and S extracted from both IMD and JTWC best track are considered. However, it should be noted that IMD provides the intensity of 3-minute maximum sustained wind speed information, while JTWC provides 1-minute maximum sustained wind speed information. Further, it is noticed that the IMD does not provide information on storm size. Hence, information on storm size, such as the radius of maximum wind (R_{max}), and the radius of hurricane-force wind (R) was extracted from JTWC. However, storm size information provided by JTWC is available from 2001─2021 (Priya et al., 2022). Based on a comparison of the frequency of cyclone events in BoB between 1990 and 2021, it is noticed that JTWC missed reporting four cyclones that were reported by the IMD. Further, IMD missed reporting one cyclone that was reported by the JTWC. A similar analysis was also previously reported by Sebastian and Behera, (2022).

Considering IMD datasets (Fig. 5.3), it is observed that, overall, 73 landfalling TCs were reported in the BoB from 1990–2021. In terms of IMD's TC intensity classification (Fig. 5.4), 26 TCs were reported as CS, 15 TCs as SCS, 15 TCs as VSCS, 13 TCs as ESCS, and 4 TCs as SuCS. Considering track direction, it is observed that TCs often exhibit a significant inclination to travel in a northwestern direction., followed by northeast and north directions in the BoB. Thus, 42 TCs have made landfall along the Region 1 coast, 15 along the Region 2 coast, and 16 along the Region 3 coast. This analysis is consistent with the findings of Bell et al., (2020) and Priya et al., (2022)

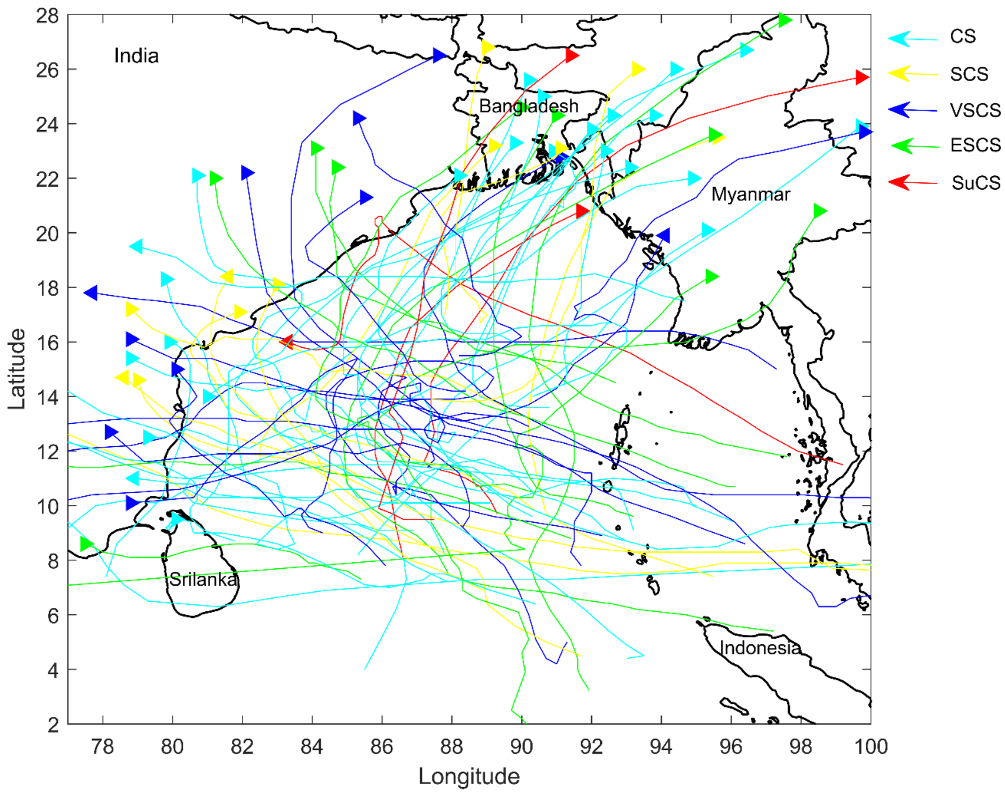

Fig 5. 3. Cumulative tracks and their respective IMD classification of landfalling TCs in the BoB region from 1990–2021.

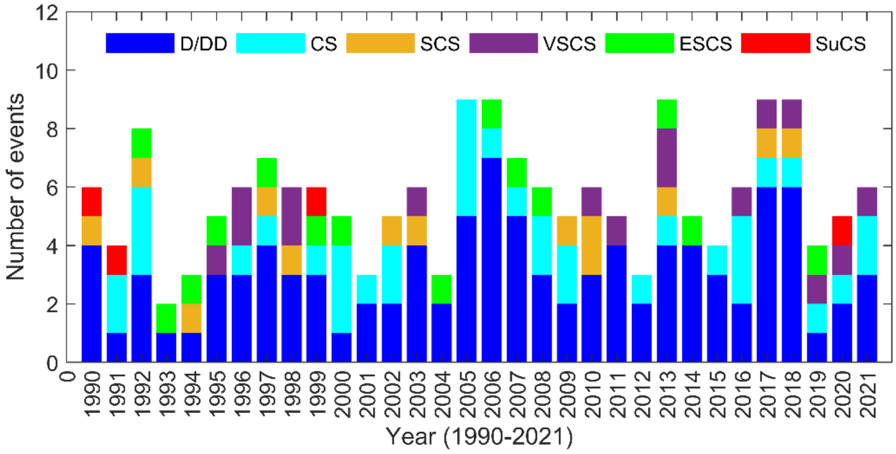

Fig 5. 4. IMD Classification and yearly frequency of historical TCs in the BoB for years (1990─2021). D and DD, indicate the frequency of Depressions and Deep Depressions respectively.

5.2.3. Surge Data

Previously, the implementation of SSHPI using Eqn. (1.8) by Islam et al., (2021) was carried out with respect to the observed tide gauge stations. Whereas HSI, SS, SSI, and TCSI were implemented using Eqns (2.1), (2.5), (2.6), and (2.7) by Kantha (2008), Irish and Resio (2010), Kantha (2010), Rezapour and Baldock (2014) at TCs landfall locations along the coast. However, the availability of tide gauge observation data in the BoB is extremely limited. To the best of the author's knowledge, only eight tide gauge water level observations associated with storm surge for the TCs reported in the literature (as shown in Table. 5.1). Moreover, the BoB does not have a dense network of tide gauges, and the TC-associated hazards are more likely to occur at the location where the TC will make landfall. Therefore, the present study cannot rely on the surge data associated with TCs obtained from tide gauges. Hence, the study utilizes the peak surge data associated with TCs reported by Government meteorological agencies and literature. The reported peak surge values are considered as observed surge values in thie study.

Table 5.1. Available tide gauge water level observation associated with TC storm surge in the BoB from 1990─2021 from literature.

SL No.	Year	Tropical Cyclone	Tide gauge station	Peak Surge (m)	Source

1.	2009	Aila	Hiron point,	1.73	Antony et al., (2020)
2.	2011	Thane	Nagapattanam	0.19	Bhaskaran et al., (2014)
			Ennore	0.12	
3.	2012	Nilam	Chennai	0.28	Kolukula and Murty. (2022)
4.	2013	Phailin	Paradeep	0.58	Murty et al., (2014)
5.	2014	Hudhud	Vishakhpattanam	0.95	Pandey and Rao, (2018)
6.	2019	Fani	Paradeep	0.68	Kolukula and Murty. (2022)
7.	2020	Amphan	Haldia	2.5	Saichenthur and Murali. (2021)
			Dhamra	1.05	Kolukula and Murty. (2022)
8.	2021	Yaas	Dhamra	1.94	Shashank et al., (2022b)

Government meteorological agencies provide limited information on peak surges associated with TC events over the BoB region. Most of the peak surge information associated with TCs that have made landfall along the coasts of the BoB is obtained from annual TC review reports and TC bulletins published by IMD on its website [https://rsmcnewdelhi.imd.gov.in]. However, the data are available from 1990─2021. The annual TC review reports provided by the IMD give various natural hazards information associated with TCs, including storm surge guidance, which is based on post-storm survey estimations (Gupta. 2003; Annual TC Review over NIO, 2013), observations, nomograms (Annual TC Review over NIO, 2016), and numerical hydrodynamic models (IIT Delhi Storm Surge Model and ADCIRC Model) (Annual TC Review over NIO, 2013, 2016, 2018). Apart from IMD, few peak surge data associated with TCs that have made landfall along the Region 2, and Region 3 coasts are obtained from the Bangladesh Meteorology Department (BMD), The Myanmar Department of Meteorology and Hydrology (MDMH), and literature. The JTWC also provides an archive of Annual TC Reports from 1959─2011; however, the web links to these reports have been broken (Needham et al., 2015). Thus, 48 peak surge data out of 73 TC events that occurred in the BoB were collected from the various sources as mentioned above. However, it should be noted that the present study considers the average peak surge value reported from various sources for each TC event. For example, IMD reported that based on a post-storm survey, the peak surge height ranges from 2 m to 2.5 m above astronomical tide near the landfall location area for TC Phailin (Annual TC Review over NIO, 2013). However, the study considers 2.25 m as a peak surge observed value, which is an average of 2 m and 2.5 m for TC Phailin (2013).

5.2.4. ADCIRC Model Setup

The present study evaluates the performance of TCSPI with peak surge data obtained from numerical simulations using ADCIRC model. Brief description of ADCIRC model is presented in Chapter─2.

Shashank et al., (2021, 2022a) recommended using the Generalized Asymmetric Holland Model (GAHM) for the BoB region. GAHM requires R information apart from V_{max}, ΔP, coordinates of the cyclone center, and R_{max}. However, it should be noted that R_{max}, and R information is not available for the years 1990─2001, and there is no study to determine R information using empirical relations. Therefore, we have used the symmetric Holland (HL80) model (Holland, 1980) for the wind field forcing in the ADCIRC model for the generation of the peak surge height. The HL80 model requires the surface wind parameters, such as V_{max}, ΔP, coordinates of the cyclone center, and R_{max} information from the best track. The ΔP information is also not available for the years 1990─2000 in the JTWC best track archive. Therefore, the surface wind parameters from the IMD best track archive are used as input to the ADCIRC simulations in the present study. However, as discussed earlier, IMD best track archive does not provide R_{max} information, and therefore, the present study incorporates an empirical relationship proposed by Willoughby et al., (2006) based on 493 cyclonic system profiles from aircraft observation. Thus, the predicted R_{max} is given as input along with track parameters associated with TCs from IMD for the ADCIRC simulations.

$$R_{max} = 51.6\exp(-0.0223V_{max} + 0.0281\varphi) \qquad (5.2)$$

Where R_{max} and V_{max} are having units of nautical miles and knots, respectively, and φ is latitude (degrees). The description of the finite element grid, parameters considered for setting up the model, and performance of validation of simulated water levels from the model setup with observed sea level are given in Shashank et al., (2021). The study also demonstrated validation of the ADCIRC model for a TC case study i.e., Hudhud (2014) as presented in Fig. 5.5. ADCIRC simulated surge residuals are validated with observed residuals obtained from the nearest available tide gauge station located at Visakhapatnam (83.28°E, 17.68°N) is shown in Fig. 5.5. The comparison shows a strong agreement between the model's calculations and the observed data with CC = 0.92 and RMSE = 20 cm (0.2 m). This result is in good agreement with a previous study by Murthy et al., (2020) and Pandey and Rao (2018). Thus, the present study provides ADCIRC simulated comprehensive peak surge data for the 73 historical TCs that occurred in the BoB from 1990 to 2021. In total, 146 simulations were performed (73 for surge tide simulation and 73 for astronomical tide simulation) to obtain the peak residual water levels (peak surge height) near the landfall location for each of the 73 TC events that occurred in the BoB. It is assumed that the bathymetry has been the same for 30 years due to the lack of availability of the data in the past years.

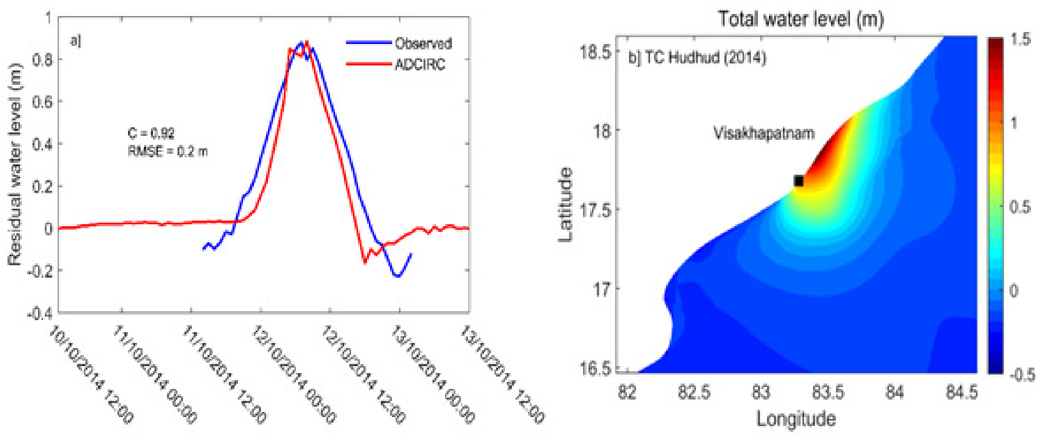

Fig 5. 5. a) Validation of computed residual water levels with observed surge residuals obtained from the in-situ tide gauge located at Visakhapatnam. b) Despeciation of ADCIRC model computed total water level (m) at the landfall location. The black square dot represents the tide gauge station located at Visakhapatnam (83.28°E, 17.68°N)

5.2.5. ML Models

Due to the lack of availability of observational data, previously several studies created synthetic track data to incorporate it as an input to the neural network models to predict the storm surges associated with TCs (Lee, 2006; Tseng et al., 2007; Lee, 2008; De Oliveira et al., 2009; Hashemi et al., 2016; Kim et al., 2019). The peak surge prediction at the landfall locations is based on hypothetical assumptions, and most of the studies have incorporated only meteorological features from the best track archive as input for the neural network models. It is one of the common problems in data-driven surrogate models when it comes to small sample sizes. The small sample size tends to give inappropriate results when using neural network models (Babic et al., 2014; Zhang and Ling, 2018; Feng et al., 2019; Kokol et al., 2022). Therefore, the present study incorporates the most used regression-based machine learning algorithms on small sample size datasets, such as LR, TR, SVM, EnTR, and GPR (Zhang et al., 2017; Alvarsson et al., 2016; Cao et al., 2017; Shaikhina et al., 2019; Razzak et al., 2020). However, the sample used in the study is comparatively smaller than the sample used in previous studies in which LR, TR, SVM, EnTR, and GPR algorithms have been employed. Further, the study incorporates only observed track parameters instead of incorporating the synthetic track parameters, which are based on hypothetical assumptions. Apart from observed historical track meteorological parameter features, such as V_{max}, R, S, and θ, the present study also incorporates bathymetry (L_{30}) feature as input (as same given to TCSPI) to the model for training the rapid prediction of peak surge height. However, it should be noted that the meteorological parameters associated with TCs given as input to ML models are from IMD alone.

A detailed description of the LR, TR, SVM, EnTr, and GPR models along with their fitting parameters, is given in Bang et al., (2020); Wang et al., (2022). The different types of above-mentioned ML models have been used with three different types of datasets (as shown in Table. 5.3) for learning and prediction. All the inputs and output datasets are processed using the normalization method. Normalized input datasets are used for training and testing to avoid variable differences. This improved the performance of the ML models (Wong et al., 2013; Wang et al., 2022). The following equation is used for this normalization so that all data can be intervals between 0 and 1.

$$y = \frac{x - x_{min}}{x_{max} - x_{min}} \tag{5.3}$$

where x and y represent the input and output sets respectively, the subscripts "min" and "max" denote the smallest and largest values within the input data set. Further, the observational track parameters along with bathymetry information associated with each TC data are shuffled randomly, and 70% of the dataset is used in training, and rest 30% dataset used in testing. After building the model with the training dataset, the CC and RMSE have been calculated with the overall dataset. In the present study, all the ML models perform hyperparameter tuning by using Bayesian optimization and prevent the overfitting problem. For reproducibility, Table. 5.2 represents the tuned hyperparameter values. The K-fold cross-validation step has been applied. By considering the limited sample data size, K is set to 5. The study used the Bayesian optimization method

Table 5.2. Optimized hyperparameter values for each of the models used in the present study

Model	Fitting Parameter	Hyperparameter	Optimized Hyperparameter values		
			N1	N2	N3
Linear regression	Linear Regression	Terms	Linear	Linear	Linear
	Interaction Linear Regression	Terms	Interactions	Interactions	Interactions
	Robust Linear Regression	Terms	Robust Linear	Robust Linear	Robust Linear
	Stepwise Linear Regression	Initial term	Linear	Linear	Linear
		Upper bound on terms	Interactions	Interactions	Interactions
		Maximum number of steps	1000	1000	1000
Ensemble of Trees	Boosted Trees	Minimum leaf size	7	5	5
		Number of learners	39	58	79
		No. of predictors to sample	5	4	4

	Bagged Trees	Minimum leaf size	5	5	3
		Number of learners	75	13	13
		No. of predictors to sample	5	4	4
Support Vector Machine (SVM)	Linear	Kernel function	Linear	Linear	Linear
		Box constraint	0.5463	18.330	984.83
		Epsilon	0.000408	0.5874	0.4454
	Quadratic	Kernel function	Quadratic	Quadratic	Quadratic
		Box constraint	0.0012	2.9735	4.6877
		Epsilon	0.0014	0.2303	0.0072
	Cubic	Kernel function	Cubic	Cubic	Cubic
		Box constraint	0.0010	1.1777	243.963
		Epsilon	0.0279	0.0013	0.6188
	Fine Gaussian	Kernel function	Fine Gaussian	Fine Gaussian	Fine Gaussian
		Box constraint	976.108	5.5820	8.4087
		Epsilon	0.0185	0.000810	0.0010
	Medium Gaussian	Kernel function	Medium Gaussian	Medium Gaussian	Medium Gaussian
		Box constraint	6.2419	3.2866	5.3181
		Epsilon	0.00214	0.0010	0.0301
	Coarse Gaussian	Kernel function	Coarse Gaussian	Coarse Gaussian	Coarse Gaussian
		Box constraint	5.1219	6.1678	7.4087
		Epsilon	0.0112	0.0272	0.0261
Tree	Fine Tree	Minimum leaf size	4	4	4
	Medium Tree	Minimum leaf size	12	12	12
	Coarse Tree	Minimum leaf size	36	36	36
Gaussian Process Regression	Rational Quadratic	Basis function	Linear	Zero	Constant
		Sigma	0.0022	12.881	0.1655
		Standardize	False	True	True
		isotropic kernel	True	True	True
	Squared Exponential	Basis function	Zeo	Zero	Constant
		Sigma	0.9275	6.4081	10.665
		Standardize	True	True	True
		isotropic kernel	True	True	True
	Matern 5/2	Basis function	Constant	Zero	Zero
		Sigma	0.0015	0.1295	0.000487
		Standardize	True	True	True
		isotropic kernel	True	True	True
	Exponential	Basis function	Constant	Zero	Zero
		Sigma	0.000109	3.3476	0.000114

		Standardize	True	True	True
		isotropic kernel	True	True	True

5.2.6. Methodology

In the present study, depending on the availability of observed meteorological parameters from IMD/JTWC and observed/simulated peak surge data, the datasets have been classified into three types (as shown in Table. 5.3). The N1 dataset, consisting of 33 samples, includes meteorological parameter information associated with TCs from IMD and JTWC between 2001 and 2021. N1 includes V_{max}, S, L_{30}, θ, R_{max} and R. The TCSPI and ML model performance were validated for the N1 dataset, with peak surge data associated with TCs obtained solely from the IMD source. Similarly, the N2 dataset has 48 samples consisting of meteorological parameters information associated with TCs from both IMD and JTWC between 1990 and 2021. N2 dataset includes V_{max}, S, L_{30}, θ, and peak surge information from various sources (i.e., IMD, BMD, MDMH, and literature). Further, the N3 dataset with 73 samples consists of meteorological parameters information associated with TCs from IMD source alone between 1990 and 2021. N3 includes V_{max}, S, L_{30}, θ, and peak surge information from the ADCIRC simulations. However, to perform ADCIRC simulations, the meteorological parameter information associated with TCs from the IMD source is incorporated as an input to the ADCIRC model.

Table 5.3. Classification of data based on the availability of meteorological parameters and peak surge height information from different sources

Sample size	V_{max}	ΔP	R_{max}	R	S	L_{30}	θ	Peak surge (IMD)	Peak surge (IMD, BMD, MDMH)	Peak surge (ADCIRC)
N1 = 33 (JTWC/IMD) (2001–2021)	☑	☑	☑ (JTWC)	☑ (JTWC)	☑	☑	☑	☑	☒	☒
N2 = 48 (JTWC/IMD)	☑	☒ (JTWC)	☒	☒	☑	☑	☑	☒	☑	☒

(1990–2021)										
N3 = 73 (IMD) (1990–2021)	☑	☑	☑ Willoughby et al., (2006)	☒	☑	☑	☑	☒	☒	☑

Fig.5.6 illustrates the flowchart outlining the general methodology incorporated in the present study. This describes the utilization of historical cyclone tracks and bathymetric parameters, and corresponding peak surge height data, within both the TCSPI and ML models to predict the potential peak surge height. The flowchart also outlines the implementation of a uniform procedure for comparing the performance of TCSPI and ML models. It should be noted that the results and discussion presented in the Section 4.4.1, 4.4.2, and 4.4.3 aim to illustrate how various TC track and bathymetry parameters (V_{max}, R, S, L_{30}, θ) and geometry coefficients (a and b) enhance the TCSPI accuracy in predicting peak surge height for N1, N2, and N3 datasets. Here the entire datasets were utilized for index-to-surge height conversion. This approach aligns with prior studies by Islam et al., (2021); Kantha, (2008), (2010), (2013); Irish and Resio, (2010). However, in the Sections 5.3.6 and 5.3.7 we have followed a uniform procedure for comparing the simplified physics-based regression model (TCSPI) and statistical-based ML models. In both TCSPI and ML models 70% of the same data will be used for developing the model (training) and the performance of TCSPI and ML models evaluated and compared on rest 30% of testing datasets. The comparison of TCSPI and ML models carried out for N1, N2, and N3 samples considering IMD datasets alone.

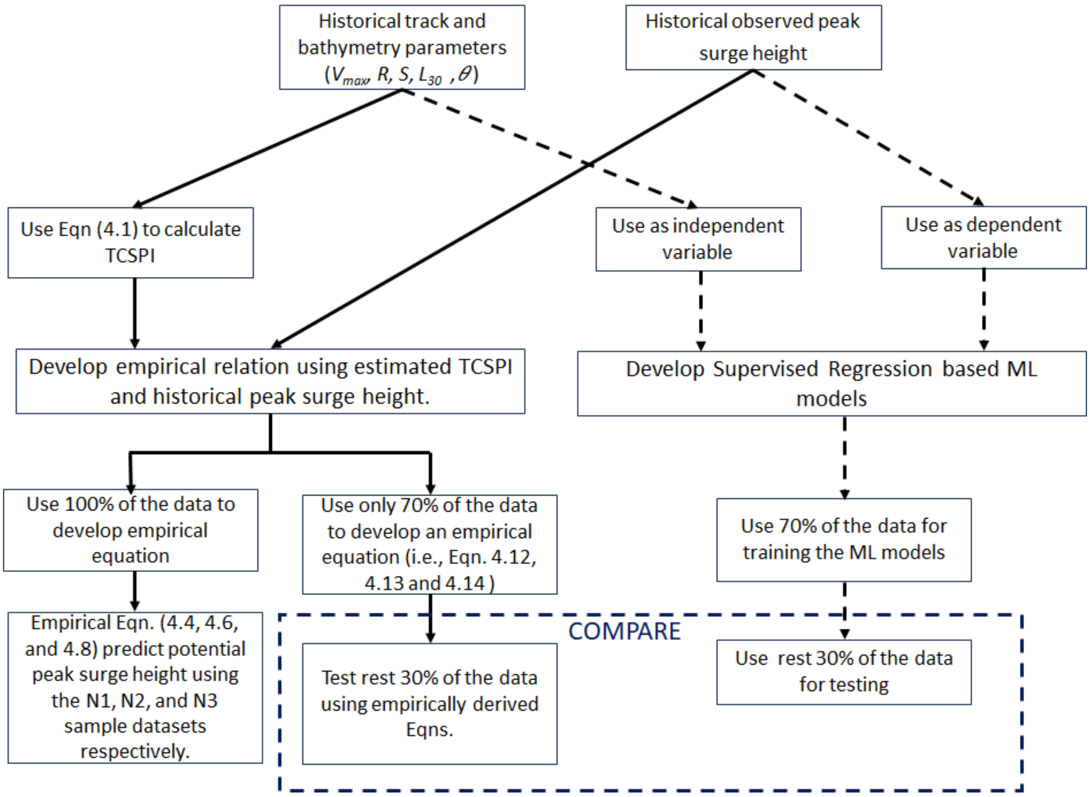

Fig 5. 6. Flow chart of the methodology

5.3.Results and Discussion

5.3.1. Evaluation of TCSPI model performance for N1 dataset

The TCSPI is positively proportional to the peak surge height for both the IMD and JTWC datasets. Fig. 5.7a illustrates that the Pearson CC between TCSPI and the observed surge height is 0.9217, with a significance level of $p < 0.01$ at a 95% confidence interval. This accounts for approximately 84% of the variance observed in the JTWC dataset. The validation of TCSPI was carried out using IMD dataset by including the R parameter from JTWC dataset. It is found that the Pearson CC is improved to 0.9487 ($p < .01$ at 95% confidence level) and explains about ~90% of the observed variance for the IMD dataset as shown in Fig. 5.7c. For both IMD and JTWC datasets a least squares fit between surge height and TCSPI (Fig. 5.7a, 5.7c) provides an empirical relationship (as given below). These empirical equations are used for estimating potential peak surge height. Further, the validation of estimated potential peak surge height and observed peak surge height are performed (Fig. 5.7b and Fig 5.7d) for both JTWC and IMD datasets.

$$\eta_{est\ (JTWC)}\ (cm) = 30.86 \times TCSPI + 108.69 \tag{5.4}$$

$$\eta_{est\ (IMD)}(cm) = 41.60 \times TCSPI + 102.65 \tag{5.5}$$

From the analysis, it is observed that the performance of the TCSPI model based on IMD datasets gives better results compared to the JTWC. The estimated peak surge height based on IMD's 3-minute maximum wind speed information performs better (RMSE of 37 cm) than the JTWC's 1-minute maximum sustained wind speed (RMSE of 46 cm) using Eqn (12) and Eqn (13) for JTWC and IMD datasets respectively as shown in Fig. 5.7b and Fig. 5.7d.

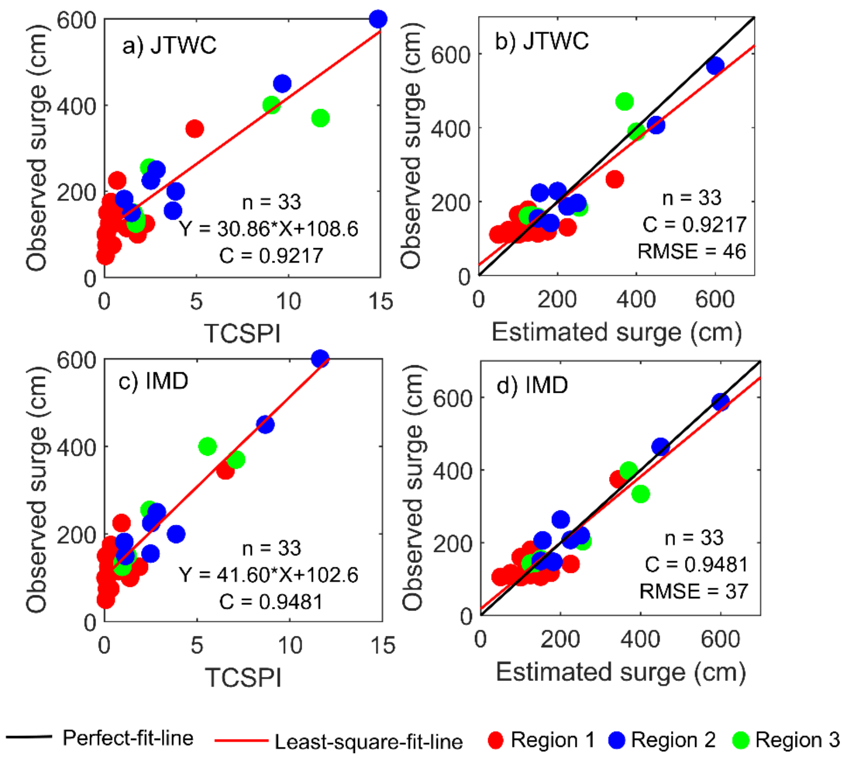

Fig 5. 7. (a, c) Observed TC peak surges (η) versus TCSPI (Eqn. 5.1) as a function of V_{max}, R, S, L_{30}, and θ parameter using N1 sample for the JTWC and IMD datasets, respectively. (b, d) Scatter plot of estimated (Eqn. 5.4, and Eqn. 5.5) and observed peak storm surge heights at landfall locations for JTWC and IMD datasets, respectively. The red line and black line indicate the least square fit and perfect fit of the observed peak surge and TCSPI (estimated potential peak surge η). The red, blue,

and green scatter dots indicate landfall locations associated with coasts of the Region 1, Region 2, and Region 3, respectively. ‘C’ denotes the correlation coefficient.

The present study performs sensitivity analysis to understand the dependency of V_{max}, R, S, L_{30}, and θ parameter in improving the accuracy of the TCSPI model for both JTWC and IMD datasets using the Taylor diagram (as shown in Fig. 5.8a, 5.8b). Firstly, we performed validation of the TCSPI model with observed surge values considering only V_{max} parameter in the TCSPI. The result shows that TCSPI performed poorly with CC of 0.6084, $p < 0.01$ and RMSE of 94 cm for the JTWC dataset. For the IMD dataset, CC of 0.5903, $p < 0.01$, and RMSE of 96 cm are obtained. Next, the validations are performed by including the R parameter along with V_{max} in TCSPI. The result indicates a slight improvement in statistics with CC of 0.6132, $p < 0.01$, RMSE of 94 cm for the JTWC dataset, and CC of 0.5990, $p < 0.01$, RMSE of 95 cm for the IMD dataset. The statistics improved better by considering the S parameter along with R and V_{max} in the TCSPI (CC = 0.6754, $p < 0.01$, RMSE = 88 cm for JTWC, and CC = 0.6658, $p < 0.01$, RMSE = 89 cm for IMD). The results indicate gradual improvement in statistics for L_{30} parameter along with V_{max}, R, and S (CC = 0.9122, $p < 0.01$, RMSE = 49 cm for JTWC, and CC = 0.9265, $p < 0.01$, RMSE = 45 cm for IMD).

The validation was performed again by including θ parameter along with V_{max}, R, S and L_{30} in TCSPI. The result indicates improvement in statistics with CC = 0.9217, $p < 0.01$, RMSE = 46 cm for the JTWC dataset, and CC = 0.9487, $p < 0.01$, RMSE = 37 cm for IMD dataset. Thus, the incorporation of θ parameter improved the accuracy of TCSPI by 17%. Finally, in the sensitivity analysis the importance of V_{max} and ΔP are also ascertain. By replacing V_{max} with ΔP, the resulting statistics between TCSPI and observed surge height slightly reduced with CC = 0.9073, $p < 0.01$, RMSE = 50 cm for JTWC, and CC = 0.8877, $p < 0.01$, RMSE = 55 cm for IMD. This indicates that V_{max} and ΔP are strongly associated with each other andalign well with findings from earlier research (Rosendal and Shaw, 1982; Callaghan and Smith, 1998; Raj et al., 2010; Kossin, 2015).

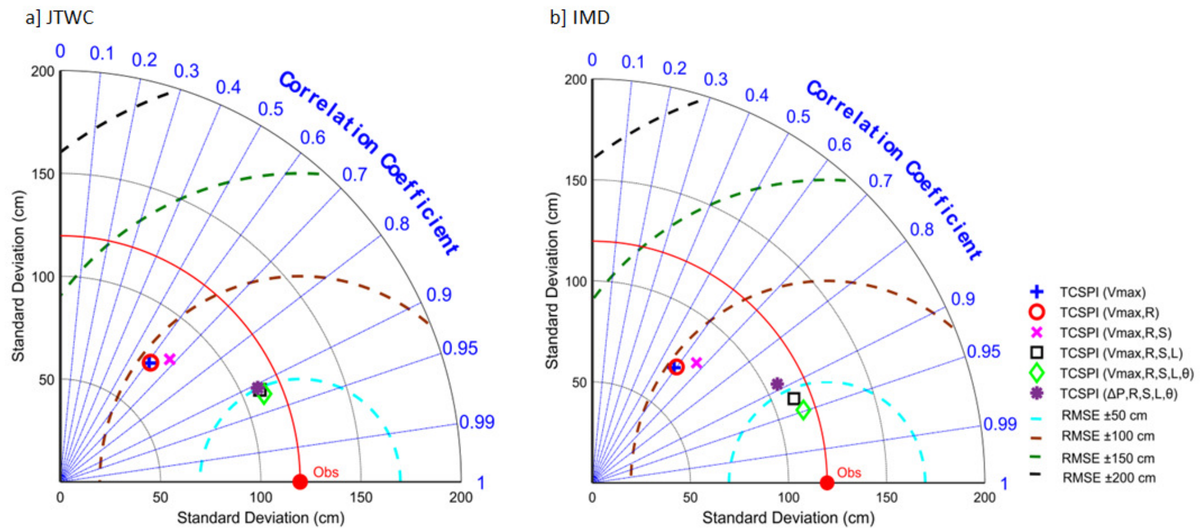

Fig 5. 8. A Taylor diagram utilizing (a) the JTWC dataset and (b) the IMD dataset shows how TCSPI performs in comparison to its reduced versions. The correlation is shown by the azimuthal angle, the standard deviation by the radial distance, and the RMSE by the semicircles centered on the "Obs" marker. The observed peak surge heights are referred to as "Obs" in this context. The standard deviation of the recorded peak surge heights for the N1 dataset is shown by the red line.

Further, the cumulative IMD observed peak surge and corresponding calculated TCSPI values using Eqn. (5.1) for each of the TC events considered from the N1 dataset are presented in Fig. 5.9. Overall, it is observed that the calculated TCSPI values are higher for the higher observed peak surge values associated with TCs, e.g., the TC Sidr (2007), Aila (2009), and Amphan (2020). It is also observed that the TCSPI values obtained from JTWC datasets are slightly higher than values obtained from IMD datasets for higher observed peak surge values associated with TCs. This slight overestimation of TCSPI is due to the consideration of 1-mins sustained V_{max} from JTWC. However, it is observed that for a few of the observed peak surge values, the calculated TCSPI values are much lower, e.g., TC Laila (2010), and Phailin (2013), which may lead to underestimation of estimated potential peak surge values. This may be caused by to combined effect of wave-induced surge, inverse barometric effect, and a steeper slope of bathymetry along the Region 1 coast of BoB, where these cyclones have made landfall. This slight accuracy can be overcome by considering the bathymetry slope information in TCSPI. Overall, the calculated TCSPI values using the

IMD dataset correlate better with the observed peak surge compared to the JTWC dataset. However, the correlation between TCSPI and observed surge could have been improved further by considering wind waves ("Bhaskaran et al., 2013; Murty et al., 2014, 2020; Wannawong and Ekkawatpanit. 2014; Thai et al., 2017; Chen et al., 2017; Pandey & Rao. 2019"), astronomical tides ("Dube et al., 2009, 2013; Johns et al., 1983,1985; Johns and Ali, 1980; Rao et al., 2010, 2013; Antony et al., 2020; Shashank et al., 2021"), riverine inflow (Gayathri et al., 2021), rain mass, and rain stress effects (Wong and Toumi. 2016) in the TCSPI formulation.

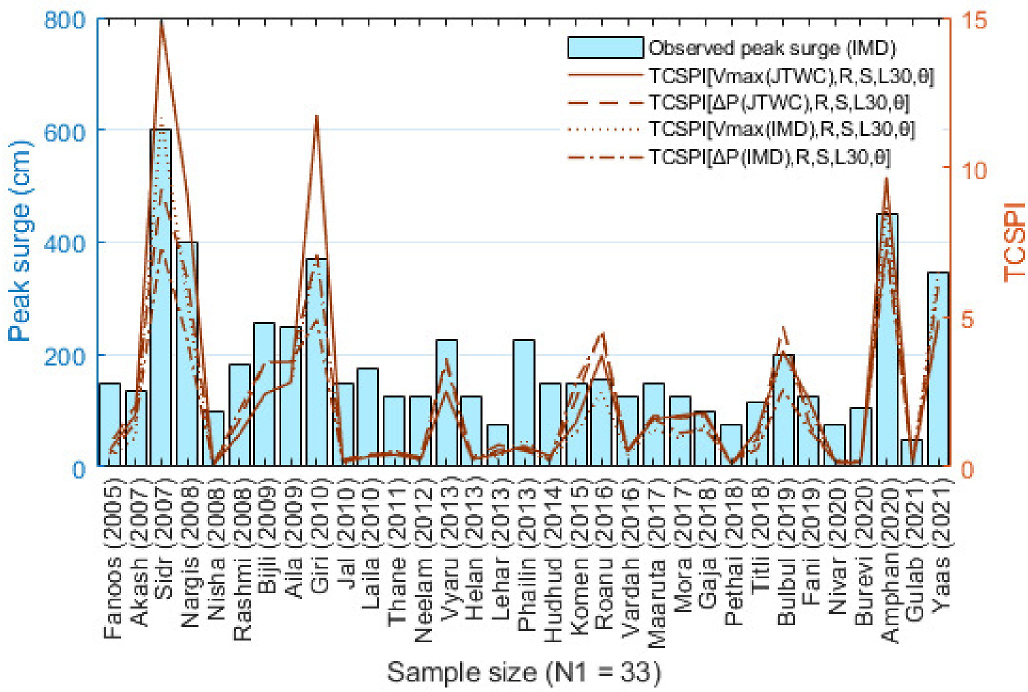

Fig 5. 9. Available IMD observed peak surge (y-axis-left) and corresponding calculated TCSPI (y-axis-right) values for the historical TC events that occurred between 2001─2021 in the BoB using the N1 dataset.

5.3.2. Evaluation of TCSPI model performance for N2 dataset.

The Pearson CC between TCSPI and observed surge height is 0.7358, $p < 0.01$ for the JTWC dataset, and CC of 0.7564, $p<0.01$ for the IMD dataset (as shown in Fig. 5.10a, and Fig. 5.10c). Thus, about ~54% observed variance for the JTWC dataset and about ~57% of the observed variance for the IMD datasets. Further, the validation of the estimated potential peak surge height and observed peak surge height is shown in the scatter plot (Fig. 5.10b, and Fig. 5.10d). The empirical relationship between the TCSPI and observed peak surge for both JTWC and IMD datasets is given below

$$\eta_{est\ (JTWC)}(cm) = 42.16 \times TCSPI + 145.52 \quad (5.6)$$
$$\eta_{est\ (IMD)}(cm) = 51.98 \times TCSPI + 141.61 \quad (5.7)$$

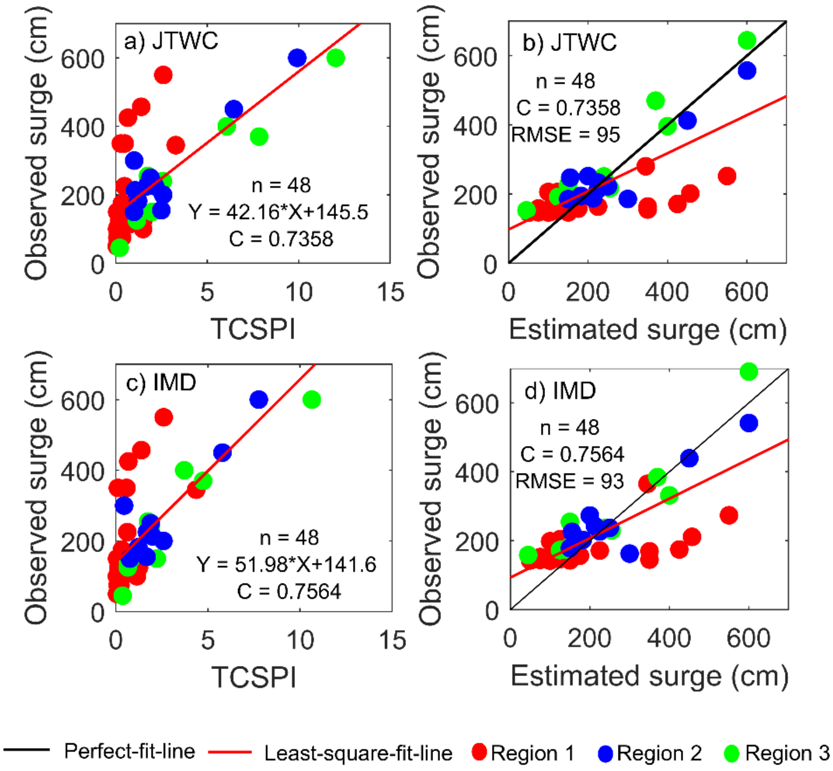

Fig 5. 10. (a, c) Observed TC peak surges (η) versus TCSPI (Eqn. 5.1) as a function of V_{max}, R, S, L_{30}, and θ parameter using N2 sample for the JTWC and IMD datasets respectively. (b, d) Scatter plot of estimated (Eqn. 5.6, and Eqn. 5.7) and observed peak storm surge heights at landfall locations for JTWC, and IMD datasets respectively. The red line and black line indicate the least square fit and perfect fit of the observed peak surge and TCSPI (estimated potential peak surge η). The red, blue, and green scatter dots indicate landfall locations associated with coasts of the Region 1, Region 2, and Region 3 respectively. 'C' denotes the correlation coefficient.

A similar sensitivity test was performed for the N2 dataset to understand the dependency of V_{max}, S, L_{30}, and θ parameter in improving the accuracy of the TCSPI model for both JTWC and IMD datasets as presented in the Taylor diagram (Fig. 5.11a and Fig. 5.11b). It is observed that validation of the TCSPI model with observed peak surge improved the performance with CC = 0.6729, 0.6791, 0.7133, 0.7362and RMSE = 104 cm, 104 cm, 97 cm, 95 cm by systematically including the parameters such as V_{max}, S, L_{30}, and θ parameter, respectively using the JTWC dataset. Similarly, the TCSPI performance improved with CC =0.6744, 0.6815, 0.7246, 0.7537 and RMSE = 104 cm, 103 cm, 95 cm, 93 cm by systematically including the parameters such as V_{max}, S, L_{30}, and θ parameter, respectively using the IMD dataset. Further, it should be noted that, the sensitivity analysis of ΔP parameter in replacement of V_{max} and inclusion of the R parameter in the TCSPI Eqn (9) has not been performed using the N2 dataset due to the unavailability of continuous data of ΔP and the R parameter in the BoB for the years 1990─2021.

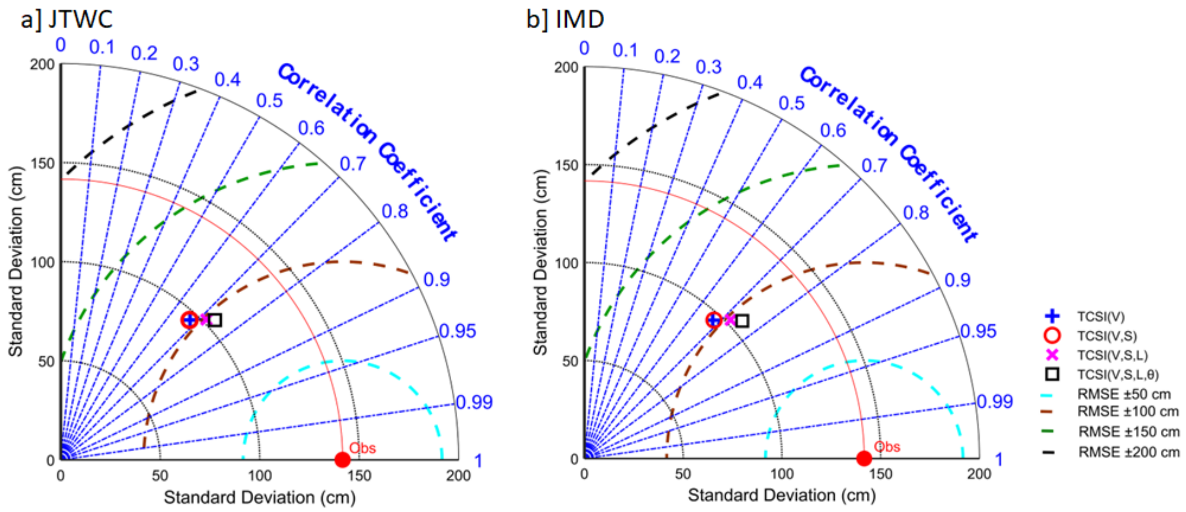

Fig 5. 11. A Taylor diagram utilizing (a) the JTWC dataset and (b) the IMD dataset that shows how TCSPI performs in comparison to its reduced versions. The observed peak surge heights are referred to as "Obs" in this context. The standard deviation of the recorded peak surge heights for the N2 dataset is shown by the red line.

Further, the cumulative observed peak surge associated with TCs for the BoB from 1990─2021, and corresponding calculated TCSPI values from the N2 dataset are presented in Fig. 5.12. It is observed that the calculated TCSPI values using both JTWC and IMD datasets are poorly correlating with observed peak surge values associated with TCs obtained from various sources (i.e., IMD, BMD, MDMH, and literature) compared to N1 dataset. However, V_{max} and L_{30} is contributing significantly in improving the accuracy of TCSPI as compared to R, S, and θ information for both N1 and N2 datasets. The relative underestimation of TCSPI values associated with observed peak surge is mostly seen along the coasts of the Region 1 (as shown in Fig. 5.10a, and Fig. 5.10c). In corresponding to the observed peak surge associated with TCs, specifically for the year 1990─2008 (Fig. 5.12), e.g., TC BOB01 (1990), BOB02 (1993), BOB03 (1994), BOB07 (1999), OGNI (2006), and Maala (2006). The present study suspects that the peak observed surge data for this period along the coasts of the Region 1 is majorly obtained from the IMD's annual TC review reports (except for TC OGNI (Pradhan et al., 2012), and TC Maala (Source: MDMH)) are not qualitative enough in terms of accuracy. For example, TC BOB01 (1990) having an intensity of 102 knots made landfall along the coast of Andhra Pradesh (Region 1), where a 30 m bathymetry contour is having a width (L_{30}) of about 15 km. This resulted in a maximum peak surge of 5 m as per reported in the Annual TC Review over NIO, (1990). However, TC Titli (2018) with similar intensity (slightly less intensity i.e., 80 knots) and having a width (L_{30}) of about 18 km, which made landfall along the coast of Andhra Pradesh (same along the Region 1 coast) could able to produce a maximum surge of only 1.5 m as per Annual TC Review over NIO, (2018). The same applicable to TC BOB02 (1993), BOB03 (1994), BOB07 (1999), OGNI (2006), and Maala (2006). This is probably because the surge guidance provided for the early years (1990─2008) by the IMD is based on the IIT Delhi Storm Surge Model (Annual TC Review over NIO, 2016). However, the study by Rao et al., (2009) reported that the errors associated with predicting storm surges using a finite difference-based IIT Delhi storm surge model are significant. Therefore, the proposed TCSPI is largely dependent on the quality in terms of the accuracy of the information used in the TCSPI.

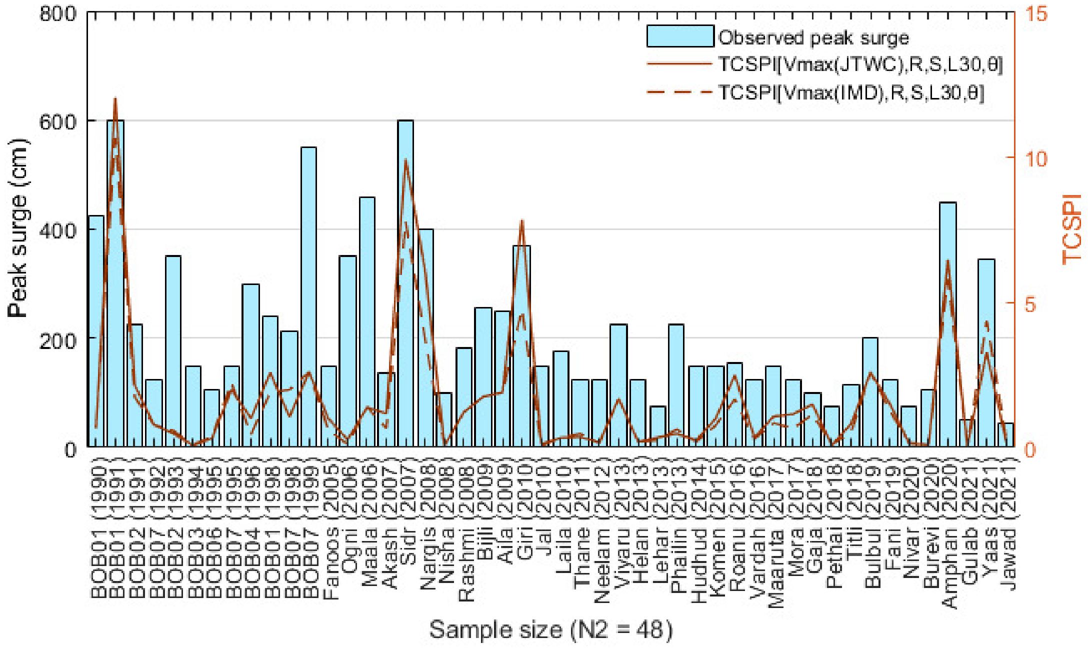

Fig 5. 12. Available observed peak surge (y-axis-left) from different sources (i.e., IMD, BMD, MDMH, and literature) and corresponding calculated TCSPI (y-axis-right) values for historical TC events that occurred between 1990–2021 in the BoB using the N2 dataset.

5.3.3. Evaluation of TCSPI model performance for the N3 dataset

The Pearson CC between TCSPI and observed surge height is 0.9553, $p < 0.01$, and explains ~91% observed variance for the N3 dataset, as shown in Fig. 5.13a. Further, the validation of the estimated potential peak surge height and simulated peak surge height is shown in the scatter plot (Fig. 5.13b). The empirical relationship between the TCSPI and ADCIRC simulated peak surge height for the IMD datasets is given below

$$\eta_{est\,(IMD)}\,(cm) = 57.43 \times TCSPI + 43.48 \qquad (5.8)$$

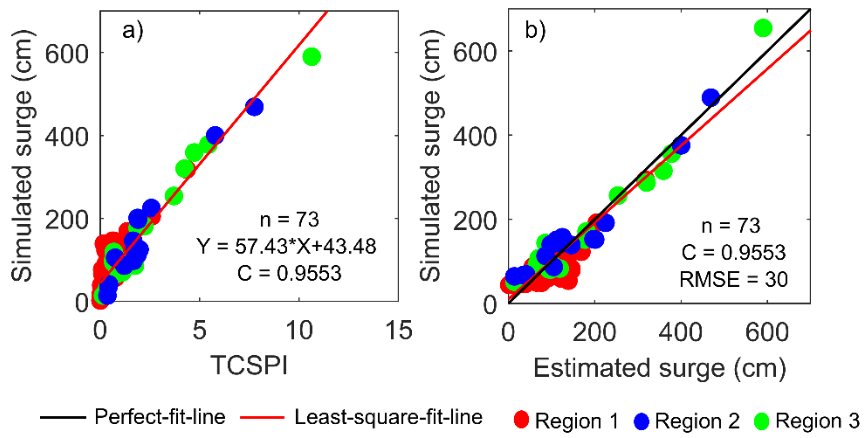

Fig 5. 13. (a) ADCIRC simulated TC peak surges (η) versus TCSPI (Eqn. 5.1) as a function of V_{max}, S, L_{30}, and θ parameter using the N3 sample. (b) Scatter plots of estimated (Eqn. 5.8) and ADCIRC simulated peak storm surge heights at landfall locations. The red line and black line indicate the least square fit and perfect fit of the simulated peak surge and TCSPI (estimated potential peak surge η). The red, blue, and green scatter dots indicate landfall locations associated with the coasts of Region 1, Region 2, and Region 3, respectively. 'C' denotes the correlation coefficient.

A similar sensitivity test was performed for the N3 dataset to understand the dependency of V_{max}, S, L_{30}, and θ parameter in improving the accuracy of the TCSPI model for N3 datasets in the Taylor diagram (Fig. 5.14). It is observed that validation of the TCSPI model with ADCIRC simulated peak surge improved the performance with CC = 0.7192, 0.7811, 0.9415, 0.9553 and RMSE = 78 cm, 70 cm, 37 cm, 30 cm by systematically including the parameters such as V_{max}, S, L_{30}, and θ parameter, respectively. The sensitivity analysis of ΔP parameter instead of V_{max} is also performed. The resulting statistics between TCSPI and ADCIRC simulated peak surge height slightly decreased (CC = 0.9098, p <.01, and RMSE = 46 cm).

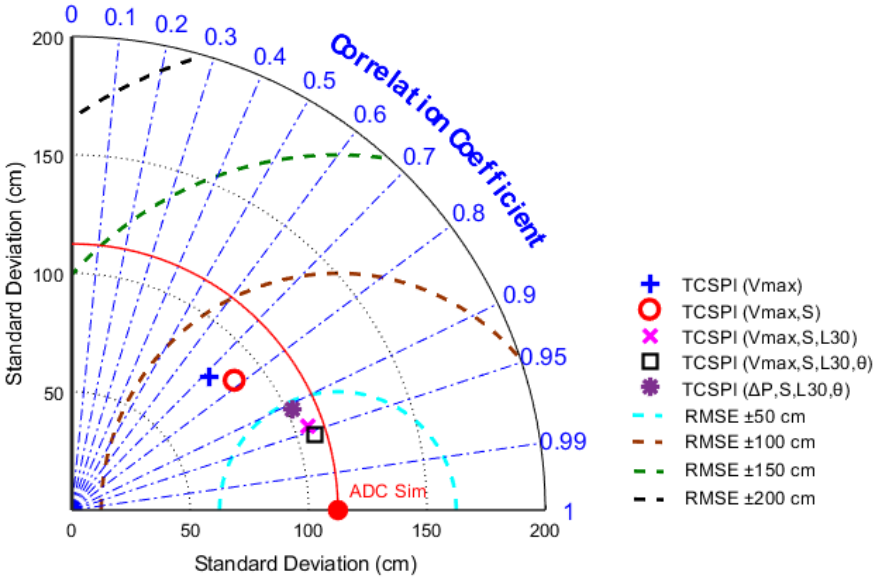

Fig 5. 14. A Taylor diagram utilizing the IMD dataset shows how well TCSPI performs in comparison to its reduced versions. The ADCIRC simulated peak surge heights are referred to as "ADC Sim" in this context. The standard deviation of the recorded peak surge heights for the N3 dataset is shown by the red line.

Further, the cumulative ADCIRC simulated peak surge values associated with TCs for the BoB and corresponding estimated TCSPI values of the N3 dataset are presented in Fig. 5.15. It is observed that the calculated TCSPI and ADCIRC simulated peak surge values using the IMD dataset are well correlated. The TCSPI pattern is closely following the pattern of peak surge height values associated with TCs. The statistics show TCSPI is highly correlated with peak surge height using the N3 dataset compared to the N2 (see Section 5.3.2) and N1 datasets (see section 5.3.1). It is because both TCSPI and ADCIRC models do not include additional surge influencing factors such as wind wave, riverine inflow, rain mass, and rain stress effect information apart from V_{max},S, L_{30}, and θ. However, the inclusion of R information in TCSPI and taking into account of errors due to the parametric Holland wind field in the ADCIRC model could have improved the correlation between TCSPI and ADCIRC simulated surge values even better (Shashank et al., 2022a).

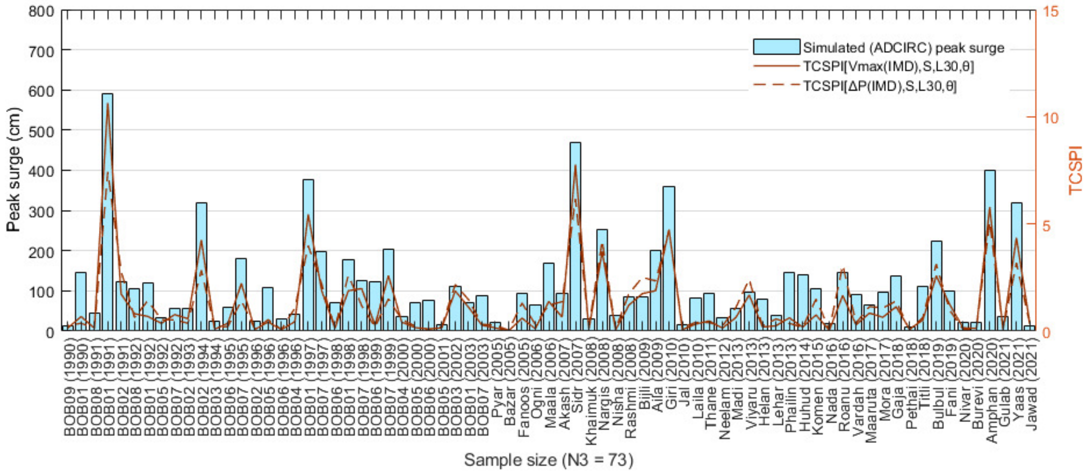

Fig 5. 15. Peak surge height obtained from ADCIRC simulations (y-axis-left), and corresponding TCSPI variations (y-axis-right) for historical TC events that occurred between 1990─2021 in the BoB using the N3 dataset.

5.3.4. Evaluation of characteristic coastal geometry values in TCSPI

In order to understand the importance of characteristic coastal geometry features (*a* and *b*) in the TCSPI, we considered N1 and N3 datasets to understand the necessity of the appropriate consideration of values *a*, and *b* in the Eqn. (5.1). N2 datasets have not been evaluated since errors associated with N2 datasets in the validation of TCSPI with observed peak surge height are significant, as discussed in Section 5.3.3. As discussed earlier, the characteristic coastal geometry feature (the default value a = 1) associated with forward speed information is considered in the TCSPI equation to evaluate N1 and N3 datasets for all the coasts of Region 1, Region 2, and Region 3. Peng et al., (2004); Islam and Takagi (2020) found that increased forward speed results in decreased surge height along the estuary and semi-enclosed bay coasts, respectively. Islam et al., (2021) found that the value of a = -1 is suitable in SSHPI Eqn. (1.8) for the semi-enclosed coast. However, no study in the literature suggests the effect of forward speed associated with TCs along the coasts of the delta region (i.e., Region 2 in our study area). Therefore, the study also looked at the performance of the TCSPI (Eqn. 5.1), considering the coastal geometry value a = -1 with peak surge height using the N1 and N3 datasets along the coast of the Region 2. Fig. 5.16a and Fig. 5.16c show validation of TCSPI with peak surge height considering a = -1 in Eqn. (5.1) for the coasts along the Region 2 using the N1 and N3 datasets, respectively. It is observed from the scatter plot (Fig. 5.16a and Fig. 5.16c) that the values associated with the Region 2 (blue dots) are away from the least square fit line, resulting in the underestimation of peak surge height (Fig. 5.16b and Fig. 5.16d). The estimated potential peak surge height (Fig. 5.16b, and Fig. 5.16d) resulted in poor statistics as compared to results discussed in section 5.3.1 and section 5.1.3 for N1 and N3 respectively (CC = 0.7649 (<0.9487), p <.01 and RMSE = 77 cm (>37 cm) for N1 dataset and, CC = 0.8642 (<0.9553), p <0.01 and RMSE = 56 cm (>30 cm) for N3 dataset). Thus, overall statistics indicate that an increase in forward speed associated with TCs would result in increased peak surge height along the coasts of the GBM delta region (Region 2) of northern BoB, the same as that of open coast (Region 1 and 3). Therefore, it is recommended to use a default value of a = 1 in the proposed TCSPI Eqn. (5.1) for all the coasts in the Region 1, 2, and 3.

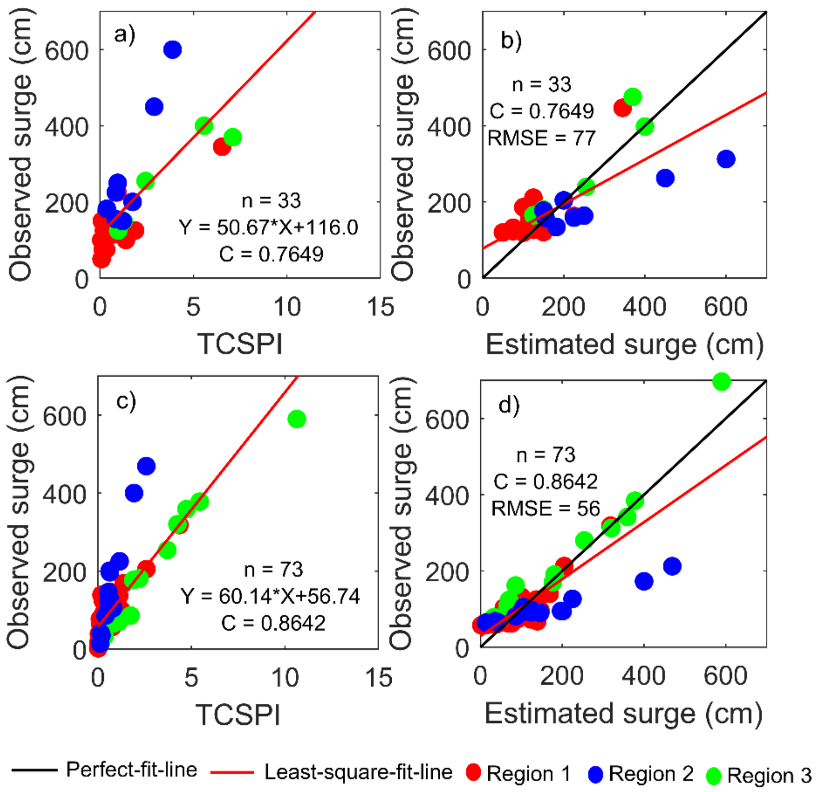

Fig 5. 16. (a, c) Observed/simulated TC peak surges (η) versus TCSPI considering a = -1 for the coasts of the Region 2. (b, d) Scatter plot of estimated and observed/simulated peak storm surge heights at landfall locations. The red and black line shows the least square fit and perfect fit of the estimated peak surge (η) and

observed/simulated peak surge. The red, blue, and green scatter dots indicate landfall locations of TCs associated with coasts of the Region 1, Region 2, and Region 3, respectively. 'C' denotes the correlation coefficient.

Similarly, TCSPI Eqn. (5.1) is validated with peak surge heights using N1 and N3 datasets to evaluate characteristic coastal geometry feature (b) associated with the approach angle of TCs. As discussed earlier, the default value of $b = 1$ is considered for the open coasts in the Region 1 and 3. In the case of the semi-enclosed coasts $b = 0$ is considered. Several studies have suggested the importance of considering the approach angle in storm surge. However, none of them discussed the importance of considering approach angle for varying characteristic coastal geometry and bathymetry. Fig. 5.17a and 5.17c shows validation of TCSPI with peak surge height considering $b = 1$ for the coasts along the Region 2 in the TCSPI Eqn. (5.1). The results indicate poor statistics as compared to results discussed in section 5.3.1 and section 5.3.3 (CC = 0.8595 (<0.9487) and RMSE = 61 cm (>37 cm) for the N1 dataset, and CC = 0.9122 (<0.9553), and RMSE = 46 cm (>30 cm) for N3 dataset). It is observed from the scatter plot (Fig. 5.17a and Fig. 5.17c) that the values associated with coasts of the Region 2 (blue dots) are away from the least square fit line, resulting in mostly underestimation of peak surge height (Fig. 5.17b and Fig. 5.17d). This indicates that consideration of approach angle in TCSPI Eqn. (5.1) is not suitable for the curvy geometry of the coasts along the Region 2 for the overall estimation of potential peak surge height in the BoB. Therefore, it is recommended to use the value $b = 0$ in the TCSPI Eqn. (5.1) for the coasts along the Region 2. Further, the consideration of approach angle information in TCSPI (Eqn. 5.1) is based on the numerical study (Pandey and Rao, 2019) for the BoB. However, these studies investigated the effect of approach angle for the landfalling TCs along the coasts of the Region 1 alone. Therefore, the present study makes further investigation on the effect of the approach angle associated with characteristic coastal geometry for the open coast along the Region 3. Fig. 5.17e and Fig. 5.17g show validation of TCSPI with peak surge height considering $b = 0$. The results indicate slightly reduced statistics compared to results discussed in section 5.3.1 and section 5.3.3 for N1 and N3, respectively (CC = 0.9249 (<0.9487) and RMSE = 45 cm (>30 cm) for the N1 dataset, and CC = 0.9485 (<0.9553), and RMSE = 35 cm (>30 cm) for N3 dataset). It is observed from the scatter plot (Fig. 5.17f and Fig. 5.17h) that the values associated with the coasts along the Region 3 (green dots) are away from the least square fit line, which indicates the importance of approach angle information in TCSPI (Eqn. 5.1) for the coasts along the Region 3. Therefore, it is valid to consider the value $b = 1$ in the TCSPI for the coasts along the Region 3 same as coasts along the Region 1. From the discussion in section 4.3.1, and section 4.3.2, it is evident that the inclusion of the approach angle has improved the accuracy of TCSPI by up to 17% and 19% for N1 and N3 datasets, respectively. However, it is evident that consideration of $b = 1$ in Eqn. (5.1) for the Region 3 coastline has minimal impact on enhancing the accuracy of TCSPI in predicting the potential peak surge height across the BoB.

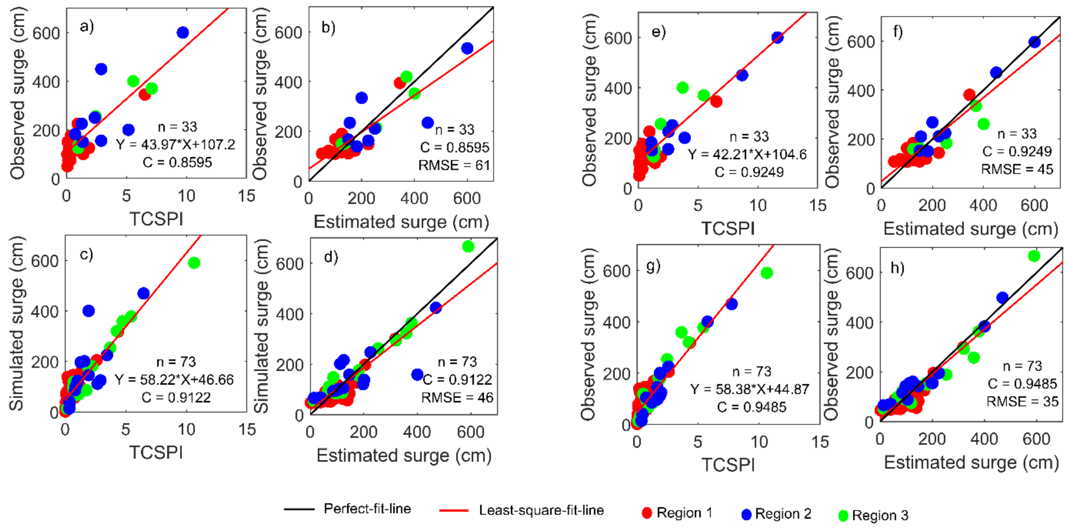

Fig 5. 17. (a, c) Observed/simulated TC peak surges (η) versus TCSPI considering b = 1 for the surge heights at landfall locations. (e, g) Observed/simulated TC peak surges (η) versus TCSPI considering b = 0 for the coasts of Region 3. (f, h) Scatter plot of estimated and observed/simulated peak storm surge heights at landfall locations for N1, and N3 datasets, respectively. The red and black line shows the least square fit and perfect fit of the estimated peak surge (η) and observed/simulated peak surge. The red, blue, and green scatter dots indicate landfall locations associated with the coasts of Region 1, Region 2, and Region 3, respectively. 'C' denotes the correlation coefficient.

5.3.5. Verification score

Next, the verification score was quantified using the probability of detection (POD), the false alarm ratio (FAR), and the critical success score (CSI) to assess quantitatively the accuracy of the TCSPI model for using N1, N2, and N3 samples from the IMD datasets. The mathematical forms of POD, FAR, and CSI (Jolliffe et al., 2012) are given as

$$POD = \frac{(hits)}{(hits) + (misses)} \quad 0 \leq POD \leq 1;\ the\ perfect\ score\ is\ 1 \tag{5.9}$$

$$FAR = \frac{(false\ alaram)}{(hits) + (false\ alaram)} \quad 0 \leq FAR \leq 1;\ the\ perfect\ score\ is\ 0 \tag{5.10}$$

$$CSI = \frac{(hits)}{(hits)+(misses)+(false\ alaram)} \quad 0 \leq CSI \leq 1;\ the\ perfect\ score\ is\ 1 \tag{5.11}$$

To calibrate the verification score for peak surge heights ≤ threshold value, we have considered hits, misses, and false alarm as in Jolliffe et al., 2012. The hits represent observed peak surge height and predicted peak surge height values are ≤ threshold value. The misses represent observed peak surge height values is ≤ threshold value, and the predicted peak surge height value > threshold value. Finally, the false alarm represents the observed peak surge height value is > threshold value and the predicted peak surge height value ≤ threshold value. In a similar way, we also calibrated the verification score for peak surge heights ≥ threshold value.

All three scores (Fig. 5.18a, b, and c) suggest that the TCSPI performs better for events with smaller peak surge height values than the threshold values (threshold value is average of observed/simulated peak surge height) compared to peak surge heights higher than the threshold value. For example, the CSI score for minor surge events (< threshold peak surge values) is slightly higher than significant peak surge events (> threshold peak surge values). These results are in accordance with the previous study by Islam et al., (2021).

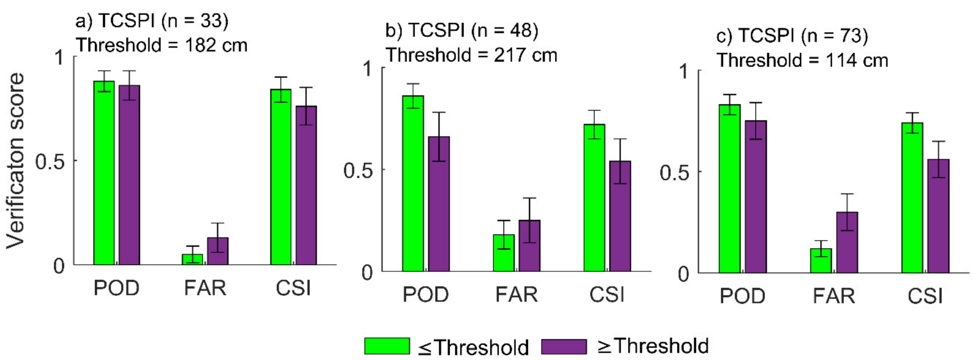

Fig 5. 18. (a, b, c) Verification scores for TCSPI, estimated storm surges. (d, e, f) Verification scores for ML (LR-Stepwise) estimated storm surges using N1, N2, and N3 datasets, respectively. Error bars show two-sided 95% confidence intervals.

5.3.6. Evaluation of ML Models Performance

The performance of regression-based LR, TR, SVM, EnTR, and GPR ML models for each of their respective fitting parameters for the training (70% of data) and test (30% of the data) datasets is given in the Table. 5.4. However, the validation for only the best-performing ML model in each of the training, and testing, datasets for N1, N2, and N3 samples are presented in the scatter plot (Fig. 5.19). It is observed that the LR model with stepwise fitting parameter is performing better compared to the rest of the ML models in terms of statistics (CC = 0.9431, 0.7535, 0.9555 and RMSE = 77 cm, 115 cm, 30 cm for considering test datasets using N1, N2 and N3 samples respectively). Overall considering N1, N2, and N3 datasets, the LR and GPR model is performing better, followed by the SVM, TR and EnTR models for different fitting parameters as presented in Table. 5.4.

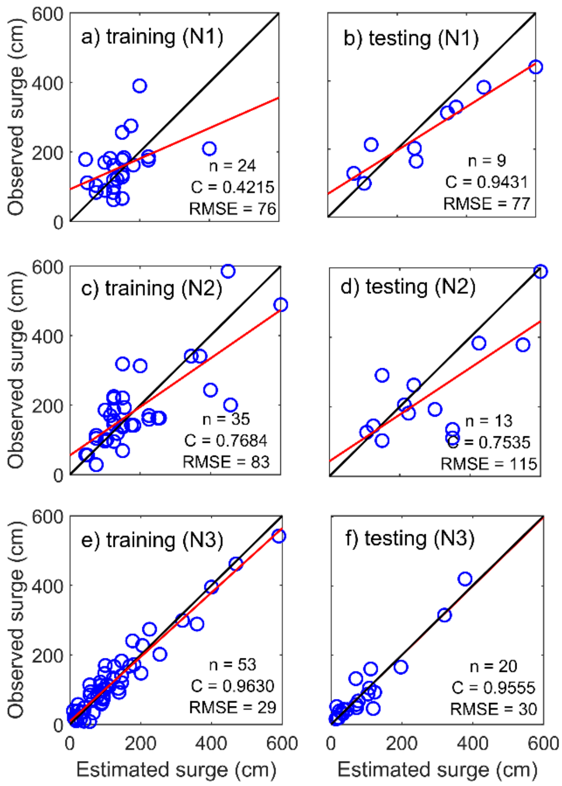

Fig 5. 19. (a, b) Scatter plot of ML (LR-Stepwise) estimated and observed storm surge heights at landfall locations for training and testing datasets, respectively, for the N1 sample. Similarly, (c, d) for the N2 sample and (e, f) for the N3 sample. The red and black line indicates the least square fit and perfect fit of the respective ML estimated surge and observed/simulated surge. ‘C’ denotes the correlation coefficient. ‘n’ denotes the number of sample datasets used for training and testing.

Table 5.4. CC and RMSE of training and testing datasets of the regression-based ML models with the machine learning methods for N1, N2, and N3 sample

Model	Fitting Method	N1				N2				N3			
		Training		Testing		Training		Testing		Training		Testing	
		CC	RMSE (cm)	CC	RMSE (cm)	CC	RMSE (cm)	CC	RMSE (cm)	CC	RMSE (cm)	CC	RMSE (cm)
Linear Regression (LR)	Basic	0.3441	72	0.7983	140	0.6469	100	0.5960	146	0.8365	55	0.9260	37
	Interaction	0.0984	306	0.8991	107	0.7840	82	0.6972	125	0.9685	29	0.9499	31
	Robust	0.4186	63	0.8520	160	0.6719	95	0.5898	146	0.9019	50	0.9349	56
	Stepwise	0.4215	76	0.9431	77	0.7684	83	0.7535	115	0.9630	29	0.9555	30
Tree Regression (TR)	Fine	0.1709	73	0.6962	171	0.6881	93	0.5613	153	0.7395	80	0.8353	58
	Medium	-0.4859	73	0.7962	197	0.1056	136	0.4398	163	0.4289	109	0.7722	61
	Coarse	-0.5215	74	0.1222	216	-0.2167	129	0.4624	183	-0.2281	99	0.1000	98
Support Vector Machine (SVM)	Linear	0.2236	68	0.8813	197	0.6856	102	0.5760	164	0.9212	47	0.9178	51
	Quadratic	0.2214	68	0.8446	191	0.7755	80	0.6734	131	0.9566	30	0.9540	31
	Cubic	0.1606	71	0.8524	134	0.8288	72	0.8202	106	0.8925	43	0.9633	28
	Fine Gaussian	-0.1632	70	0.0123	221	-0.2630	134	0.0999	197	0.6181	85	0.3956	90
	Medium Gaussian	0.0833	70	0.4590	206	0.3034	124	0.5983	164	0.9250	36	0.9553	37
	Coarse Gaussian	-0.0907	71	0.8528	212	0.3180	129	0.5349	194	0.8216	65	0.9265	62
Ensemble Tree (EnTR)	Boosted Trees	0.1146	71	0.6508	194	0.6689	95	0.4594	168	0.7846	66	0.9337	46
	Bagged Tress	0.1761	68	0.4979	198	0.6038	108	0.4559	164	0.6835	80	0.9195	53
Gaussian processes regression (GPR)	Squared exponential	-0.1458	75	0.0844	197	0.4938	113	0.6913	128	0.9607	27	0.9513	31
	Matern 5/2	0.0132	70	0.1662	196	0.4899	113	0.6721	132	0.9688	27	0.9484	31
	Exponential	-0.0687	76	0.2378	201	0.7865	80	0.6349	139	0.9203	35	0.9530	33
	Rational Quadratic	0.0293	72	0.0844	197	0.8018	76	0.6913	128	0.9551	30	0.9543	30

5.3.7. Comparison of peak surge events estimated by TCSPI, ML, and ADCIRC model

In the present study, we examined the accuracy of TCSPI, ML (LR-Stepwise), and ADCIRC models predicted peak surge height with IMD observations for the past 9 notable cyclonic events that occurred along the entire BoB coast over the past 20 years (2001 to 2021). The peak surge height is estimated using TCSPI, ML (LR-Stepwise) using N1 datasets alone as it consists of all the meteorological parameters (V_{max}, R, S, L_{30}, and θ), and bathymetry (L_{30}) information. It should be noted that, for the comparison 70% of the randomly selected data used for both developing the TCSPI and ML models and rest 30% of the data treated as test (unknown) data. The empirical Eqn (4.12) derived from 70% of the data has been used to develop the TCSPI model. It should also be noted that the same meteorological parameter information (V_{max}, R, S, L_{30}, and θ) provided as input to the both TCSPI and ML models. While the ADCIRC model setup is prepared for the numerical simulations for the 9 notable cyclone test cases as per discussed model setup section 5.2.4. The results indicate TCSPI estimated potential peak surge values are close to IMD observation as compared to ML (LR-Stepwise) and ADCIRC estimated peak surge values. However, ADCIRC simulated peak surges are mostly underestimating the observed values, which is closely align with the previous studies by Pandey and Rao, (2018); Antony et al., (2020); Murty et al., (2020) for the BoB region. Table. 5.5 indicates the performance of TCSPI, LR-Stepwise, and ADCIRC model predicted peak surge height with the IMD observations for the 9 notable TC events. From the Fig. 5.20 and Table 5.5, it can be noted that the ADCIRC model's error in predicting the peak surge height for 9 test cases from the N1 sample dataset is 59 cm. Nevertheless, when examining all 33 TCs from the same N1 sample dataset, the error associated with ADCIRC model in predicting the peak surge height increases to 65 cm with the observation.

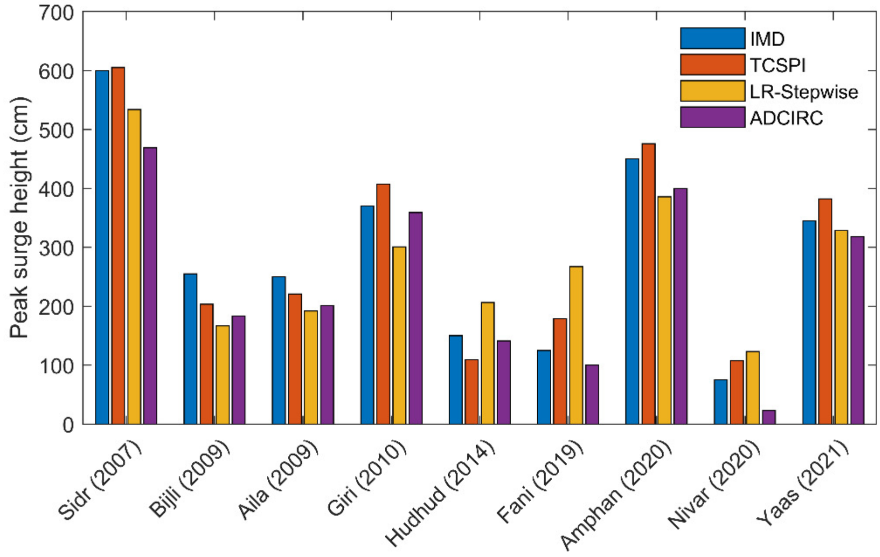

Fig 5. 20. The x-axis denotes notable cyclonic events in the BoB from 2001─2021, and the y-axis denotes the IMD observed peak surge height and estimated peak surge height using TCSPI, ML (LR-Stepwise), and ADCIRC model for comparison.

Table 5.5. Performance of TCSPI, ML (LR-Stepwise) and ADCIRC model using N1 (test) sample data.

	TCSPI	ML (LR-Stepwise)	ADCIRC
CC	0.9753	0.9431	0.9688
RMSE (cm)	38	77	59

5.3.8. Comparison of peak surge events estimated by TCSPI and ML models for N1, N2 and N3 datasets.

In the present study, we compared the performance of both TCSPI and ML-based LR-Stepwise models on testing datasets for N1, N2, and N3 data samples as shown in Fig. 5.21. The empirical Eqn (4.12), (4.13), and (4.14) shown below are derived from 70% of the data, this has been used to develop the TCSPI model for N1, N2, and N3 datasets respectively. Using these equations, we tested the remaining 30% of the data using TCSPI, as presented in Fig. 5.21a, c, and e for the N1, N2, and N3 datasets respectively. Similarly, we trained 70% of the data using ML models and the remaining 30% for testing. The best performing ML model (LR-Stepwise) for the test dataset is presented in Fig. 5.21b, d and f for N1, N2, and N3 datasets respectively.

$$\eta_{est\,(N1)}\,(cm) = 43.64 \times TCSPI + 97.19 \tag{5.12}$$

$$\eta_{est\,(N2)}\,(cm) = 62.94 \times TCSPI + 103.58 \tag{5.13}$$

$$\eta_{est\,(N3)}\,(cm) = 56.40 \times TCSPI + 44.34 \tag{5.13}$$

Considering the N1 dataset, it is observed that the ML-based LR model with stepwise fitting parameter performs poorly in terms of statistics compared to the TCSPI model (LR-Stepwise CC = 0.9431 < TCSPI CC = 9753 and LR-Stepwise RMSE = 77 cm > TCSPI RMSE = 38 cm). This indicates that TCSPI performs better even with a smaller sample size compared to ML models. However, for the N2 dataset, the LR model with stepwise fitting parameter performs relatively better with statistics as compared to the TCSPI model (LR-Stepwise CC = 0.7535 > TCSPI CC = 0.6062 and LR-Stepwise RMSE = 115 cm < TCSPI RMSE = 159 cm). The accuracy of TCSPI depends on the accuracy of the observed track variables and observed/forecasted peak surge information. Whereas the ML models are capable of learning better with the increase in sample size. For the N3 dataset, it is observed that the LR model with stepwise fitting parameter performs nearly same as compared to the TCSPI (LR-Stepwise CC = 0.9555 < TCSPI CC = 0.9423 and LR-Stepwise RMSE = 30 cm < TCSPI RMSE = 33 cm). Thus, the regression-based TCSPI model performs comparatively better than ML models even with a smaller sample size. The results of The TCSPI aligns closely with the surge index used in prior study by Islam et al., (2021) for the Japan coast.

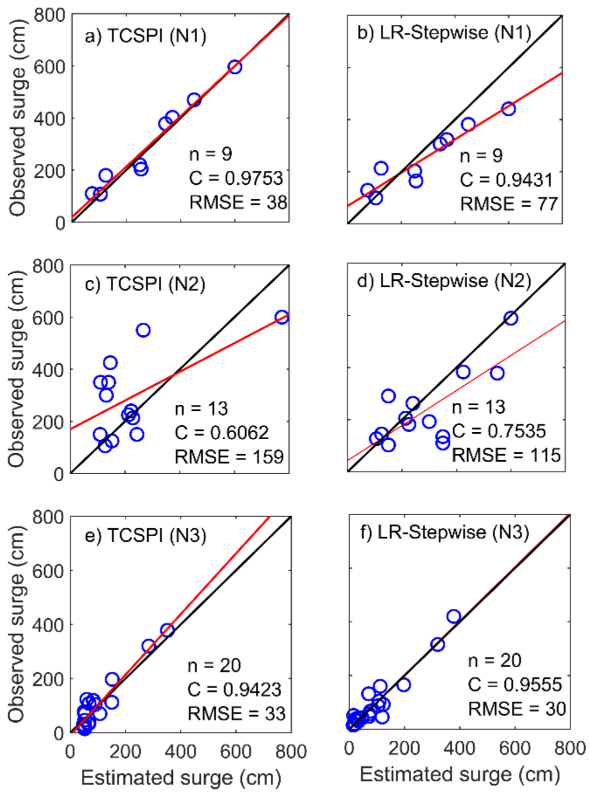

Fig 5. 21. (a, b) Scatter plot of ML (LR-Stepwise) and TCSPI estimated and observed storm surge heights at landfall locations for testing datasets, respectively, for the N1 sample. Similarly, (c, d) for the N2 sample and (e, f) for the N3 sample. The red and black line indicates the least square fit and perfect fit of the respective ML estimated surge and observed/simulated surge. 'C' denotes the correlation coefficient. 'n' denotes the number of sample datasets used for training, testing, and overall.

5.4.SUMMARY

This summary outlines the development and evaluation of TCSPI using IMD and JTWC datasets. The study also investigated the influence of track parameters, bathymetry, and geometrical coefficients on peak surge height using TCSPI. TCSPI was validated against peak surge height values derived from the ADCIRC model to determine if the TCSPI and ADCIRC models exhibit similar trends in predicting peak surge height. Verification assessments were presented to understand the predictive capability of TCSPI with respect to the peak surge height threshold values for the N1, N2, and N3 datasets. Various regression-based machine learning models were developed and evaluated to determine the most suitable model for the BoB, particularly considering the challenges posed by small sample datasets. A uniform comparison method was employed to analyze and compare the performance of TCSPI, ML, and ADCIRC models.

CHAPTER 6

STORM SURGE HAZARD MAP[4]

6.1. GENERAL

The Indian east coast is highly susceptible to cyclones and storm surges from the Bay of Bengal, making surge hazard maps essential for identifying high-risk areas and guiding effective disaster management. These maps support better planning, evacuation strategies, and infrastructure resilience, ultimately reducing damage and saving lives. While several past studies have produced surge hazard maps, their methodologies are often complex and time-consuming. The present study proposes a simplified, accurate, and computationally efficient methodology, eliminating the need for synthetic track generation and cyclone pressure drop estimations. By focusing on peak surge height estimation for various return periods, combined with climate change scenarios, an enhanced version of the Tropical Cyclone Surge Potential Index (TCSPI) model is introduced. The present chapter provides detailed discussion of the model validation and its applications in generating surge hazard maps, along with an analysis of surge hazard vulnerability for each coastal state situated along the eastern coast of India.

6.2. MODEL, DATA, AND METHODOLOGY

6.2.1. Model

In the present study, we incorporated a novel tropical cyclone surge potential index (TCSPI) proposed by Shashank et al., (2024) for estimating TC-induced potential peak surge levels near the landfall locations for the entire coast of the BoB. For the calibration of peak surge height, the simplified physics-based TCSPI model was found to be more useful than the full physics-based hydrodynamic model (i.e., ADCIRC model) and statistical-based data-driven supervised Machine Learning (ML) models on small sample datasets (Shashank et al., 2024). The physical significance of each storm

[4] This work is submitted to: "Shashank, V. G., Sriram, V., Schüttrumpf, H., & Sannasiraj, S. A. (2024). Mapping Storm Surge Risk for the Indian East Coast using a Tropical Cyclone Surge Potential Index Model. ISH Journal of Hydralic Engineering"

parameter (V_{max}, R, S, and θ), and bathymetry parameter (L_{30}) used in the TCSPI is discussed in detail in Shashank et al., (2024). However, in the present study, we have incorporated TCSPI only for the coastal states of the Indian east coast. Also, the present study has incorporated slight adjustments to the TCSPI model that is specifically suitable for the Indian east coast, enhancing its capability to provide even more accurate estimates of peak surge values. The modified form of the TCSPI model is given below:

$$If\ V_{max} \leq 47\ Knots$$

$$Surge(cm) = 57.43 \times TCSPI + 43.48$$

$$If\ Vmax > 47\ Knots$$

$$Surge(cm) = 41.60 \times TCSPI + 102.65$$

$$Where\ \ TCSPI = \left(\frac{V_{max}}{V_{max0}}\right)^2 \left(\frac{R}{R_0}\right) \left(\frac{L_{30}}{L_*}\right) \left(\frac{S}{S_0}\right)^a \left(\frac{\theta}{\theta_0}\right)^b \qquad (6.1)$$

$$\left(\frac{R}{R_0}\right) = \begin{cases} 1.5 & if\ \left(\frac{R}{R_0}\right) \geq 1.5 \\ \left(\frac{R}{R_0}\right) & if\ 0.5 < \left(\frac{R}{R_0}\right) < 1.5 \\ 0.5 & if\ \left(\frac{R}{R_0}\right) \leq 0.5 \end{cases} ; \quad \left(\frac{S}{S_0}\right)^a = \begin{cases} 1.5 & if\ \left(\frac{S}{S_0}\right)^a \geq 1.5 \\ \left(\frac{S}{S_0}\right)^a & if\ 0.5 < \left(\frac{S}{S_0}\right)^a < 1.5 \\ 0.5 & if\ \left(\frac{S}{S_0}\right)^a \leq 0.5 \end{cases}$$

$$\left(\frac{\theta}{\theta_0}\right)^b = \begin{cases} \left(\frac{\theta}{\theta_{01}}\right)^b & if\ \theta \leq 90° \\ \left(\frac{\theta}{\theta_{02}}\right)^{-b} & if\ \theta > 90° \end{cases} \quad and \quad \left(\frac{\theta}{\theta_0}\right)^b = 0.5\ if \left(\frac{\theta}{\theta_0}\right)^b \leq 0.5$$

In the present study, if a TC makes landfall with a V_{max} not exceeding 47 knots, categorizing it as a cyclonic storm (CS) or depression (D) or deep depression (DD), according to the IMD's cyclone classification. We had incorporated the empirical Eqn. (14) from the study of Shashank et al., (2024) to calculate the peak surge height caused by cyclones. If the landfalling V_{max} of the cyclone exceeds 47 knots, it is categorized as SCS, or VSCS, or ESCS or SuCS, according to the IMD's cyclone classification. We had incorporated the empirical Eqn. (13) from the study of Shashank et al., (2024) to calculate the peak surge height caused by cyclones. Adopting this approach, enhanced the accuracy of predicting the potential peak surge height more effectively (as discussed in Section 5.3.1) in the study. This is because Eqn. (14), and Eqn. (13) are found to be more suitable for predicting peak surge height with lower-intensity storms ($V_{max} \leq 47$ *Knots*) and higher-intensity storms ($Vmax > 47$ *Knots*), respectively. Previously, Shashank et al., (2024) used Eqn. (13) and Eqn. (14) for validating IMD observed peak surge heights and ADCIRC simulated peak surge heights.

The subscript 0 refers to climatological reference constants. In the present study, V_{max0} is 33 ms^{-1}. This value is the same as in Shashank et al., (2024). However, the present study considers (R/R_0) = 1. This is because the parameter R has a relatively minor influence on accurately predicting peak surge height along the BoB coast compared to other parameters ($Vmax$, S, L_{30}, and θ) using the TCSPI model (Shashank et al., 2024). Moreover, in the present study, we are utilizing only IMD data to develop the storm surge hazard map (as discussed in Section 2.2), and IMD best track data does not provide R information. Shashank et al., (2024) incorporated bathymetry information L_{30}. However, in this study, for estimating the peak surge height along the Indian east coastline exclusively, an optimized value of $L_* = 40$ km was employed in TCSPI. This L_* was determined through an iterative minimization process that adjusts parameters to reduce the objective function (Lagarias et al., 1998). Also, this L_* value is approximately the average of L_{30} values along the eastern coast of India. Shashank et al., (2024) used the climatological reference constant for forward speed $S_0 = 3.77$ ms^{-1} and reference constants for approach angle θ_0 that has a lower limit $\theta_{01} = 60°$ and an upper limit $\theta_{02} = 110°$. The constants employed in this study for forward speed and approach angle references remain consistent, except where $\theta_{01} = 50$ and $\theta_{02} = 120°$. The minor adjustments mentioned above are crucial in improving the precision of peak surge height forecasts (as discussed in section 3.1). This improved version of the TCSPI model is freely accessible to the public via the IITM Surge Calculator website at [*https://iitmaisurge.in/*]. A guide for users to operate the IITM Surge Calculator to calculate the potential peak surge height value for a cyclone test case Hudhud (2014) is given in Appendix A.

6.2.2. Track Data

In this study, the best track archives from IMD were utilized, as the 3-minute maximum sustained wind speed data from IMD is more suitable for generating precise peak surge height forecasts compared to the 1-minute maximum sustained wind speed data from the JTWC (Shashank et al., 2024). The IMD has provided the cyclone track information since 1891. However, the best track data is available only from 1982. This includes the track parameters, such as track position, V_{max}, and ΔP. It should be noted that the IMD does not provide information on storm size. In the present study, only cyclones classified as Cyclonic Storms (CS) by the IMD TC classification and those TCs whose maximum V_{max} during the storm duration is at least exceeding 47 knots were considered. Based on the frequency of cyclone events in BoB between 1982 and 2022, it is observed that, overall, 65 landfalling TCs across the Indian east coast were reported in the BoB (Fig. 5.1). From 1982–2022 in terms of IMD's TC intensity classification (Fig. 2), 19 TCs were reported as CS, 22 TCs as SCS, 12 TCs as VSCS, 6 TCs as ESCS, and 3 TCs as SuCS. The coastal districts of Andhra Pradesh experience the most frequent occurrences of cyclone landfalls among the coastal states along the Indian east coast, based on the IMD best track data from 1982-2022 (depicted in Fig. 5.2). Tamil Nadu, Odisha, and West Bengal are the subsequent states with closely following frequency of cyclone landfalls. It is observed that 26 TCs have made landfall along the coasts of Andhra Pradesh state, 18 TCs along the coast of Tamil Nadu state, 11 TCs along the coast of Odisha state, and 7 TCs along the coast of West Bengal state in the past 40 years. However, analyzing the frequency of occurrence of TCs based on IMD track data from 1891 along the Indian east coast indicates that more frequent occurrence of landfalling TCs observed along the Odisha and West Bengal state coast, followed by Andhra Pradesh and Tamil Nadu state coast (Rao et al., 2019).

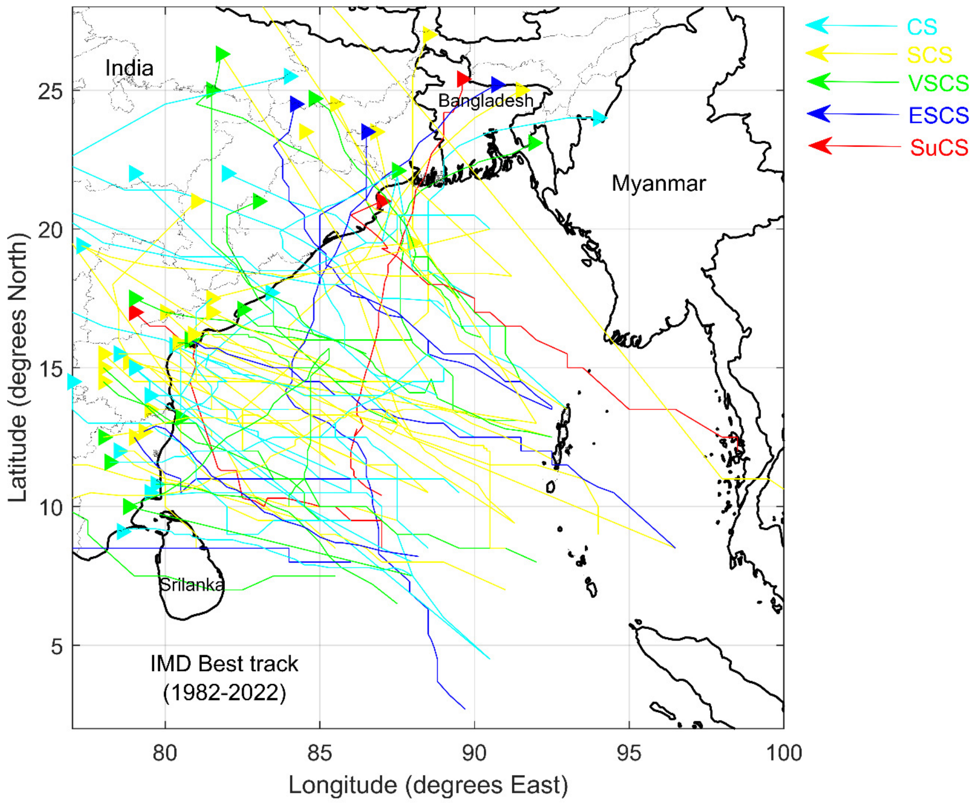

Fig 6.1. Cumulative tracks and their respective IMD classification of landfalling TCs along the Indian east coast from 1982–2022. Plotting style of cyclone tracks is inspired from the study presented by Shashank et al., (2024)

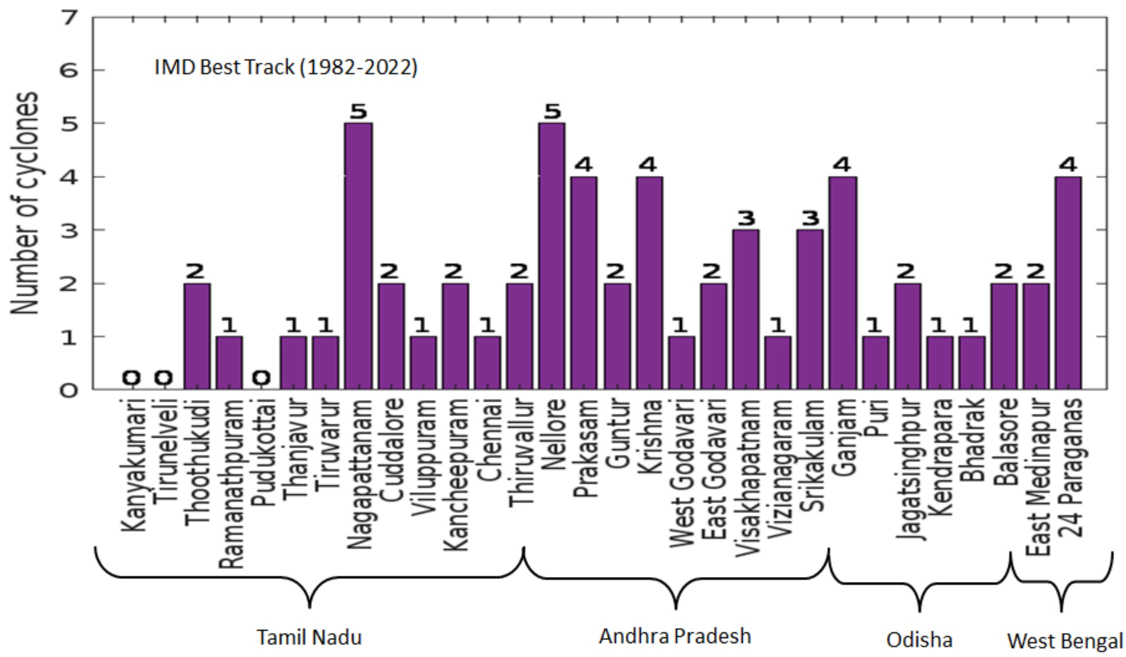

Fig 6.2. District-wise occurrence of landfalling TCs from 1982 to 2022.

6.2.3. Indian East Coast

The present study is focused only along the Indian east coast, which includes 30 coastal districts in four coastal states, as discussed above. The box in Fig. 6.3 indicates the domain of interest for creating a surge hazard map based on the different return periods and Climate Change Scenario (CCS) along the coastal regions where cyclones have historically made landfall. Shashank et al., (2024) classified the entire BoB region into three distinct coastal regions, assigning a coastal geometry coefficient ($b = 0$) to the northern region encompassing coasts of West Bengal and part of Bangladesh. The present study adopts the same assumption. However, we incorporated the measured distance between the coastline and the 40 m bathymetry contour (as shown in Fig. 6.3) line in estimating peak surge height using modified TCSPI. This replaces the 30 m bathymetry contour previously employed by Shashank et al., (2024).

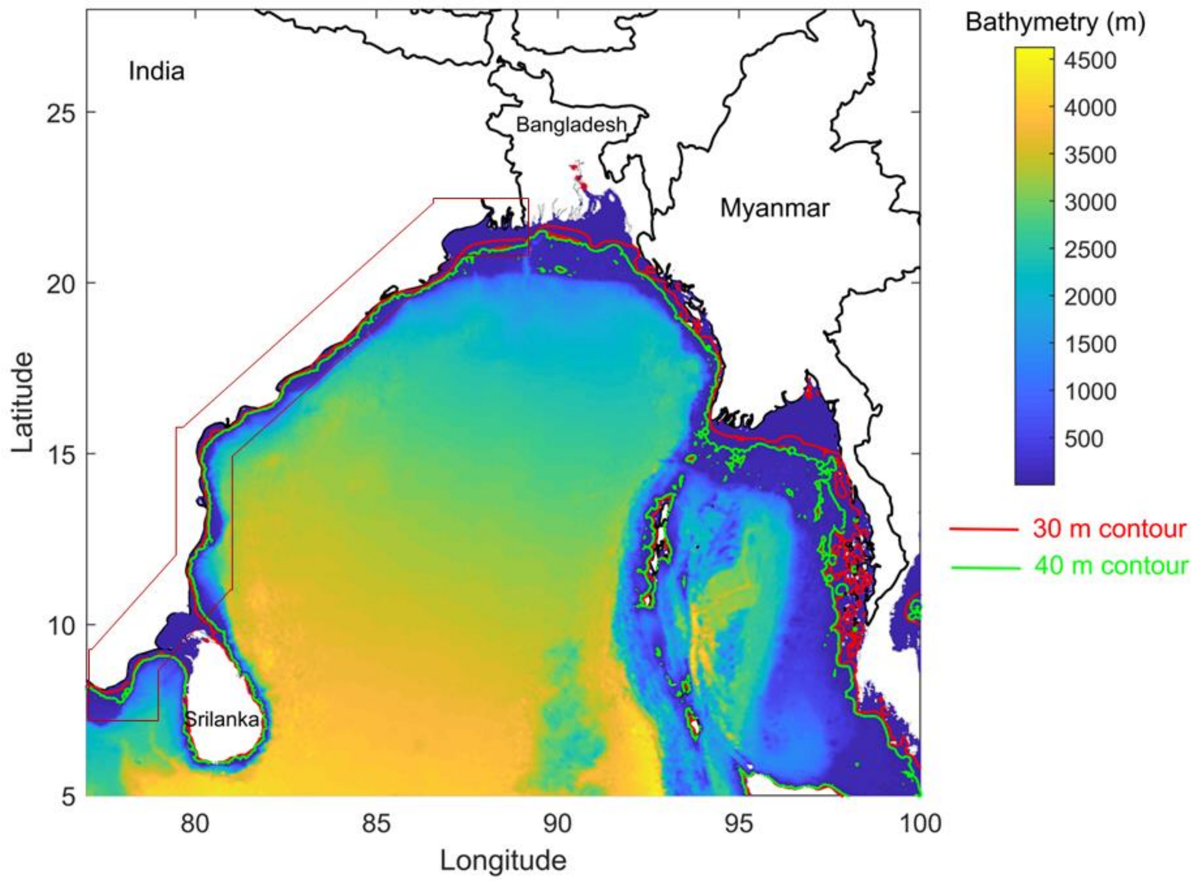

Fig 6.3. The color bar denotes the bathymetry depth of the BoB basin constructed using GEBCO data. The red-bordered box indicates the eastern coast of India (domain of interest). The red and green lines indicate 30 m and 40 m contour bathymetry, respectively.

6.2.4. Surge Data

The present study, the observed peak surge height from the IMD is collected to validate the TCSPI model, as referenced by Shashank et al., (2024).

6.2.5. Methodology

Initially, this research validated the estimated peak surge height accuracy utilizing the modified TCSPI Eqn (6.1). The comparison was made with the observed peak surge height from the IMD. The parameters such as V_{max}, S, L_{30}, and θ for the recent cyclones (2007-2022) at the landfall time frame were considered to estimate the peak surge height. This is due to the availability of more precise storm surge reported values in recent times (post-2007) (Shashank et al., 2024). In order to assess the predictive accuracy of the modified TCSPI Eqn, (6.1) the estimated peak surge height is validated and compared with the previous version of TCSPI proposed by Shashank et al., (2024). In the present study, the modified TCSPI Eqn. has been referred to as TCSPI-2, while the original TCSPI Eqn. is denoted as TCSPI-1. Further, the modified TCSPI Eqn. (TCSPI-2) will be incorporated to estimate the peak surge height for all the TCs IMD best track data from 1982-2022 that have made landfall along the Indian east coast. Thus, this research offers a comprehensive dataset of estimated peak surge heights for the TCs along the maritime states of the Indian east coast. A map depicting coastal hazards in districts are initially generated. This map is based on the district-wise maximum available peak surge height data derived using the modified TCSPI Eqn. near point of landfall for the historical TC data of 40 years (from 1982-2022). The following step generates a map depicting surge hazards to different coastal districts based on the track parameters' return period at the landfall time frame and CCS.

Literature shows that the wind data is modeled using Weibull distribution, especially when the aim is to characterize the annual resource (Hennessey, 1977, Kaminsky, 1977, Corotis et al., 1978, Weisser, 2003, Ettoumi et al., 2003). The study by Kumar and Philip, (2010) found that Weibull distribution fits better than Gumbel distribution for the extreme wind speeds estimation based on NCEP/NCAR reanalysis data for a 100-year return period. The details of the Weibull distribution are given by Palutikof et al., (1999). Therefore, the present study estimates the return period using Weibull distribution for 100 years based on 40 years of historical IMD best track TC parameters (wind speed and forward speed) collected at the landfall time frame for each of the maritime states (Fig. 6.4). The estimated return period values of wind speed and forward speed for 25 years, 50 years, and 100 years for each of the maritime states along Indian east coast using Weibull distribution is given in Table. 5.1.

The present study distinguishes the coastal area of Tamil Nadu into two parts, Northern and Southern, owing to their unique coastal features. The southern part of Tamil Nadu encompasses the coastal region from Kanyakumari district to Tiruvarur district, while the northern part extends from Nagapattinam district to Thiruvallur district. Analyzing historical data from 1982-2022 using IMD best track data reveals an increased vulnerability to TCs in the northern region of Tamil Nadu (14 observed TCs). Whereas, the southern part experienced only 4 TCs, which made landfall during the same period. However, the wind intensity of TCs making landfall along the northern Tamil Nadu coast tends to be higher compared to those TCs making landfall along the southern region of the Tamil Nadu coast. This is due to the geographical positioning of Sri Lanka, which influences the atmospheric flow in that region, resulting in fewer and less intense storms in the southern part of Tamil Nadu. Moreover, the northern part of Tamil Nadu features a narrower continental shelf, while the southern region has a broader continental shelf. If all TCs over the entire Tamil Nadu coast are considered for estimating the return period and positioned over the southern Tamil Nadu coast for estimating the peak surge height, the predicted peak surge values would be overstated and unrealistic. Thus, it is imperative to partition Tamil Nadu state into northern and southern regions to estimate the return periods of TC wind intensities. Thus, distinguishing India's entire eastern coast into five marine states.

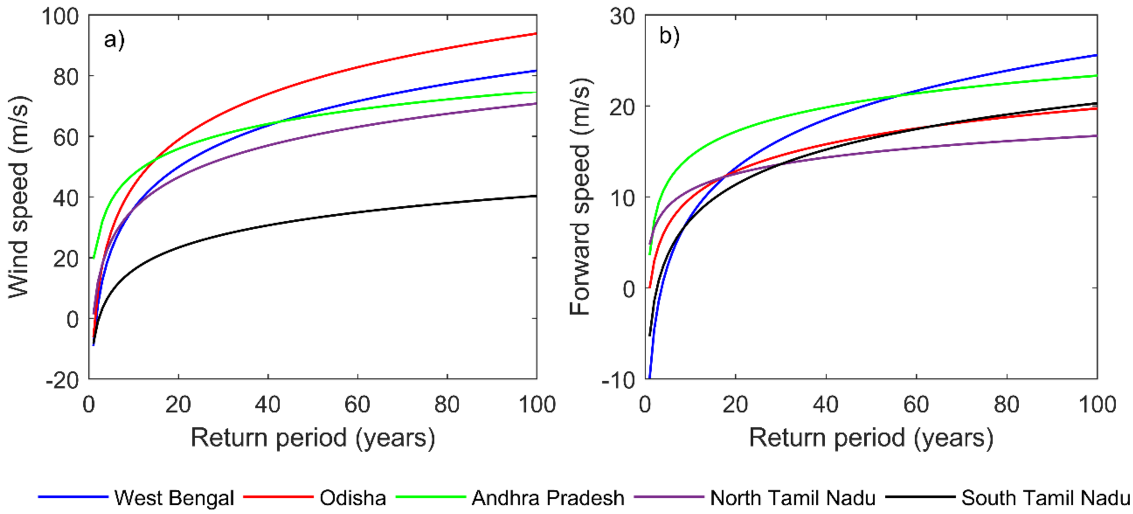

Fig 6.4. a) Estimated wind speed (y-axis) and b) forward speed of TC for return period up to 100 years (x-axis) using Weibull distribution.

Table 6.1. Estimated 25-year, 50-year, and 100-year return periods for wind speed and forward speed of TC for the five maritime states along the Indian east coast.

	West Bengal	Odisha	Andhra Pradesh	North Tamil Nadu	South Tamil Nadu

Return period	V_{max} (ms^{-1})	S (ms^{-1})	V_{max} (ms^{-1})	S (ms^{-1})	V_{max} (ms^{-1})	S (ms^{-1})	V_{max} (ms^{-1})	S (ms^{-1})	V_{max} (ms^{-1})	S (ms^{-1})
25 years	54.31	8.32	63.70	7.44	58.54	9.73	49.89	7.08	25.68	6.8
50 years	67.98	10.93	78.79	9.04	66.68	11.17	60.34	8.05	33.18	8.88
100 years	81.65	13.82	93.88	10.65	74.77	12.59	70.79	9.02	40.35	10.96

To demonstrate the methodology, the present study has initially considered the maritime state Andhra Pradesh as an example for a meanwhile (as shown in Fig. 6.5). Later, the same methodology was incorporated for all the maritime states along the Indian east coast. We assumed that cyclones make landfall every 30 km along the coast. However, the present study assumed that all the landfalling tracks are perpendicular to the coast, considering the worst-case scenario for the storm surges. This mean approach angle (θ) of TC is 90°. Therefore, the present study considered (θ / θ_0) = 1.5 in TCSPI Eqn. (1) for computing the peak surge height. The estimated return period values of wind speed at landfall will be considered to compute the peak surge height using TCSPI Eqn. (5.1) at every 30 km distance. Therefore, in the present study does not need to take into consideration synthetic tracks. It is noted that the return period values of the forward speed of TCs are overestimated and unrealistic (as shown in Fig. 6.4b). Moreover, it is observed that the estimated return period values (for 25 years, 50 years, and 100 years) of forward speed across different maritime states along the Indian east coast were found to be more than 1.5 times the climatological average of the TCs' forward speed (i.e., 3.77 ms^{-1}). Therefore, to ensure the worst-case scenarios, the present study also considers a maximum limit of (S/S_0) = 1.5 for the forward speed in TCSPI Eqn. (5.1) to predict the peak surge height for different return periods (25 years, 50 years, and 100 years) and to create the surge hazard map due to TCs.

It should be noted that, the present study does not even require computing the return period of pressure drop values. This is because TCSPI Eqn does not include pressure drop information to estimate peak surge height along the landfall locations of TCs. The dominance of wind stress over the inverse barometer effect in shallow waters for surge generation is the reason for this exclusion (Bertin, 2014, Kantha, 2013, Islam et al., 2021, Shashank et al., 2024). Thus, the TCSPI is entirely dependent on the estimated V_{max} values for different return periods for each of the maritime states and the bathymetry (L_{30}) information for computing peak surge height at every 30 km along the Indian East Coast. Furthermore, this study evaluates the impact of CCS on peak surge height predictions. Thus, incorporating a 10% increase in cyclonic wind speed based on recent IPCC (AR6) reports. This wind speed increase is considered under an extreme-case scenario for a one-time slice analysis in 2100.

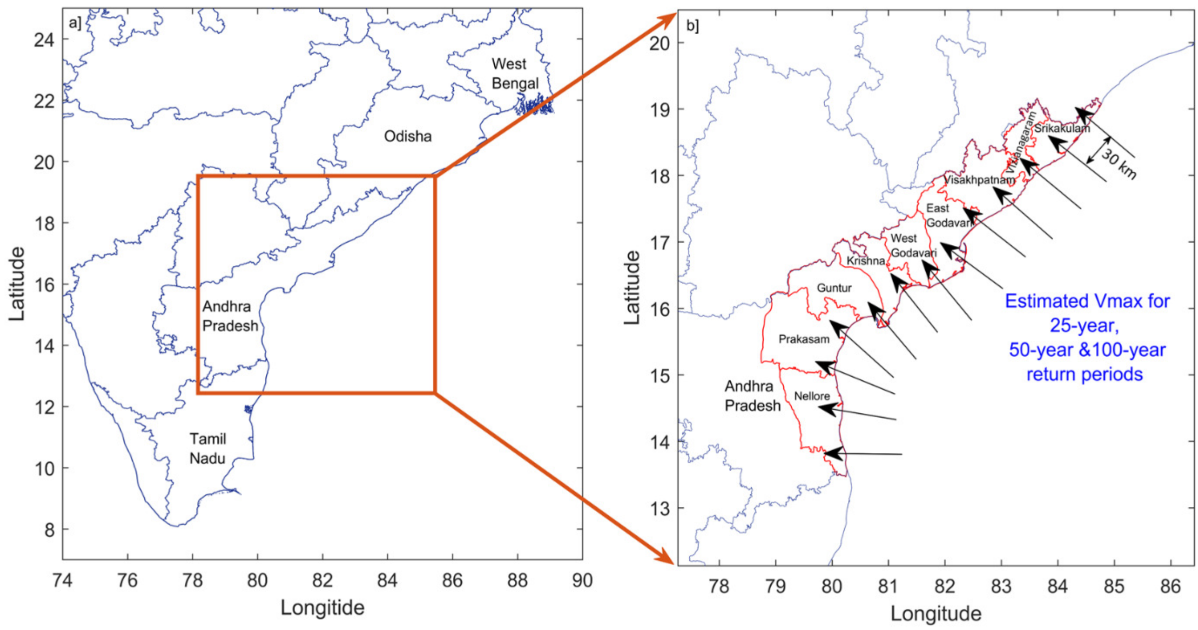

Fig 6.5. a) Coastal regions of Andhra Pradesh. b) depiction in an enlarged view of the state with a maritime area consisting of coastal districts. The arrows signify the assumption of TC making landfall perpendicular to the coast. The estimation of peak surge height is performed at about 30 km intervals along the coastline.

6.3.RESULTS AND DISCUSSION

6.3.1. Validation of modified TCSPI model

The present study examined the performance of the original TCSPI Eqn. published by Shashank et al., (2024), (i.e., TCSPI-1) and validated the modified TCSPI Eqn. (TCSPI-2) for the 14 TCs that have recently occurred and made landfall along the Indian east coast. It is noted that even the low-intensity landfalling TCs from 2001-2021 (less than or equal to the CS category) reported higher surge values by the IMD. Thus, TCSPI-1 is well suited for validating storm surges associated with historical TCs from 2001-2021. However, from 2007 onwards, it has been observed that IMD improved the accuracy of the prediction of storm surges by providing surge guidance (Shashank et al., 2024). Therefore, it is essential to bring slight modifications to the existing TCSPI-1 Eqn. to improve the performance of validating storm surges associated with the recently occurred TCs (2007-2021). Fig. 6.6a depicts the observed peak surge height by the IMD and estimated peak surge height by TCSPI-1 and TCSPI-2. It is evident that the peak surge height calculated by TCSPI-2 is closer to the IMD observation than that of TCSPI-1, particularly for lower surge height values (i.e., < 1 m). The performance of the TCSPI-1 and TCSPI-2 is presented through a scattered plot, as shown in Fig. 6.6b and Fig. 6.6c., respectively. The CC = 0.96 and RMSE = 35 cm indicate that TCSPI-2 outperformed TCSPI-1 (which has CC = 0.94 and RMSE = 42 cm). The scattered points are closer to the best-fit line in the case of TCSPI-2 (Fig. 7c) than TCSPI-1 (Fig. 7b). Thus, considering the minor modifications in TCSPI-2 helped improve the accuracy of prediction of peak surge height by up to 20% compared to TCSPI-1 for the recent cyclones.

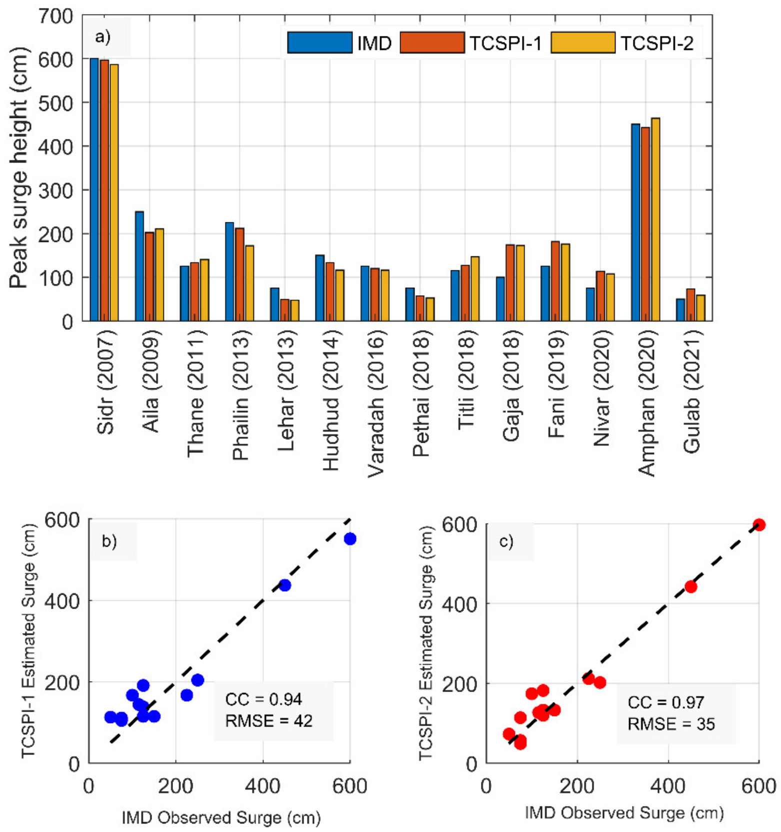

Fig 6.6. a) Bar plot depicting the observed and estimated peak surge height values. Scatter plot of observed and estimated peak storm surge heights at landfall locations using b) TCSPI-1 and c) TCSPI-2.

The values of the bathymetry parameters (i.e., L_{30}) and atmospheric parameters (i.e., V_{max}, S, and θ) for the recent TCs were taken into consideration for the validation as shown in Fig. 7a. The details are presented in Table. 2. TCSPI-1 and TCSPI-2 uses V_{max}, S, L_{30}, and θ to estimate the peak surge height. The climatological average reference constant $S_0 = 3.77$ ms^{-1} has been used in TCSPI-1 and TCSPI-2. The estimated TCSPI values and corresponding estimated peak surge heights are shown in Table 2. It is observed that TCSPI-1 estimates peak surge height values that are always greater than 1 m. Thus, TCSPI-1 is not suitable when considering low-intensity TCs making landfall along the coast with lower surge values (< 1 m). TCSPI-2 is well suited for low-intensity TCs with lower surge values (< 1 m). Apart from that, the selection of optimized L_* value according to Lagarias et al., (1998) within TCSPI-2 also contributes to improving the accuracy prediction of peak surge height values.

Table 6.2. The atmospheric bathymetry parameters and estimated peak surge height values using TCSPI-1, and TCSPI-2.

Cyclone	Year	Wind speed (V_{max}) (ms^{-1})	Forward speed (S) (ms^{-1})	L_{30} (km)	θ	IMD Observed surge (m)	TCSPI-1	TCSPI-2	Estimated surge (TCSPI-1)	Estimated surge (TCSPI-2)
GULAB	2021	23.15	7.87	8.69	83.15	0.5	0.25	0.26	1.13	0.58
AMPHAN	2020	46.30	5.92	97.98	Region-2	4.5	8.04	8.67	4.37	4.63
NIVAR	2020	33.44	2.22	8.92	116.57	0.75	0.16	0.12	1.09	1.07
FANI	2019	54.01	6.48	16.96	106.4	1.25	2.14	1.76	1.91	1.75
GAJA	2018	36.01	6.20	23.39	80.42	1	1.56	1.67	1.67	1.72
TITLI	2018	41.15	3.61	18.11	78.69	1.15	1.00	1.06	1.44	1.46
PETHAI	2018	23.15	5.28	8.46	101.31	0.75	0.20	0.15	1.11	0.52
VARADAH	2016	30.86	4.17	8.83	76.19	1.25	0.31	0.32	1.15	1.16
HUDHUD	2014	51.44	4.44	3.13	72.05	1.5	0.31	0.32	1.15	1.16
LEHAR	2013	15.43	3.61	7.02	78.42	0.75	0.05	0.05	1.05	0.46
PHAILIN	2013	59.16	5.92	7.69	90	2.25	1.54	1.66	1.67	1.72
THANE	2011	38.58	4.07	13.69	89.97	1.25	0.86	0.90	1.38	1.40
AILA	2009	28.29	5.18	85.56	Region-2	2.5	2.45	2.59	2.04	2.10
SIDR	2007	59.16	14.07	80.48	Region-2	6	10.78	11.63	5.51	5.86

6.3.2. Hazard map based on estimated peak surge heights from historical TCs (1982-2022)

Following the validation of TCSPI-2 for recent TCs (as discussed in section 5.3.1), the TCSPI-2 will be used to compute the peak surge height for all historical TCs (from 1982-2022) that made landfall along the Indian east coast. Table. 6.3 lists the historical TCs, their predicted peak surge height values (derived from TCSPI-2), and their corresponding landfall across the districts of each maritime state on the Indian east coast. It is observed that the estimated peak surge height associated with historical TCs along the Indian east coast ranges between 0.45 m and 4.6 m. Hence, each maritime district is classified into four categories: (a) less prone, (b) moderately prone, (c) highly prone, and (d) very high prone, based on the maximum estimated peak surge height (derived from TCSPI-2).

If the peak surge height falls between 0 and 1 m, the district is labeled as "less prone" to storm surges; the district is indicated by a green color on the map. When the peak surge height ranges from 1 m to 2 m, the district is classified as "moderately prone" to storm surges and represented by a blue color on the map. If the peak surge height ranges from 2 m to 3 m, it is classified as "highly prone" to storm surges and marked with a yellow color on the map. If the peak surge height exceeds 3 m, the district is classified as "very high prone" to storm surges, denoted by a red color on the map. Based on this, a map detailing coastal hazard levels across districts of maritime states along the Indian east coast is shown in Fig. 6.7. This map is constructed based on peak surge height (derived from TCSPI-2) associated with historical TCs. It can be observed from the map that the northern part of the east coast of India is prone to higher storm surges than the southern part. Specifically, the districts of West Bengal and northern Odisha states of the Indian east coast are more prone to storm surges, followed by the districts of Andhra Pradesh and Tamil Nadu state. It should be noted that this hazard map represents only the peak surge height associated with the historical TCs and does not represent the information-related frequency of TCs. The present study classified districts such as Kanyakumari and Tirunelveli as less prone to storm surges, where historically no TCs have made landfall (as shown in Fig. 6.2).

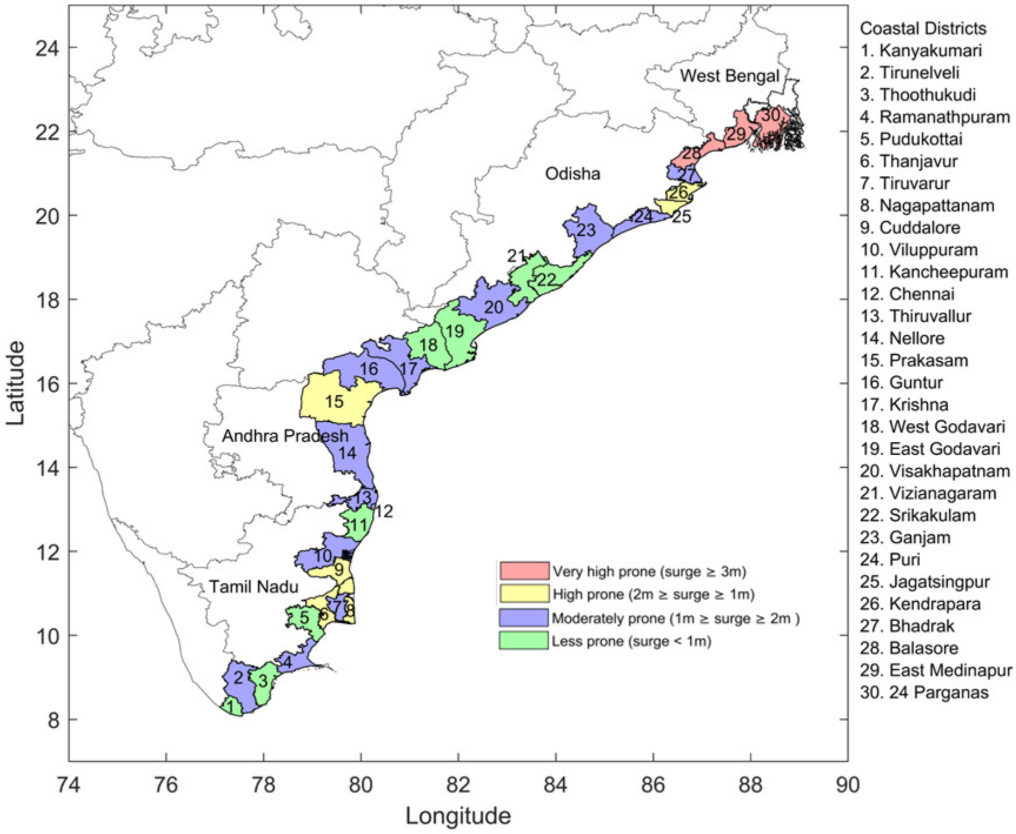

Fig 6.7. Surge hazard proneness map based on TCSPI-2 estimates of peak surge heights associated with historical TCs.

Table 6.3. List of storm surge predictions generated from TCSPI-2 associated with historical TCs, along with the district information where these TCs have made landfall.

	Cyclone	Year	Observed surge (m)	Estimated surge (m)	Landfall District
South Tamil Nadu	BUREVI'	2020	1.05	0.62	Ramanathpuram
	MADI	2013	No Data	0.50	Thanjavuru
	BOB-06	2000	No Data	0.80	Toothukodi
	BOB-07	1992	No Data	1.58	Toothukodi
North Tamil Nadu	MANDOUS	2022	0.6	0.56	Kancheepuram
	NIVAR	2020	0.75	1.07	Thiruvallur
	GAJA	2018	1	1.72	Nagapatanam
	NADA	2016	No Data	0.49	Nagapatanam
	VARDAH	2016	1.25	1.16	Chennai
	NILAM	2012	1.25	0.58	Kancheepuram
	THANE	2011	1.25	1.40	Cuddalore

	JAL	2010	1.5	0.52	Chennai
	NISHA	2008	1	0.52	Nagapatanam
	FANOOS	2005	1.5	0.49	Nagapatanam
	BOB-09	1996	1.5	0.63	Kancheepuram
	BOB-03	1994	No Data	1.22	Chennai
	BOB-01	1993	3.5	1.67	Nagapatanam
	BOB-08	1991	No Data	0.57	Cuddalore
	BOB-06	1984	No Data	2.82	Nagapatanam
Andhra Pradesh	ASANI	2022	0.5	1.05	Krishna
	GULAB	2021	0.5	0.73	Srikakulam
	TITLI	2018	1.15	1.46	Srikakulam
	PETHAI	2018	0.75	0.52	East Godavari
	HUDHUD	2014	1.5	1.16	Visakhapatanm
	HELEN	2013	1.25	1.11	Krishna
	LEHAR	2013	0.75	0.46	Krishna
	LAILA	2010	1.5	1.18	Guntur
	KHAIMUK	2008	No Data	0.49	Praksam
	OGNI	2006	3.5	0.48	Praksam
	PYARR	2005	No Data	0.54	Srikakulam
	BOB-07	2003	No Data	1.24	Krishna
	BOB-05	2001	1.5	0.57	Nellore
	BOB-08	1998	No Data	1.17	Visakhapatanm
	BOB-02	1996	No Data	0.52	Krishna
	BOB-08	1996	No Data	1.17	East Godavari
	BOB-01	1990	4.25	1.18	Guntur
	BOB-05	1989	No Data	0.70	Srikakulam
	BOB-08	1989	No Data	2.87	Praksam
	BOB-06	1987	No Data	0.68	Praksam
	BOB-07	1987	No Data	1.28	Nellore
	BOB-08	1987	No Data	0.65	Krishna
	BOB-09	1985	No Data	0.67	Visakhapatanm
	BOB-13	1985	No Data	0.51	Nellore
	BOB-05	1984	No Data	1.06	Nellore
	BOB-09	1982	No Data	0.44	East Godavari
	BOB-10	1982	No Data	1.10	Nellore
Odisha	YAAS	2021	3.45	2.06	Balasore
	FANI	2019	1.25	1.75	Puri
	DAYE	2018	No Data	0.52	Ganjam
	PHAILIN	2013	2.25	1.72	Ganjam
	BOB-06	1999	No Data	1.10	Ganjam
	BOB-07	1999	5.5	2.88	Jagatsinghpur
	BOB-07	1995	1.5	1.39	Ganjam
	BOB-06	1985	No Data	0.75	Jagatsinghpur
	BOB-10	1985	No Data	0.84	Balasore
	BOB-04	1984	No Data	1.67	Bhadrak
	BOB-02	1982	No Data	2.39	Kendrapara
West Bengal	AMPHAN	2020	4.5	4.63	East Medinapur
	BULBUL	2019	2	1.84	South Paraganas
	AILA	2009	2.5	2.10	East Medinapur
	BOB-04	2002	No Data	2.27	South Paraganas
	BOB-04	2000	1.65	0.87	South Paraganas
	BOB-01	1989	No Data	4.46	East Medinapur

	BOB-08	1988	No Data	3.438	South Paraganas

6.3.3. Surge hazard map based on return period and CCS estimations

To analyze the variation in peak surge heights across different scenarios, the average peak surge height for each district is calculated for all maritime states along the east coast of India. Fig. 6.8a illustrates the average peak surge heights across districts in Tamil Nadu for various scenarios across different return periods. The values displayed for each bar in the plot represent the peak surge heights associated for various return periods along with or without CSS. The results derived from TCSPI-2 indicates that out of all scenarios, the districts of Ramanathapuram and Pudukottai are observed to experience significant impact on storm surges reaching approximately 2.5 m for a 25-year return period. The primary cause of increased storm surges in this region is majorly due to the characteristics of the local coastal geometry and bathymetry. The calculations of peak surge heights for the 50- and 100-year return periods exhibit a comparable trend, with higher surge levels, with a maximum peak surge height of about 4.7 m for these districts in the CCS. In the Kanyakumari district, a minimum peak surge height of approximately 1.3 m is observed under all 25-year return period scenarios.

Similarly, Fig. 6.8b shows the average peak surge heights for each Andhra Pradesh district. It appears that the southern districts are more affected than the northern districts. The peak surge height ranges from 1.5 to 5.7 m. Prakasam, Guntur, and Krishna are the districts most likely to see higher peak surge heights irrespective return periods and CCS. These districts are mainly located in the river delta region, where the continental shelf width is higher. Similarly, Visakhapatnam and Vizianagaram districts are the least affected in terms of risk as they are situated along the steeper continental slope region. However, the frequency of TCs landfall along this region is observed to be higher. Therefore, the structural damage risk due to wind from TCs is higher in this region.

Maximum peak surge heights along the Indian east coast are more likely to occur in Odisha and West Bengal as compared to the maritime states of Andhra Pradesh and Tamil Nadu (Fig. 6.8c). The TCSPI-2 estimate of peak surge height for the Odisha state shows that peak surge heights along the coast of the northern region are higher than those in the southern region. The geometry of the shoreline and the near-shore topography may be the reason for this. Considering both the 100-year return period and the CCS, the maximum peak surge height is approximately 9.4 m and 9.1 m, respectively, in the Bhadrak and Balasore districts.

The coastal districts in West Bengal that regularly experience cyclonic storms are Medinipur and 24 Parganas. The surge levels are typically high in this vicinity due to its delta nature, characterized by shallow bathymetry and sediment deposits stretching approximately 200 km south from the shoreline. The peak surge height for a 25-year return period is observed to be relatively low, around 4.5 m, compared to the surge heights for the 50- and 100-year return periods. Additionally, the East Medinipur district consistently experiences a maximum peak surge height of about 9.8 m in all scenarios. The increased surface wind stress resulting from CCS acting on the ocean surface for varying return periods is observed as increasing peak surge height by approximately 10 % to 18% across different districts. The outcomes obtained from TCSPI-2 align well with those from the comprehensive physics-based hydrodynamic model (ADCIRC) as given in Rao et al., (2019) for various return durations and CCS.

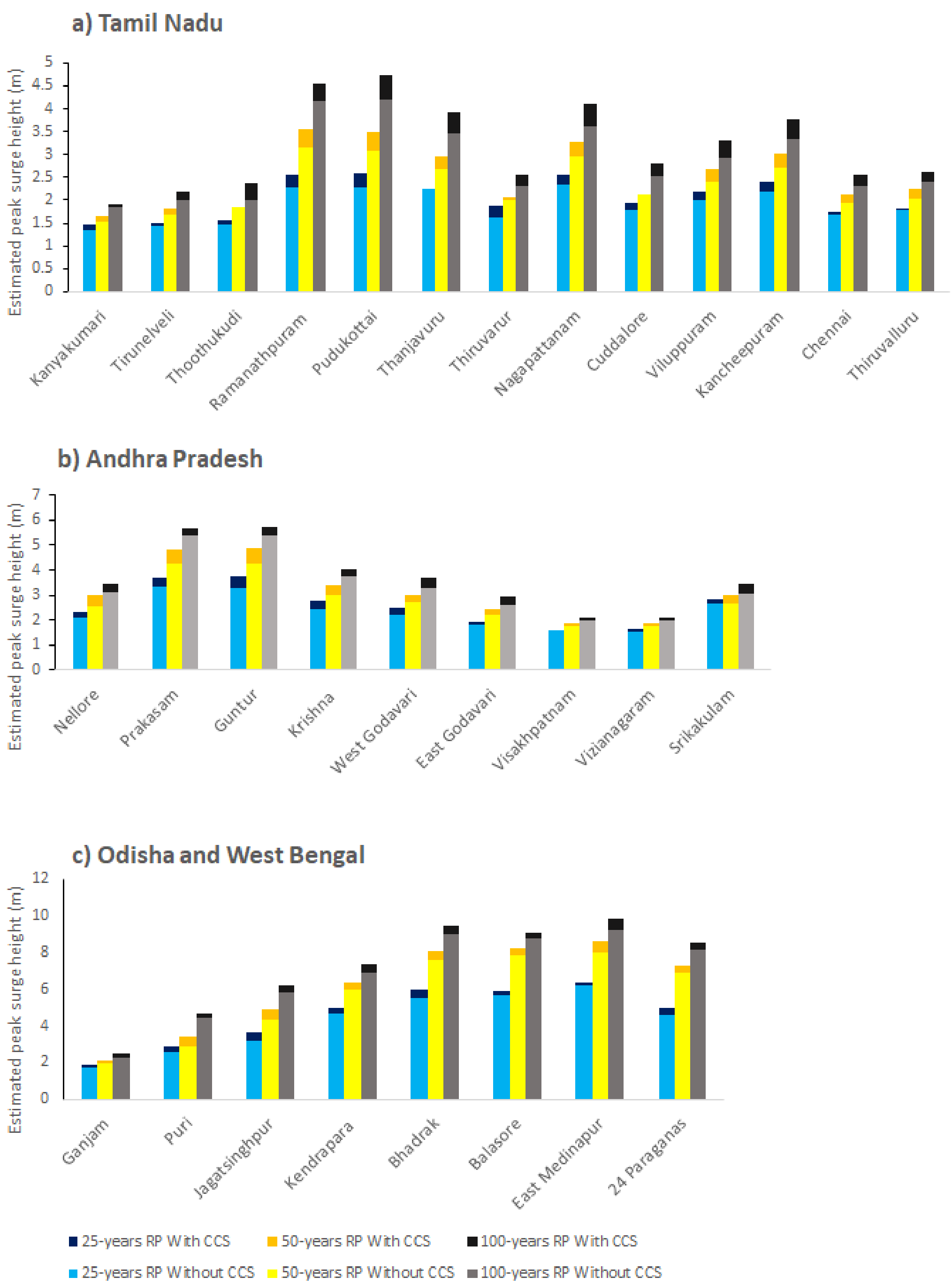

Fig. 6.8. District-wise averaged peak surge height values for coastal states of a) Tamil Nadu, b) Andhra Pradesh, c) Odisha and West Bengal along the Indian east coast.

The map derived from TCSPI-2 peak surge height values, based on estimated wind speeds for 25, 50, and 100-year return periods with CCS is shown in Fig. 6.9. The severity is classified based on peak surge height values as outlined in Fig. 6.8. The surge hazard map is developed considering the extreme conditions. The comparison between the surge hazard map (Fig. 6.9a) of 25-year return period (with CCS) and the hazard proneness map derived from historical TCs' peak surge heights (Fig. 6.7) reveals that coastal districts, initially classified as having low proneness, shifted to the moderately prone and high prone category. Comparing the surge hazard maps for different return periods (25 years, 50 years, and 100 years with CCS), reveals, a similar trend of shifting from lower to higher prone categories to storm surges over increasing return periods across the different districts of coastal states.

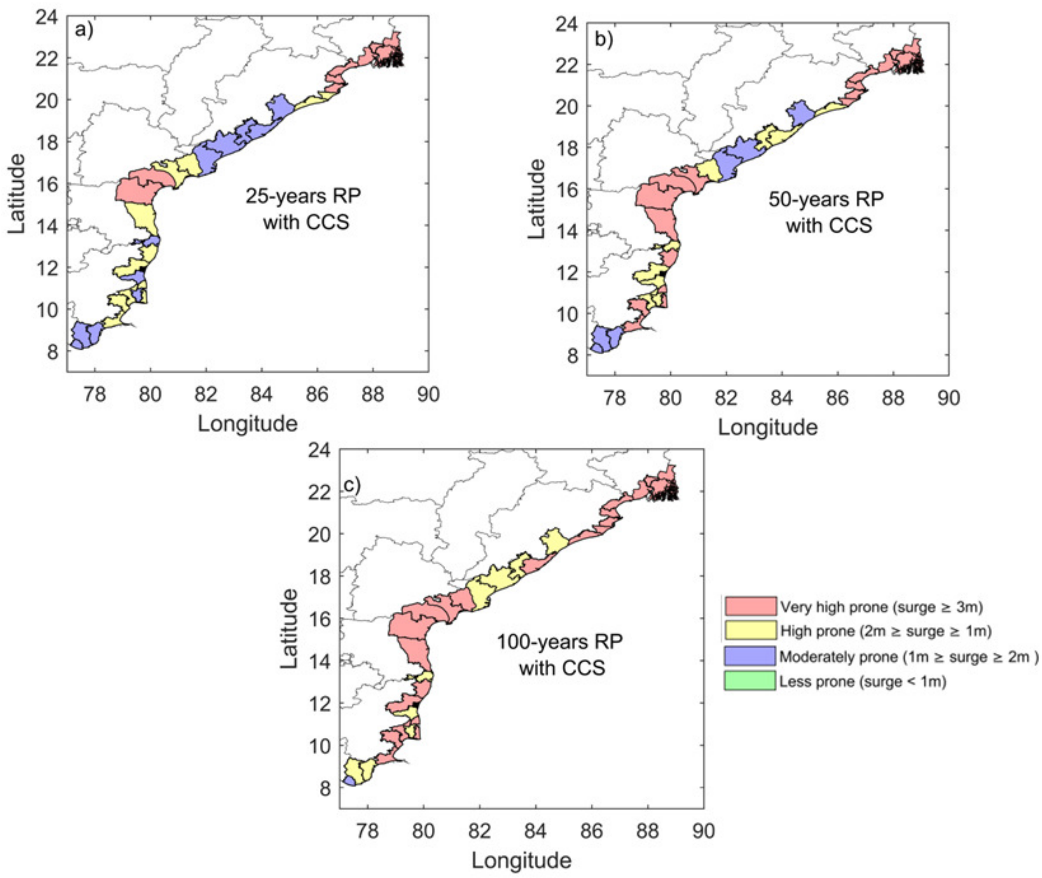

Fig 6.9. Surge hazard proneness map based on TCSPI-2 estimates of peak surge heights based on estimated wind speeds for a) 25 years, b) 50 years, and c) 100-year return periods with CCS.

Fig. 6.10 depicts the number of districts (y-axis) affected by various hazard proneness categories (i.e., Less, Moderate, High, and Very High) for historical and different return periods (with and without CCS) based on peak surge heights. The number of districts with lower proneness category is only identified on the surge hazard proneness map derived from historical TC peak surge height estimates. It can be noticed that with increase in return periods from 25 years to 100 years, the moderate prone category leads to decrease in the number of districts affected. Conversely, for very high prone category an increasing trend in the number of districts affected can be seen. In consideration of CCS, it is observed that no change in the number of affected district proneness categories for a 100-year return period. However, consideration of CCS depicts few districts have shifted from a lower to a higher prone category for 25 and 50 years return period. Overall, it is noted that 19 out of 30 coastal districts along the eastern coast of India exhibits a high prone to storm surges for a 100-year return period with CCS.

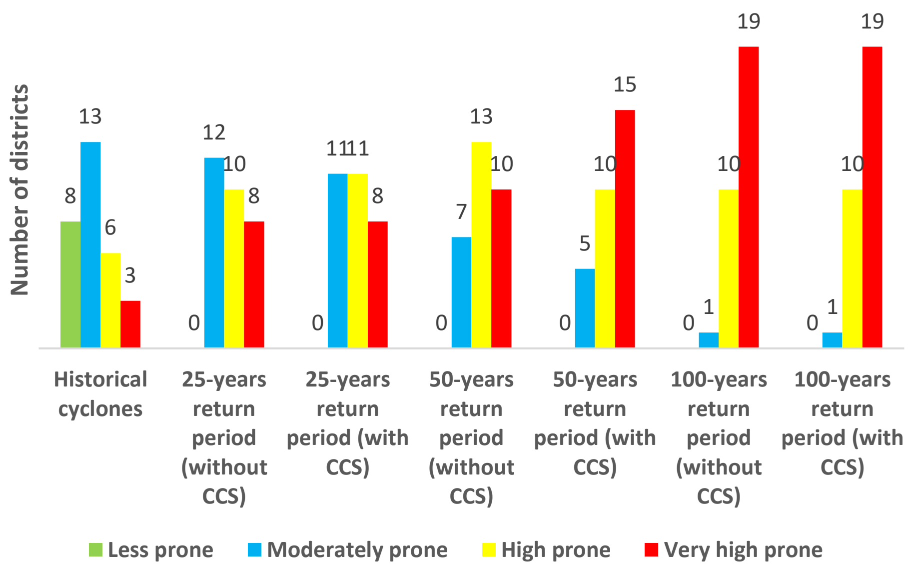

Fig 6.10. The number of districts (y-axis) for historical and different (25, 50, and 100 years) return periods (with and without CCS) estimated peak surge heights that are affected by different hazard proneness categories (i.e., Less, Moderate, High, and Very High).

6.4.SURGE CALCULATOR WEBSITE

A guide for users to operate the surge calculator [https://iitmaisurge.in/] to estimate the peak surge height value for a cyclone test case Hudhud (2014).

- Point A (83.4E, 17.6N) marks the final recorded coordinates of Cyclone Hudhud over the ocean, just before landfall. In contrast, point B (83E, 17.8N) indicates the first recorded location of the cyclone over land immediately after landfall, as shown in Fig. 6.11a. The time interval is typically set to 3 hours, as the IMD provides coordinate data every three hours. We input the Vmax (knots) value of Cyclone Hudhud, which is recorded at Point A to estimate the peak surge height.

- The map will be displayed within a few seconds, showing the shoreline, Point A, Point B, L40, and the intersection points as shown in Fig. 6.11b. Select the suitable intersection point from the drop-down list and press the submit button to estimate the peak surge height. The estimated peak surge height for Cyclone Hudhud using the improved TCSPI model is 1.34 m (Fig, 6.11c), which is in good agreement with the IMD's reported peak surge height of 1.5 m.

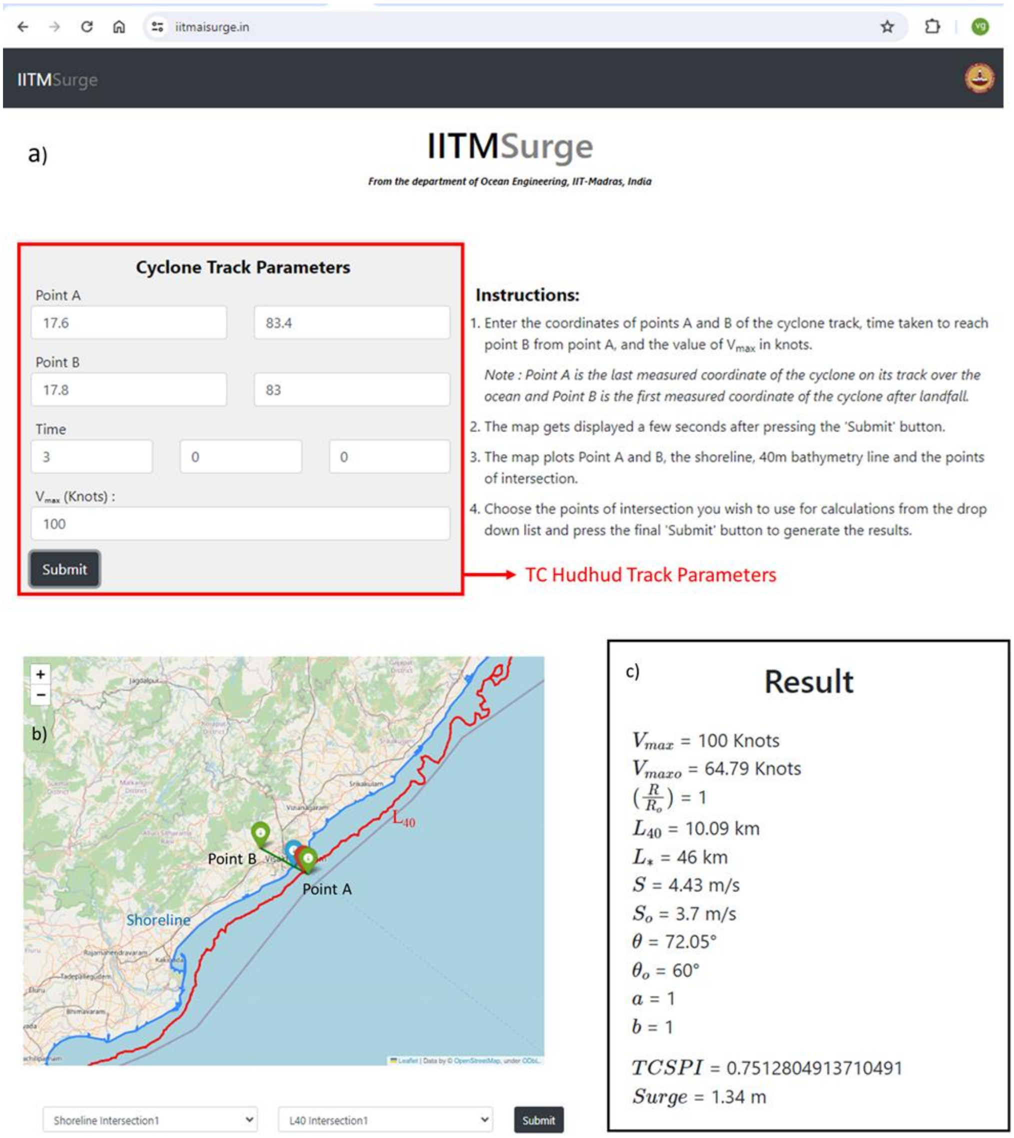

Fig 6.11. a) Homepage of surge calculator where track parameters can be input b) A map displaying Point A and B, the shoreline, 40m bathymetry line, and the points of intersection c) Values for estimated TCSPIs and peak surge heights are displayed.

6.5.SUMMARY

The present study proposes an enhancement of the TCSPI model with slight modifications to improve its accuracy and utility. A detailed methodology is provided to estimate return periods using probabilistic distribution methods, incorporating climate change scenarios to assess future worst-case hazards. The study includes a thorough evaluation, validation, and comparison of the existing and newly modified TCSPI models. The enhanced TCSPI is then applied to develop surge hazard maps for the Indian east coast, considering historical cyclones, various return periods, and the impacts of climate change. Additionally, the hazard proneness of each maritime state is comprehensively analyzed and discussed. A concise tutorial is provided on using the surge calculator website to estimate a cyclone's peak surge height, accompanied by an illustrative example.

CHAPTER 7

SUMMARY AND CONCLUSIONS

7.1. GENERAL

Studying tropical storms and their effect on water levels (storm surges), wind waves, inundation, and morphodynamics—is vital for safeguarding coastal communities and ecosystems. These phenomena profoundly impact coastal regions, leading to catastrophic flooding, erosion, and structural damage. By understanding how these forces interact and influence each other, The present study concentrated on both statistical and numerical modeling, enhancing predictive model capabilities and facilitating more effective and accurate forecasting and early warning systems. This knowledge is essential for designing resilient infrastructure, planning evacuation routes, and implementing sustainable coastal management practices. This chapter presents a summary of the entire research work and the comprehensive conclusions drawn from the study. The potential scope for future investigations in line with the present study is also discussed.

7.2. SUMMARY

- The present study shows descriptions and equations for various parametric and background models. A coupled ADCIRC+SWAN model setup for the BoB domain is presented. The study evaluates SLOSH, RV, WL06, HL80, and GAHM parametric models using 10 historical cyclonic events in the BoB. Also, the assessment of wind fields from ECMWF Reanalysis and WRF models is performed. The best-performing parametric and background wind models are used within the blending approach. Sensitivity analyses for storm surge, wind wave, and inundation by different wind models are thoroughly discussed.
- The study provides a detailed description of individual hydrodynamic (TELEMAC-2D), wave (TOMAWAC), and morphodynamic (GAIA) models, along with the coupling framework. It introduces a modified cyclone parametric wind model for

the BoB. The validation of models for storm surges, wind waves, and morphodynamic bed evolution is extensively covered. Additionally, it evaluates various total bed load transport formulations for predicting morphodynamic bed changes due to storm-induced currents and waves, using the Brier skill score.

- A statistical-based index model is introduced, presenting the development of TCSPI suited to the BoB. Evaluation of TCSPI using IMD and JTWC datasets are performed. Investigation of the influence of track parameters, bathymetry, and geometrical coefficients on peak surge height are presented. TCSPI was regressed against ADCIRC model predictions to understand the correlation pattern in predicting peak surge height. Verification was conducted to evaluate TCSPI's predictive capability. Various regression-based machine learning models were developed and compared to identify the best fit for the BoB, given the challenges of small sample sizes, using a uniform comparison method presented to assess the performance of TCSPI, machine learning, and ADCIRC models in predicting peak surge height.
- The present study also introduced enhancd TCSPI model with incorporation of slight modifications. The study thoroughly evaluates and compares the existing and modified TCSPI models. The study demonstrated the application of the enhanced TCSPI model to generate surge hazard maps for the Indian East Coast with a simple and effective methodology, taking into account historical cyclones, return periods, and the effects of climate change scenarios. Additionally, the hazard proneness of each maritime state is analyzed. A tutorial on using the surge calculator website, with an example, is also provided.

7.3. CONCLUSIONS

7.3.1. Modeling of Cyclonic Wind Field

The study highlights that the accuracy of storm surge, wind wave, and inundation projections depends on the spatial distribution of the disturbance brought on by the cyclonic pressure system as well as the track and intensity of the cyclone. To our knowledge, particularly in the BoB region, Due to a lack of thorough evaluation of wind models, there was no agreement on the choice of parametric and background wind models. Five different parametric models, namely, SLOSH, RV, WL06, HL80, and

GAHM, are investigated. The asymmetric modifications are employed for SLOSH, RV, WL06, and HL80 parametric wind models. To assess these model's effectiveness in the BoB region, the historical ten cyclones that occurred in the past ten years were analyzed. The analysis reveals that the GAHM performs better in this region based on the nearest measurement available for these cyclones. A similar analysis can be performed based on the past cyclones in the Arabian sea and other tropical regions to choose the best-performing models. The various forms and attributes of coastal features, including bays, estuaries, width, and the slope of the continental shelf along the coasts of various tropical regions, affect how well the model performs.

Further, an assessment was carried out during a particular cyclonic event TC Varadah for the wind field's spatial distribution and radial profile. The analysis shows that the GAHM's composite radial wind profiles compare better with JTWC isotachs. The rest of the models (based on the single-isotach) underestimate the modeled winds. To further strengthen the analysis, parametric models are compared with the measured wind near the cyclone track of TC Varadah. It reveals that GAHM performs better.

WRF seems to be promising when analyzing the global wind models compared to ECWMF data for the BoB region. Hence, WRF can be considered the best suitable background wind field. In recent years, blending parametric and global models has been common to take advantage of their merits in predicting inner and outer regions. Thus, based on the above analysis, the blending of GAHM and WRF was attempted in the present study, showing the promising approach for the BoB region.

It is widely recognized that variations in atmospheric wind forcing play a crucial role in determining the accuracy of predictions related to significant wave heights, surges, and flooding events. The analysis reveals that an error of more than 20% in estimating peak wind speed near the storm center can lead to an error greater than 35% in signification wave height predictions and depends upon the wind model in BoB, India. Torres et al., (2019) reported a similar observation for the US coasts. In comparison to conventional parametric TC wind models, a wind model that has ability to reproduce both the background wind (located far from the storm centre) and the cyclone structure (located near the storm centre) may yield more accurate results over the entire domain and over the storm's duration.

The inter-comparisons with different models reveal that the GAHM and blended wind fields better predict surge height. Compared to other models, the blended model shows a smooth surge extending on the right and left-hand side of the landfall, up to 200 km. Thus, better atmospheric forcing models for the inner and outer cores of the cyclone are required. Regarding the inundation extend, the ECWMF shows no inundation at some stretches. The research highlights the importance of accounting for wave-current interactions when calculating storm surge levels and the extent of inundation. The coupled ADCIRC+SWAN performed significantly better, indicating a contribution of 13.68% up to a 24% increase in surge heights at the peak surge. Morphodynamic Response To Cyclone Events.

7.3.2. Morphodynamic Response to The Cyclone Events

In the study, a coupled hydrodynamic (TELEMAC-2D) – wave (TOMAWAC) – morphodynamic (GAIA) model has been successfully established to predict water levels, wind waves, and morphodynamic changes during cyclonic events in the BoB. The cyclonic wind is the primary force required to precisely predict the storm surges, wind waves, and morphodynamic bed evolution caused by storms. Hence, accurately representing cyclonic wind fields is essential. Therefore, the present study introduced a GAHM+RV model, a modified version of the parametric wind model tailored for the BoB. Based on observed wind data for historical storms in the BoB, this modified GAHM+RV wind model is validated and compared to other modified parametric wind formulations proposed for the BoB by Murty et al., (2016) model and Pandey and Rao, (2018) model. The combined strengths of the GAHM and RV models, which represent the wind field near the cyclone center ($r \leq R\_max$) and away from the cyclone center ($r > R\_max$) respectively, show better accuracy compared to the modified wind field models proposed by Pandey and Rao (2018), and Murty et al., (2016). Therefore, the modified GAHM+RV wind model is utilized to predict morphodynamic bed evolution for cyclonic events Nivar (2020), Hudhud (2014), Vardah (2016).

Further, the validation of simulated storm surges and significant wave heights using the internally coupled model framework for TC Hudhud (2014) and TC Vardah (2016) was conducted against in-situ observations. The results show that the modeled storm-induced water levels and significant wave heights align well with the observed wave heights. This indicates that the utilized coupled framework setup is reliable for estimating storm surges and wind waves in the BoB.

Further, eight simulations were performed using various sediment transport formulations within the coupled framework to examine the impact of storm-induced currents and current-wave interactions on bed evolution for the TC Nivar (2020). Upon evaluation, the BSS metric indicates that the EH formulation outperforms the MPM, EB, and VR formulations for predicting morphodynamic bed evolution when considering storm-induced currents. This demonstrates EH formulation’s capability to manage the region's dynamic hydrodynamic conditions, appropriately handle sediment characteristics, its empirical relevance to similar environments, practical application, and proven predictive accuracy. When predicting morphodynamic bed evolution with storm-induced current-wave interaction, the BJ formulation performs best, followed by the SVR formulation. Meanwhile, BL and DW formulations perform poorly. This indicates that BJ and SVR formulas provide a more comprehensive approach to the complex interactions of waves and currents during storm conditions. Whereas BL and DW formulations offer simplicity but may fail to handle the full range of interactions necessary for accurate predictions in the coastal environment of BoB.

Furthermore, the study assessed the suitability of the EH and BJ formulations for other storm events along the open coast of the BoB, given their effective prediction of morphodynamic bed evolution during Cyclone Nivar (2020). To do this, TC Hudhud (2014) and Vardah (2016) were selected to simulate the morphodynamic bed evolution caused by these storms. Results show that the same coupled framework effectively predicts the morphodynamic bed evolution caused by the storm-induced currents and wave-current interaction during Hudhud (2014) and Varadah (2016). Further, the results indicate that the inclusion of waves with currents increases the magnitude of predicted morphological bed evolution at landfall for TC Hudhud (2014) and TC Vardah (2016). This is nearly consistent with the findings of TC Nivar (2020). The results also show that including the effects of waves along with currents has improved the predictive capability of the coupled model framework.

7.3.3. Statistical Modeling of Storm Surge

The present study demonstrated the new development of a simplified regression-based approach for a tropical cyclone surge potential index (TCSPI) that provides an instantaneous overall estimate of peak surge potential associated with TCs considering the underlying physical process involved in the storm surge for the entire BoB coast. The proposed TCSPI depends upon wind speed, storm size, forward speed, bathymetry, and coastal geometry. A fundamental difference between the TCSPI and existing indices that are applied elsewhere is that it considers approach angle and associated coastal geometry in potential peak surge height estimates. When TCSPI is applied retrospectively, it has about ~84% and ~90% of the observed variance for JTWC and IMD best track parameters, respectively, using the N1 dataset. This indicates that the estimated peak surge height using the linear empirical model for N1 datasets from the IMD best track parameters is close to the recorded peak surge height with an RMSE of 37 cm. This error is smaller compared to the ADCIRC-derived peak surge height error (i.e., 65 cm) with the observation for the N1 dataset. Therefore, the present study recommends the empirically derived Eqn (4.6) be used to estimate the potential peak surge height for an unknown or future cyclone case (For example: let's assume a cyclone occurring in 2022 whose track parameters are known). Thus, TCSPI can serves as a complementary tool to computationally intensive TC surge models, aiding in the prediction of potential peak surge heights.

TCSPI and observed peak surge height have 54% and 57% variance for JTWC and IMD best track parameters, respectively, using the N2 dataset. The poor performance of the proposed TCSPI is mainly due to the poor quality of reported peak surge data for the period 1990–2008 from various sources (IMD, BMD, MDMH, and literature). The accuracy of the TCSPI depends on the quality of the parameters as well as the reported surge. Therefore, the present study does not recommend any of the empirically derived equations from N2 sample dataset for estimating potential peak surge height. Further, the simulations are carried out with the ADCIRC to understand the performance of TCPSI. By using IMD best track parameter for the N3 dataset, 92% variance was observed. This indicates that the simplified physics-based TCSPI closely correlates the pattern with peak surge height derived from hydrodynamic model simulations. However, a hydrodynamic model (i.e., ADCIRC model) inherently proved to have some error with the observation, especially when considering a large number of cyclone events (Salcines et al., 2019). This can possibly compound TCSPI's observation-based errors even more. Therefore, the present does not recommend the empirically derived equations from the N3 sample dataset for estimating potential peak surge height.

Furthermore, the study reveals the characteristic coastal geometry for the forward speed can be taken as a constant value (a = 1) in the proposed TCSPI for the coasts of the entire BoB. Whereas the approach angle in the coastal geometry (b) depends upon the region. For the semi-enclosed coast (Region 2), the recommended value is 0, and open coast (Region 1 and Region 3) is 1. In the present study, we have noticed for the semi-enclosed/estuary coast, the increase in forward speed increases the peak surge height. This is in contrast to the existing study in other coasts, wherein it is reported that the increase in forward speed reduces the peak surge along the semi-enclosed/estuary coasts (Peng et al., 2004; Islam and Takagi, 2020; Islam et al., 2021)

Moreover, the present study incorporated the five most renowned ML-based models LR, TR, SVM, EnTR, and GPR which are suitable for smaller sample sizes. We used N1, N2, and N3 datasets for learning and prediction. The results indicate LR model with stepwise fitting parameters performs better as compared to the rest of the ML models. The estimated peak surge by the LR model with stepwise fitting parameter is ~88%, ~57%, and ~92% of variance for N1, N2, and N3 test datasets, respectively. This illustrates the accuracy of the ML model. Additionally, it is proportionate to the sample dataset size. Machine learning algorithms are less effective and precise when the dataset size is smaller (Kokol et al., 2022). In comparison with the LR model (stepwise parameters), the regression-based TCSPI performs better even with a smaller sample size.

The verification score indicates both TCSPI and LR models (stepwise parameters) predict with better accuracy for both smaller and higher than the peak surge threshold value considering N1, N2, and N3 datasets. However, the accuracy associated with smaller peak surge threshold values is slightly better than higher peak surge threshold value. Further, considering the N1 dataset, for the 9 randomly selected notable cyclone events, in the recent 20 years, the prediction by TCSPI is better than the ML and ADCIRC.

7.3.4. Storm Surge Hazard Map

This study presents a simplified and computationally efficient alternative to traditional methods for generating surge hazard maps. Eliminating the need for synthetic track generation and cyclone pressure drop estimations offers a simpler and more practical solution for creating surge hazard maps. The peak surge heights are estimated in response to the historical TCs, various return periods, and CCS for the coastal states of the Indian east coast. For this, a modified TCSPI-2 model has been introduced and adopted for calculating the potential peak surge height. These findings underscore the importance of timely generated maps in enhancing planning, evacuation strategies, and infrastructure resilience, which can significantly mitigate damage and save lives. This study also introduces the IITM Surge Index website (as discussed in Section 6.4), built on the enhanced TCSPI-2 model, which provides a freely accessible platform for estimating peak surge heights. Estimating peak surge using the proposed method is valuable for creating surge hazard maps using enhanced TCSPI-2. However, incorporating coastal inundation caused by storm surges would benefit coastal communities. As a future potential implication, developing an empirical model to predict coastal inundation extent based on peak surge heights predicted by TCSPI-2 for various return periods, along with climate change projections for the Indian east coast, could strengthen disaster preparedness and enhance resilience in vulnerable coastal areas.

This study estimates peak storm surge heights along the Indian east coast in response to historical TCs, various return periods, and climate change scenarios using a modified TCSPI-2 model. The model improves prediction accuracy by 25% compared to TCSPI-1. The peak surge heights were calculated at 30 km intervals along the coast, incorporating an average of 9% wind intensity increase based on IPCC scenarios. For a 100-year return period, peak surges could reach 10 m in the northern regions of the Indian east coast, with a 10% to 18% increase due to climate change. Nineteen out of thirty coastal districts of maritime states of the Indian east coast are classified as highly vulnerable to storm surges. This study provides detailed projections of surge heights, identifying the most affected areas under present and future conditions.

7.4. KEY CONTRIBUTION FROM THIS THESIS

- Improvement of Wind Field Forecasting: Proposed an improved blending technique for accurately forecasting cyclonic wind fields, along with a sensitivity analysis of storm surges, wind waves, and coastal inundation influenced by different wind models.
- Introduction of a Modified Parametric Wind Model: Introduced a new modified parametric wind model tailored for the BoB, which improves the representation of cyclonic wind fields and enhances predictive accuracy.
- Effectiveness of Bed Load Transport Formulations: Developed a methodology to evaluate the effectiveness of different bed load transport formulations in nearshore coastal regions of the BoB during storm surges, utilizing a hydrodynamic-wave-morphodynamic model framework setup.
- Development of TCSPI Model: Developed a novel TCSPI model specifically designed to predict peak surge heights for the entire coast of the Bay of Bengal (BoB).
- Surge Hazard Mapping Methodology: Developed a simple, accurate, and efficient methodology to generate surge hazard maps, aiding in better visualization and understanding of surge risk along the BoB coast.

This study primarily focuses on improving the predictive capability of storm surge models, which is the main objective, while the investigation of morphodynamics during storm surge is included, which serves as a complementary aspect rather than a primary focus. The improved wind field hindcasts enhance storm surge predictions using numerical models along the coastal region. This enables accurate evacuation warnings and reduces false alarms. Coastal engineers need accurate surge estimates to design resilient structures. The inclusion of the approach angle parameter within the surge index model improves the accuracy of peak surge forecasts, aiding insurance companies in better risk assessments. Offshore industries benefit from informed operational decisions, minimizing storm-related damage. Lastly, improved forecasting supports climate adaptation policies, ensuring effective long-term flood mitigation strategies. These contributions collectively enhance the predictive capabilities of storm surge models, which helps in management of storm surge risks for the BoB region.

7.5. SCOPE FOR FUTURE WORK

It is observed no significant difference was observed in the inundation extent for the different atmospheric forcing considered as discussed in Chapter─3. This may require further studies by investigating finer mesh resolutions near the coasts within the numerical stability of the GWCE in ADCIRC. As a future implication, focusing on investigating the role of mangroves in mitigating the effects of storm surges, wind waves, and morphodynamic changes using a similar coupled hydrodynamic wave morphodynamic model setup for the northern BoB. This would help us in understanding effect of mangroves in protecting the communities.

As a future research scope, it is necessary to conduct a numerical experiment to investigate the impact of approach angles along the bay regions. This can help improve the accuracy of TCSPI. Furthermore, the accuracy associated with TCSPI can be improved further by incorporating parameters such as continental slope, wind wave, tide, gust wind, rain stress, and rain mass effect information in the TCSPI formulation.

An improved statistical modeling approach for storm surge prediction is essential for the BoB region to accurately forecast time series data on water surface elevations. Additionally, a statistical model that can predict the inundation extent based on estimated peak surge heights values would be highly benaficial for the coastal communities.

A similar surge index model could be developed for the Arabian Sea, along with creating surge hazard maps for the coastal districts along the western coast of India, taking into account return periods and climate change scenarios. This is because the West Coast is densely populated, and the frequency of cyclones in the Arabian Sea has increased in the past decade. A hazard map would offer crucial information for disaster preparedness, helping to identify high-risk areas, plan evacuation routes, and implement protective measures to reduce the impact of future storm surges.

APPENDIX A

EFFECT OF BOTTOM FRICTION AND WIND DRAG ON STORM SURGES[5]

A.1. GENERAL

Studying bottom friction and wind drag during storm surges in the northern BoB is crucial as they significantly affect surge height and inland penetration. Accurate modeling improves surge forecasts by predicting energy dissipation and wind force on water. This understanding is vital for enhancing coastal protection in this vulnerable region. Numerous studies have analysed wind drag and bottom friction coefficients across ocean basins, but there's a notable gap in combining these formulations for storm surge modeling in the BoB. Therefore, the present study proposes a methodology to examine the impact of combining different bottom friction and wind drag coefficient formulations on storm surges by systematically adjusting their coefficients.

A.1.1. Bottom friction and wind drag coefficient formulations

The northern coastline of the BoB is highly vulnerable to severe cyclonic events and storm surges. The magnitude of storm surges is influenced by parameters such as bottom friction and wind drag coefficients. In the low-lying areas of the northern BoB, where storm surges significantly impact coastal communities, the recent tropical cyclones Bulbul (2019), Amphan (2020), and Yaas (2021) underscore the importance of enhancing surge prediction accuracy. The storm surge model depends on wind stress, influenced by the wind drag coefficient. While traditional methods use fixed or linear formulations (“Bryant et al., 2016; Jones and Davies, 1998”), recent nonlinear

[5] This work is taken from: “Shashank, V. G., et al. "Effect of Bottom Friction and Wind Drag Coefficient on Tropical Cyclone Storm Surge Hindcast in the Bay of Bengal." International Association for Hydraulic Environmental Engineering and Research-Asia Pacific Division, physical conference. Singapore: Springer Nature Singapore, 2022. DOI: https://doi.org/10.1007/978-981-97-6009-1_51”

equations offer improved estimates during cyclones ("Large and Yeager, 2009; Peng and Li, 2015"). In shallow coastal areas (<10 m depth), bottom friction dominates momentum balance by dissipating energy in the bottom boundary layer, influencing hydrodynamics, erosion, and sedimentation. Various models, including Manning, Chezy, and hybrid friction laws, adapt friction coefficients based on depth to capture nearshore and deep-water dynamics. Previous studies (e.g., "Peng & Li, 2015; Bryant et al., 2016; Yu et al., 2017; Shankar & Behera, 2019") analyzed the effects of wind drag coefficient formulations on storm surges. Chu et al., (2019) and Akbar et al., (2017) further explored wind drag and bottom friction impacts on storm surge using FVCOM and ADCIRC models, respectively. This study examines the impact of varying wind drag and bottom friction coefficient formulations on storm surge modeling for the BoB region, using a systematic parameterization approach. It reassesses the claim that such variations minimally influence hindcasting, focusing on TC Yaas (2021).

A.2. METHODOLOGY

In the present study, apart from ADCIRC's inbuilt linear, constant quadratic, and nonlinear hybrid bottom friction formulations, the sensitivity experiments are performed also using Manning, Chezy's White-Colebrook (W-C), and Koutitas bottom friction coefficients formulations, and the parameter values of each respective bottom friction formulation are systematically increased and decreased from their default values as presented in (Table A.1), where τ_b is bottom stress. ADCIRC has an option of constant linear quadratic, and nonlinear hybrid type of bottom friction, defined by the choice of the drag coefficient C_D. v is current velocity, C_f is the bottom friction coefficient, for the linear friction relationship $C_D = C_f$ considered. For quadratic relationship $C_D = C_f\ ||v||$ is being substituted in the τ_b equation. $\boldsymbol{\tau_{bx}}$ and $\boldsymbol{\tau_{by}}$ are bottom stresses in x and y directions respectively in which spatially varying Manning, Chezy, and hybrid friction coefficient equations can be substituted (same as ca onstant quadratic equation). H is water depth, n is Manning roughness factor, g = 9.81 m/s^2 is the acceleration due to gravity, k = 0.4 is the von Karman constant, z_0 = 0.002 mm is the bottom roughness parameter, $Hbreak$ = 2 m is the control water depth, and The value of θ, set at 10 determines how rapidly C_f approaches its asymptotic limit, approaches its asymptotic limits, whereas the exponent γ, set at 1.33 controls the rate of increase in the friction coefficient as water depth decreases. The default value for constant linear, quadratic, and hybrid bottom friction coefficient is 0.00250. The default parameters have been increased to 0.00375 (+50%) and decreased to 0.00125 (-50%). Similarly, the manning roughness factor has been increased to 0.030 (+50%) and decreased to 0.010 (-50%) from its standard default value of 0.020. The Chezy roughness coefficient C typically falls within the range of 55 to 65. However, rather than utilizing a constant Chezy value, it is determined by White-Colebrook (W-C) roughness formulas, which are dependent on both water depth and the equivalent geometrical roughness coefficient of Nikuradse, *Ks*, which varies from 0.003 to 0.009 (Morris et al., 2001). Each of the bottom friction formulations will have 15 simulation scenarios with varying parameter values, as indicated in (Table. A.1).

Table A.1. Bottom drag coefficient formulations.

SL No.	Bottom friction law	Formulation	Parameters
1	**Linear friction relationship**	$\tau_b = C_D v$	0.00125
			0.00250
		C_D=C_f	0.00375
2	**Nonlinear spatially constant quadratic friction law**		0.00125
		C_D=$C_f \|\|v\|\|$	0.00250
			0.00375
3	**Nonlinear spatially varying quadratic friction law** $\boldsymbol{\tau_{bx} = \rho C_f u\sqrt{u^2 + v^2}}$ $\boldsymbol{\tau_{by} = \rho C_f v\sqrt{u^2 + v^2}}$	1. Manning coefficient	0.010
			0.020
		$C_f = \frac{n^2 g}{\mathrm{H}^{1/3}}$	0.030
		2. Chezy coefficient $C_f = \frac{g}{C^2}$	C = 55 to 65
		a. White-Colebrook (W-C) formulation $C = 18 \times log\left(\frac{12 \times \mathrm{H}}{K_s}\right)$	K_s=0.003 & 0.009
		3. Kotitas friction coefficient	NA

		$$C_f = \frac{k^2}{\left[\log\left(\frac{H}{z_0}+1\right)-1\right]^2}$$	
4	**Nonlinear hybrid friction law**	$$C_D = C_{fmin}\left[1+\left(\frac{H_{break}}{H}\right)^{\theta_f}\right]^{\gamma_f/\theta_f}$$	0.00125 0.00250 0.00375

The wind drag coefficient formulations used to calculate wind stresses in this study are presented in Table A.2. 15 distinct parameterizations of bottom friction are simulated in conjunction with each of the four wind drag coefficient formulations. Therefore, the present study consists of an overall 60 simulations (15×4=60). To evaluate the behavior of different bottom friction equations as a function of depth, the behavior of different predominant wind speed-dependent empirical wind drag coefficient equations are presented in the comparison plots (Fig. A.1a, A.1b).

Table A.2. Wind drag coefficient formulations

SL No.	Wind drag Law	Equation
1.	Garret's wind drag formulation (1972)	$C_d \times 10^3 = a + b\lvert u_{10} \mid for\ u_{10} < 41m/s$ $C_d \times 10^3 = 3.5\ for\ u_{10} > 41m/s$ *Where a=0.75 and b=0.067*
2.	Wu's wind drag formulation (1967)	$C_d \times 10^3 = 0.5 \times {u_{10}}^{0.5}\ for\ u_{10} < 15m/s$ $C_d \times 10^3 = 2.6\ for$ u_10> $15m/s$
3.	Zijlema's Relationship (1982)	$C_d \times 10^3 = 0.55 + 2.97\bar{u} - 1.49\bar{u}^2$ $\bar{u} = \frac{u_{10}}{u_{ref}}\ where, u_{ref} = 31.5\ m/s$
4.	Powell's formulation (2003)	Sector based (Azimuthal angle) wind drag formulation (Powell et al., 2003)

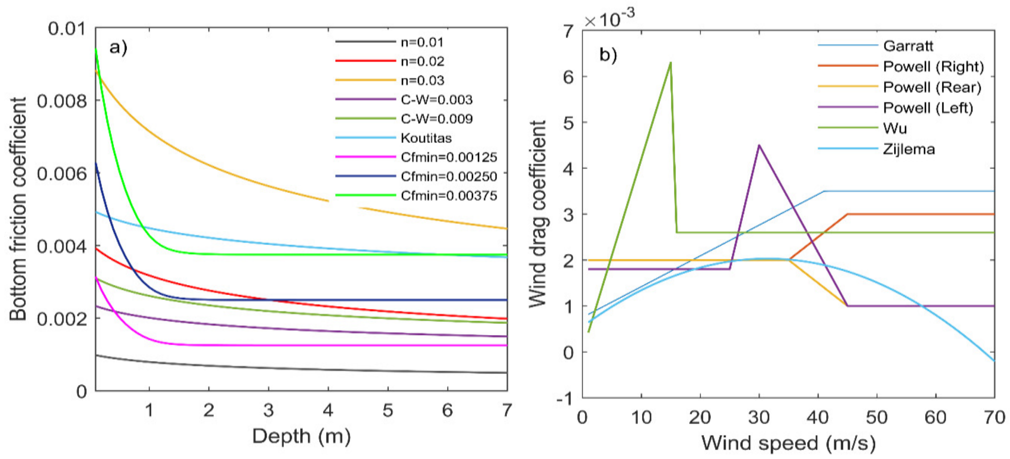

Fig. A.1. a) Depth dependence of differently parametrized constant linear, constant quadratic, spatially quadratic (Manning, Chezy's White-Colebrook and Koutitas), and hybrid bottom friction coefficient formulations b) The wind drag coefficient expressed as a function of wind speed is evaluated for various formulations given in Table. A2.

A.3. MODEL SETUP FOR THE TC YAAS

A.3.1. Yaas Cyclone

In the present study, ADCIRC model setup for TC Yaas was carried out. VSCS Yaas made landfall in Odisha and affected West Bengal significantly in late May 2021. Yaas developed from a tropical disturbance and later became a deep depression. Upon turning to the northeast, the system intensified further, becoming a severe cyclonic storm on May 24. Yaas accelerated to a VSCS. On May 25 with marginally favorable conditions. On May 26, Yaas crossed the northern Odisha coast as VSCS.

A.3.2. Model Setup

For the present study, the ADCIRC model is employed, with a detailed explanation of the model presented in Chapter–2. The parameters used to setup the model are presented in Chapter–3. An unstructured triangular grid from the GEBCO database was created with 66303 elements, 130395 nodes, and a resolution ranging from 700 m nearshore to 10 km offshore.

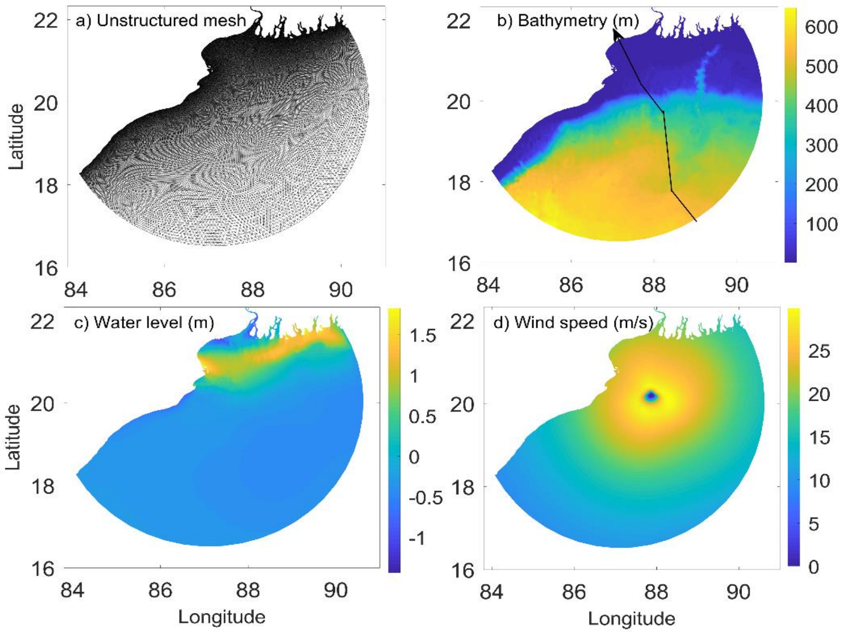

Fig. A.2. a) The finite element method implemented to the unstructured triangular grid b) The bathymetry depth of the entire domain from GEBCO is indicated by the colour bar. The black line denotes track of TC Yaas (JTWC) c) The spatial representations of water level elevation (in m) simulated by the model.d) The spatial spread of cyclonic wind fields just prior to the landfall (at 23:00 hrs on 25 May).

A.4. RESULTS AND DISCUSSION

Initially, 15 cases of simulations for the different bottom friction coefficient formulations were carried out in combination with considering Garratt's wind drag coefficient formulation to compute the water levels due to TC Yaas using Generalized Asymmetric Holland Model (GAHM) wind field. A sample snapshot water level (m) and wind speed (m/s) captured on 25 May 2021 at 23:00 hrs as shown in the Fig. A.2c & A.2d. An accuracy assessment of predicted residual water levels is performed for all 60 simulation cases in comparison to the observed values obtained from the Dhamra tide gauge station located at 86.95E, 20.78N. Along the north of Odisha coast. Considering Garratt's wind drag coefficient formulation in combination with different bottom friction coefficient formulas for the varied parameters, the constant linear bottom friction coefficient formula underestimates residual water levels poorly with RMSE ranging from 0.633 to 0.738, and attenuating surge propagation as the C_f value is increasing from 0.00125 to 0.00375 as shown in temporal (Fig. A.3a, and Fig. A.3c), and corresponding spatial plots (Fig. A.4a, A.4b, and A.4c). While, the constant quadratic bottom friction coefficient is predicting residual water levels with better with RMSE ranging from 0.252 to 0.326. Coming to the spatially varying quadratic and nonlinear hybrid bottom friction coefficients formulations, Chezy's C-W slightly overestimates the residual water levels to the observed value with RMSE (MBE) ranging from 0.307 (0.043) to 0.338 (-0.003) (The negative value of MBE indicates overestimation as shown in Fig. A.3c), while Manning and nonlinear hybrid bottom friction coefficient formulation perform better in terms of estimating residual water levels, with RMSE values of 0.257 and 0.250, respectively for the decreased C_f parameter (0.00125), followed by Koutitas bottom friction coefficient formulation with RMSE of 0.261. The RMSE increases as the bottom friction coefficient parameter C_f is increasing from the default value, while the opposite is true for decreasing the parameter from the default value.

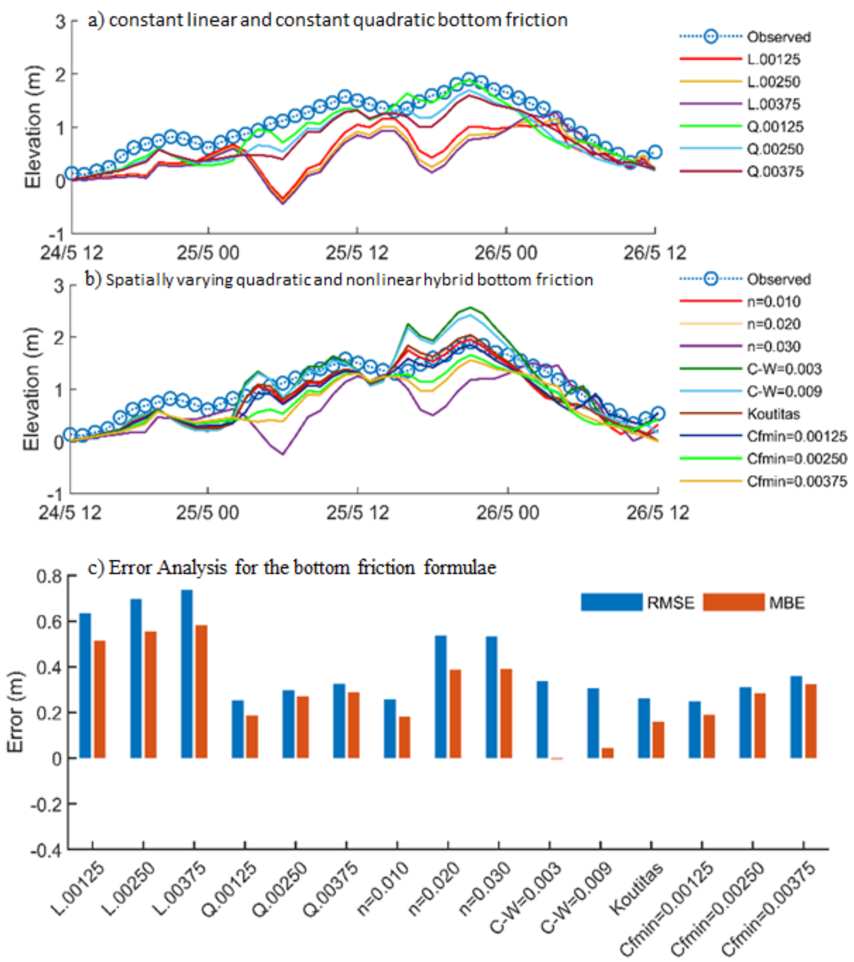

Fig. A.3. a) The model results of time series of residual water levels produced from constant linear and constant quadratic bottom friction coefficient formulae b) Spatially varying quadratic (Manning and Chezy's C-W and Koutitas) and nonlinear hybrid bottom friction formulations versus observed values measured at Dhamra tide gauge station for the increased (decreased) parameters in combination with Garratt's wind drag formulation for the TC Yaas

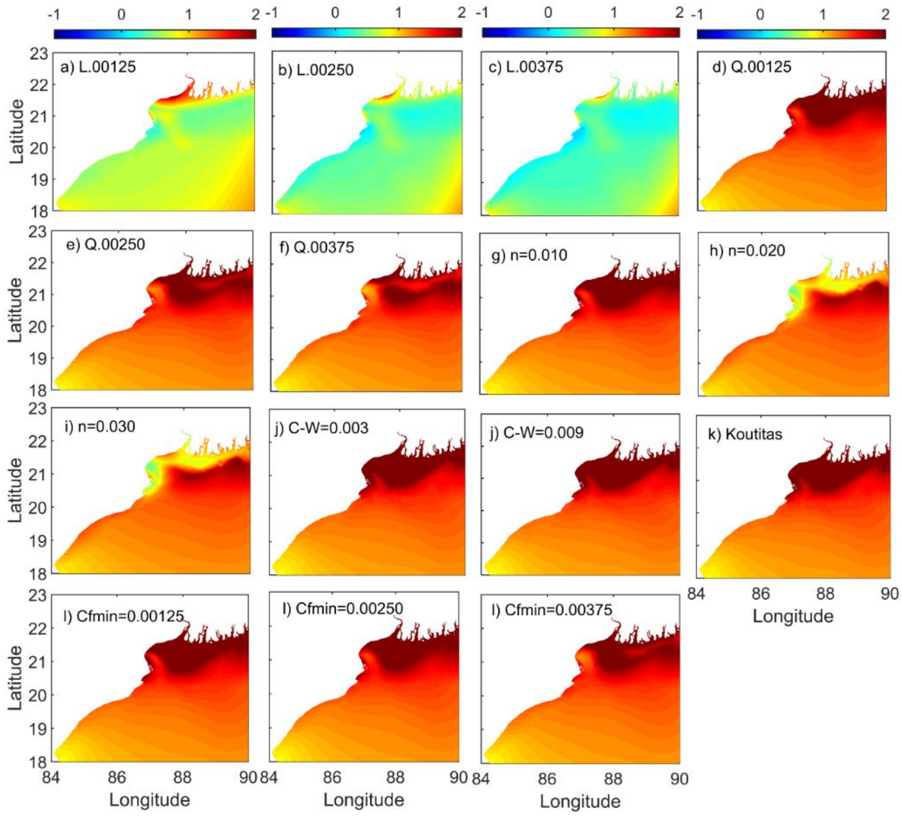

Fig. A.4. Contour plots of total water levels (m) for different cases of bottom friction formulation considering in combination with Garratt wind drag formulation

Furthermore, as previously discussed, a similar experiment was carried out in which 15 cases of different bottom friction coefficient formulations in combination with each wind drag coefficient formulations (as presented in Table. A2) were used to compute the residual water levels due to TC Yaas. The RMSE and MBE plotted for each of the wind drag coefficient formulation cases have been shown in the bar plot (Fig. A.5). It is observed that Wu's wind drag formulation overestimates the residual water levels with observed values in most of the quadratic and nonlinear hybrid bottom friction coefficient cases of simulation with RMSE (MBE) ranging from 0.191 (-0.023) to 0.584

(-0.354), while the Zijlema and the sector-based Powell's wind drag coefficient is underestimating for all the cases of bottom friction coefficient formulations.

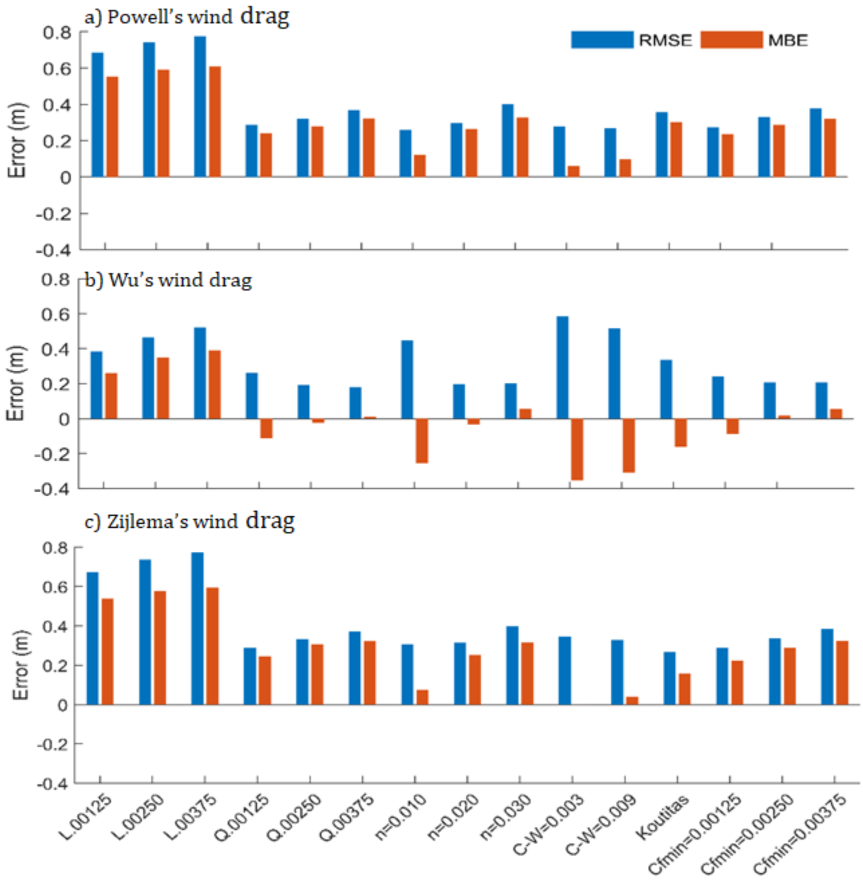

Fig A.5. 15 cases of different bottom friction coefficient formulations in combination with a) Powell b) Wu and c) Zijlema's wind drag coefficient formulations

A.5. SUMMARY

Overall, for all the wind drag coefficient formulations considered in the study, it is observed that decreased parameters (by 50%) from the default values of bottom friction coefficient formulations indicate relatively less errors, and the errors increase as the parameters of the bottom friction coefficient formulation increase for TC Yaas in the BoB. The nonlinear hybrid bottom friction performs best (RMSE: 0.235–0.384 m), followed by the quadratic (0.181–0.584 m) and linear formulations (0.384–0.775 m). Wu's wind drag formula overestimates surge (RMSE: 0.191–0.584 m), while Garratt, Powell, and Zijlema's formulations underpredict considering all 15 bottom friction cases. Across all 15 bottom friction and 4 wind drag formulations, RMSE ranged from 0.235 m to 0.775 m, aligning well with previous studies. The findings suggest using lower bottom friction parameters than the default values for the northern BoB region.

APPENDIX B

BRIEF INTRODUCTION TO SEDIMENT TRANSPORT FORMULATIONS

B.1 GENERAL

This Appendix B provides an overview of the sediment transport formulations implemented to evaluate their performance during storm surges, as discussed in Chapter─4. These formulations are essential for understanding how sediments are mobilized and redistributed under the influence of high-energy conditions associated with TCs.The appendix includes a detailed listing and description of sediment transport formulations that consider both currents alone and combined currents and wave action. These formulations, presented in Table 2.1, represent various theoretical and empirical approaches commonly used to morphodlogical bed evolution under different hydrodynamic conditions. Each formulation is briefly outlined, highlighting its fundamental principles, and suitability for storm surge scenarios. This comparison aims to assist in assessing which formulations are best suited for accurate predictions of sediment movement and deposition in coastal regions impacted by storms. The appendix serves as a quick reference to the different models used, ensuring clarity on their roles and performance in the analyses conducted in Chapter─4.

B.1.1. Meyer-Peter-Muller (MPM)

The Meyer-Peter-Muller (1948) formula is one of the classical bed load transport equations used for estimating the bed load sediment transport rate. It is particularly effective for coarse sediments in rivers. The bed load transport rate is calculated as:

$$Q_b = \frac{8(\tau_b - \tau_{cr})^{3/2}}{\rho_s g D_{50}} u_b \tag{B.1}$$

where Q_b is the sediment transport rate per unit width, τ_b is the bed shear stress, τ_c is the critical shear stress, u_b is near bed flow velocity vector, and D_{50} is median grain diameter (50 represents the particle diameter where 50% of the sediment is finer and 50% is coarser).

B.1.2. Einstein-Brown (EB)

The Einstein-Brown (1950) formulation is an empirical bed load transport equation derived from laboratory experiments. It focuses on the probability of particle movement based on fluid dynamics and sediment properties. A complex function of flow intensity and particle size gives the transport rate.

$$Q_b = \phi_b \left(\frac{\tau_b - \tau_c}{\gamma_s D_{50}} \right) \tag{B.2}$$

where γ_s is the specific weight of the sediment

B.1.3. Engelund-Hansen (EH)

The Engelund-Hansen (1967) formula is a widely used empirical equation for estimating the total bed load transport (bed and suspended load) in open channel flows, particularly for sandy riverbeds. Developed by Engelund and Hansen in 1967, it provides a framework for calculating the total sediment transport rate based on flow parameters and sediment characteristics.

$$Q_b = 0.05 \gamma_s U^2 \left[\frac{D_{50}}{g\left(\frac{\gamma_s}{\gamma} - 1\right)} \right] \left[\frac{\tau}{(\gamma_s - \gamma) D_{50}} \right]^{3/2} \tag{B.3}$$

where γ is the specific weight of the water, and U is the depth averaged currents.

B.1.4. Van Rijn (VR)

The Van Rijn (1984) total bed load transport formula is a widely used empirical approach for estimating sediment transport in rivers and coastal environments. This formula is primarily applied to bed load transport, which involves the movement of sediment particles along the riverbed due to the action of flowing water. Van Rijn's approach accounts for key factors such as flow velocity, sediment characteristics, and bed shear stress.

$$Q_b = 0.053 \frac{D_{50}^{1.5} \cdot (\rho_s - \rho)}{\rho} g^{0.5} \left(\frac{\tau_b - \tau_c}{\tau_c} \right)^{1.5} \tag{B.4}$$

B.1.5. Bijker (BJ)

The Bijker (1968) total bed load transport formula is used in coastal engineering to estimate sediment transport along the seabed, especially in environments with waves and currents. It accounts for both bed shear stress generated by currents and additional effects of wave motion on sediment mobilization. The total bed load transport is expressed as:

$$Q_b = b.\tau_{cu}^{0.5}\exp\left(-0.27.\frac{1}{\mu\tau_{cuw}}\right) + 11.6\sqrt{\frac{\tau_c}{\rho}.r.C_a\left[I_1.\ln\left(\frac{33h}{r}\right) + I_2\right]} \tag{B.5}$$

where τ_{cu} is the non-dimensional shear stress due to currents alone, τ_{cuw} is the non-dimensional shear stress due to wave-current interaction, and μ is a correction factor that accounts for the effect of ripples, b is a constant value set equal to 2 in the GAIA model, r is the thickness of the bottom layer, $C_a$is reference concentration, h is local water depth, $I_1$and I_2 are Einstein integrals.

B.1.6. Soulsby-van Rijn (SVR)

The Soulsby-van Rijn (1997) total bed load transport formula is an empirical equation used to calculate the total sediment transport (bed load and suspended load) in a river or coastal environment. It is particularly useful for predicting sediment movement in sandy or gravelly beds under current and wave action. This formula includes factors such as grain size, bed shear stress, and fluid velocity to predict the rate of sediment movement over the bed. The total sediment transport rate is expressed as:

$$Q_b = A_{bs}U\left[\left(U^2 + 2\frac{0.018}{C_D}U_0^2\right)^{0.5} - U_{cr}\right]^{2.4} \tag{B.6}$$

where A_{bs} is an empirical coefficient that is a function of h, D_{50}, g and s. U_0 is the Root Mean Square (RMS) orbital velocity of waves, and C_D is the quadratic drag coefficient due to current alone. U_{cr} is critical entrainment velocity, which is a function of h, D_{50}, and D_{90}.

B.1.7. Bailard (BL)

The Bailard (1981) formulation is used for calculating sediment transport under wave conditions, focusing on energetics. The Bailard formula is derived from energetics concepts, where sediment transport is driven by the balance of work done by fluid forces on the sediment particles. The total sediment transport rate is expressed as:

$$Q_b = \frac{F_{cw}}{g(s-1)} < \left|\overrightarrow{U(t)}\right|^2 \overrightarrow{U(t)} > \left(\frac{\epsilon_c}{\tan\theta} - \frac{\epsilon_s}{W_s}\right) \tag{B.7}$$

where F_{cw} friction coefficient which accounts for wave-current interactions. ϵ_c, and ϵ_s are constants with values 0.1 and 0.02 respectively. $< >$ is the time-averaged time-averaged over a wave period, θ sediment friction angle, and W_s is the settling velocity. $\overrightarrow{U(t)}$ is the time-varying velocity vector.

B.1.8. Dibajnia and Watanabe (DB)

The Dibajnia and Watanabe (1992) total bed load transport formulation is commonly used in sediment transport modeling to predict the movement of bed load, which refers to sediment particles transported along the bottom of a water body by rolling, sliding, or hopping. This approach was developed to account for complex factors such as sediment mobility and wave-current interactions in coastal environments. The total sediment transport rate is expressed as:

$$Q_b = \delta W_s D_{50} \frac{\vec{\Gamma}}{\left|\vec{\Gamma}\right|^{1-\beta}} \tag{B.8}$$

where δ = 0.0001 and $\beta = 0.55$ empirical model coefficients, and $\vec{\Gamma}$ the difference between the amounts of sediments transported in the onshore and offshore directions.

B.1.9. SUMMARY

The study provides brief descriptions of various sediment transportation formulations. These descriptions include an overview of the principles and mechanisms governing sediment transport and the mathematical equations used to represent these processes.

The formulations are discussed in the context of their specific applications, highlighting the conditions under which each method is most effective.

REFERENCES

1. **Ahsan, M. E.** (2013). *Coastal zone of Bangladesh: Fisheries resources and its potentials*. Lap Lambert Academic Publishing.
2. **Akbar, M. K.**, **Kanjanda, S.**, & **Musinguzi, A.** (2017). Effect of bottom friction, wind drag coefficient, and meteorological forcing in hindcast of Hurricane Rita storm surge using SWAN+ ADCIRC model. *Journal of Marine Science and Engineering, 5*(3), 38.
3. **Alvarsson, J.**, **Lampa, S.**, **Schaal, W.**, **Andersson, C.**, **Wikberg, J. E.**, & **Spjuth, O.** (2016). Large-scale ligand-based predictive modelling using support vector machines. *Journal of Cheminformatics, 8*(1), 1-9. https://doi.org/10.1186/s13321-016-0151-
4. **Angusamy, N.**, & **Rajamanickam, G. V.** (2007). Coastal processes of Central Tamil Nadu, India: Clues from grain size studies. *Oceanologia, 49*(1).
5. Annual TC Review over NIO. (2013). Available at [https://rsmcnewdelhi.imd.gov.in/download.php?path=uploads/report/27/27_14ab8f_rsmc-2013.pdf]
6. Annual TC Review over NIO. (1990). Available at [https://rsmcnewdelhi.imd.gov.in/uploads/report/27/27_736e8a_35_d4f6b7_RSMC%20REPORT%201990.pdf]
7. Annual TC Review over NIO. (2016). Available at [https://rsmcnewdelhi.imd.gov.in/uploads/report/27/27_ad292c_rsmc-2016.pdf]
8. Annual TC Review over NIO. (2018). Available at [https://rsmcnewdelhi.imd.gov.in/uploads/report/27/27_60dae9_rsmc-2018.pdf]
9. **Antony, C.**, **Unnikrishnan, A. S.**, **Krien, Y.**, **Murty, P. L.**, **Samiksha, S. V.**, & **Islam, A. K.** (2020). Tide–surge interaction at the head of the Bay of Bengal during Cyclone Aila. *Regional Studies in Marine Science, 35*(1), 101133. https://doi.org/10.1016/j.rsma.2020.101133
10. **Asher, T. G.**, **Luettich, R. A. Jr.**, **Fleming, J. G.**, & **Blanton, B. O.** (2019). Low frequency water level correction in storm surge models using data assimilation. *Ocean Modelling, 144*, 101483.
11. **ATCF**. Automated Tropical Cyclone Forecast. Retrieved from [https://www.nrlmry.navy.mil/atcf_web/]
12. **Audouin, Y.**, **Benson, T.**, **Delinares, M.**, **Fontaine, J.**, **Glander, B.**, **Huybrechts, N.**, **Kopmann, R.**, **Leroy, A.**, **Pavan, S.**, **Pham, C. T.**, & **Taccone, F.** (2019). Introducing

GAIA, the brand new sediment transport module of the TELEMAC-MASCARET system. In *XXVIth TELEMAC-MASCARET User Conference* (pp. 15th to 17th October).

13. **Ayyad, M.**, **Hajj, M. R.**, & **Marsooli, R.** (2022). Machine learning-based assessment of storm surge in the New York metropolitan area. *Scientific Reports, 12*(1), 1-2. https://doi.org/10.1038/s41598-022-23627-6
14. **Babic, M.**, **Kokol, P.**, **Belic, I.**, **Panjan, P.**, **Kovacic, M.**, & **Balic, J.** (2014). Using genetic programming in engineering. *Elektrotehnički Vestnik/Electrotechnical Review, 81*(3), 143. Retrieved from https://ev.fe.uni-lj.si/3-2014/Babic.pdf
15. **Bailard, J. A.** (1981). An energetics total load sediment transport model for a plane sloping beach. *Journal of Geophysical Research: Oceans, 86*(C11), 10938-10954. https://doi.org/10.1029/JC086iC11p10938
16. **Bang, H. T.**, **Yoon, S.**, & **Jeon, H.** (2020). Application of machine learning methods to predict a thermal conductivity model for compacted bentonite. *Annals of Nuclear Energy, 142*(1), 107395. https://doi.org/10.1016/j.anucene.2020.107395
17. **Bass, B.**, & **Bedient, P.** (2018). Surrogate modeling of joint flood risk across coastal watersheds. *Journal of Hydrology, 558*(1), 159-173. https://doi.org/10.1016/j.jhydrol.2018.01.014
18. **Bates, P. D.**, **Anderson, M. G.**, & **Hervouet, J. M.** (1995). TELEMAC 2D, & RMA 2: Initial comparison of two two-dimensional finite element codes for river flood simulation. *Proceedings of the Institution of Civil Engineers - Water Maritime and Energy, 112*(3), 238-248.
19. **Bayram, A.**, **Larson, M.**, **Miller, H. C.**, & **Kraus, N. C.** (2001). Cross-shore distribution of longshore sediment transport: Comparison between predictive formulas and field measurements. *Coastal Engineering, 44*(2), 79-99. https://doi.org/10.1016/S0378-3839(01)00023-0
20. **Bell, S. S.**, **Chand, S. S.**, **Tory, K. J.**, **Ye, H.**, & **Turville, C.** (2020). North Indian Ocean tropical cyclone activity in CMIP5 experiments: Future projections using a model-independent detection and tracking scheme. *International Journal of Climatology, 40*(15), 6492-6505. https://doi.org/10.1002/joc.6594
21. **Benoit, M.**, **Marcos, F.**, & **Becq, F.** (1997). Development of a third generation shallow-water wave model with unstructured spatial meshing. In *Coastal Engineering* (pp. 465-478). https://doi.org/10.1061/9780784402429.037

22. **Bertin, X.** (2016). Storm surges and coastal flooding: Status and challenges. *La Houille Blanche, (2)*, 64-70. https://doi.org/10.1051/lhb/2016020
23. **Bhaskaran, P. K.**, **Gayathri, R.**, **Murty, P. L. N.**, **Bonthu, S.**, & **Sen, D.** (2014). A numerical study of coastal inundation and its validation for Thane cyclone in the Bay of Bengal. *Coastal Engineering, 83*, 108-118.
24. **Bhaskaran, P. K.**, **Nayak, S.**, **Bonthu, S. R.**, **Murty, P. L.**, & **Sen, D.** (2013). Performance and validation of a coupled parallel ADCIRC–SWAN model for THANE cyclone in the Bay of Bengal. *Environmental Fluid Mechanics, 13*(6), 601-623. https://doi.org/10.1007/s10652-013-9284-5
25. **Bhaskaran, P. K.**, **Rao, A. D.**, & **Murty, T.** (2020). Tropical cyclone–induced storm surges and wind waves in the Bay of Bengal. In *Techniques for Disaster Risk Management and Mitigation* (pp. 237-294). https://doi.org/10.1002/9781119359203.ch17
26. **Bhavithra, R. S.**, & **Sannasiraj, S. A.** (2022). Climate change projection of wave climate due to Vardah cyclone in the Bay of Bengal. *Dynamics of Atmospheres and Oceans, 97*, 101279.
27. **Bijker, E. W.** (1969). Littoral drift as function of waves and current. In *Coastal Engineering* (pp. 415-435). https://doi.org/10.1061/9780872620131.026
28. **Bijker, E. W.** (1992). Mechanics of sediment transport by the combination of waves and current. In *Design and Reliability of Coastal Structures*, short course during the 23rd ICCE in Venice.
29. **Blanton, B.**, **McGee, J.**, **Fleming, J.**, **Kaiser, C.**, **Kaiser, H.**, **Lander, H.**, **Luettich, R.**, **Dresback, K.**, & **Kolar, R.** (2012). Urgent computing of storm surge for North Carolina's coast. *Procedia Computer Science, 9*, 1677-1686. https://doi.org/10.1016/j.procs.2012.04.185
30. **BMD**. (n.d.). Bangladesh Meteorological Department. Retrieved from [http://live.bmd.gov.bd/]
31. **Booij, N. R. R. C.**, **Ris, R. C.**, & **Holthuijsen, L. H.** (1999). A third-generation wave model for coastal regions: 1. Model description and validation. *Journal of Geophysical Research: Oceans, 104*(C4), 7649-7666.
32. **Boore, D. M.** (1989). The Richter scale: Its development and use for determining earthquake source parameters. *Tectonophysics, 166*(1-3), 1-4. https://doi.org/10.1016/0040-1951(89)90200-X

33. **Bretschneider, C. L.** (1972). A non-dimensional stationary hurricane wave model. In *Offshore Technology Conference*.

34. **Bryant, K. M.**, & **Akbar, M.** (2016). An exploration of wind stress calculation techniques in hurricane storm surge modeling. *Journal of Marine Science and Engineering, 4*(3), 58.

35. **Bureau of Meteorology**. (2022). Australia's official weather forecasts & weather radar—Bureau of Meteorology. Retrieved from [http://www.bom.gov.au/?ref=logo]

36. **Bushra, N.**, **Trepanier, J. C.**, & **Rohli, R. V.** (2019). Joint probability risk modelling of storm surge and cyclone wind along the coast of Bay of Bengal using a statistical copula. *International Journal of Climatology, 39*(11), 4206-4217. https://doi.org/10.1002/joc.6068

37. **Callaghan, J.**, & **Smith, R.** (1998). The relationship between maximum surface wind speeds and central pressure in tropical cyclones. *Australian Meteorological Magazine, 47*(3), 191-202. Retrieved from [https://www.meteo.physik.unimuenchen.de/~roger/Publications/AMM_1998_Callaghan&Smith.pdf]

38. **Camenen, B.**, & **Larroudé, P.** (2003). Comparison of sediment transport formulae for the coastal environment. *Coastal Engineering, 48*(2), 111-132. https://doi.org/10.1016/S0378-3839(03)00002-4

39. **Cao, J.**, **Fang, Z.**, **Qu, G.**, **Sun, H.**, & **Zhang, D.** (2017). An accurate traffic classification model based on support vector machines. *International Journal of Network Management, 27*(1), e1962. https://doi.org/10.1002/nem.1962

40. **Chang, T. Y.**, **Chen, H.**, **Hsiao, S. C.**, **Wu, H. L.**, & **Chen, W. B.** (2021). Numerical analysis of the effect of binary typhoons on ocean surface waves in waters surrounding Taiwan. *Frontiers in Marine Science, 8*, 749185.

41. **Chao, W. T.**, & **Young, C. C.** (2022). Accurate storm surge prediction with a parametric cyclone and neural network hybrid model. *Water, 14*(1), 96. https://doi.org/10.3390/w14010096

42. **Chavas, D.**, **Yonekura, E.**, **Karamperidou, C.**, **Cavanaugh, N.**, & **Serafin, K.** (2013). US hurricanes and economic damage: Extreme value perspective. *Natural Hazards Review, 14*(4), 237-246.

43. **Chen, W. B.**, **Chen, H.**, **Hsiao, S. C.**, **Chang, C. H.**, & **Lin, L. Y.** (2019). Wind forcing effect on hindcasting of typhoon-driven extreme waves. *Ocean Engineering, 188*, 106260.

44. **Chu, D.**, **Zhang, J.**, **Wu, Y.**, **Jiao, X.**, & **Qian, S.** (2019). Sensitivities of modelling storm surge to bottom friction, wind drag coefficient, and meteorological product in the East China Sea. *Estuarine, Coastal and Shelf Science, 231*, 106460. https://doi.org/10.1016/j.ecss.2019.106460

45. **Cialone, M. A.**, **Massey, T. C.**, **Anderson, M. E.**, **Grzegorzewski, A. S.**, **Jensen, R. E.**, **Cialone, A.**, **Mark, D. J.**, **Pevey, K. C.**, **Gunkel, B. L.**, & **McAlpin, T. O.** (2015). North Atlantic Coast Comprehensive Study (NACCS) coastal storm model simulations: Waves and water levels. *Engineer Research and Development Center Vicksburg MS Coastal and Hydraulics Lab*. Retrieved from https://apps.dtic.mil/sti/pdfs/ADA621343.pdf

46. **Conner, W. C.**, **Kraft, R. H.**, & **Harris, D. L.** (1957). Empirical methods for forecasting the maximum storm tide due to hurricanes and other tropical storms. *Monthly Weather Review, 85*(4), 113-116.

47. **Corotis, R. B.**, **Sigl, A. B.**, & **Klein, J.** (1978). Probability models of wind velocity magnitude and persistence. *Solar Energy, 20*(6), 483-493. https://doi.org/10.1016/0038-092X(78)90065-8

48. **Das, H. S.**, **Jung, H.**, **Ebersole, B.**, **Wamsley, T.**, & **Whalin, R. W.** (2011). An efficient storm surge forecasting tool for coastal Mississippi. *Coastal Engineering Proceedings, 1*(32), 21. https://doi.org/10.9753/icce.v32.currents.21

49. **Das, Y.** (2018). Parametric modeling of tropical cyclone wind fields in India. *Natural Hazards, 93*(2), 1049-1084. https://doi.org/10.1007/s11069-018-3340-x

50. **De Oliveira, M. M.**, **Ebecken, N. F.**, **De Oliveira, J. L.**, & **de Azevedo Santos, I.** (2009). Neural network model to predict a storm surge. *Journal of Applied Meteorology and Climatology, 48*(1), 143-155. https://doi.org/10.1175/2008JAMC1907.1

51. **Deltares**. (2014). *User manual Delft3D (No. 4.00)*. Deltares. Retrieved from www.delftsoftware.com

52. **Deppermann, C. E.** (1947). Notes on the origin and structure of Philippine typhoons. *Bulletin of the American Meteorological Society*, 399-404. Retrieved from https://www.jstor.org/stable/26257691

53. **Dhiman, R.**, **Tirodkar, J.**, & **Inamdar, A. B.** (2016). Integrating sustainable coastal development initiatives along Maharashtra coast, using ICM guidelines. In *Proceedings of the 10th Biennial LAKE Conference-2016*, Moodbidri, Karnataka.
54. **Dibajnia, M.**, & **Watanabe, A.** (1993). Sheet flow under nonlinear waves and currents. In *Coastal Engineering 1992* (pp. 2015-2028). https://doi.org/10.1061/9780872629332.154
55. **Dube, S. K.**, **Jain, I.**, **Rao, A. D.**, & **Murty, T. S.** (2009). Storm surge modelling for the Bay of Bengal and Arabian Sea. *Natural Hazards, 51*, 3-27. https://doi.org/10.1007/s11069-009-9397-9
56. **Dube, S. K.**, **Rao, A. D.**, **Sinha, P. C.**, **Murty, T. S.**, & **Bahulayan, N.** (1997). Storm surge in the Bay of Bengal and Arabian Sea: The problem and its prediction. *Mausam, 48*(2), 283-304.
57. **Dube, S. K.**, **Poulose, J.**, & **Rao, A. D.** (2013). Numerical simulation of storm surge associated with severe cyclonic storms in the Bay of Bengal during 2008-11. *Mausam, 64*(1), 193-202. https://doi.org/10.54302/mausam.v64i1.666
58. **Einstein, H. A.** (1950). The bed-load function for sediment transportation in open channel flows. *US Department of Agriculture*.
59. **Engelund, F.**, & **Hansen, E.** (1967). *A monograph on sediment transport in alluvial streams*. Technical University of Denmark.
60. **Ettoumi, F. Y.**, **Sauvageot, H.**, & **Adane, A. E. H.** (2003). Statistical bivariate modelling of wind using first-order Markov chain and Weibull distribution. *Renewable Energy, 28*(11), 1787-1802. https://doi.org/10.1016/S0960-1481(03)00019-3
61. **Fanous, M.**, **Daneshkhah, A.**, **Eden, J. M.**, **Remesan, R.**, & **Palade, V.** (2023). Hydro-morphodynamic modelling of mangroves imposed by tidal waves using finite element discontinuous Galerkin method. *Coastal Engineering, 182*, 104303.
62. **Feng, S.**, **Zhou, H.**, & **Dong, H.** (2019). Using deep neural network with small dataset to predict material defects. *Materials Design, 162*, 300-310. https://doi.org/10.1016/j.matdes.2018.11.060
63. **Fleming, J. G.**, **Fulcher, C. W.**, **Luettich, R. A.**, **Estrade, B. D.**, **Allen, G. D.**, & **Winer, H. S.** (2008). A real-time storm surge forecasting system using ADCIRC. In *Estuarine and Coastal Modeling (2007)* (pp. 893-912).

64. **Flierl, G. R.**, & **Robinson, A. R.** (1972). Deadly surges in the Bay of Bengal: Dynamics and storm-tide tables. *Nature, 239*(5369), 213-215. https://doi.org/10.1038/239213a0
65. **Gao, J.** (2018). *On the surface wind stress for storm surge modeling* (Doctoral dissertation). The University of North Carolina at Chapel Hill. https://doi.org/10.17615/zpeb-7k73
66. **Gao, J.**, **Luettich, R.**, & **Fleming, J.** (2013). Development and initial evaluation of a generalized asymmetric tropical cyclone vortex model in ADCIRC. In *Proceedings of the ADCIRC Users Group Meeting*, Vicksburg, MS, USA (Vol. 16).
67. **Garcia, M.** (Ed.). (2008). *Sedimentation engineering: Processes, measurements, modeling, and practice*. American Society of Civil Engineers.
68. **Garratt, J. R.** (1977). Review of drag coefficients over oceans and continents. *Monthly Weather Review, 105*(7), 915-929.
69. **Gayathri, R.**, **Bhaskaran, P. K.**, & **Murty, P. L. N.** (2021). River-tide-storm surge interaction characteristics for the Hooghly estuary, East coast of India. *ISH Journal of Hydraulic Engineering, 27*(sup1), 483-495. https://doi.org/10.1080/09715010.2019.1601036
70. **GEBCO**. (n.d.). *General Bathymetric Chart of the Oceans*. Retrieved from https://www.gebco.net/
71. **Girishkumar, M. S.**, & **Ravichandran, M.** (2012). The influences of ENSO on tropical cyclone activity in the Bay of Bengal during October–December. *Journal of Geophysical Research: Oceans, 117*(C2).
72. **Gupta, H. K.** (Ed.). (2003). *Disaster management*. Universities Press. Retrieved from https://books.google.de/books?id=m7UD_y4vP0C&lpg=PP7&ots=412h7_uB5K&dq=Disaster%20management.%20Universities%20Press%3B%202003.&lr&pg=PP7#v=onepage&q=Disaster%20management.%20Universities%20Press;%202003.&f=false
73. **Han, X.**, **Kuang, C.**, **Zhu, L.**, **Gong, L.**, & **Cong, X.** (2022). Hydrodynamical and morphological patterns of a sandy coast with a beach nourishment suffering from a storm surge. *Coastal Engineering Journal, 64*(1), 83-99. https://doi.org/10.1080/21664250.2021.1992997
74. **Harris, D. L.** (1959). An interim hurricane storm surge forecasting guide. *US Department of Commerce*.

75. **Hashemi, M. R.**, **Spaulding, M. L.**, **Shaw, A.**, **Farhadi, H.**, & **Lewis, M.** (2016). An efficient artificial intelligence model for prediction of tropical storm surge. *Natural Hazards, 82*(1), 471-491. https://doi.org/10.1007/s11069-016-2193-4
76. **Hebert, C. G.**, **Weinzapfel, R. A.**, & **Chambers, M. A.** (2008). Hurricane Severity Index: A new way of estimating a tropical cyclone's destructive potential. In *Tropical Meteorology Special Symposium/19th Conference on Probability and Statistics*, New Orleans, LA: American Meteorological Society (Vol. 4).
77. **Hemer, M. A.**, **Wang, X. L.**, **Church, J. A.**, & **Swail, V. R.** (2010). Coordinating global ocean wave climate projections. *Bulletin of the American Meteorological Society, 91*(4), 451-454.
78. **Hennessey, J. P., Jr.** (1977). Some aspects of wind power statistics. *Journal of Applied Meteorology and Climatology, 16*(2), 119-128. https://doi.org/10.1175/1520-0450(1977)016<0119
79. >2.0.CO;2
80. **Hervouet, J. M.**, **Hubert, J. L.**, **Janin, J. M.**, **Lepeintre, F.**, & **Peltier, E.** (1994). The computation of free surface flows with TELEMAC: An example of evolution towards hydroinformatics. *Journal of Hydraulic Research, 32*(S1), 45-64. https://doi.org/10.1080/00221689409498804
81. **Hervouet, J. M.** (1999). TELEMAC, a hydroinformatic system. *La Houille Blanche, 1*(3-4), 21-28. https://doi.org/10.1051/lhb/1999029
82. **Hodges, K.**, **Cobb, A.**, & **Vidale, P. L.** (2017). How well are tropical cyclones represented in reanalysis datasets? *Journal of Climate, 30*(14), 5243-5264.
83. **Holland, G. J.** (1980). An analytic model of the wind and pressure profiles in hurricanes. *Monthly Weather Review, 108*(8), 1212-1218.
84. **Holland, G. J.**, **Belanger, J. I.**, & **Fritz, A.** (2010). A revised model for radial profiles of hurricane winds. *Monthly Weather Review, 138*(12), 4393-4401. https://doi.org/10.1175/2010MWR3317.1
85. **Holthuijsen, L. H.**, **Booij, N.**, & **Ris, R.** (1993). A spectral wave model for the coastal zone. In *Ocean Wave Measurement and Analysis* (pp. 630-641). American Society of Civil Engineers.
86. **Houston, S. H.**, **Shaffer, W. A.**, **Powell, M. D.**, & **Chen, J.** (1999). Comparisons of HRD and SLOSH surface wind fields in hurricanes: Implications for storm surge modeling. *Weather and Forecasting, 14*(5), 671-686.

87. **Hsiao, S. C.**, **Chen, H.**, **Chen, W. B.**, **Chang, C. H.**, & **Lin, L. Y.** (2019). Quantifying the contribution of nonlinear interactions to storm tide simulations during a super typhoon event. *Ocean Engineering, 194*, 106661.
88. **Hsiao, S. C.**, **Chen, H.**, **Chen, W. B.**, **Chang, C. H.**, & **Lin, L. Y.** (2019). Quantifying the contribution of nonlinear interactions to storm tide simulations during a super typhoon event. *Ocean Engineering, 194*, 106661.
89. **Hsiao, S. C.**, **Wu, H. L.**, **Chen, W. B.**, **Guo, W. D.**, **Chang, C. H.**, & **Su, W. R.** (2021). Effect of depth-induced breaking on wind wave simulations in shallow nearshore waters off Northern Taiwan during the passage of two super typhoons. *Journal of Marine Science and Engineering, 9*(7), 706. https://doi.org/10.3390/jmse9070706
90. **Huges, L. A.** (1952). On the low level wind structure of tropical cyclones. *Journal of Meteorology, 9*, 422-428.
91. **IMD**. (n.d.). *Indian Meteorological Department*. Retrieved from https://mausam.imd.gov.in/
92. **INCOIS**. (n.d.). *Indian National Centre for Ocean Information Services*. Retrieved from https://incois.gov.in/
93. **IPCC**. (2007). *Climate change 2007: Impacts, adaptation and vulnerability: Contribution of Working Group II to the fourth assessment report of the Intergovernmental Panel*. Geneva, Switzerland. https://doi.org/10.1256/004316502320517344
94. **IPCC**. (2013a). Climate phenomena and their relevance for future regional climate change. In *Climate Change 2013: The Physical Science Basis* (Section 14.6, Chapter 14, pp. 1248–1251). Retrieved from https://www.ipcc.ch/report/ar5/wg1/
95. **IPCC**. (2013b). Climate phenomena and their relevance for future regional climate change—Supplementary material. In *Climate Change 2013: The Physical Science Basis* (Section 14. SM.4, pp. 14SM-8–14SM-9). Retrieved from https://www.ipcc.ch/report/ar5/wg1/
96. **Irish, J. L.**, & **Resio, D. T.** (2010). A hydrodynamics-based surge scale for hurricanes. *Ocean Engineering, 37*(1), 69-81. https://doi.org/10.1016/j.oceaneng.2009.07.012
97. **Irish, J. L.**, **Resio, D. T.**, & **Cialone, M. A.** (2009). A surge response function approach to coastal hazard assessment. Part 2: Quantification of spatial attributes of response functions. *Natural Hazards, 51*(1), 183-205. https://doi.org/10.1007/s11069-009-9381-4

98. **Irish, J. L.**, **Resio, D. T.**, & **Ratcliff, J. J.** (2008). The influence of storm size on hurricane surge. *Journal of Physical Oceanography, 38*(9), 2003-2013. https://doi.org/10.1175/2008JPO3727.1
99. **Islam, M. R.**, **Lee, C. Y.**, **Mandli, K. T.**, & **Takagi, H.** (2021). A new tropical cyclone surge index incorporating the effects of coastal geometry, bathymetry, and storm information. *Scientific Reports, 11*(1), 16747. https://doi.org/10.1038/s41598-021-95825-7
100. **Islam, M.**, **Lee, C. Y.**, **Mandli, K. T.**, & **Takagi, H.** (2021). A new tropical cyclone surge index incorporating the effects of coastal geometry, bathymetry, and storm information. *Scientific Reports, 11*(1), 1-4. https://doi.org/10.1038/s41598-021-95825-7
101. **Islam, R.**, & **Takagi, H.** (2021). Statistical significance of tropical cyclone forward speed on storm surge generation: Retrospective analysis of best track and tidal data in Japan. *Georisk, 15*(3), 247-257. https://doi.org/10.1080/17499518.2020.1756345
102. **Jain, I.**, **Rao, A. D.**, **Jitendra, V.**, & **Dube, S. K.** (2010). Computation of expected total water levels along the east coast of India. *Journal of Coastal Research, 26*(4), 681-687. https://doi.org/10.2112/08-1170.1
103. **Jain, I.**, **Rao, A. D.**, & **Ramesh, K. J.** (2010). Vulnerability assessment at village level due to tides, surges, and wave setup. *Marine Geodesy, 33*(2-3), 245-260.
104. **Jakobsen, F.**, & **Madsen, H.** (2004). Comparison and further development of parametric tropical cyclone models for storm surge modelling. *Journal of Wind Engineering and Industrial Aerodynamics, 92*(5), 375-391.
105. **Jelesnianski, C. P.** (1966). Numerical computations of storm surges without bottom stress. *Monthly Weather Review, 94*(6), 379-394. https://doi.org/10.1175/1520-0493(1966)094<0379
106. >2.3.CO;2
107. **Jeong, C. K.**, **Panchang, V.**, & **Demirbilek, Z.** (2012). Parametric adjustments to the Rankine vortex wind model for Gulf of Mexico hurricanes. *Journal of Offshore Mechanics and Arctic Engineering, 134*(4).
108. **Jia, G.**, & **Taflanidis, A. A.** (2016). Surrogate modeling for peak or time-dependent storm surge prediction over an extended coastal region using an existing

database of synthetic storms. *Natural Hazards, 81*(2), 909-938. https://doi.org/10.1007/s11069-015-2111-1

109. **Johns, B.**, & **Ali, M. A.** (1980). The numerical modelling of storm surges in the Bay of Bengal. *Quarterly Journal of the Royal Meteorological Society, 106*(447), 1-8. https://doi.org/10.1002/qj.49710644702

110. **Johns, B.**, **Rao, A. D.**, **Dubinsky, Z.**, & **Sinha, P. C.** (1985). Numerical modelling of tide-surge interaction in the Bay of Bengal. *Philosophical Transactions of the Royal Society A: Mathematical, Physical and Engineering Sciences, 313*(1526), 507-535.

111. **Johns, B.**, **Sinha, P. C.**, **Dube, S. K.**, **Mohanty, U. C.**, & **Rao, A. D.** (1983). On the effect of bathymetry in numerical storm surge simulation experiments. *Computers & Fluids, 11*(3), 161-174. https://doi.org/10.1016/0045-7930(83)90028-2

112. **Jolliffe, I. T.**, & **Stephenson, D. B.** (Eds.). (2012). *Forecast verification: A practitioner's guide in atmospheric science*. John Wiley & Sons.

113. **Jones, J. E.**, & **Davies, A. M.** (1998). Storm surge computations for the Irish Sea using a three-dimensional numerical model including wave–current interaction. *Continental Shelf Research, 18*(2-4), 201-251.

114. **JTWC**. (n.d.). *Joint Typhoon Warning Center*. Retrieved from https://www.metoc.navy.mil/jtwc/jtwc.html

115. **Kalsi, S. R.**, **Jayanthi, N.**, **Raj, Y. E. A.**, & **Bhomik, S. R.** (2007). *Probable maximum storm surge heights for the maritime districts of India*. New Delhi: Indian Meteorological Department Mono No. Synoptic Meteorology.

116. **Kaminsky, F. C.** (1977). Four probability densities/log-normal, gamma, Weibull, and Rayleigh/and their application to modelling average hourly wind speed. In *International Solar Energy Society, Annual Meeting* (pp. 19_6-19_10).

117. **Kantha, L.** (2006). Time to replace the Saffir-Simpson hurricane scale? *Eos, Transactions American Geophysical Union, 87*(1), 3-6. https://doi.org/10.1029/2006EO010003

118. **Kantha, L.** (2008). Tropical cyclone destructive potential by integrated kinetic energy. *Bulletin of the American Meteorological Society, 89*(2), 219-221. https://www.jstor.org/stable/26216782

119. **Kantha, L.** (2013). Classification of hurricanes: Lessons from Katrina, Ike, Irene, Isaac, and Sandy. *Ocean Engineering, 70*, 124-128. https://doi.org/10.1016/j.oceaneng.2013.06.007

120. **Kantha, L.** (2010). Discussion of "A hydrodynamics-based surge scale for hurricanes." *Ocean Engineering, 37*(11-12), 1081-1084. https://doi.org/10.1016/j.oceaneng.2010.04.003

121. **Kantha, L.** (2013). Classification of hurricanes: Lessons from Katrina, Ike, Irene, Isaac, and Sandy. *Ocean Engineering, 70*, 124-128. https://doi.org/10.1016/j.oceaneng.2013.06.007

122. **Kerr, P. C.**, **Donahue, A. S.**, **Westerink, J. J.**, **Luettich, R. A., Jr.**, **Zheng, L. Y.**, **Weisberg, R. H.**, ... & **Cox, A. T.** (2013). US IOOS coastal and ocean modeling testbed: Inter-model evaluation of tides, waves, and hurricane surge in the Gulf of Mexico. *Journal of Geophysical Research: Oceans, 118*(10), 5129-5172.

123. **Khan, M.**, **Uddin, J.**, **Durand, F.**, **Bertin, X.**, **Testut, L.**, **Krien, Y.**, **Islam, A. K.**, **Peizerat, M.**, & **Hossain, S.** (2021). Towards an efficient storm surge and inundation forecasting system over the Bengal delta: Chasing the Supercyclone Amphan. *Natural Hazards and Earth System Sciences, 21*(8), 2523-2541. https://doi.org/10.5194/nhess-21-2523-2021

124. **Khazaei, B.**, **Bravo, H. R.**, **Anderson, E. J.**, & **Klump, J. V.** (2021). Development of a physically based sediment transport model for Green Bay, Lake Michigan. *Journal of Geophysical Research: Oceans, 126*(10), e2021JC017518. https://doi.org/10.1029/2021JC017518

125. **Kim, S.**, **Pan, S.**, & **Mase, H.** (2019). Artificial neural network-based storm surge forecast model: Practical application to Sakai Minato, Japan. *Applied Ocean Research, 91*, 101871. https://doi.org/10.1016/j.apor.2019.101871

126. **Kokol, P.**, **Kokol, M.**, & **Zagoranski, S.** (2022). Machine learning on small size samples: A synthetic knowledge synthesis. *Science, 105*(1), 00368504211029777. https://journals.sagepub.com/doi/10.1177/00368504211029777

127. **Kolar, R. L.**, **Gray, W. G.**, **Westerink, J. J.**, & **Luettich, R. A., Jr.** (1994). Shallow water modeling in spherical coordinates: Equation formulation, numerical implementation, and application. *Journal of Hydraulics Research, 32*(1), 3-24. https://doi.org/10.1080/00221689409498786

128. **Kolar, R. L.**, **Westerink, J. J.**, **Cantekin, M. E.**, & **Blain, C. A.** (1994). Aspects of nonlinear simulations using shallow-water models based on the wave continuity equation. *Computers & Fluids, 23*(3), 523-538. https://doi.org/10.1016/0045-7930(94)90017-5

129. **Kolukula, S. S.**, & **Murty, P. L. N.** (2022). Improving cyclone wind fields using deep convolutional neural networks and their application in extreme events. *Progress in Oceanography, 202*, 102763. https://doi.org/10.1016/j.pocean.2022.102763

130. **Kossin, J. P.** (2015). Hurricane wind–pressure relationship and eyewall replacement cycles. *Weather and Forecasting, 30*(1), 177-181. https://doi.org/10.1175/WAF-D-14-00121.1

131. **Kowaleski, A. M.**, **Morss, R. E.**, **Ahijevych, D.**, & **Fossell, K. R.** (2020). Using a WRF-ADCIRC ensemble and track clustering to investigate storm surge hazards and inundation scenarios associated with Hurricane Irma. *Weather and Forecasting, 35*(4), 1289-1315.

132. **Kuehl, S. A.**, **Allison, M. A.**, **Goodbred, S. L.**, & **Kudrass, H. E.** (2005). The Ganges-Brahmaputra Delta. *Special Publication-SEPM, 83*, 413. https://doi.org/10.2110/pec.05.83.0413

133. **Kuiry, S. N.**, **Ding, Y.**, & **Wang, S. S.** (2014). Numerical simulations of morphological changes in barrier islands induced by storm surges and waves using a supercritical flow model. *Frontiers in Structural and Civil Engineering, 8*, 57-68. https://doi.org/10.1007/s11709-014-0235-0

134. **Kyprioti, A. P.**, **Taflanidis, A. A.**, **Nadal-Caraballo, N. C.**, & **Campbell, M.** (2021). Storm hazard analysis over extended geospatial grids utilizing surrogate models. *Coastal Engineering, 168*, 103855. https://doi.org/10.1016/j.coastaleng.2021.103855

135. **Lakshmi, D. D.**, **Murty, P. L. N.**, **Bhaskaran, P. K.**, **Sahoo, B.**, **Kumar, T. S.**, **Shenoi, S. S. C.**, & **Srikanth, A. S.** (2017). Performance of WRF-ARW winds on computed storm surge using hydrodynamic model for Phailin and Hudhud cyclones. *Ocean Engineering, 131*, 135-148.

136. **Landman, W. A.**, **Seth, A.**, & **Camargo, S. J.** (2005). The effect of regional climate model domain choice on the simulation of tropical cyclone-like vortices in the southwestern Indian Ocean. *Journal of Climate, 18*(8), 1263-1274.

137. **Large, W. G.**, & **Pond, S.** (1981). Open ocean momentum flux measurements in moderate to strong winds. *Journal of Physical Oceanography, 11*(3), 324-336.

138. **Large, W.**, & **Yeager, S. G.** (2009). The global climatology of an interannually varying air–sea flux data set. *Climate Dynamics, 33*(2), 341-364.

139. **Larson, M.**, **Hanson, H.**, & **Kraus, N. C.** (2003). Numerical modeling of beach topography change. In *Elsevier Oceanography Series* (Vol. 67, pp. 337-365). Elsevier.

140. **Le Provost, C.**, **Lyard, F.**, **Molines, J. M.**, **Genco, M. L.**, & **Rabilloud, F.** (1998). A hydrodynamic ocean tide model improved by assimilating a satellite altimeter-derived data set. *Journal of Geophysical Research: Oceans, 103*(C3), 5513-5529.

141. **Lechtenbörger, C.** (2006). CEDIM-Risk Map Germany: First results. In *RISK21-Coping with Risks due to Natural Hazards in the 21st Century* (pp. 149-156). CRC Press.

142. **Lee, J. W.**, **Irish, J. L.**, **Bensi, M. T.**, & **Marcy, D. C.** (2021). Rapid prediction of peak storm surge from tropical cyclone track time series using machine learning. *Coastal Engineering, 170*, 104024. https://doi.org/10.1016/j.coastaleng.2021.104024

143. **Lee, T. L.** (2006). Neural network prediction of a storm surge. *Ocean Engineering, 33*(3-4), 483-494. https://doi.org/10.1016/j.oceaneng.2005.04.012

144. **Lee, T. L.** (2008). Back-propagation neural network for the prediction of the short-term storm surge in Taichung harbor, Taiwan. *Engineering Applications of Artificial Intelligence, 21*(1), 63-72. https://doi.org/10.1016/j.engappai.2007.03.002

145. **Lin**, N., & **Chavas**, D. (2012). On hurricane parametric wind and applications in storm surge modelling. *Journal of Geophysical Research: Atmospheres, 117*(D19).

146. **Liu**, X., **Jiang**, W., **Yang**, B., & **Baugh**, J. (2018). Numerical study on factors influencing typhoon-induced storm surge distribution in Zhanjiang Harbor. *Estuarine, Coastal and Shelf Science, 215*, 39-51.

147. **Luettich**, R. A., & **Westerink**, J. J. (2004). Formulation and numerical implementation of the 2D/3D ADCIRC finite element model version 44. XX. Chapel Hill, NC, USA: R. Luettich.

148. **Mandal**, S., **Sil**, S., **Shee**, A., & **Venkatesan**, R. (2018). Upper ocean and subsurface variability in the Bay of Bengal during cyclone Roanu: A synergistic view using in situ and satellite observations. *Pure and Applied Geophysics, 175*(12), 4605-4624.

149. **Martinez**, G., **Bizikova**, L., **Blobel**, D., & **Swart**, R. (2011). Emerging climate change coastal adaptation strategies and case studies around the world. In *Global change and Baltic coastal zones* (pp. 249-273). Springer. https://doi.org/10.1007/978-94-007-0400-8_15

150. **Mathiventhan**, T., & **Jayasingam**, T. (2018). Geomorphological changes along the East Coast of Sri Lanka. *International Journal of Research Studies in Biosciences, 6*, 6-12.

151. **Mattocks**, C., & **Forbes**, C. (2008). A real-time, event-triggered storm surge forecasting system for the state of North Carolina. *Ocean Modeling, 25*(3-4), 95-119.

152. **Mercer**, D., **Sheng**, J., **Greatbatch**, R. J., & **Bobanović**, J. (2002). Barotropic waves generated by storms moving rapidly over shallow water. *Journal of Geophysical Research: Oceans, 107*(C10), 16. https://doi.org/10.1029/2001JC001140

153. **Meyer-Peter**, E., & **Müller**, R. (1948). Formulas for bed-load transport. In *IAHSR 2nd meeting*, Stockholm, appendix 2. IAHR.

154. **Mishra**, S. P. (2016). Estuaries and lateral channel development along the east coast of India. *International Journal of Advanced Research and Publications, 4*(12), 2360-2371.

155. **Mishra**, S. P., **Sethi**, K. C., **Ojha**, A. C., & **Barik**, K. K. (2020). Fani, an outlier among pre-monsoon intra-seasonal cyclones over Bay of Bengal. *International Journal of Emerging Technologies, 11*(2), 271-282.

156. **Morris**, B. J. (2001). Nearshore wave and current dynamics (Ph.D. dissertation). Naval Postgraduate School, Monterey, CA.

157. **Muis**, S., **Verlaan**, M., **Winsemius**, H. C., **Aerts**, J. C., & **Ward**, P. J. (2016). A global reanalysis of storm surges and extreme sea levels. *Nature Communications, 7*(1), 1-12.

158. **Murty**, P. L. N., **Sandhya**, K. G., **Bhaskaran**, P. K., **Jose**, F., **Gayathri**, R., **Nair**, T. B., & **Shenoi**, S. S. C. (2014). A coupled hydrodynamic modeling system for PHAILIN cyclone in the Bay of Bengal. *Coastal Engineering, 93*, 71-81. https://doi.org/10.1016/j.coastaleng.2014.08.006

159. **Murty**, P. L. N., **Bhaskaran**, P. K., **Gayathri**, R., **Sahoo**, B., **Kumar**, T. S., & **SubbaReddy**, B. (2016). Numerical study of coastal hydrodynamics using a coupled model for Hudhud cyclone in the Bay of Bengal. *Estuarine, Coastal and Shelf Science, 183*, 13-27. https://doi.org/10.1016/j.ecss.2016.10.013

160. **Murty**, P. L. N., **Srinivas**, K. S., **Rao**, E. P. R., **Bhaskaran**, P. K., **Shenoi**, S. S. C., & **Padmanabham**, J. (2020). Improved cyclonic wind fields over the Bay of Bengal and their application in storm surge and wave computations. *Applied Ocean Research, 95*, 102048. https://doi.org/10.1016/j.apor.2019.102048

161. **Murty**, P. L. N., **Rao**, A. D., **Srinivas**, K. S., **Rao**, E., & **Bhaskaran**, P. K. (2020). Effect of wave radiation stress in storm surge-induced inundation: A case study for the East Coast of India. *Pure and Applied Geophysics, 177*(6), 2993-3012. https://doi.org/10.1007/s00024-019-02379-x

162. **Nadimpalli**, R., **Mohanty**, S., **Pathak**, N., **Osuri**, K. K., **Mohanty**, U. C., & **Chatterjee**, S. (2021). Understanding the characteristics of rapid intensity changes of tropical cyclones over the North Indian Ocean. *SN Applied Sciences, 3*, 1-12. https://doi.org/10.1007/s42452-020-03995-2

163. **Nandhakumar**, S., **Kantharaj**, M., & **Vallam**, S. (2022). Evaluation of total sediment transport model in the simulation of morphodynamics in two different hydrodynamic settings. *Journal of Waterway, Port, Coastal, and Ocean Engineering, 148*(6), 04022022. https://doi.org/10.1061/(ASCE)WW.1943-5460.0000727

164. **Nayak**, S., & **Bhaskaran**, P. K. (2014). Coastal vulnerability due to extreme waves at Kalpakkam based on historical tropical cyclones in the Bay of Bengal. *International Journal of Climatology, 34*(5), 1460-1471. https://doi.org/10.1002/joc.3776

165. **Needham**, H. F., **Keim**, B. D., & **Sathiaraj**, D. A. (2015). Review of tropical cyclone-generated storm surges: Global data sources, observations, and impacts. *Reviews of Geophysics, 53*(2), 545-591. https://doi.org/10.1002/2014RG000477

166. **Needham**, H., & **Keim**, B. D. (2011). Storm surge: Physical processes and an impact scale. In *Recent Hurricane Research—Climate, Dynamics, and Societal Impacts* (pp. 385-406). https://doi.org/10.1007/s00024-019-02379-x

167. **NHC, NOAA**: National Hurricane Center. Available at https://www.nhc.noaa.gov/

168. **Nielsen**, P. (2009). How storm size matters for surge height. *Coastal Engineering, 56*(9), 1002-1004. https://doi.org/10.1016/j.coastaleng.2009.02.006

169. **Nienhuis**, J. H., **Heijkers**, L. G., & **Ruessink**, G. (2021). Barrier breaching versus overwash deposition: Predicting the morphologic impact of storms on coastal

barriers. *Journal of Geophysical Research: Earth Surface, 126*(6), e2021JF006066. https://doi.org/10.1029/2021JF006066

170. **NIOT**, National Institute of Ocean Technology. (n.d.). Retrieved from https://www.niot.res.in/niot1/index.php

171. **Niyas**, N. T., **Srivastava**, A. K., & **Hatwar**, H. R. (2009). Variability and trend in the cyclonic storms over north Indian Ocean (p. 35). India: National Climate Centre, Office of the Additional Director General of Meteorology (Research), India Meteorological Department.

172. **Palutikof**, J. P., **Brabson**, B. B., **Lister**, D. H., & **Adcock**, S. T. (1999). A review of methods to calculate extreme wind speeds. *Meteorological Applications, 6*(2), 119-132. https://doi.org/10.1017/S1350482799001103

173. **Pan**, Y., **Chen**, Y. P., **Li**, J. X., & **Ding**, X. L. (2016). Improvement of wind field hindcasts for tropical cyclones. *Water Science and Engineering, 9*(1), 58-66.

174. **Pandey**, S., & **Rao**, A. D. (2018). An improved cyclonic wind distribution for computation of storm surges. *Natural Hazards, 92*(1), 93-112. https://doi.org/10.1007/s11069-018-3193-3

175. **Pandey**, S., & **Rao**, A. D. (2019). Impact of approach angle of an impinging cyclone on generation of storm surges and its interaction with tides and wind waves. *Journal of Geophysical Research: Oceans, 124*(11), 7643-7660. https://doi.org/10.1029/2019JC015433

176. **Parth Sarthi**, P., **Agrawal**, A., & **Rana**, A. (2015). Possible future changes in cyclonic storms in the Bay of Bengal, India under warmer climate. *International Journal of Climatology, 35*(7), 1267-1277. https://doi.org/10.1002/joc.4053

177. **Passeri**, D. L., **Dalyander**, P. S., **Long**, J. W., **Mickey**, R. C., **Jenkins III**, R. L., **Thompson**, D. M., **Plant**, N. G., **Godsey**, E. S., **Gonzalez**, V. M. (2020). The roles of storminess and sea level rise in decadal barrier island evolution. *Geophysical Research Letters, 47*(18), e2020GL089370. https://doi.org/10.1029/2020GL089370

178. **Peng**, M., **Xie**, L., & **Pietrafesa**, L. J. (2004). A numerical study of storm surge and inundation in the Croatan–Albemarle–Pamlico Estuary System. *Estuarine, Coastal and Shelf Science, 59*(1), 121-137. https://doi.org/10.1016/j.ecss.2003.07.010

179. **Peng**, S., & **Li**, Y. (2015). A parabolic model of drag coefficient for storm surge simulation in the South China Sea. *Scientific Reports, 5*(1), 1-6.

180. **Persson**, A. (2001). User guide to ECMWF forecast products.

181. **Phadke**, A. C., **Martino**, C. D., **Cheung**, K. F., & **Houston**, S. H. (2003). Modeling of tropical cyclone winds and waves for emergency management. *Ocean Engineering, 30*(4), 553-578.

182. **Poulose**, J., **Rao**, A. D., & **Bhaskaran**, P. K. (2018). Role of continental shelf on non-linear interaction of storm surges, tides and wind waves: An idealized study representing the west coast of India. *Estuarine, Coastal and Shelf Science, 207*, 457-470. https://doi.org/10.1016/j.ecss.2017.06.007

183. **Powell**, M. D., & **Black**, P. G. (1990). The relationship of hurricane reconnaissance flight-level wind measurements to winds measured by NOAA's oceanic platforms. *Journal of Wind Engineering and Industrial Aerodynamics, 36*, 381-392. https://doi.org/10.1016/0167-6105(90)90322-4

184. **Powell**, M. D., **Houston**, S. H., **Amat**, L. R., & **Morisseau-Leroy**, N. (1998). The HRD real-time hurricane wind analysis system. *Journal of Wind Engineering and Industrial Aerodynamics, 77-78*, 53-64.

185. **Powell**, M. D., **Vickery**, P. J., & **Reinhold**, T. A. (2003). Reduced drag coefficient for high wind speeds in tropical cyclones. *Nature, 422*(6929), 279-283.

186. **Powell**, M. D., & **Reinhold**, T. A. (2007). Tropical cyclone destructive potential by integrated kinetic energy. *Bulletin of the American Meteorological Society, 88*(4), 513-526. https://doi.org/10.1175/BAMS-88-4-513

187. **Pradhan**, D., **Mitra**, A., & **De**, U. K. (2012). Estimation of pressure drop and storm surge height associated with tropical cyclone using Doppler velocity. Retrieved from https://nopr.niscpr.res.in/handle/123456789/14373

188. **Prakash**, K. R., & **Pant**, V. (2020). On the wave-current interaction during the passage of a tropical cyclone in the Bay of Bengal. *Deep-Sea Research Part II: Topical Studies in Oceanography, 172*, 104658. https://doi.org/10.1016/j.dsr2.2019.104658

189. **Priya**, P., **Pattnaik**, S., & **Trivedi**, D. (2022). Characteristics of the tropical cyclones over the North Indian Ocean Basins from the long-term datasets. *Meteorology and Atmospheric Physics, 134*(4), 1-20. https://doi.org/10.1007/s00703-022-00904-7

190. **Proudman**, J. (1954). Note on the dynamics of storm surges. *Geophysical Journal International, 7*, 44-48.

191. **Qi**, J., **Chen**, C., **Beardsley**, R. C., **Perrie**, W., **Cowles**, G. W., & **Lai**, Z. (2009). An unstructured-grid finite-volume surface wave model (FVCOM-SWAVE): Implementation, validations and applications. *Ocean Modelling, 28*(1-3), 153-166.

192. **Qiao**, W., **Song**, J., **He**, H., & **Li**, F. (2019). Application of different wind field models and wave boundary layer model to typhoon waves numerical simulation in WAVEWATCH III model. *Tellus A: Dynamic Meteorology and Oceanography, 71*(1), 1657552.

193. **Raj**, Y. E. (2010). Relation between pressure defect and maximum wind in the field of a tropical cyclone–Theoretical derivation of proportionality constant based on an idealised surface pressure model. *Mausam, 61*(3), 291-316.

194. **Ramaswamy, V.**, & **Rao, P. S.** (2014). The Myanmar continental shelf. *Geological Society, London, Memoirs, 41*(1), 231-240. https://doi.org/10.1144/M41.17

195. **Rankine, W. J. M.** (1882). *A manual of applied physics*. Charles Griffin and Co.

196. **Rao, A. D.**, **Jain, I.**, & **Venkatesan, R.** (2010). Estimation of extreme water levels due to cyclonic storms: A case study for Kalpakkam coast. *The International Journal of Ocean and Climate Systems, 1*(1), 1-14. https://journals.sagepub.com/doi/pdf/10.1260/1759-3131.1.1.1

197. **Rao, A. D.**, **Murty, P. L. N.**, **Jain, I.**, **Kankara, R. S.**, **Dube, S. K.**, & **Murty, T. S.** (2013). Simulation of water levels and extent of coastal inundation due to a cyclonic storm along the east coast of India. *Natural Hazards, 66*(3), 1431-1441. https://doi.org/10.1007/s11069-012-0193-6

198. **Rao, A. D.**, **Upadhaya, P.**, **Ali, H.**, **Pandey, S.**, & **Warrier, V.** (2020b). Coastal inundation due to tropical cyclones along the east coast of India: An influence of climate change impact. *Natural Hazards, 101*, 39-57. https://doi.org/10.1007/s11069-020-03861-9

199. **Rao, A. D.**, **Upadhaya, P.**, **Pandey, S.**, & **Poulose, J.** (2020a). Simulation of extreme water levels in response to tropical cyclones along the Indian coast: A climate change perspective. *Natural Hazards, 100*, 151-172. https://doi.org/10.1007/s11069-019-03804-z

200. **Rao, A. D.**, **Jain, I.**, **Murthy, M. V.**, **Murty, T. S.**, & **Dube, S. K.** (2009). Impact of cyclonic wind field on interaction of surge–wave computations using finite-element and finite-difference models. *Natural Hazards, 49*(2), 225-239. https://doi.org/10.1007/s11069-008-9284-9

201. **Razzak, I.**, **Zafar, K.**, **Imran, M.**, & **Xu, G.** (2020). Randomized nonlinear one-class support vector machines with bounded loss function to detect outliers for

large scale IoT data. *Future Generation Computer Systems, 112*, 715-723. https://doi.org/10.1016/j.future.2020.05.045

202. **Rego, J. L.**, & **Li, C.** (2009). On the importance of the forward speed of hurricanes in storm surge forecasting: A numerical study. *Geophysical Research Letters, 36*(7). https://doi.org/10.1029/2008GL036953

203. **Reid, R. O.** (1956). *Approximate response of water level on a sloping shelf to a wind fetch which moves towards shore*. Beach Erosion Board Technical Memorandum No. 83. United States Army Corps of Engineers, Washington.

204. **Rezapour, M.**, & **Baldock, T. E.** (2014). Classification of hurricane hazards: The importance of rainfall. *Weather and Forecasting, 29*(6), 1319-1331. https://doi.org/10.1175/WAF-D-14-00022.1

205. **Ribas, F.**, **Falques, A.**, **De Swart, H. E.**, **Dodd, N.**, **Garnier, R.**, & **Calvete, D.** (2015). Understanding coastal morphodynamic patterns from depth-averaged sediment concentration. *Reviews of Geophysics, 53*(2), 362-410. https://doi.org/10.1002/2014RG000457

206. **Riehl, H.** (1963). Some relationships between wind and thermal structure of steady state hurricanes. *Journal of Atmospheric Sciences, 20*, 276–287.

207. **Rohini, S.**, **Sannasiraj, S. A.**, & **Sundar, V.** (2023). Investigation of morphodynamic evolution in a shelf region of Bay of Bengal under extreme conditions. *Natural Hazards, 116*(3), 3043-3062. https://doi.org/10.1007/s11069-022-05797-8

208. **Rosendal, H. E.**, & **Shaw, S. L.** (1982). Relationship of maximum sustained winds to minimum sea level pressure in central North Pacific tropical cyclones. *Journal of Applied Meteorology, 21*(7), 1016-1020.

209. **Ruiz-Salcines, P.**, **Salles, P.**, **Robles-Díaz, L.**, **Díaz-Hernández, G.**, **Torres-Freyermuth, A.**, & **Appendini, C. M.** (2019). On the use of parametric wind models for wind wave modeling under tropical cyclones. *Water, 11*(10), 2044. https://doi.org/10.3390/w11102044

210. **Sahoo, B.**, & **Bhaskaran, P. K.** (2016). Assessment on historical cyclone tracks in the Bay of Bengal, east coast of India. *International Journal of Climatology, 36*(1), 95-109. https://doi.org/10.1002/joc.4331

211. **Sahoo, B.**, & **Bhaskaran, P. K.** (2018). A comprehensive data set for tropical cyclone storm surge-induced inundation for the east coast of India. *International Journal of Climatology, 38*(1), 403-419. https://doi.org/10.1002/joc.5184

212. **Sahoo, B.**, & **Bhaskaran, P. K.** (2019a). Prediction of storm surge and coastal inundation using artificial neural network: A case study for 1999 Odisha Super Cyclone. *Weather and Climate Extremes, 23*, 100196. https://doi.org/10.1016/j.wace.2019.100196

213. **Sahoo, B.**, & **Bhaskaran, P. K.** (2019b). Prediction of storm surge and inundation using climatological datasets for the Indian coast using soft computing techniques. *Soft Computing, 23*(23), 12363-12383. https://doi.org/10.1007/s00500-019-03775-0

214. **Saichenthur, N.**, & **Murali, K.** (2021). Prediction of storm surge due to Super Cyclone Amphan using a hybrid finite volume and finite element based SWE solver. In *OCEANS IEEE-San Diego–Porto* (pp. 1-8).

215. **Šakić Trogrlić**, R., **van den Homberg**, M., **Budimir**, M., **McQuistan**, C., **Sneddon**, A., & **Golding**, B. (2022). Early warning systems and their role in disaster risk reduction. In *Towards the "Perfect" Weather Warning: Bridging Disciplinary Gaps through Partnership and Communication* (pp. 11-46). Cham: Springer International Publishing.

216. **Samiksha**, V., **Vethamony**, P., **Antony**, C., **Bhaskaran**, P., & **Nair**, B. (2017). Wave–current interaction during Hudhud cyclone in the Bay of Bengal. *Natural Hazards and Earth System Sciences, 17*(12), 2059-2074. https://doi.org/10.5194/nhess-17-2059-2017

217. **Sanchez**, A., **Wu**, W., & **Beck**, T. M. (2016). A depth-averaged 2-D model of flow and sediment transport in coastal waters. *Ocean Dynamics, 66*(11), 1475-1495. https://doi.org/10.1007/s10236-016-0994-3

218. **Sandeep**, C. P. R., **Krishnamoorthy**, C., & **Balaji**, C. (2018). Impact of cloud parameterization schemes on the simulation of cyclone Vardah using the WRF model. *Current Science, 115*(6), 1143-1153.

219. **Sanil Kumar**, V., & **Sajiv Philip**, C. (2010). Variations in long term wind speed during different decades in Arabian Sea and Bay of Bengal. *Journal of Earth System Science, 119*, 639-653. https://doi.org/10.1007/s12040-010-0051-4

220. **Sarwar**, S., & **Borthwick**, A. G. (2023). Estimate of uncertain cohesive suspended sediment deposition rate from uncertain floc size in Meghna estuary, Bangladesh. *Estuarine, Coastal and Shelf Science, 281*, 108183. https://doi.org/10.1016/j.ecss.2022.108183

221. **Schloemer**, R. W. (1954). Analysis and synthesis of hurricane wind patterns over Lake Okeechobee, Florida. US Department of Commerce, Weather Bureau.

222. **Sebastian**, M., **Behera**, M. R., **Prakash**, K. R., & **Murty**, P. L. N. (2024). Performance of various wind models for storm surge and wave prediction in the Bay of Bengal: A case study of Cyclone Hudhud. *Ocean Engineering, 297*, 117113. https://doi.org/10.1016/j.oceaneng.2024.117113

223. **Sebastian**, M., & **Behera**, M. R. (2022). Impact of highest maximum sustained wind speed and its duration on storm surges and hydrodynamics along Krishna–Godavari coast. *Climate Dynamics, 19*, 1-22. https://doi.org/10.1007/s00382-022-06173-9

224. **Sebastian**, M., **Behera**, M. R., & **Murty**, P. L. N. (2019). Storm surge hydrodynamics at a concave coast due to varying approach angles of cyclone. *Ocean Engineering, 191*, 106437. https://doi.org/10.1016/j.oceaneng.2019.106437

225. **Selvaraj**, R., **Sannasiraj**, S. A., & **Vallam**, S. (2022). Hydrodynamic modelling of storm surge with modified wind fields along the East Coast of India. *Marine Geodesy*.

226. **Shaikhina**, T., **Lowe**, D., **Daga**, S., **Briggs**, D., **Higgins**, R., & **Khovanova**, N. (2019). Decision tree and random forest models for outcome prediction in antibody incompatible kidney transplantation. *Biomedical Signal Processing and Control, 52*, 456-462. https://doi.org/10.1016/j.bspc.2017.01.012

227. **Shankar**, C. G., & **Behera**, M. R. (2019). Wave boundary layer model based wind drag estimation for tropical storm surge modelling in the Bay of Bengal. *Ocean Engineering, 191*, 106509. https://doi.org/10.1016/j.oceaneng.2019.106509

228. **Shao**, Z., **Liang**, B., **Li**, H., **Wu**, G., & **Wu**, Z. (2018). Blended wind fields for wave modeling of tropical cyclones in the South China Sea and East China Sea. *Applied Ocean Research, 71*, 20-33. https://doi.org/10.1016/j.apor.2017.11.012

229. **Shashank**, V. G., **Mandal**, S., & **Sil**, S. (2021). Impact of varying landfall time and cyclone intensity on storm surges in the Bay of Bengal using ADCIRC model. *Journal of Earth System Science, 130*(4), 1-16. https://doi.org/10.1007/s12040-021-01695-y

230. **Shashank**, V. G., **Sriram**, V., & **Sannasiraj**, S. A. (2022). Improvements in wind field hindcast for storm surge predictions in the Bay of Bengal: A case study for

the tropical cyclone Varadah. *Applied Ocean Research, 127*, 103324. https://doi.org/10.1016/j.apor.2022.103324

231. **Shashank**, V. G., **Sriram**, V., **Schüttrumpf**, H., & **Sannasiraj**, S. A. (2024). A new surge index with the incorporation of cyclone track approach angle information for the Bay of Bengal. *Coastal Engineering, 188*, 104429. https://doi.org/10.1016/j.coastaleng.2023.104429

232. **Shashank**, V. G., **Sriram**, V., & **Sannasiraj**, S. A. (2022). Effect of bottom friction and wind drag coefficient on tropical cyclone storm surge hindcast in the Bay of Bengal. In *IAHR-APD Conference*.

233. **Sheng**, Y. P., **Zhang**, Y., & **Paramygin**, V. A. (2010). Simulation of storm surge, wave, and coastal inundation in the Northeastern Gulf of Mexico region during Hurricane Ivan in 2004. *Ocean Modelling, 35*(4), 314-331.

234. **Silva**, J. P., **Hagopian**, J., **Burdiat**, M., **Dufrechou**, E., **Pedemonte**, M., **Gutiérrez**, A., **Cazes**, G., & **Ezzatti**, P. (2014). Another step to the full GPU implementation of the weather research and forecasting model. *Journal of Supercomputing, 70*, 746-755. https://doi.org/10.1007/s11227-014-1193-y

235. **Singh**, O. P., **Ali Khan**, T. M., & **Rahman**, M. S. (2000). Changes in the frequency of tropical cyclones over the North Indian Ocean. *Meteorology and Atmospheric Physics, 75*(1-2), 11-20. https://doi.org/10.1007/s007030070011

236. **Soulsby**, R. (1997). *Dynamics of marine sands: A manual for practical applications*. Telford.

237. **Sridharan**, B., **Chaitanya**, R. K., **Sudheer**, K. P., & **Kuiry**, S. N. (2022). Improved accuracy of storm surge simulations by incorporating changing along-track parameters. *International Journal of Climatology, 42*(13), 6908-6926. https://doi.org/10.1002/joc.7620

238. **State of the Global Climate**. (2020). WMO Report No-1264. Available at https://library.wmo.int/index.php?lvl=notice_display&id=21880#.YIpS8LUzZPY

239. **Taflanidis**, A. A., **Jia**, G., **Kennedy**, A. B., & **Smith**, J. M. (2013a). Implementation/optimization of moving least squares response surfaces for approximation of hurricane/storm surge and wave responses. *Natural Hazards, 66*(2), 955-983. https://doi.org/10.1007/s11069-012-0520-y

240. **Taflanidis**, A. A., **Kennedy**, A. B., **Westerink**, J. J., **Smith**, J., **Cheung**, K. F., **Hope**, M., & **Tanaka**, S. (2013b). Rapid assessment of wave and surge risk during

landfalling hurricanes: Probabilistic approach. *Journal of Waterway, Port, Coastal, and Ocean Engineering, 139*(3), 171-182. https://doi.org/10.1061/(ASCE)WW

241. **Taflanidis, A. A.**, **Kennedy, A. B.**, **Westerink, J. J.**, **Smith, J.**, **Cheung, K. F.**, **Hope, M.**, & **Tanaka, S.** (2013b). Rapid assessment of wave and surge risk during landfalling hurricanes: Probabilistic approach. *Journal of Waterway, Port, Coastal, and Ocean Engineering, 139*(3), 171-182. https://doi.org/10.1061/(ASCE)WW.1943-5460.0000178

242. **Takagi, H.**, **Islam, M. R.**, **Anh, L. T.**, **Takahashi, A.**, **Sugiu, T.**, & **Furukawa, F.** (2020). Investigation of high wave damage caused by 2019 Typhoon Faxai in Kanto region and wave hindcast in Tokyo Bay. *Journal of Japan Society of Civil Engineers, Series B, 3*, 12-21.

243. **Tassi, P.** (2014). *Sisyphe v6.3 user's manual*. Recherche et Développement, Électricité de France: Chatou, France.

244. **Tassi, P.**, **Benson, T.**, **Delinares, M.**, **Fontaine, J.**, **Huybrechts, N.**, **Kopmann, R.**, **Pavan, S.**, **Pham, C. T.**, **Taccone, F.**, & **Walther, R.** (2023). GAIA—a unified framework for sediment transport and bed evolution in rivers, coastal seas, and transitional waters in the TELEMAC-MASCARET modelling system. *Environmental Modelling & Software, 159*, 105544. https://doi.org/10.1016/j.envsoft.2022.105544

245. **Taylor, H. T.**, **Ward, B.**, **Willis, M.**, & **Zaleski, W.** (2010). *The Saffir-Simpson hurricane wind scale*. Atmospheric Administration: Washington, DC, USA.

246. **Thai, T. H.**, **Thuy, N. B.**, **Dang, V. H.**, & **Kim, S. H.** (2017). Impact of the interaction of surge, wave and tide on a storm surge on the north coast of Vietnam. *Procedia IUTAM, 25*, 82-91.

247. **Thomas, A.**, **Dietrich, J. C.**, **Asher, T. G.**, **Bell, M.**, **Blanton, B. O.**, **Copeland, J. H.**, & **Luettich, R. A.** (2019). Influence of storm timing and forward speed on tides and storm surge during Hurricane Matthew. *Ocean Modelling, 137*, 1-19. https://doi.org/10.1016/j.ocemod.2019.03.004

248. **Torres, M. J.**, **Reza Hashemi, M.**, **Hayward, S.**, **Spaulding, M.**, **Ginis, I.**, & **Grilli, S. T.** (2019). Role of hurricane wind models in accurate simulation of storm surge and waves. *Journal of Waterway, Port, Coastal, and Ocean Engineering, 145*(1), 04018039.

249. **Tory, K. J.**, **Dare, R. A.**, **Davidson, N. E.**, **McBride, J. L.**, & **Chand, S. S.** (2013). The importance of low-deformation vorticity in tropical cyclone formation. *Atmospheric Chemistry and Physics, 4*, 2115-2132.

250. **Tseng, C. M.**, **Jan, C. D.**, **Wang, J. S.**, & **Wang, C. M.** (2007). Application of artificial neural networks in typhoon surge forecasting. *Ocean Engineering, 34*(11-12), 1757-1768. https://doi.org/10.1016/j.oceaneng.2006.09.005

251. **United States Geological Survey**. (n.d.). Largest and deadliest earthquakes by year. Retrieved from http://earthquake.usgs.gov/eqcenter/eqarchives/year/byyear.php

252. **van Ormondt, M.**, **Nelson, T. R.**, **Hapke, C. J.**, & **Roelvink, D.** (2020). Morphodynamic modelling of the wilderness breach, Fire Island, New York. Part I: Model set-up and validation. *Coastal Engineering, 157*, 103621. https://doi.org/10.1016/j.coastaleng.2019.103621

253. **van Ormondt, M.**, **van Dongeren, A.**, & **Roelvink, D.** (2021). A semi-empirical method for computing storm surges on open coasts during tropical cyclones. *Coastal Engineering, 165*, 103839. https://doi.org/10.1016/j.coastaleng.2020.103839

254. **van Rijn, L. C.**, **Walstra, D. J.**, **Grasmeijer, B.**, **Sutherland, J.**, **Pan, S.**, & **Sierra, J. P.** (2003). The predictability of cross-shore bed evolution of sandy beaches at the time scale of storms and seasons using process-based profile models. *Coastal Engineering, 47*(3), 295-327. https://doi.org/10.1016/S0378-3839(02)00120-5

255. **van Rijn, L. C.** (1984). Sediment transport, part I: Bed load transport. *Journal of Hydraulics Engineering, 110*(10), 1431-1456. https://doi.org/10.1061/(ASCE)0733-9429(1984)110:10(1431)

256. **van Rijn, L. C.** (2007). Unified view of sediment transport by currents and waves. I: Initiation of motion, bed roughness, and bed-load transport. *Journal of Hydraulics Engineering, 133*(6), 649-667. https://doi.org/10.1061/(ASCE)0733-9429(2007)133:6(649)

257. **van Wiechen, P. P. J.**, **de Vries, S.**, **Reniers, A. J. H. M.**, & **Aarninkhof, S. G. J.** (2023). Dune erosion during storm surges: A review of the observations, physics and modelling of the collision regime. *Coastal Engineering*, 104383. https://doi.org/10.1016/j.coastaleng.2023.104383

258. **Venkatesan, R.**, **Shamji, V. R.**, **Latha, G.**, **Mathew, S.**, **Rao, R. R.**, **Muthiah, A.**, & **Atmanand, M. A.** (2013). In situ ocean subsurface time-series measurements

from OMNI buoy network in the Bay of Bengal. *Current Science*, 1166–1177. https://www.jstor.org/stable/24092396

259. **Vickery, P. J.**, **Skerlj, P. F.**, **Steckley, A. C.**, & **Twisdale, L. A.** (2000). Hurricane wind field model for use in hurricane simulations. *Journal of Structural Engineering, 126*(10), 1203-1221. https://doi.org/10.1061/(ASCE)0733-9445(2000)126:10(1203)

260. **Walsh, K.** (1997). Objective detection of tropical cyclones in high-resolution analyses. *Monthly Weather Review, 125*(8), 1767-1779.

261. **Wang, H.**, **Ji, C.**, **Su, T.**, **Shi, C.**, **Ge, Y.**, **Yang, J.**, & **Wang, S.** (2022). Comparison and implementation of machine learning models for predicting the combustion phases of hydrogen-enriched Wankel rotary engines. *Fuel, 310*, 122371. https://doi.org/10.1016/j.fuel.2021.122371

262. **Wang, X.**, **Yao, C.**, **Gao, G.**, **Jiang, H.**, **Xu, D.**, **Chen, G.**, & **Zhang, Z.** (2020). Simulating tropical cyclone waves in the East China Sea with an event-based, parametric-adjusted model. *Journal of Oceanography, 76*(6), 439-457.

263. **Wannawong**, W., & **Ekkawatpanit**, C. (2012). Tropical cyclone wind-wave, storm surge, and current in meteorological prediction. *Natural Disasters, 2*(1), 65-86.

264. **Warner**, J. C., **Sherwood**, C. R., **Signell**, R. P., **Harris**, C. K., & **Arango**, H. G. (2008). Development of a three-dimensional, regional, coupled wave, current, and sediment-transport model. *Computers & Geosciences, 34*(10), 1284-1306. https://doi.org/10.1016/j.cageo.2008.02.012

265. **Weatherall**, P., **Marks**, K. M., **Jakobsson**, M., **Schmitt**, T., **Tani**, S., **Arndt**, J. E., & **Wigley**, R. (2015). A new digital bathymetric model of the world's oceans. *Earth and Space Science, 2*(8), 331-345.

266. **Weisberg**, R. H., & **Zheng**, L. (2006). Hurricane storm surge simulations for Tampa Bay. *Estuaries and Coasts, 29*(6), 899-913. https://doi.org/10.1007/BF02798649

267. **Weisser**, D. (2003). A wind energy analysis of Grenada: An estimation using the Weibull density function. *Renewable Energy, 28*(11), 1803-1812. https://doi.org/10.1016/S0960-1481(03)00016-8

268. **Willoughby**, H. E., **Darling**, R. W. R., & **Rahn**, M. E. (2006). Parametric representation of the primary hurricane vortex. Part II: A new family of sectionally continuous profiles. *Monthly Weather Review, 134*(4), 1102-1120.

269. **Willoughby**, H. E., & **Rahn**, M. E. (2004). Parametric representation of the primary hurricane vortex. Part I: Observations and evaluation of the Holland (1980) model. *Monthly Weather Review, 132*(12), 3033-3048.

270. **Willoughby**, H. E., **Darling**, R. W. R., & **Rahn**, M. E. (2006). Parametric representation of the primary hurricane vortex. Part II: A new family of sectionally continuous profiles. *Monthly Weather Review, 134*(4), 1102-1120. https://doi.org/10.1175/MWR3106.1

271. **WMO** (2022). *World Meteorological Organisation*. Available at https://public.wmo.int/en

272. **Wong**, K. I., **Wong**, P. K., **Cheung**, C. S., & **Vong**, C. M. (2013). Modeling and optimization of biodiesel engine performance using advanced machine learning methods. *Energy, 55*, 519-528. https://doi.org/10.1016/j.energy.2013.03.057

273. **Wu**, G. F., **He**, Z. G., **Zhao**, L., & **Liu**, G. H. (2018). A well-balanced positivity preserving two-dimensional shallow flow model with wetting and drying fronts over irregular topography. *Journal of Hydrodynamics, 30*(4), 618-631. https://doi.org/10.1007/s42241-018-0069-7

274. **Wu**, G., **Shi**, F., **Kirby**, J. T., **Liang**, B., & **Shi**, J. (2018). Modeling wave effects on storm surge and coastal inundation. *Coastal Engineering, 140*, 371-382. https://doi.org/10.1016/j.coastaleng.2018.08.011

275. **Wu**, J. (1967). *Laboratory studies of wind-wave interactions*. Hydronautics Inc.

276. **Wu**, J. (1982). Wind-stress coefficients over sea surface from breeze to hurricane. *Journal of Geophysical Research: Oceans, 87*(C12), 9704-9706.

277. **Wu**, W., **Wang**, S. S., & **Jia**, Y. (2000). Nonuniform sediment transport in alluvial rivers. *Journal of Hydraulic Research, 38*(6), 427-434. https://doi.org/10.1080/00221680009498296

278. **Xie**, L., **Bao**, S., **Pietrafesa**, L. J., **Foley**, K., & **Fuentes**, M. (2006). A real-time hurricane surface wind forecasting model: Formulation and verification. *Monthly Weather Review, 134*(5), 1355-1370.

279. **Xie**, L., **Liu**, H., **Liu**, B., & **Bao**, S. (2011). A numerical study of the effect of hurricane wind asymmetry on storm surge and inundation. *Ocean Modelling, 36*(1-2), 71-79.

280. **Xu**, P., **Mao**, X., & **Jiang**, W. (2017). Estimation of the bottom stress and bottom drag coefficient in a highly asymmetric tidal bay using three independent methods. *Continental Shelf Research, 140*, 37-46.

281. **Yalla**, V., **Sriram**, V., & **Murali**, K. (2023). Influence of maximum water level and coastal inundation on the east coast of India based on future tropical cyclones. *Natural Hazards*, 1-32. https://doi.org/10.1007/s11069-023-06244-y

282. **Yang**, S. Q., & **Lim**, S. Y. (2003). Total load transport formula for flow in alluvial channels. *Journal of Hydraulic Research, 129*(1), 68-72. https://doi.org/10.1061/(ASCE)0733-9429(2003)129:1(68)

283. **Yu**, X., **Pan**, W., **Zheng**, X., **Zhou**, S., & **Tao**, X. (2017). Effects of wave-current interaction on storm surge in the Taiwan Strait: Insights from Typhoon Morakot. *Continental Shelf Research, 146*, 47-57.

284. **Zhang**, C. (2012). Effect of hurricane forward speed and approach angle on coastal storm surge. *Digital Commons LSU*. https://digitalcommons.lsu.edu/gradschool_theses/3468

285. **Zhang**, C., & **Li**, C. (2019). Effects of hurricane forward speed and approach angle on storm surges: An idealized numerical experiment. *Acta Oceanologica Sinica, 38*(7), 48-56. https://doi.org/10.1007/s13131-018-1081-z

286. **Zhang**, W., **Harff**, J., **Schneider**, R., & **Wu**, C. (2010). Development of a modelling methodology for simulation of long-term morphological evolution of the southern Baltic coast. *Ocean Dynamics, 60*, 1085-1114. https://doi.org/10.1007/s10236-010-0311-5

287. **Zhang**, Y., & **Ling**, C. A. (2018). Strategy to apply machine learning to small datasets in materials science. *npj Computational Materials, 4*(1), 1-8. https://doi.org/10.1038/s41524-018-0081-z

288. **Zhang**, Z., **Song**, Y., **Cui**, H., **Wu**, J., **Schwartz**, F., & **Qi**, H. (2016). Topological analysis and Gaussian decision tree: Effective representation and classification of biosignals of small sample size. *IEEE Transactions on Biomedical Engineering, 64*(9), 2288-2299. https://doi.org/10.1109/TBME.2016.2634531

289. **Zhao**, L., **Wang**, S. S., **Becker**, E., **Yoon**, J. H., & **Mukherjee**, A. (2020). Cyclone Fani: The tug-of-war between regional warming and anthropogenic aerosol effects. *Environmental Research Letters, 15*(9), 094020. https://doi.org/10.1088/1748-9326/ab91e7

290. **Zhao**, S., **Liu**, Z., **Wei**, X., **Li**, B., & **Bai**, Y. (2021). Intercomparison of empirical formulations of maximum wind radius in parametric tropical storm modeling over Zhoushan Archipelago. *Sustainability, 13*(21), 11673.

291. **Zheng**, J. H., **Wang**, J. C., **Zhou**, C. Y., **Zhao**, H. J., & **Sang**, S. (2017). Numerical simulation of typhoon-induced storm surge along Jiangsu coast, Part II: Calculation of storm surge. *Water Science and Engineering, 10*(1), 8-16.

292. **Zijlema**, M., **Van Vledder**, G. P., & **Holthuijsen**, L. H. (2012). Bottom friction and wind drag for wave models. *Coastal Engineering, 65*, 19-26.

293. **Lynch**, D. R., & **Gray,** W. G. (1979). A wave equation model for finite element tidal computations. Computers & fluids, 7(3), 207-228.

294. **Mandal**, G. S., & **Mohapatra**, M. (2010). Cyclone hazard prone districts of India: a report. National Disaster Management Authority, Government of India, New Delhi, 44.

295. **Ministry of Home Affairs (MHA)**. (2024). Ministry of Home Affairs. Retrieved February 24, 2025, from https://www.mha.gov.in/en

296. **Black, K. P., Baba, M., Mathew, J., Chandra, S., Singh, S. S., Shankar, R., ... & Ray, G. (2018)**. Climate change adaptation guidelines for coastal protection and management in India. Prepared by GCGANZDEC (New Zealand) for the Global Environmental Facility and Asian Development Bank.

297. **Intergovernmental Panel on Climate Change (IPCC)**. (2021). Sixth Assessment Report (AR6), Working Group I: The Physical Science Basis. Retrieved from https://www.ipcc.ch/report/sixth-assessment-report-working-group-i/

298. **Lagarias, J. C., Reeds, J. A., Wright, M. H., & Wright, P. E. (1998)**. Convergence properties of the Nelder–Mead simplex method in low dimensions. SIAM Journal on Optimization, 9(1), 112–147.

CURRICULAM VITAE

Name: **V. G. Shashank**

Date of birth: 2^{nd} October, 1992

EDUCATIONAL QUALIFICATIONS

2014: Bachelor of Engineering (B. E.)

Institution: Dayanand Sagar College of Engineering, Bangalore, India

Specialization: Aeronautical Engineering

2020: Master of Technology (M. Tech.)

Institution: Indian Institute of Technology Bhubanesawar, India

Specialization: Climate Science and Technology

2025: Doctor of Philosophy (Ph. D.)

Institution: Indian Institute of Technology Madras, India & RWTH Aachen University, Aachen, Germany

Specialization: Ocean Engineering and Hydraulic Engineering

Registration Date: 31-08-2020

DOCTORAL COMMITTEE AT IIT MADRAS

CHAIR PERSON	**Dr. Nilanjan Saha** Professor Department of Ocean Engineering Indian Institute of Technology Madras
GUIDE(S)	**Dr. S. A. Sannasiraj** Professor Department of Ocean Engineering Indian Institute of Technology Madras
	Dr. V. Sriram Professor Department of Ocean Engineering Indian Institute of Technology Madras
	Dr.-Ing. Holger Schüttrumpf Head and Professor Institute of Hydraulic Engineering and Water Resources Management RWTH Aachen University
MEMBERS	**Dr. Soumendra Nath Kuiry** Associate Professor Department of Civil Engineering Indian Institute of Technology Madras
	Dr. Suresh Kumar G Professor Department of Ocean Engineering Indian Institute of Technology Madras
	Dr. Narendran K Assistant Professor Department of Ocean Engineering Indian Institute of Technology Madras